Quantum-enhanced imaging and sensing with spatially correlated biphotons

Ermes Toninelli

A thesis submitted in fulfilment of the requirements for the degree of
Doctor of Philosophy

School of Physics and Astronomy
College of Science and Engineering
University of Glasgow

March 2020

Abstract

In this thesis I discuss the experimental demonstration of quantum-enhanced imaging and sensing schemes able to surpass the performance of their classical counterparts. This is achieved by exploiting the spatial properties of quantum correlated biphotons. Over the next chapters I first discuss the production and detection of quantum correlated photons using a type-I nonlinear crystal and a single-photon sensitive electron-multiplying CCD camera. I then provide a simple yet powerful description of the spatially resolved detection of biphotons, allowing to accurately model and assess the performance of the quantum-enhanced schemes featured in this thesis. These consist of a shadow-sensing and an imaging scheme able to respectively beat the shot-noise-limit in the optical measurement of the position of a shadow and the diffraction limit in the full-field imaging of real-world objects. A combination of simulated and experimental results are used to investigate both the achieved and theoretically available quantum advantage. Optical losses and detector noise are found to limit the better-than-classical performance of the schemes, which rely on the ability to jointly detect an as high as possible number of spatially correlated biphotons.

Contents

List of Figures

List of Tables

Acknowledgements

I am grateful to my wife and life companion Shi Ying for providing meaning and wisdom. I am also grateful to my families in Italy and China: Silvana, Aldo, Luisa, Camillo, Itala, Valerio, Enrica, Stefano, Lorenzo, Manuela, Alessandro, Arianna, Laura, Efrem, Ruben; and Li Jie, Ma Shi Xin, Yan Xuan, Xing Yuan, Yan Hua, Ri Xin, Guan Xin, Brandon, Mimi; and Guo Li, Liu Cai, Cheng Min, Yang Hang, Guo Wei, Huo Ning. You are my foundation.

I would like to thank Miles Padgett, Andrew Harvey, Andrew Forbes, and Pietro Collura for being incredible role models and for being a source of inspiration, ambition, persistence, and curiosity.

I would also like to thank colleagues and friends for being there: Graham Gibson, Johannes Courtial, Sonja Arnold, Paul-Antoine Moreau, Thomas Gregory, Matthew Edgar, Neal Radwell, Daan Stellinga, Euan Cowie, Adam Mihalyi, Jakub Bělín, Ryan Hawley, Reuben Aspden, Peter Morris, Chen Shou Qian, Qi Nan, Sun Bao Qing, Su Su, Zhang Yiwei, Liu Rue Feng, Rui Qing, David Phillips, Markus Nemitz, Alastair Doye, Yan Shu and Ewan Adams; and Cui Yu Lie, Mr. Gao, Chen Peng, Ji li Er, Ming Dan, Mr. Jiang Shi, Liu Bo; and Zhang Jie, Yao Ge, Lele, Yueyue; and Li Xia, Su Yuyang, Xixi, Nuanuan; and Carmelo, Adam, Bereneice, Isaac, Mitch, Nkosiphile, Hentz, Bienvenu; and Christophe Petit, Camile Asmar, Wang Meng, Yassine Mokdad; Sara, Roger, Annie, and many others!

Lastly, I would like to thank the EPSRC Centre for Doctoral Studies in Intelligent Sensing and Measurement, especially Michelle Carmichael and Jennifer Dickson for the amazing support during my PhD.

Declaration of Authorship

I hereby declare that this thesis is the result of my own work, except where explicit reference is made to the work of others, and has not been presented in any previous application for a degree at this or any other institution.

Ermes Toninelli

Publications

This thesis is the culmination of the work carried out during my PhD in the Optics group at the University of Glasgow, under the supervision of Prof. Miles Padgett and in the Structured Light group, during my visit in South Africa at Wits University, under the supervision of Prof. Andrew Forbes. A list of the peer-reviewed papers co-authored during my PhD is given below.

- **E. Toninelli**, R. S. Aspden, D. Phillips, G. M. Gibson, and M. J. Padgett. "The Transition from a Coherent Optical Vortex to a Rankine Vortex: Beam Contrast Dependence on Topological Charge." Journal of Modern Optics 63, no. sup3 (December 15, 2016): S51–56.

- **E. Toninelli**, M. P. Edgar, P.-A. Moreau, G. M. Gibson, G. D. Hammond, and M. J. Padgett. "Sub-Shot-Noise Shadow Sensing with Quantum Correlations." Optics Express 25, no. 18 (September 4, 2017): 21826–40.

- **E. Toninelli**, M. P. Edgar, P.-A. Moreau, G. M. Gibson, G. D. Hammond, and M. J. Padgett. "Quantum Position Measurement of a Shadow: Beating the Classical Limit." In Frontiers in Optics, FTu5E-3, 2017.

- **E. Toninelli**, P.-A. Moreau, A. Mihalyi, T. Gregory, M. P. Edgar, and M. J. Padgett. "Resolution-Enhanced Imaging with Quantum Correlations." In Conference on Lasers and Electro-Optics, FF1B.1. Conference on Lasers and Electro-Optics. Optical Society of America, 2018.

- P.-A. Moreau*****, **E. Toninelli***, T. Gregory, and M. J. Padgett. "Ghost Imaging Using Optical Correlations." Laser and Photonics Reviews 12, no. 1 (January 1, 2018) (***equal contributions**)

- G. M. Gibson*, **E. Toninelli***, S. AR. Horsley, G. C. Spalding, E. Hendry, D. Phillips, and M. J. Padgett. "Reversal of Orbital Angular Momentum Arising from an Extreme Doppler Shift." Proceedings of the National Academy of Sciences, 2018, 201720776. (***equal contributions**)

- P.-A. Moreau, **E. Toninelli**, P. A. Morris, R. S. Aspden, T. Gregory, G. Spalding, R. W. Boyd, and M. J. Padgett. "Resolution Limits of Quantum Ghost Imaging." Optics Express 26, no. 6 (March 19, 2018): 7528–36.

- P.-A. Moreau, P. A. Morris, **E. Toninelli**, T. Gregory, R. S. Aspden, G. Spalding, R. W. Boyd, and M. J. Padgett. "Experimental Limits of Ghost Diffraction: Popper's Thought Experiment." Scientific Reports 8 (2018).

- M. J. Padgett, **E. Toninelli**, T. Gregory, and P. -A. Moreau. "Beating classical imaging limits with entangled photons." Proc. SPIE 10934, Optical, Opto-Atomic, and Entanglement-Enhanced Precision Metrology, 109341R (2019).

- **E. Toninelli***, B. Ndagano*, A. Vallés, B. Sephton, I. Nape, A. Ambrosio, F. Capasso, M. J. Padgett, and A. Forbes. "Concepts in quantum state tomography and classical implementation with intense light: a tutorial" Advances in Optics and Photonics 1, no. 11 (2019). (***equal contributions**)

- **E. Toninelli**, P.-A. Moreau, T. Gregory, A. Mihalyi, M. Edgar, N. Radwell, and M. J. Padgett. "Resolution-enhanced quantum imaging by centroid estimation of biphotons." Optica 6, no. 8, (2019).

- P.-A. Moreau, R. S. Aspden, **E. Toninelli**, T. Gregory, P. A. Morris, and M. J. Padgett. "Testing a Bell inequality in full field images of spontaneous parametric down-conversion." (QIM) V: Quantum Technologies, T5A.61, (2019).

- P.-A. Moreau, **E. Toninelli**, T. Gregory, and M. J. Padgett. 'Imaging with Quantum States of Light'. Nature Reviews Physics 1, no. 6 (June 2019).

- M. A. Cox, **E. Toninelli***, L. Cheng, M. J. Padgett, and A. Forbes. 'A High-Speed, Wavelength Invariant, Single-Pixel Wavefront Sensor With a Digital Micromirror Device'. IEEE Access 7 (2019). (***equal contributions**)

- **E. Toninelli**, M. A. Cox, G. M. Gibson, S. D. Brown, M. P. Edgar, A. Forbes, and M. J. Padgett. 'A Compact Acoustic Spanner to Rotate Macroscopic Objects'. Scientific Reports 9, no. 1 (1 May 2019).

- P.-A. Moreau, **E. Toninelli**, T. Gregory, R. S. Aspden, P. A. Morris, and M. J. Padgett. 'Imaging Bell-Type Nonlocal Behavior'. Science Advances 5, no. 7 (1 July 2019).
- T. Gregory, P.-A. Moreau, **E. Toninelli**, and M. J. Padgett. "Imaging Through Noise With Quantum Illumination". Science Advances 6, no. 6 (1 February 2020)
- **E. Toninelli**, D. Stellinga, B. Sephton, A. Forbes, and M. J. Padgett. "Single-pixel imaging using caustic patterns." In production.

Additionally, the following manuscripts are currently being reviewed/prepared.

- **E. Toninelli**, P.-A. Moreau, T. Gregory, and M. J. Padgett. "A model for quantum imaging and sensing experiments based on the detection of correlated biphotons using a photon-counting camera." In preparation.
- T. Gregory, **E. Toninelli**, P.-A. Moreau, and M. J. Padgett. "Reducing camera noise for low light-level imaging." In preparation.

Abbreviations

BBO	β- **B**arium **B**orate
CEBs	**C**entroid **E**stimation of **B**iphotons
CIC	**C**lock **I**nduced **C**harge
EMCCD	**E**lectron **M**ultiplying **C**harge-**C**oupled **D**evice
DOC	**D**egree **O**f **C**orrelation
DMD	**D**igital **M**icromirror **D**evice
EPR	**E**instein **P**odolsky **R**osen
ESF	**E**dge **S**pread **F**unction
FWHM	**F**ull **W**idth **H**alf **M**aximum
HL	**H**eisenberg **L**imit
HWP	**H**alf **W**ave **P**late
ICCD	**I**ntensified **C**harge-**C**oupled **D**evice
LCD	**L**iquid **C**rystal **D**isplay
LSF	**L**ine **S**pread **F**unction
MTF	**M**odulation **T**ransfer **F**unction
MTFA	**M**odulation **T**ransfer **F**unction **A**rea
NA	**N**umerical **A**perture
OCM	**O**ptical **C**entroid **M**easurement
OTF	**O**ptical **T**ransfer **F**unction
PSF	**P**oint **S**pread **F**unction
PTF	**P**hase **T**ransfer **F**unction

QE	**Q**uantum **E**fficiency
QNR	**Q**antum **N**oise **R**eduction
ROI	**R**egion **O**f **I**nterest
sCMOS	**s**cientific **C**omplementary **M**eta **O**xide **S**emiconductor
SD	**S**tandard **D**eviation
SLM	**S**patial **L**ight **M**odulator
SNL	**S**hot **N**oise **L**evel
SNR	**S**ignal to **N**oise **R**atio
SPAD	**S**ingle- **P**hoton **A**valanche **D**iode
SPDC	**S**pontaneous **P**arametric **D**own **C**onversion
SQL	**S**tandard **Q**uantum **L**imit
UV	**U**ltra **V**iolet

Glossary of Symbols

A, B	Two halves of the split-photodiode and the corresponidng event counts.
$*$	Convolution operation.
$**$	Two-dimensional convolution operation.
::	Normal and time ordering.
$\approx$	Approximately.
α	Adjustment constant used to compensate various approximations in the formulation of the mode function of collinear signal and idler photons.
$B(x, y)$	Bright-events coordinates function.
$C(\boldsymbol{\rho_1}, \boldsymbol{\rho_2})$	Intensity correlation function.
$\tilde{C}(\boldsymbol{\rho_1}, \boldsymbol{\rho_2})$	Normal ordered covariance between two pixels of coordinates $\boldsymbol{\rho_1}$ and $\boldsymbol{\rho_2}$.
$\chi^{(1)}$, $\chi^{(2)}$, $\chi^{(3)}$	Linear susceptibility, second-, and third-order nonlinear susceptibilities.
d	Frame of width in pixels.
$D(x, y)$	Dark-events coordinates function.
$\overrightarrow{\Delta k}$, $\overrightarrow{\Delta k_z}$	Phase-mismatch term.
$\overrightarrow{k_p}$, $\overrightarrow{k_s}$, $\overrightarrow{k_i}$	Angular wavevectors of the pump, signal and idler photons.
$\Delta\ell$	Separation between two point-sources.

Δp	Range of momenta.
Δs	Spatial width of the bins of the oversampled ESF.
Δx	Range of positions.
$\delta(x)1(y)$	Line-source object: a delta-function in x and a constant in y.
$\delta(x, y)$	Two-dimensional delta-function: a function defined in the xy-plane, that is infinite at the origin and zero everywhere else.
δX_c	Mid-point between the detected position of the s and i photons of a biphoton packet.
δX_i, δX_s	Distances between the detected positions of the s and i photons in the transverse plane of the detector and their original transverse positions in the plane of the object.
E_{ij}	Set of discrete samples of the ESF of the system.
$E(t)$	Strength of an applied optical field.
ϵ_0	Permittivity of free space.
ESF(s)	Oversampled edge-spread function.
η_{EMCCD}	The QE of the EMCCD camera detector.
η_{total}	Total effective QE of the detection channel, including optical, detector, and thresholding losses.
f	Focal length.
f_e	Effective focal length.
$f_{\text{mes.}}(x)$	Measured intensity-profile used in the model to determine the overall intensity distribution of the bright-events.
$F(x, y)$	Detected pixel-coordinates function.
$\mathcal{FF}$	Two-dimensional Fourier transform.
$g_c(x)$, $g_m(x)$	Gaussian curves used in the model to approximate the intensity profiles of the downconverted beam and of the correlation peak.
$G^{(2)}(t, t')$	Normal- and time-ordered intensity correlation function.
$g^{(2)}(\tau)$	Degree of second order temporal coherence.

$g(x, y)$	Output intensity distribution of an imaging system.
$h(x, y)$	Impulse response of an imaging system.
$I(t)$	Photon-flux operator.
k, Δk_z	Wavenumber and range of longitudinal projections of the wavenumber.
$k_{s,i,p}$	Wavevector of signal, idler, or pump photon.
l_{min}	Minimum free-path.
L	Length of the crystal along the propagation direction of the pump.
$\lambda_{s,i,p}$	Wavelength of signal, idler, or pump photons.
M	Magnification of the imaging system.
$\langle\ \rangle$	Mean operation.
$\mathcal{C}$	Total volume of the correlation function.
$\langle\mathcal{C}\rangle$	Mean integral of the correlation function.
$\mathcal{C}_q(\boldsymbol{\rho})$	Contribution of the correlation function due to biphotons.
$\mathcal{C}_{exp}$	Experimental correlation function $\mathcal{C}_{exp}$ found by cross-correlating a frame with the 180-degree rotated copy of itself.
$\langle N\rangle$	Mean number of detected events or photons.
$\langle N\rangle_{\text{exp.}}$	Mean number of experimentally detected events.
$\mu_{readout}$	Mean of the electronic readout noise of the EMCCD camera, measured in ADC counts.
n	Tag-number associated with a pair of modelled pixel-coordinates of a bright-event.
N_B	Number of bright events.
N_c	Number of spatially-correlated events.
N_D	Number of dark events.
$n_{e,o}$	Extraordinary, ordinary refractive indices.
$\hat{n}$	Photon-number operator.
N	Number of photons or events.

n_k	Number of pixels whose distance from the edge falls within $(k - \frac{1}{2}\Delta s)$ and $(k + \frac{1}{2}\Delta s)$.
N_p	Number of biphotons generated by the SPDC source as set in the model.
N_{pe}	Number of detected biphoton-events or photon-pair events.
$N(\boldsymbol{\rho})$	Number of detectable photons in a frame at coordinates $\boldsymbol{\rho}$.
N_s	Number of single (or unpaired) photons.
N_t	Total number of generated photons.
N_u	Total number of spatially uncorrelated events.
Ω	Detection operator that determines whether a photon is detected or missed.
ω_p, ω_s, ω_i	Angular frequencies of the pump, signal and idler photons.
p	Momentum.
$P(n_{th})$	Probability of detecting the n_{th} photon.
$\mathcal{P}(\boldsymbol{\rho_1}, \boldsymbol{\rho_2})$	Joint-detection probability for photon-pairs.
$\mid \beta\rangle$	Glauber coherent state of a single-mode electromagnetic field.
$P(t)$	Dipole moment per unit volume of a material system.
p_z	Longitudinal momentum.
φ	Angle between the optic axis of the nonlinear crystal and the direction of propagation of the pump.
$\mid \psi\rangle$	NOON state in bra-ket notation.
r	Mean loss in resolution.
$\boldsymbol{\rho_1}$, $\boldsymbol{\rho_2}$	Two pixel coordinates in the plane of the detector.
ρ'	Dummy variable.
$(\sigma_c)_{\text{detected}}$	Detected size of the transverse correlation width.
S_b	Transverse area of the downconverted beam at the detector plane.
$s(i, j)$	Edge function.
S_m	Transverse area of a mode at the detector plane.

SD_p	Standard deviation of the Gaussian pump beam, measured from the beam axis.
$\mathrm{SD}_{readout}$	Standard deviation of the electronic readout noise of the EMCCD camera, measured in ADC counts.
$step(x)1(y)$	Unit-step function.
σ_+	Normalised variance of the sum of the integrated signals A and B of a split-detector.
σ_c	Detected transverse correlation width in the image or momentum plane of the crystal.
σ_{DOC}	Degree of correlation or quantum noise reduction factor.
σ_m	Overall transverse spatial extent of the downconverted beam, as measured in plane of the detector.
σ_{PSF}	Size of the detected diffraction limited spot of the system.
σ_p	Momentum transverse correlation width in a collinear and degenerate type-I phase matching process.
σ_x	Position transverse correlation width in a collinear and degenerate type-I phase matching process.
T	Photon-discriminating threshold.
τ	Time delay between detector signals.
θ	Angle of the slanted-edge or optimal phase-matching angle.
$u(0,1)$	Uniform distribution used to computationally generate pseudo-random numbers between 0 and 1.
u, v	Reciprocal variables in Fourier space of x, y.
Var	Variance operation.
w_{ROI}	Width of the ROI in the plane of the detector.
w_{shadow}	Width of the shadow in the plane of the detector.
x	Position.

$x_{m,c}$	Generated pseudo-random values from a Gaussian distribution.
x_n	Pseudo-random number between 1 and d generated from the uniform distribution $u_D(1, d)$.
x_n, y_n	Pair of pixel-coordinates x_n, y_n of a modelled biphoton packet.
$X_{s,i}$	X-offsets (abscissae) to the modelled pixel-coordinates of the position anticorrelated signal and idler photons.
ξ_{max}	Cut-off frequency of an MTF curve defined as the maximum spatial frequency at which the MTF goes to zero or reaches the noise-floor.
xy-plane	Transverse plane.
$y_{m,c}$	Generated pseudo-random values from a Gaussian distribution.
y_n	Pseudo-random number between 1 and d generated from the uniform distribution $u_D(1, d)$.
$Y_{s,i}$	Y-offsets (ordinates) to the modelled pixel-coordinates of the position anticorrelated signal and idler photons.

When bananas don't work, try a cookie.

L. M. Fields

Chapter 1

Introduction

1.1 Preamble

Significant progress has been made in the field of quantum optics, starting from the early postulates of quantum mechanics and continuing with validity-tests and failed falsification attempts. Nowadays the field has reached a certain maturity and it is possible to harness the power of quantum mechanics for the realisation of quantum-enhanced, real-world applications [1, 2]. Nonetheless, many unanswered questions remain, such as: "What is the future of quantum coherence, squeezing and entanglement for enhanced super-resolution and sensing?" or "What new technologies and fundamental discoveries might quantum optics achieve by the end of this century?". These and other questions were recently the object of some serious pondering by world-leading physicists and engineers at the Winter Colloquium on the Physics of Quantum Electronics [3].

How can quantum mechanics deliver an enhancement in real-world sensing and imaging applications?

This question has motivated my co-workers and I in the development of quantum-enhanced schemes able to surpass the performance their classical counterparts. The bar was set high by choosing to improve upon already optimised classical realisations of a certain sensing or imaging scheme, as well as previous state-of-the-art quantum-imaging realisations by fellow researchers in the Optics Group in Glasgow.

The quantum-enhanced schemes developed by my co-workers and I were able to respectively beat the shot-noise-limit in the optical measurement of the position of a shadow and the diffraction limit of a limited numerical-aperture imaging system, as discussed in the works reported in this thesis. As shown in the next chapters, better-than-classical performance was achieved by exploiting the quantum correlations of downconverted biphotons , specifically their spatial correlations of entangled photon-pairs generated through spontaneous parametric downconversion (SPDC), as detected by state-of-the-art, single-photon sensitive camera technology.

The work in this thesis was born as a natural continuation of the work by M. Edgar et al [4], in which an electron-multiplying CCD (EMCCD) camera (Andor iXon 3 897) was employed to image the high-dimensional spatial entanglement of biphotons produced by a type-I nonlinear crystal. When I started my Ph.D (2.5 years post the work by M. Edgar), the research efforts of the Optics Group had shifted to quantum ghost imaging [5, 6], using intensified CCD cameras and single-photon avalanche detectors (SPADs). Therefore, my early efforts started by setting up a quantum imaging system, based on SPDC illumination, investigating the detection of spatially correlated biphotons as detected by an EMCCD camera, placed in either the near-field or far-field of a type-I nonlinear crystal.

Using the funds made available by the Integrative Sensing and Measurement Centre for Doctoral Training, the latest state-of-the-art EMCCD camera was purchased,

an Andor ULTRA 888, and I proceeded by coding in LabVIEW the acquisition, data handling, and analysis programmes required to operate the camera. I then characterised the EMCCD camera noise sources and learned the effects of its many acquisition parameters over the number of detected spatially correlated biphotons.

This early work lead to the quantum-enhanced sensing and imaging experiments discussed in this thesis. Under the supervision of Prof. Miles Padgett I designed and realised these schemes, as well as compiled them into manuscripts, which I presented at conferences [7, 8], and published on mainstream research journals [9, 10]. Dr. Paul-Antoine Moreau, whom joined the Optics group at the beginning of the second year of my PhD, assisted with some of the mathematical formulations of the manuscripts I wrote thereafter, as well as providing useful discussions. A number of co-workers (co-authors of the published manuscripts of which some of the results in this thesis are featured) also assisted providing useful discussions.

Two quantum-enhanced schemes are featured in this thesis [1]:

1. Sub-shot-noise shadow-sensing with quantum correlations,

2. Resolution-enhanced quantum imaging by centroid estimation of biphotons (CEBs).

[1] Some of the results featured in this thesis are based on the following published manuscripts:
E. Toninelli, M. P. Edgar, P.-A. Moreau, G. M. Gibson, G. D. Hammond, and M. J. Padgett. "Quantum Position Measurement of a Shadow: Beating the Classical Limit." In Frontiers in Optics, FTu5E-3, 2017 [7];
E. Toninelli, M. P. Edgar, P.-A. Moreau, G. M. Gibson, G. D. Hammond, and M. J. Padgett. "Sub-Shot-Noise Shadow Sensing with Quantum Correlations." Optics Express 25, no. 18 (September 4, 2017): 21826–40 [9];
E. Toninelli, P.-A. Moreau, A. Mihalyi, T. Gregory, M. P. Edgar, and M. J. Padgett. "Resolution-Enhanced Imaging with Quantum Correlations." In Conference on Lasers and Electro-Optics, FF1B.1. Conference on Lasers and Electro-Optics. Optical Society of America, 2018 [8];
E. Toninelli, P.-A. Moreau, T. Gregory, A. Mihalyi, M. Edgar, N. Radwell, and M. J. Padgett. "Resolution-enhanced quantum imaging by centroid estimation of biphotons." Optica 6, no. 8, (2019) [10].

In the next sections I introduce both topics, establishing the issues being tackled, the approaches taken by my co-workers and I, and the significance of these works with respect to what other people have done.

1.2 Sub-shot-noise shadow-sensing with quantum correlations

Shadow-sensing (i.e. a type of 'split-field' sensing) was brought into the spotlight following the work by L. Carbone et al. on the optical sensors used for the Birmingham Optical Sensor and Electro-Magnetic actuator of the Advanced LIGO mirror suspensions [11]. The proposed design was then 'borrowed' and applied to much smaller scale apparatus: the 'WeeG' MEMS gravimeter device [12], recently developed at the University of Glasgow.

A shadow-sensor is a type of optical position measurement device consisting of three main components: a light-source (LED), a shadow-casting object, and a split-photodiode detector, as shown in Fig. 1.1.

This type of sensor is used to optically measure forces that are coupled to the motion of the shadow-casting object, by detecting relative changes in the intensity of light incident on the two-halves (A and B) of the photo-diode. The generated photocurrents, represented in Fig. 1.1(b), are amplified by low-noise electronics, allowing the WeeG device to measure variations in local gravitational acceleration smaller than 10μGal [12, 13], corresponding to 1 nm relative-displacement of the shadow-casting object over a one-day timescale [14].

The ultimate precision limit of a device based on an optical displacement measurement is linked to the ability to measure the intensity of a probing light-field, which in

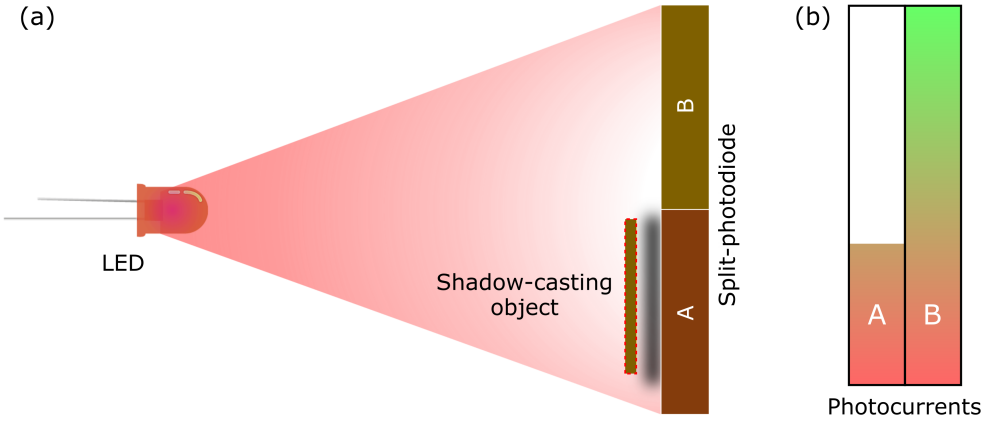

FIGURE 1.1: **Optical position measurement of a shadow.** A shadow-sensor is a type of optical position measurement device that is able to measure physical quantities coupled to the position of a shadow-casting object. As shown in (a) the main components of this device are a light-source (LED), which illuminates a shadow-casting object. This projects a shadow on a split-photodiode resulting in varying levels of photocurrents produced by the two halves of the split-photodiode A and B. The position of the shadow-casting object can be determined for instance, by taking the difference of the two signals produced by the two halves of the split-detector, represented in (b) in the case of one of the two halves of the split-detector being almost completely obscured by the shadow.

other words is the ability to precisely count photons. Even in the case of a perfectly noiseless detector able to produce a well-defined signal for each incoming photon, the measured noise performance will not be better than the shot-noise-limit (SNL). Indeed, in the absence of excess noise of either the source or the detector, the error associated to the measurement of the intensity of a classical light-source cannot be lower than the SNL, which determines the lowest photon-number fluctuations of a classical light-source. Such limit can in principle be reached in the case of photons in the coherent state, such as those produced by an ideal laser.

Thus, in the case of a classical shadow-sensor in which a quasi-thermal LED light-source is employed, as shown in Fig. 1.1, the number of detected photons over the two halves of the split-detector A and B will cause the fluctuations of $(A - B)$ to

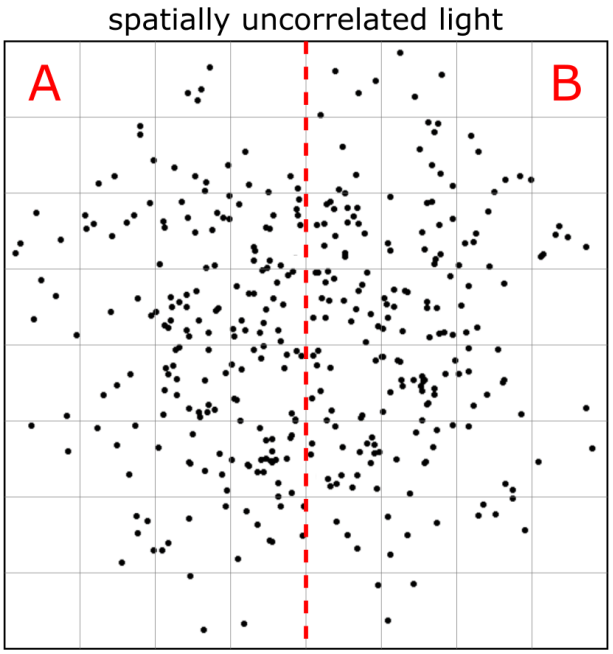

FIGURE 1.2: **Shadow-sensing with a spatially uncorrelated classical light-source.** In the case of a thermal or quasi-thermal light source, such as an incandescent light-bulb or an LED, the variance of the difference of the photons detected by the two halves of a noiseless split-detector (A and B) is greater than the mean of the total number of detected photons. This type of statistics has super-Poissonian properties and in the context of an optical measurement is characterised by noise fluctuations that are worse than the SNL.

be greater than those associated to the SNL (i.e. super-Poissonian), such that:

$$\mathrm{Var}(A - B) > \langle A + B \rangle \,, \tag{1.1}$$

where Var( ) indicates the variance operation. This is represented in Fig. 1.2, in which the spatially resolved detections of uncorrelated photons over the two halves of the split-detector are highlighted.

1.2.1 Quantum noise-reduction techniques

As discussed in the previous section, the SNL sets an important benchmark for the noise performance of a sensing scheme. I also discussed that a classical optical measurement can only reach the SNL in the case of an ideal detector and light in the so

called coherent state. Noise reduction using quantum states of light finds applications in quantum metrology [1, 15], for instance in increasing the sensitivity of measurement schemes, as in the case of gravitational wave detectors [16, 17]. With the advent of quantum squeezed light [18, 19] and definite number of photons states [20, 21], a series of quantum noise reduction (QNR) techniques were developed, able to reach and beat the SNL by exploiting the properties of quantum states [22–29].

As a result of more than 30 years of research, enhanced sensitivity in phase [30], absorption estimation [31–35], beam localisation [36, 37], and in the detection of entanglement between a few spatial modes [38–40] were achieved using squeezed light. This approach to noise reduction is based on technically advanced interferometers and homodyne detection schemes and an impressive 15 dB noise suppression below the vacuum noise level was recently demonstrated by H. Vahlbruch et al. as applied to the calibration of the quantum efficiency (QE) of photoelectric detectors [41].

A technically simpler approach to quantum-enabled noise reduction that does not require a homodyne detection is the exploitation of intensity correlations between twin-beams in a lower photon-flux regime dominated by spontaneous emission. The noise reduction relies on the very similar photon-number fluctuations of the signal and idler beams, since each spontaneous decay of a high energy pump photon results in the production of exactly one signal and one idler photon [42]. Under this condition and employing a differential measurement strategy by which the desired observable is equal to the difference of the detected signal and idler photons, it is possible in principle to perform a noise-free measurement. Interestingly, whereas either the pump, signal, or idler beams may be characterised by super-Poissonian photon-number fluctuations, the difference in the fluctuating number of signal and idler photons will be sub-Poissonian, as the two beams fluctuate in an equal manner [43]. Such noise reduction was historically first demonstrated using single-pixel bucket detectors, used to detect the whole transverse extent of the signal and idler

beams [25, 44–48]. It can be appreciated that in this type of single-mode detection schemes, optimal noise reduction is only achieved if the whole beam falls within the extent of the detector. Indeed if only a small portion of the signal beam was to be missed, the resulting degradation of the noise-reduction scheme would also account for the now unbalanced corresponding portion of the idler beam. In practice, due to the theoretically infinite transverse extent of collimated optical beams (which therefore cannot completely be captured by the detector) and noise of the detector, the difference of signals will not be zero. Nevertheless it is still possible to achieve and beat the SNL, even in the case of extra noise introduced by a non-ideal detector, as long as the detected intensity correlations are strong enough to compensate. These photon-number spatial fluctuations of downconverted photon-pairs were investigated using both type-I [49, 50] and type-II [43, 51–53] downconversion sources, leading to the famous first experimental demonstration of sub-shot-noise quantum imaging of a highly transmissive object (≈95%) by Brida et al. [54], in which the intensity correlations between signal and idler beams of a type-II downconversion were detected by a high-efficiency CCD camera in a relatively high-photon flux regime (about 7000 photons per pixel per frame) [54].

1.2.2 Sub-shot-noise shadow-sensing

In the case of a quantum shadow-sensor scheme in which the spatial anticorrelations of SPDC biphotons are employed, the number of detected photons over the two halves of the split-detector A and B, will cause the fluctuations of $(A - B)$ to be lower than those associated to the SNL (i.e. sub-Poissonian), such that:

$$\mathrm{Var}(A - B) < \langle A + B \rangle \tag{1.2}$$

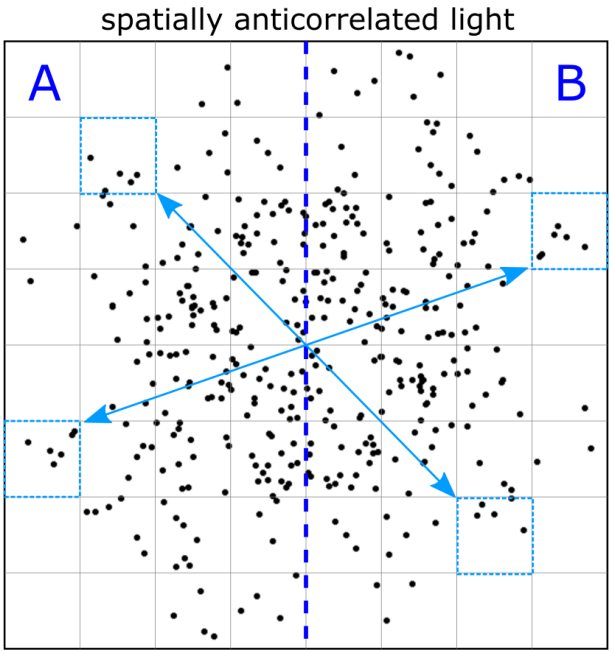

FIGURE 1.3: **Shadow-sensing with a quantum spatially correlated light-source.** In the case of a quantum correlated light-source, such as SPDC, the variance of the difference of the photons detected by the two halves of a noiseless split-detector photocurrents (A and B) is less than the mean of the total number of detected photons. This type of statistics has sub-Poissonian properties and in the context of an optical measurement is characterised by noise fluctuations that are better than the SNL. The blue-dotted boxes connected by arrows highlight the spatial anticorrelated properties of the detected photons, which allow the difference of signals A and B to tend to zero.

This is represented in Fig. 1.3, in which the spatially resolved detections of anticorrelated photons over the two halves of the split-detector are highlighted. Therefore, even in the case of noisy detector, the noise performance of a quantum shadow-sensor may be better than the SNL, provided that the signals produced by the detected anticorrelated photons is greater than that associated with the uncorrelated noise.

1.3 Resolution-enhanced quantum imaging by centroid estimation of biphotons

In this section I set the scene regarding the Rayleigh limit of the optical resolution of an imaging system, discussing previous attempts to circumvent this limit using quantum-enabled approaches. I will then show how the the spatial properties of SPDC biphotons can be exploited to overcome the limitations of previous schemes and achieve a standard-quantum-limited resolution enhancement beyond the classical bound.

The efforts toward achieving an enhancement in the optical resolution of an imaging system have resulted in a considerable number of interesting techniques, based on both classical- and quantum-illumination. These differ from computational- or technical-approaches, which are used to improve the resolution of an image using post-processing techniques, a review of which can be found in the work by S. C Park et al. [55]. On the classical front, the famous stimulation-emission-depletion (STED) microscopy [56], ground-state-depletion (GSD) microscopy [57], photoactivated-localisation microscopy (PALM) [58] and stochastic optical reconstruction microscopy (STORM) [59] have allowed to reach sub-diffraction resolutions [60, 61]. However, relying on the optically induced fluorescence (and the subsequent quenching for STED and GSD) of molecules, typically requires considerable photon-doses [62]. Additionally, a number of techniques that make use of scanning source/detector configurations have also allowed to extract a higher-resolution image of the object. These techniques are based for example on the number-resolved post-selection of classical light-sources [63], the second-order correlation of speckled-illumination [64], or 'chaotic' light [65], and higher-order correlation measurements of a double-slit interference pattern using speckled-light [66].

1.3.1 Quantum resolution-enhanced imaging schemes

For what concerns quantum protocols, it is possible to exceed the Rayleigh limit by either employing a standard-quantum-limited (SQL) or a Heisenberg-limited (HL) approach [67]. The SQL resolution advantage scales as $1/\sqrt{N}$, where N indicates the number of quantum correlated photons [68]. On the other hand, the HL advantage scales as $1/N$, where N is the number of photons of a NOON state, a multi-photon state that effectively 'behaves' as a single indissociable photon of $1/N$ wavelength [69].

For instance, a SQL resolution enhancement was achieved exploiting the nonclassical photon statistics (i.e. the antibunching time-correlations between emitted single-photons) of emitted fluorescence from single-photon quantum emitters [70], colloidal quantum dots [71–73], and fluorescent nitrogen vacancies in diamond [74, 75] (also known as nitrogen colour centres [76]). Additionally, interesting schemes have been developed which consist of a combination of classical approaches and quantum techniques, such as the very recent demonstration consisting of a combination of SIM microscopy and the quantum-enabled approach to resolution-enhancement based on the antibunching properties of fluorescent quantum dots [77] (this particular scheme also employs post-processing in the form of a Fourier filter to accentuate the contribution of high-spatial frequencies in the final reconstructed image).

In the case of HL schemes, quantum lithography stands out, in which N photon NOON states are used to achieve the same resolution advantage achievable by a single photon of N- fold smaller wavelength. Such schemes typically involve interferometric set-ups, in which the multiphoton NOON state travels in its entirety in either one of the arms of the interferometer, and, importantly, must be absorbed in a multiphoton process by a suitable material, generating Heisenberg-superresolved interference patterns [69]. Due to the technical difficulties in realising a high-efficiency

photon-number resolved absorptive material [78–80], the multi-photon absorption requirement was circumvented by a multiphoton optical centroid measurement (OCM) scheme proposed by M. Tsang [81]. This OCM protocol was experimentally realised by H. Shin et al. [82] achieving a 1/2 reduction in the width of fringes, using an interferometer consisting of a source of $N = 2$ NOON states (produced by two type-I crystals, placed in each arm) and coincidence detection between two scanning avalanche photodiodes.

Thus, it appears that in the case of quantum superresolution schemes previous implementations either rely in optically induced fluorescence of the object or on a scanning configuration. Fluorescence is not required in the case of HL schemes, however, as in the case of quantum-lithography, the resolution enhancement is limited to the formation of narrower interference patterns and does not suit image formation. In the case of the recent HL quantum imaging demonstration by M. Unternährer et al., the two-fold resolution enhancement comes at the cost of illuminating the object with twice-as-short wavelength UV light, required to generate the $N = 2$ NOON states.

1.3.2 Resolution-enhanced imaging by CEBs

The resolution-enhanced quantum imaging scheme featured in this thesis is able to achieve a SQL resolution advantage up to $1/\sqrt{2}$, by producing an image entirely made of estimated centroid positions of detected biphotons. Importantly, it does not rely on optically induced florescence and is operated in a full-field configuration at a very low-power regime (i.e. with less than 0.001 infrared photons per pixel per frame).

In the first instance, it may be useful to consider the process of image formation, in the case of a diffraction-free optical system, in which the trajectories and thus the

detected positions of each photon perfectly map the spatial features of the object. Accordingly, if all photons originate from a point, it is fair to assume that all photons will also be detected at a single point in the plane of the detector, corresponding to a delta-function. Additionally, if the source is spatially extended and the photons are partially absorbed by an object placed in the image plane of the source and of the detector, a sharp image of the edge of the object will also be formed, with a resolution only limited by the spatial-sampling of the detector.

However, in the case of a real imaging system affected by diffraction and other optical aberrations, the arrival positions of photons emitted by a point-source will spread over a finite extent. The function that describes the impulse response of an optical system, i.e. the spreading in the positions of the detected photons emitted by a point-source, is known as the point-spread-function (PSF) [83].

An intuitive way to understand how the CEBs approach can return an enhancement in spatial resolution is to consider the aforementioned finite-extent of the PSF. In the case of a centroid estimation performed over the position arrivals of N spatially correlated photons, the broadening of the PSF can be reduced by $1/N$, by only keeping the mid-point coordinates of jointly detected biphotons. Therefore, for each measurement of a biphoton packet, for which the position arrivals of both photons are known, it is possible to estimate the centroid pixel-coordinates and use these to reconstruct a resolution-enhanced image of the object.

In practice such a scheme requires a source of spatially correlated biphotons and a spatially-resolved single-photon sensitive detector. In the implementation discussed in this chapter the source of spatially correlated biphotons is achieved with a type-I nonlinear crystal, used to illuminate an object and detected by a photon-counting EMCCD camera. The acquired binary frames consisting of both noise- and bright-events are post-selected by a pair-finder algorithm, which is used to reject the majority

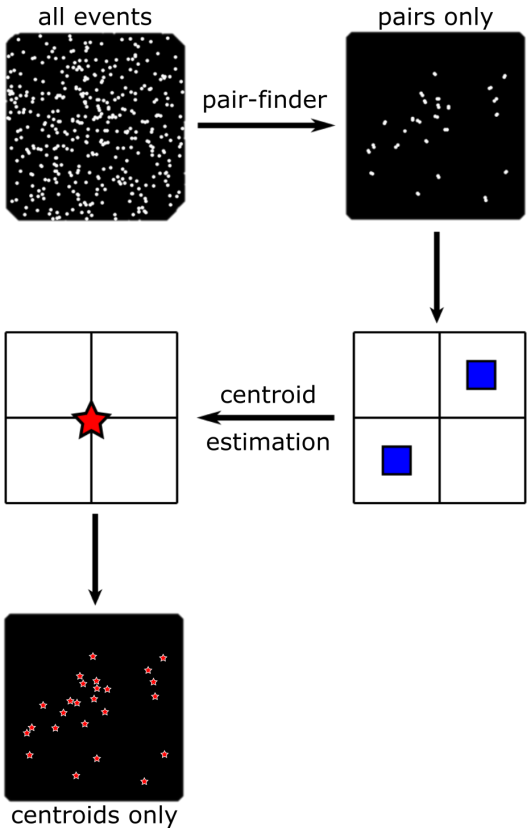

FIGURE 1.4: **Enhancement of optical resolution by estimation of centroid-pixel coordinates.** A pair-finding algorithm is used to select the pair-events from a thresholded binary frame. A centroid-estimation is performed on the positions of N jointly detected photons, i.e. $N = 2$ (blue-squares). These are used to compute the centroid-pixel coordinates of a more precisely located position (red-star). An image entirely formed by centroid-estimated pixel coordinates is sharper since these centroids are $1/\sqrt{N}$ less affected by PSF-spreading effects, as for instance caused by the limited numerical aperture of an imaging system.

of spatially uncorrelated events. The so found pairs are then used to compute centroid pixel-coordinates, which are in turn used to produce a new image, as shown in Fig. 1.4.

This process is repeated for many acquired frames of the object, eventually producing a resolution-enhanced image. The theoretical basis of the SQL resolution-enhancing CEBs scheme is discussed in chapter 6, section 6.1.

1.4 Outline

In chapter 2 I first discuss the background principles of the experiments featured in

this thesis, such as optics at the single photon level, quantum correlations, quantum statistics and distributions, as well as the optical resolution of an imaging system. In chapter 3 I address relevant technological details, such as the production of quantum correlated biphotons using SPDC, their optimised single-photon sensitive detection using an EMCCD camera, and the set-up used to produce SPDC quantum correlated biphotons. In chapter 4 I introduce a simple yet powerful model for the spatially resolved detection of biphotons, that is used in later chapters to simulated the performance of both the quantum-enhanced sensing and imaging schemes. In chapters 5 and 6 I discuss respectively the sub-shot-noise shadow sensing scheme and the resolution-enhanced quantum imaging scheme by CEBs. In Chapter 7 I conclude this thesis by summarising the finding and placing them in the context of relevant literature. Moreover, I present a possible classical realisation of the resolution-enhanced quantum imaging scheme by centroid estimation of biphotons, inspired by the underlying mechanism of its quantum counterpart.

Chapter 2

Background principles

In this chapter I discuss the required background principles, general approaches, and common terminology, in support of the quantum-enhanced schemes featured in this thesis. Specifically I will address the following topics:

1. The photon and the detection of quantum correlations,
2. Quantum statistics and distributions,
3. The optical resolution of an imaging system.

2.1 The photon and quantum correlations

The Encyclopedia Britannica defines the photon as the *"light quantum, minute energy packet of electromagnetic radiation"* [84]. This definition includes both Planck's intuition about the quantisation of the energy of electromagnetic waves [85], and Einstein's revolutionary notion of the photon as a discrete wave-packet of which electromagnetic waves are made [86]. After more than one-hundred years and as a

result of a long series of technical advances, researchers are now able to create and detect quantum states of light.

2.1.1 Optics at the single-photon level

In quantum optics, light is typically considered in a corpuscular/granular manner, such that the outcome of an experiment (which like in the classical case may cumulatively involve a very large number of photons) can be broken down to a series of elementary processes at the single-photon level. This is for instance the case in the resolution-enhancing quantum imaging scheme featured in this thesis, where a final high-resolution and high dynamic-range picture of an object is reconstructed from millions of joint-detections of exactly two-photons per measurement.

According to the widely adopted, albeit ill-defined and controversial, Copenhagen interpretation of quantum mechanics [87–89], the properties of a physical system (such as the polarisation, position, momentum, etc. of a photon) are undetermined until measured. More specifically, it is possible to determine a value for a certain property by performing a measurement, which corresponds to a random sampling of the statistical distribution of all admitted values [90–92]. Schrödinger's cat [93] is often used to illustrate this superposition of states. According to the Copenhagen interpretation, while the cat is out of sight inside a randomly-fated and life-threatening box, it has the same probability of being dead or alive; only after the box is opened and inspected is it possible to affirm the health of the cat. This concept of superposition of states is particularly interesting when considering for example a beam of light going through a piece of glass. Whereas from a classical point of view it is clear that light is transmitted through glass (as in the case of a lit lightbulb), things are less deterministic from a quantum optics perspective. In the same example, a large number of intensity measurements performed at the single-photon level (where 1 or

0 outcomes may indicate the detection or the absence of a photon) will consist of both 1s and 0s, in spite of light clearly going through the glass. It is then possible to express the number of detected 1s and 0s in terms of the probability of light to transmit through the glass. This automatically assumes that the state of the system is in a superposition of states until a measurement is made.

The ability to work with single-photons opens the possibility of engineering their quantum state (i.e. their properties), allowing for novel and useful applications. For example, it is possible to produce quantum-correlated photons with peculiar properties in terms of time, space, momentum, spin, polarisation, etc. [42].

2.1.2 Entanglement

Correlation indicates a mutual relationship between two variables or quantities of a certain strength (for instance a strong or a weak relationship). Moreover, this relationship can be positive or negative (i.e. anticorrelations), typically represented by the slope of the line fitted through data-points plotted against the two quantities in question [94]. For example, the number of favourable/unfavourable votes in a referendum may be found to be correlated/anticorrelated to certain variables, like in the 2016 Brexit referendum [95].

Stronger-than-classical correlations (i.e. quantum correlations) indicates a relationship between quantities of two particles that is better-defined than classically allowed (in the case of plotted data-points against the two correlated quantities, the points would be very closely distributed along a line). In such a strongly correlated system, information about the quantity of one particle (as gained from one measurement) is enough to also infer the corresponding value of a correlated particle within the bounds defined by the strength of the correlation.

Historically, the concept of entanglement appeared in 1935 in a proposed *gedanken* experiment, in the famous paper by Einstein, Podosky, and Rosen (EPR) [96]. The authors considered the situation of two photons entangled simultaneously in two continuous variables, such as position and momentum. In this case, by measuring either the position or momentum of one particle it would be possible to predict with absolute certainty the position or momentum of its entangled partner. The problem of this seemingly action-at-a-distance was that it assumed the simultaneous reality of the position and momentum of the unmeasured particle, thus violating Heisenberg's uncertainty relation. Alternatively, the situation would have called for a hidden variable: a priori arrangement of all properties of the system, such that both positions and momenta of the particles would be determined from some point in time (possibly at their birth). Later works, such as the simplified version of the experiment in which the entanglement was considered over discreet variables such as the spin entanglement of 1/2-spin particles [97] and the milestone achievement represented by the formulation of Bell's inequalities [98–102], resulted in today's view that particles do indeed interact at a distance, thus addressing the issue of non-locality originally raised by the authors of the EPR paradox.

Thus, in the case of position and momentum of photons in an EPR state, quantum-correlations are those by which the product of the uncertainties of these two quantities is less or equal to $\hbar^2/4$ [96]. In the case of two quantum-correlated photons (labelled for example s and i), it is possible to design an experiment to measure their minimum uncertainty in position x or momentum p, violating the following inequality:

$$\Delta^2_{\min}(x_s \mid x_i)\Delta^2_{\min}(p_s \mid p_i) > \frac{\hbar^2}{4}, \tag{2.1}$$

where the notation $\Delta^2_{\min}(a \mid b)$ indicates the minimum inferred variance of the measurement of a, conditional on the measurement of variable b. In practice, it is possible to measure a range of a for instance by scanning a detector, while another detector

is left at a fixed position measuring b; accordingly either detector could be placed in the image plane (i.e. position basis) or Fourier plane (i.e. momentum basis) of a source of EPR entangled photons. Interestingly, the inequality expressed in Eq. 2.1 can be used to distinguish quantum-correlated EPR photons from all other 'classical' photons. Simply put, if the product of the variances of the measured positions and momenta of pairs of photons is less than $\hbar^2/4$, then the tested photons can be said to be entangled [103, 104]. According to the quality and dimensionality of entanglement, it is possible to use the properties of quantum states to surpass the classical bounds, as in the case of quantum imaging/sensing schemes, quantum computing, and quantum communications [15, 105–110].

Although the range of positions and momenta of photons are defined by both the Heisenberg and EPR inequalities, care should be taken as to avoid confusion. In the case of a system in an EPR-state, it is possible to infer the position/momentum of a photon, starting from the position/momentum of its 'twin' partner, within the strength of their quantum-correlation. Thus, according to the EPR picture, there can be quantum-correlated pairs of photons that have peculiar properties in terms of their position and momentum. In the case of the Heisenberg uncertainty principle however, it is the position and momentum (or other conjugate quantities) of any individual particle that are linked by an inequality [111]. Thus, according to the Heisenberg picture, as a particle is localised more and more precisely (for instance by shrinking the 'box' into which it exists, or by focussing a stream of photons to a smaller and smaller spot [112–114]) its momentum gets more and more uncertain, with the particle frantically bouncing around the box (or in the case of photons, the range of directions of their trajectories, i.e. their momenta, gets larger [115–117]). Finally, it should be noted that recently the concept of classical entanglement has been put forward [118], causing mixed reactions from the scientific community for its

inability to reproduce non-local behaviour, in spite of its ability to reproduce non-separability over different degrees of freedom in the case of a single particle (i.e. a local system) [119]. Nonetheless, classical entanglement is still a useful pedagogical tool in terms of intuitively representing abstract quantum concepts, for its ability to simulate certain quantum behaviours. For example, the non-separability of classical vector beams was exploited to produce statistical results resembling those associated with entangled system. More specifically, the intensities of light beams detected through a series of polarisation optics (used to engineer the 'state' of the beam), were shown to locally violate Bell's inequality [120–124].

2.1.3 The detection of quantum correlations with single-photon sensitive detectors

First through the exposure of photographic film, then by exploiting the photoelectric effect, our ability to capture visual information relayed by light has improved considerably, giving birth in the process to a flurry of classical imaging and sensing techniques [125]. Light, in these classical implementations, is a copious stream of photons, with typical fluxes of 10^5 photons per detector element [126]. The physical properties of this regime are governed by classical bounds.

In order to achieve better than classical performance (for instance in the quality of an image [54, 69, 127–130], or in the amount of information carried by a luminous signal , or the security of a communication protocol [42, 131–135]) it is possible to employ quantum illumination: that is light made of entangled photons.

For instance, in the case of position- and momentum-entangled photons, it is possible to infer the position or momentum of a photon from that of its partner, due to strong enough position and momentum correlations [104]. Photons can of course be entangled over different degrees of freedom, such as polarisation, phase and amplitude, orbital angular momentum, etc. [136]. Additionally, the number of entangled

states increases according to the dimensionality of the system, notwithstanding the number of entangled particles per state, which can be more than two, as in the case of multipartite states [137, 138].

It is possible to design quantum-enhanced schemes with better than classical performance, as long as it is possible to operate in the quantum-regime, ideally both in terms of the light-source and of the detector [1] (i.e. if it is possible to produce *and* detect quantum correlated photons, although the downfall of a noisy detector could in principle be overcome by strong enough quantum correlations [52, 139]). The type of entanglement or inseparability of continuous-variable states (i.e. position and momentum) can be represented by the transverse position and momentum of photon-pairs produced by parametric downconversion [104, 140]. These have been the focus of both experimental and theoretical investigations , for instance regarding high transverse entanglement of parametric downconversion [141], two-photon ghost interference [142], ghost-imaging [143], angular spectrum transfer in SPDC imaging [144], and the complementarity of one- and two-photon interference [145].

In the case of a broad pump beam, the extent of the resulting downconversion beam gives rise to a high-dimensional entanglement in the transverse spatial degrees of freedom [42, 146, 147]. This simply means that, within the extent of the gain profile of the pump beam, many photon pairs can be born in the crystal. In order to take advantage of the available high-dimensionality of the system (i.e. of the available large number of entangled photon-pairs) the detector should be able to capture as many transverse modes as possible.

Being able to exploit the high-dimensionality of a system is thus crucial for real-world applications of quantum schemes, and in the case of SPDC beams, it is possible to

take advantage of the high dimensionality of entanglement by using a spatially resolved detector.

Due to limitations in the available technology of the time, early quantum optics experiments relied on single-pixel bucket-detectors or few-detectors arrays [43, 143, 148–153], which were scanned across the downconverted beams, effectively negating the advantage in information capacity represented by the available high-dimensionality of the entangled states, required for secure quantum communication protocols and quantum imaging schemes.

With the advent of single-photon sensitive cameras, the first experimental detection of quantum correlations was performed in 1998, using a photon-counting intensified CCD camera (ICCD) [154]. The following decades spawned more experimental characterisations of the high-dimensionality of entanglement of light in the spatial domain [4, 146, 147, 155, 156], aimed at a range of applications, such as fundamental tests of quantum mechanics [104, 157], and quantum information processing and communications [158]. Moreover, in terms of quantum-enhanced imaging and sensing techniques, the parallel detection and characterisation of quantum correlated states was at the heart of a number of schemes, ranging from quantum ghost-imaging, sub-shot-noise, contrast-enhancement, and resolution enhancement, as summarised in the following review articles [2, 110, 159].

2.1.4 The correlation function

Here I discuss the mathematical properties of the intensity correlation function of a spatially resolved detector in the case of SPDC light. Specifically I will identify the two terms that constitute this function, highlighting its mathematical equivalence to the cross-correlation function of a pixelated image with a 180-degree rotated copy

of itself. These two terms account for spatially correlated photon-pairs (which are linked to the presence of quantum correlations) and accidental pairs. By isolating the first spatially correlated contribution, I will show how the number of generated photons that may be detected with their entangled partner can be estimated.

It is assumed that the light-source consists of photon-pairs, such as those generated by SPDC, in a regime where the number of photons per mode is low. Therefore, in the case of low gain the second order correlation $G^{(2)}$ can be expressed as the product of the joint-detection probability for photon-pairs $\mathcal{P}(\boldsymbol{\rho_1}, \boldsymbol{\rho_2})$ and the number of generated photon pairs N_p according to:

$$G^{(2)}(\boldsymbol{\rho_1}, \boldsymbol{\rho_2}) = N_p \mathcal{P}(\boldsymbol{\rho_1}, \boldsymbol{\rho_2}), \tag{2.2}$$

where $\boldsymbol{\rho_1}$ and $\boldsymbol{\rho_2}$ are two pixel coordinates in the plane of the detector.

In the present context we are concerned with the detection of spatial anticorrelations between downconverted photons in the far-field of a nonlinear crystal. The quantum theory of photo-detection [160] gives the following expression for the expected normal ordered covariance $\tilde{C}(\boldsymbol{\rho_1}, \boldsymbol{\rho_2})$ between two pixels of coordinates $\boldsymbol{\rho_1}$ and $\boldsymbol{\rho_2}$:

$$\begin{aligned} \tilde{C}(\boldsymbol{\rho_1}, \boldsymbol{\rho_2}) &= \left\langle : \delta\hat{N}_1 \delta\hat{N}_2 : \right\rangle && (2.3) \\ &= \left\langle : \hat{N}_1 \hat{N}_2 : \right\rangle - \left\langle \hat{N}_1 \right\rangle \left\langle \hat{N}_2 \right\rangle && (2.4) \\ &= C(\boldsymbol{\rho_1}, \boldsymbol{\rho_2}) - \left\langle \hat{N}_1 \right\rangle \left\langle \hat{N}_2 \right\rangle, && (2.5) \end{aligned}$$

where $C(\boldsymbol{\rho_1}, \boldsymbol{\rho_2})$ is the intensity correlation function, defined as:

$$\begin{aligned} C(\boldsymbol{\rho_1}, \boldsymbol{\rho_2}) &= \left\langle : \hat{N}_1(\boldsymbol{\rho_1}) \hat{N}_2(\boldsymbol{\rho_2}) : \right\rangle && (2.6) \\ & && (2.7) \end{aligned}$$

For stationary signals, $\tilde{C}(\boldsymbol{\rho_1}, \boldsymbol{\rho_2})$ accounts for the quantum correlations. This means that the intensity correlation signal contains contributions from both quantum correlations and from the term $\left\langle \hat{N}_1(\boldsymbol{\rho_1}) \right\rangle \left\langle \hat{N}_2(\boldsymbol{\rho_2}) \right\rangle$ that corresponds to the accidental coincidences due to the number of photons detected on each of the pixels when the signals are stationary [160]. A subtraction of this classical contribution thus gives an estimate of the local strength of the quantum correlation.

In order to highlight the mathematical equivalence of the intensity correlation function to the cross-correlation function of a pixelated image, it is required to also express the latter in terms of two contributions: one associated with spatially correlated events and one to spatially uncorrelated events. Therefore, the spatial cross-correlation function $\mathcal{C}(\boldsymbol{\rho})$ between a frame and a 180-degree rotated copy of itself can be expressed as follows:

$$\mathcal{C}(\boldsymbol{\rho}) = \sum_{\boldsymbol{\rho'}} C(\boldsymbol{\rho'}, -(\boldsymbol{\rho'} + \boldsymbol{\rho})) \tag{2.8}$$

$$= \sum_{\boldsymbol{\rho'}} \left\langle \hat{N}(\boldsymbol{\rho'}) \hat{N}(-(\boldsymbol{\rho'} + \boldsymbol{\rho})) \right\rangle, \tag{2.9}$$

where ρ' is a dummy variable and the summation $\sum_{\boldsymbol{\rho'}}$ is operated on each pixel of the original frame. With this formulation it is possible to isolate the contribution due to the presence of quantum correlations, and that due to accidentals as follows:

$$\mathcal{C}(\boldsymbol{\rho}) = \sum_{\boldsymbol{\rho'}} \Big[G^{(2)}(\boldsymbol{\rho'}, -(\boldsymbol{\rho'} + \boldsymbol{\rho})) + \left\langle \hat{N}(\boldsymbol{\rho'}) \right\rangle \left\langle \hat{N}(-(\boldsymbol{\rho'} + \boldsymbol{\rho})) \right\rangle \Big]. \tag{2.10}$$

Therefore, the contribution of the correlation function due to biphotons $\mathcal{C}_q(\boldsymbol{\rho})$ can be estimated from experimentally acquired frames, as shown below:

$$\mathcal{C}_q(\boldsymbol{\rho}) = \sum_{\boldsymbol{\rho'}} N_p \mathcal{P}(\boldsymbol{\rho'}, -(\boldsymbol{\rho'} + \boldsymbol{\rho})) \tag{2.11}$$

$$= \mathcal{C}(\boldsymbol{\rho}) - \sum_{\boldsymbol{\rho'}} \left\langle \hat{N}(\boldsymbol{\rho'}) \right\rangle \left\langle \hat{N}(-(\boldsymbol{\rho'} + \boldsymbol{\rho})) \right\rangle, \tag{2.12}$$

where $\mathcal{P}(\boldsymbol{\rho'}, -\boldsymbol{\rho'})$ is the joint-probability of detecting both photons of a biphoton packet. Moreover, the statistical averaging operation indicated by $\langle\ \rangle$ can be experimentally achieved either temporally or spatially. In the case of temporal averaging the cross-correlation is averaged over subsequent frames (as performed later in this chapter), whereas in the case of spatial averaging the cross-correlation is computed over different portions within a single frame (as performed for example by J.-L. Blanchet et al. [50]).

The number of generated photons that may be detected with their twin $2N_p$, can be estimated by computing the integral of $\mathcal{C}_q(\boldsymbol{\rho})$, thus by computing the volume of the background-subtracted cross-correlation peak, as shown below:

$$\sum_{\boldsymbol{\rho}} \mathcal{C}_q(\boldsymbol{\rho}) = \sum_{\boldsymbol{\rho}} \sum_{\boldsymbol{\rho'}} N_p \mathcal{P}(\boldsymbol{\rho'}, -(\boldsymbol{\rho'} + \boldsymbol{\rho})) = 2N_p. \tag{2.13}$$

Since the cross-correlation is performed for every photon of the original image and every photon of the same 180-degrees rotated image, each pair is taken into account twice when integrating. For this reason the number of biphotons or photon-pairs N_p in Eq. 2.13 is multiplied by a factor of 2. Moreover, in the case of spatially uncorrelated light, the number of photon-pairs N_p would tend to zero, as the averaged cross-correlation would not reveal a correlation peak.

It is also possible to link the volume of the whole correlation function to the total number of generated photons N_t. In the case of experimentally acquired frames, the experimental correlation function $\mathcal{C}_{exp}$ found by cross-correlating a frame with the 180-degree rotated copy of itself, is defined as:

$$\mathcal{C}_{exp}(\boldsymbol{\rho}) = \sum_{\boldsymbol{\rho'}} N(\boldsymbol{\rho'})N(-(\boldsymbol{\rho'} + \boldsymbol{\rho})) \tag{2.14}$$

where $N(\boldsymbol{\rho})$ is the number of detectable photons in a frame at coordinates $\boldsymbol{\rho}$. Therefore, the total volume of the correlation function $\mathcal{C}$ is found by computing the following integral:

$$\mathcal{C} = \sum_{\boldsymbol{\rho}} C_{exp}(\boldsymbol{\rho}) = \sum_{\boldsymbol{\rho}} \sum_{\boldsymbol{\rho'}} N(\boldsymbol{\rho'})N(-(\boldsymbol{\rho'} + \boldsymbol{\rho})) \tag{2.15}$$

By applying Fubini's theorem [161] it is possible to separate the double integral of Eq. 2.15 and re-express it as a product of two integrals, as follows:

$$\mathcal{C} = \sum_{\boldsymbol{\rho'}} N(\boldsymbol{\rho'}) \sum_{\boldsymbol{\rho'}} N(-\boldsymbol{\rho'}) = N_t^2 \tag{2.16}$$

Therefore, the square number of all generated photons N_t^2 that may be detected is equal to the integral of the correlation function.

Another interesting feature is that in the case of correlated illumination, the mean integral of the correlation function $\langle \mathcal{C} \rangle$ will be greater than in the case of uncorrelated light. This feature arises due to the super-Poissonian nature of the counting statistics in the presence of photon-pairs, for which $Var(N_t) > N_t$, where Var is the variance computed over multiple detected frames. Accordingly, the mean integral of

the correlation function can be expressed as follows:

$$\begin{aligned} \langle \mathcal{C} \rangle &= \left\langle N_t^2 \right\rangle = \left\langle (N_s + 2N_p)^2 \right\rangle && (2.17) \\ &= \langle (N_t) \rangle^2 + \langle (N_s) \rangle + 4 \langle (N_p) \rangle && (2.18) \\ &= \langle (N_t) \rangle^2 + \langle (N_t) \rangle + 2 \langle (N_p) \rangle && (2.19) \\ &= \langle (N_t) \rangle^2 + \langle (N_t) \rangle + \sum_{\boldsymbol{\rho}} \mathcal{C}_q(\boldsymbol{\rho}) && (2.20) \end{aligned}$$

where N_s is the number of single (or unpaired) photons, and both N_s and N_p are considered to be Poissonian (i.e. $Var(N_s) = N_s$ and $Var(N_p) = N_p$). The counting excess in the mean integral of the correlation function corresponds to the contribution of the experimentally detected photon pairs, according to:

$$2N_p = \sum_{\boldsymbol{\rho}} \mathcal{C}_q(\boldsymbol{\rho}) = \sum_{\boldsymbol{\rho}} C_{exp}(\boldsymbol{\rho}). \tag{2.21}$$

The intermediate steps linking Eq. 2.17 and 2.20 can be found in appendix A.2.

The contributions to the autocorrelation function arising from spatially correlated and spatially uncorrelated photons are represented in Fig. 2.1. It is therefore possible to clearly visualise and quantify the presence of biphotons, as shown by the red-shaded peak in the cross-section of the autocorrelation function represented in Fig.2.1 (a). In the case of spatially uncorrelated light, however, all of the generated photons are contained in the uncorrelated Gaussian 'pedestal', as shown in Fig. 2.1 (b).

It may be useful to note that the two contributions to the autocorrelation function have different spatial features. The smaller lateral extent of the correlation peak with respect to the uncorrelated pedestal is indicative of the smaller spatial features represented by the quantum correlations. This can be intuitively understood in the case of biphotons in the image-plane of the nonlinear crystal. In this case, the transverse

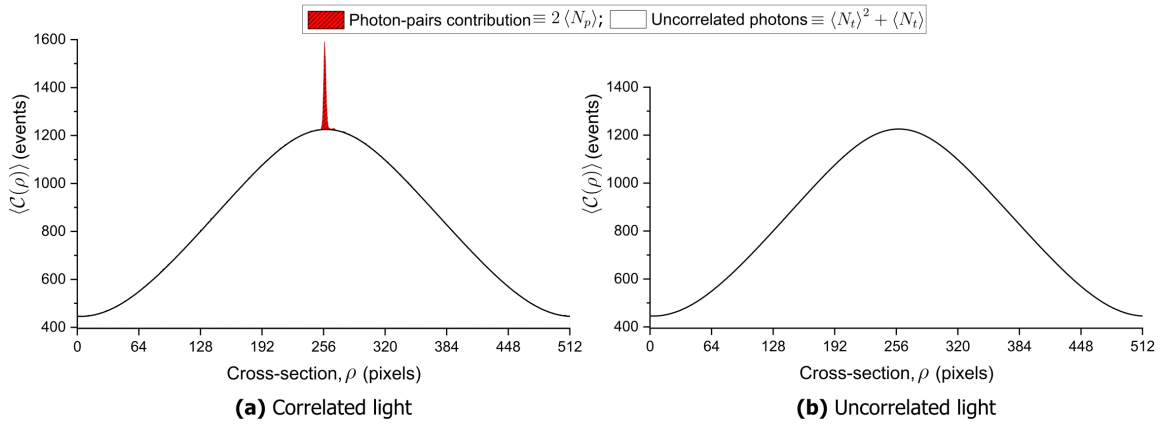

FIGURE 2.1: **Contributions to the autocorrelation function for spatially correlated and uncorrelated light.** The cross-sections of the autocorrelation function computed over 2,500 frames acquired by an EMCCD camera are shown to highlight the contributions of the autocorrelation function. In the case of spatially correlated light (a) the autocorrelation function is made of two components: a correlation peak (highlighted in red) and a Gaussian 'pedestal', which accounts for spatially uncorrelated events. In the case of spatially uncorrelated light (b), all of the detected events are within the 'pedestal' and there is no correlated contribution to the autocorrelation function. Reproduced from [162].

correlation width of the biphotons corresponds to the lateral extent of the birth-zone inside the crystal, which is typically much smaller than the beam waist of the UV-pump. Therefore, the width of the pump determines the gain-profile and consequently the lateral extent of the downconverted beam and of the Gaussian pedestal in the autocorrelation function.

In the case of experimentally acquired frames the uncorrelated events that are contained in the pedestal of the autocorrelation function include single bright events (such as partially absorbed photon-pairs), dark-events (i.e. the noise events of the camera), and perhaps more subtly a contribution from every event, whether or not spatially correlated. In fact, each detected event-pair contributes to the value of $\mathcal{C}$, regardless of it being spatially correlated or uncorrelated. The results shown in Fig. 2.1 were obtained by computing the average of the autocorrelation function over 2,500 frames, acquired using an EMCCD camera placed in the far-field of a type-I nonlinear crystal, for a collinear and degenerate phase-matching condition.

2.2 Quantum statistics and distributions

In this section I explain in a tutorial fashion what is meant by photon bunching/anti-bunching, squeezing, and shot-noise, in relation to photon-number statistics and distributions and the experiments discussed in this thesis. I also give an overview of NOON-states and the coherent-state. Where not stated otherwise, this section is based on the review article by M. Kolobov on the spatial behaviour of nonclassical light [160].

2.2.1 Photon bunching/anti-bunching

According to Mandel and Wolf's semi-classical theory of photodetection [163], the information about spectral and statistical properties of photons detected via the photoelectric effect is described in the normal- and time-ordered intensity correlation function $G^{(2)}(t,t')$. If only temporal fluctuations of light are considered (i.e. excluding any spatial effects in the transverse area of the light beam), $G^{(2)}(t,t')$ is defined as:

$$G^{(2)}(t,t') = \langle : I(t)I(t') : \rangle \,, \tag{2.22}$$

where t and t' indicate different times of detection, $I(t)$ is the photon-flux operator, and the notation :: stands for normal and time ordering. For constant intensity light, the correlation function depends only on the time difference $\tau = t - t'$ between the two photodetections at times t and t', and $G^{(2)}(t,t') = G^{(2)}(\tau)$.

In its normalised form $G^{(2)}$ is known as the degree of second order temporal coherence $g^{(2)}(\tau)$, and is defined as [164]:

$$g^{(2)}(\tau) = \frac{\langle : I(t)I(t+\tau) : \rangle}{\langle I(t) \rangle^2}, \tag{2.23}$$

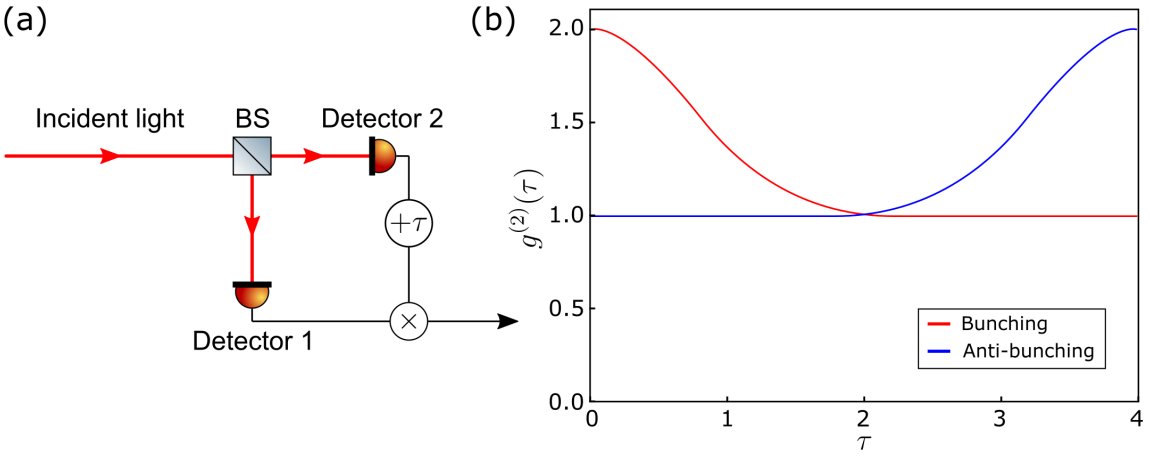

FIGURE 2.2: **Representation of photon bunching/anti-bunching in a photocurrent correlation experiment.** (a) shows a simplified experiment in which photons go through a beam-splitter (BS) and reach two detectors. The delayed signal from detector 2 (delayed by an added time delay τ) is multiplied by the signal of detector 1. The so measured degree of second-order temporal coherence $g^{(2)}(\tau)$ is qualitatively shown in (b) and can be interpreted as the conditional probability of detecting the second photon. Photon bunching (red-series) occurs if the signal from both detectors tends to be high at short time-delays; conversely, photon anti-bunching occurs for long time delays (blue-series).

where $\langle\ \rangle$ indicates the mean.

The quantity $g^{(2)}(\tau)$ is proportional to the probability that upon detection of a photon at time t, another photon is detected at another time t'. The degree of second-order coherence $g^{(2)}(\tau)$ can be measured by performing a photocurrent correlation experiment, as schematically represented in Fig. 2.2(a), with its qualitative results shown in Fig. 2.2(b). In this type of experiment, first performed by Hanbury Brown and Twiss using the thermal photons produced by a mercury arc [165], a light-field is split into two parts by a beam-splitter, which are detected by two independent detectors. The photocurrent signal of detector 2 is delayed by a time τ and then multiplied by the photocurrent signal of detector 1. In the case of chaotic light (i.e. for light with a Gaussian frequency distribution) photon-bunching is observed, as qualitatively shown by the red-series in Fig. 2.2(b), and the conditional probability of detecting the second photon is higher at shorter delays. Photon anti-bunching is shown by the blue-series in fig. 2.2(b), for which the measured conditional probability is higher for

longer delays, as in the case of resonance fluorescence of a single sodium atom driven by an external monochromatic light-field [166]. In this case, the delay between detections of the first and second photons is due to the probability of photon-emission by the sodium atom being zero just after the detection of the first photon.

The photon-bunching effect can be understood intuitively by considering classical fluctuations of light intensity. Accordingly, as the probability of detecting the first photon increases with the increasing intensity of a positive fluctuation in light intensity, so does the probability of detecting the second photon at a short time-delay, since within this time the positive intensity fluctuation is still taking place [160]. It should be noted that in the case of light in a coherent state, i.e. light without classical intensity fluctuations, the bunching effect disappears.

2.2.2 Shot-noise and Poissonian statistics

Disregarding technical noise such as Johnson-Nyquist noise and other sources of electronic/detector noise [167], a shadow-sensing scheme based on a classical light source is fundamentally limited by the quantised nature of the electromagnetic field, i.e. by shot-noise, as it is also the case for optical beam deflection schemes [168]. Indeed, the light emanated from an everyday source, both from a temporal and spatial point of view, consists of a stream of photons, originating at a not well-defined rate and at not well-defined positions [169] (even though an average rate and position are known). As it happens, Poissonian statistics governs both the rate of ideal generation (and thus ideal detection) of photons, as well as their detected positions in a plane transverse to the direction of propagation. This means that in the *ideal* case of light generated by a single-mode laser and detected by a noiseless photodiode, the photon-number fluctuations follow Poissonian statistics and the mean number of

detected photons is equal to the variance [163]. This noise-statistics corresponds to the shot-noise-limit (also known as the SQL [49, 170]).

In practice, the shot-noise-limit sets an important benchmark which is hard to beat, due to the noise of a real-world detector which inevitably pollutes the measured photon-statistics. In practice, a single-mode laser operated well-above threshold can be used [171]. Since in practice there is the need to detect photons, the statistics both of the light-source and of the detector are important in determining whether the noise-performance of a scheme can reach the shot-noise-limit. For example, even in the case of an ideal single-mode laser, the extra-noise introduced by a non-ideal detector may cause the noise performance of the sensing scheme to be worse than the shot-noise-limit. Thus, from a classical point of view, the SNL sets an important benchmark for the quality of a measurement, which can however be beaten using the properties of quantum states [1].

For the purpose of a quantitative assessment of the noise performance of a sensing scheme, it is useful to define sub-, super-, and Poissonian statistics, in terms of the fluctuations of photon-counted signals. Under this condition a 'click' of the detector corresponds to one detected photon or one detection event. With the help of a simple simulation it is possible to visualise the three statistical regimes, by plotting the histograms of the detected events N, as shown in Fig. 2.3.

In the case of Poissonian statistics (i.e. the combination of a noiseless light-source in the coherent state and a noiseless detector), the ratio of the variance to the mean number of detected photons is unity, as shown in Fig. 2.3(a). A detector or source characterised by this statistics is said to operate at the SNL or at the standard-quantum-limit.

The red-series in Fig. 2.3(c) is indicative of a super-Poissonian detection scheme, for

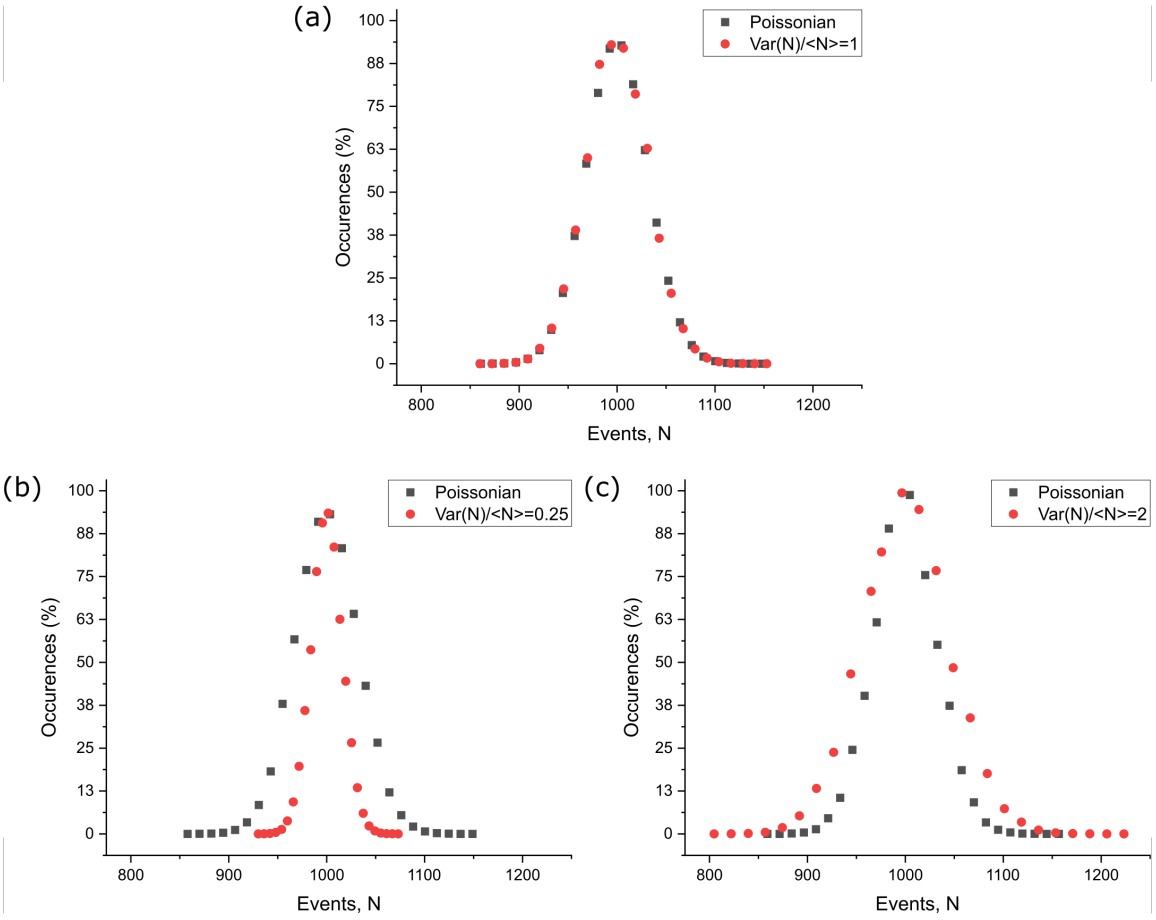

FIGURE 2.3: **Histogram representations of Poissonian, sub-Poissonian, and super-Poissonian statistics.** Poissonian statistics like the one represented in (a) is characteristic of photons produced in the coherent state and measured by a noiseless detector. Sub-Poissonian statistics like the one represented in (b) is characteristic of the detection of quantum correlated photons, for which the photon-number fluctuations are smaller than the mean number of detected events. The super-Poissonian statistics shown in (c) is characteristic of excess noise, either associated with the light-source or the detector.

which the fluctuations in the number of photons are twice the mean number of photons. This type of fluctuations (even much larger fluctuations) are typical of thermal or chaotic sources (such as sun-light or light from an incandescent light-bulb), or quasi-thermal sources (such as LEDs, and multi-mode laser light) [172]. A detector or source characterised by this statistics is said to operate above the shot-noise-limit. In the case of sub-Poissonian statistics, as shown by the red-series in Fig. 2.3(b), the ratio of the variance by the mean number of photons is less than unity. A detected

TABLE 2.1: **Example of statistical parameters for different Poissonian distributions.** The mean $\langle N \rangle$, standard-deviation SD (N), and the variance Var (N) are tabulated for three different examples of Poissonian distributions. The ratio between the mean and the variance (last-row) is a useful metric to quantify the level of noise. This parameter can be < 1, $= 1$ or > 1 in case of sub-Poissonian, Poissonian, or super-Poissonian distributions, which in the case of noise associated with the statistics of measurements would correspond to sub-shot-noise, shot-noise, and excess-noise levels respectively.

	Sub-Poissonian (sub-shot-noise level)	**Poissonian** (shot-noise level)	**Super-Poissonian** (excess noise level)
$\langle N \rangle$	999.96	999.98	1000.05
SD (N)	15.74	31.58	44.69
Var (N)	247.68	997.14	1997.43
$\frac{\text{Var}(N)}{\langle N \rangle}$	0.25	1.00	2.00

sub-Poissonian statistics is indicative of quantum behaviour enabled by the properties of quantum states (such as when computing the difference between the detected signal and idler beams of a quantum correlated SPDC source [173, 174]).

A summary of the relevant key-features for the three types of simulated statistics plotted in Fig. 2.3 is shown in Table 2.1.

2.2.3 The coherent state

In the absence of excess noise of either the source or the detector, the error associated to the measurement of the intensity of a classical light-source cannot be lower than the SNL, which determines the lowest photon-number fluctuations of a classical light-source. Such limit can in principle be reached in the case of photons in the coherent state, such as those produced by an ideal laser: a light-source without classical intensity fluctuations.

A Glauber coherent state $\mid \beta\rangle$ of a single-mode electromagnetic field is governed by Poissonian statistics. The probability $p(N)$ of finding N photons in the state $\mid \beta\rangle$ is given by a Poissonian distribution [169]:

$$p(N) = |\langle N \mid \beta\rangle|^2 = \exp(-\langle N\rangle)\frac{\langle N\rangle^N}{N!} \tag{2.24}$$

where $\langle N\rangle = |\beta|^2$ indicates the average photon number equal to the classical intensity of the wave.

More generally, the probability $p(N)$ of detecting (or emitting) N photons for a known average number of detected (or emitted) photons $\langle N\rangle$ and variance $\mathrm{Var}(N) = \langle N\rangle/\alpha$, can be expressed as:

$$p(N) = \exp\left(-\langle N\rangle \cdot \alpha\right)\frac{\left(\langle N\rangle \cdot \alpha\right)^{N\cdot\alpha}}{(N\cdot\alpha)!} \tag{2.25}$$

in the case of a Poissonian ($\alpha = 1$), super-Poissonian ($\alpha < 1$), or sub-Poissonian ($\alpha > 1$) distribution (given $N \cdot \alpha \in \mathbb{N}$, where $\mathbb{N} = \{0, 1, 2, 3, ...\}$ are positive natural numbers) [175].

2.2.4 NOON-states

NOON states are nonclassical states of light that find applications in super-resolution interferometry. They were introduced in quantum metrology to surpass the SNL for phase sensitivity, allowing one to improve upon the SQL by a factor of $1/\sqrt{N}$, thus reaching the $1/N$ Heisenberg limit [109].

The typical form of NOON states between two distinct modes of light is defined as [69, 176, 177]:

$$\mid \psi\rangle = \frac{1}{\sqrt{2}} \left(\mid N, 0\rangle + e^{i\phi} \mid 0, N\rangle \right), \tag{2.26}$$

where $\mid \psi\rangle$ represents the NOON state in bra-ket notation, composed as an equal coherent superposition of N photons in the first mode and vacuum in the second mode, with the reverse vacuum in the first mode and N photons in the second mode.

Due to the fragility of these highly nonclassical states, and thus the difficulty in producing them, to date $N = 5$ NOON states have been realised at optical frequencies [178, 179]. Other non-optical approaches to the creation of NOON states include spin-systems in magnetic fields [180], and in superconducting circuits [181, 182].

2.2.5 Squeezing

A squeezed state of light can be defined as one in which the uncertainty along one of the two optical quadrature components of the electric field (i.e. the two orthogonal components of the electric field defined in terms of the time-varying phasors that rotate in the complex plane as time progresses) is reduced compared to the corresponding field-quadrature of a coherent or vacuum state [160]. In other words, the uncertainty in one monitored observable can be reduced below what is classically

achievable, at the cost of its complementary observable in a Heisenberg trade-off, if the two observables are non-commuting. This condition is not met in the case of minimum uncertainty states of light, such as the coherent state and vacuum state, in which the uncertainty of both optical quadrature components are equal. Thus, it is possible in principle to have a definite photon number state, at the expense of the knowledge of phase. A detailed description of squeezed states can be found in the following literature [183–186].

2.3 The optical resolution of an imaging system

In the case of an aberration-free imaging system, the spatial resolution of the formed image of an object depends on the wavelength of the illumination λ and the diameter of the light-collecting lens or mirror D, as studied by Abbe and Rayleigh [187, 188]. Under these conditions, the image of a point-source will be an Airy pattern produced by Fraunhofer diffraction at the circular aperture used to collect the light [189].

In terms of incoherent image formation, the image of an extended object can be regarded as the sum of partially overlapping Airy patterns, each produced by a portion of the object, acting as an independent 'reflector' or point-source [190]. In the simplest case, the resolution limit of the system is the minimum distance between two point-sources, for which it is still possible to distinguish them, for example in the case of two distant stars imaged through a telescope [191], or two fluorescent microbeads imaged through a microscope [192].

Two point-sources are said to be well-resolved or unresolved depending on their separation, as shown in Fig. 2.4(a) and (d). As the separation between the two point-sources decreases, it is somewhat more arbitrary to tell when they are resolved. Two main resolving-criteria exist that define the resolving limit (i.e. the minimum resolvable distance) and the resolving power (i.e. the inverse of the resolving limit)

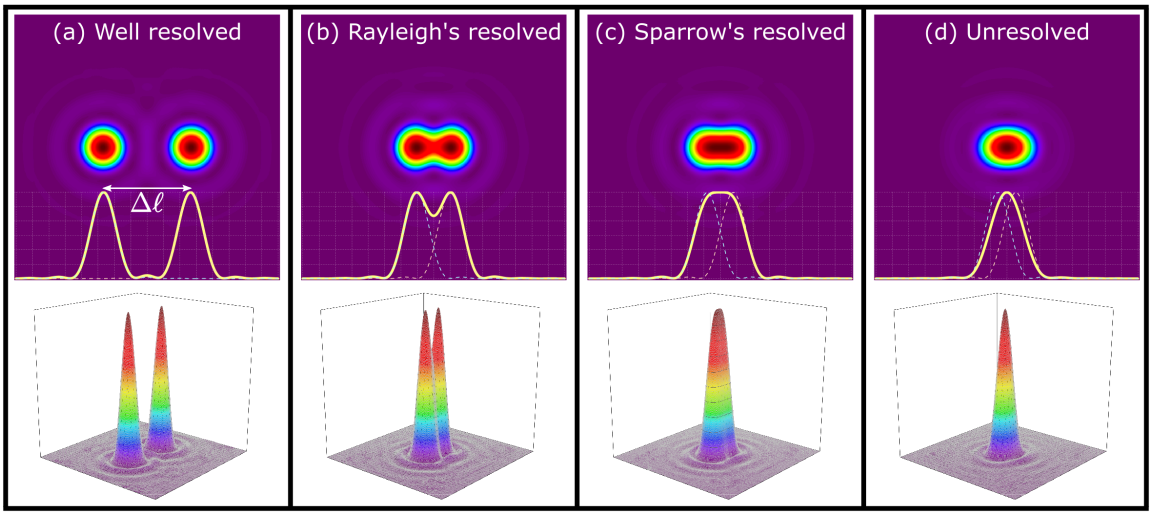

FIGURE 2.4: **Optical-resolution criteria.** The ability to distinguish two point-sources depends on the separation between them, $\Delta\ell$. In the case of a large separation (a), it is possible to fully resolve the two point-sources. However, if the separation is low enough (d), the two point-sources become indistinguishable. The minimum separation which allows to just resolve the two point-sources can be defined using Rayleigh's criterion or Sparrow's. According to the former, the minimum separation is found when the first minimum intensity of one source coincides with the maximum intensity of the other source (b). According to the latter, the minimum separation is that for which the second derivative of the overall intensity cross-section becomes zero (c)(i.e. the central region becomes a flat-top).

of an imaging system: Lord Rayleigh's and Sparrow's criteria [190]. According to the Rayleigh criterion, the minimum separation for which two point-sources are just resolved is found when the first intensity minimum of one source corresponds to the intensity maximum of the Airy disk of the second, as shown in Fig. 2.4(b), according to [190]:

$$(\Delta\ell)_{min} = 1.22 f\lambda/D, \tag{2.27}$$

where f and D are the focal length and diameter of the light-collecting lens or mirror, and λ is the wavelength of light. Sparrow's criterion offers an alternative definition, for which the minimum distance for two-point sources to be just resolved is found when the second derivative of their intensity computed at the mid-point is zero, as

shown in Fig. 2.4(c), according to [193]:

$$\frac{\delta^2 I}{\delta^2 x^2} = 0 \text{ when } x = 0, \tag{2.28}$$

where x maps the distance between the two-point sources.

One obvious strategy to improve the resolution limit may be to decrease the wavelength of the probing field, for instance using UV instead of visible light, or in the case of electron microscopy, using the comparatively much shorter Heisenberg wavelength of massive particles. However, the approach of using shorter wavelength illumination introduces the risk of damaging the sample, either by direct photobleaching by high energy photons, or by sample-preparation as required in the case of electron microscopy. Another effective approach is that of increasing the collecting angle of the imaging optics. This approach however can only provide limited improvement, as the maximum numerical aperture (NA) typically achieved using oil immersion objectives is limited to ≈1.4 [194].

2.3.1 The PSF, LSF, and ESF routes to the measurement of the MTF

In order to enable a quantitative comparison between the quantum-enhanced and the classical-equivalent imaging schemes it is important to choose a reliable quantity able to characterise the imaging performance of a system. This is fully represented by the modulation transfer function (MTF), which in terms of linear system control corresponds to the modulus of the normalised transfer function of the imaging system. The MTF can be measured using a variety of methods. In the context of low-light imaging, the slanted-edge standard is arguably the most appropriate method, due to the minimum amount of light being wasted using a slanted-edge target as opposed to a pin-hole or a slit, as employed by other methods [83].

In this section I first introduce the MTF, PSF (and related functions), and the slanted-edge method used to measure the MTF. I also highlight the detrimental effect of shot-noise on the noise-floor of the measured MTF, which is relevant in the context of images produced in the photon-sparse regime.

From a linear system response perspective, the process of image formation that generates the output intensity distribution $g(x, y)$ of an imaging system is the result of the two-dimensional convolution between an input intensity distribution $f(x, y)$, and the system's impulse response $h(x, y)$, according to [195]:

$$g(x, y) = h(x, y) * *f(x, y), \tag{2.29}$$

where $**$ is used to indicate the two-dimensional convolution operation.

The performance of a linear system can be fully assessed by measuring its transfer function, which in this context is known as the optical transfer function (OTF). Like all transfer functions, the OTF is a complex function. When normalised, its magnitude and phase contributions are known as the modulation transfer function and the phase transfer function (PTF), as shown below [195]:

$$OTF(u, v) \equiv MTF(u, v) \cdot e^{-i \cdot PTF(u,v)} \tag{2.30}$$

In order to assess the quality of an image in terms of contrast and spatial resolution, the MTF is all that is needed. There are different approaches to measuring the MTF, three of which are schematically represented in Fig. 2.5. These three methods are based on the close relation between the MTF and the PSF and the ability to compute the former from the latter.

In the case of a true point-like light-source (for example obtained by illuminating

a pin-hole), the system impulse response corresponds to the PSF of the system, as represented in Fig. 2.5(a) and as expressed below [195]:

$$PSF(x,y) \equiv g(x,y) = h(x,y) * *\delta(x,y) = h(x,y) \tag{2.31}$$

where $\delta(x,y)$ is a two-dimensional delta-function: a function that in this case is defined in the xy plane, where it is infinite at the origin and zero everywhere else[1]. Knowledge of the two-dimensional PSF can allow to compute the response of the imaging system (i.e. its OTF) over the full extent of the xy plane, by computing its two-dimensional Fourier transform (indicated by the $\mathcal{FF}$ notation), as shown below [83]:

$$\mathcal{FF}[PSF(x,y)] = OTF(u,v,\gamma), \tag{2.32}$$

where u, v are the reciprocal variables in Fourier space of x, y, and with γ they fully define the OTF in the complex Fourier space. The MTF is readily obtained by taking the modulus of the OTF, which in terms of the PSF is expressed as follows [83]:

$$MTF(u,v) = \left|\mathcal{FF}\left[PSF(x,y)\right]\right|. \tag{2.33}$$

Often however, it is possible to take advantage of the symmetry of an imaging system, and the system response can be satisfactorily represented by one (or few) cross-sections of the two-dimensional PSF or MTF. In this case, it is possible to compute a very close approximation of the one-dimensional PSF and MTF by measuring the very similar line spread function (LSF) of the imaging system. This approximation allows to use more flexible measurement methods, such as the slanted-edge analysis, represented in Fig. 2.5(c).

[1] In the case of a detected intensity distribution, the maximum value of $\delta(x,y)$ will correspond to the upper limit of the dynamic range of the detector, which may be normalised to unity for convenience.

In the case of a line-source (for example obtained by illuminating a slit), the formed image will consist of a series of displaced PSFs. This is because the line-source can be considered as a collection of point-sources, arranged along a line, as represented in Fig. 2.5(b). Thus, the output of the system can be expressed as the result of the two-dimensional convolution the line-source[2] $f(x,y) = \delta(x)1(y)$ with the impulse response of the system $h(x,y) \equiv PSF(x,y)$, as follows [83]:

$$g(x,y) \equiv LSF(x) = f(x,y) * *h(x,y) = [\delta(x)1(y)] * *PSF(x,y). \tag{2.34}$$

Since the one-directional convolution of a function with a constant is equivalent to an integration over that direction [196], it follows that [83]:

$$g(x,y) \equiv LSF(x) = \int_{-\infty}^{\infty} h(x,y')dy', \tag{2.35}$$

where y' is a dummy variable of integration. The corresponding one-dimensional MTF corresponds to the modulus of the Fourier transform of the LSF, as shown below [83]:

$$MTF(u,0) = \left|\mathcal{F}\left[LSF(x)\right]\right|. \tag{2.36}$$

In the case of a step-source (for example obtained by illuminating a knife-edge), the formed image will consist of the cumulative sum of displaced LSFs, as represented in Fig. 2.5(c). This is because the transmissive part of the step-source can be considered as a collection of line-sources combined side-by-side. Since the image of a line-source corresponds to a series of displaced PSFs, a collection of line-sources corresponds to a two-dimensional arrangement of displaced PSFs. Thus, the output of the system can be expressed as the result of the two-dimensional convolution of the unit-step function

[2] The line-source object $\delta(x)1(y)$ is a delta-function in x and a constant in y, that extends in height over the field of view of the lens under test [83].

TABLE 2.2: **Comparison of the PSF, LSF, and ESF.** Typically employed light-sources (including its spatial coherence and light-intensity requirements) for the measurement of the PSF, LSF, and ESF, as well as the retrievable information from these different functions are compared. The mathematical definitions of the three functions are also provided in terms of the convolution between the relevant input function with the impulse response of an imaging system (also schematically represented in Fig. 2.5).

	PSF(x,y)	**LSF**(x)	**ESF**(x)
Source	point-source (e.g. pinhole)	line-source (e.g. slit)	edge-source (e.g. knife-edge)
Coherence	insensitive	sensitive	sensitive
Light level	high	high	low
Information	full OTF	almost the same as $PSF(x)$ (absence of zeros)	same as LSF
Definition	$\delta(x,y) * *h(x,y)$	$\delta(x)1(y) * *PSF(x,y)$	$step(x)1(y) * *PSF(x,y)$

$step(x)1(y)$, with the impulse response (or PSF) of the system, as follows [83]:

$$g(x,y) \equiv ESF(x) = PSF(x,y) * *step(x)1(y). \tag{2.37}$$

The edge spread function (ESF) can then be expressed as the commutative sum (or integral if small enough displacements are considered) of the displaced LSFs, as follows [83]:

$$ESF(x) \approx \sum_{i=1}^{\infty} LSF(x - x_i) = \int_{-\infty}^{\infty} LSF(x')dx' \tag{2.38}$$

The spatial derivative of the ESF produces the LSF corresponding to the position and orientation of the unit-step function (i.e. of the knife-edge), according to [83]:

$$LSF(x) = \frac{d}{dx}\left\{ESF(x)\right\}, \tag{2.39}$$

from which the one-dimensional MTF can be obtained according to Eq. 2.36. Salient properties of the PSF, LSF, and ESF are summarised in table 2.2. It should be noted that, since both the LSF and the ESF are the result of the linear combination

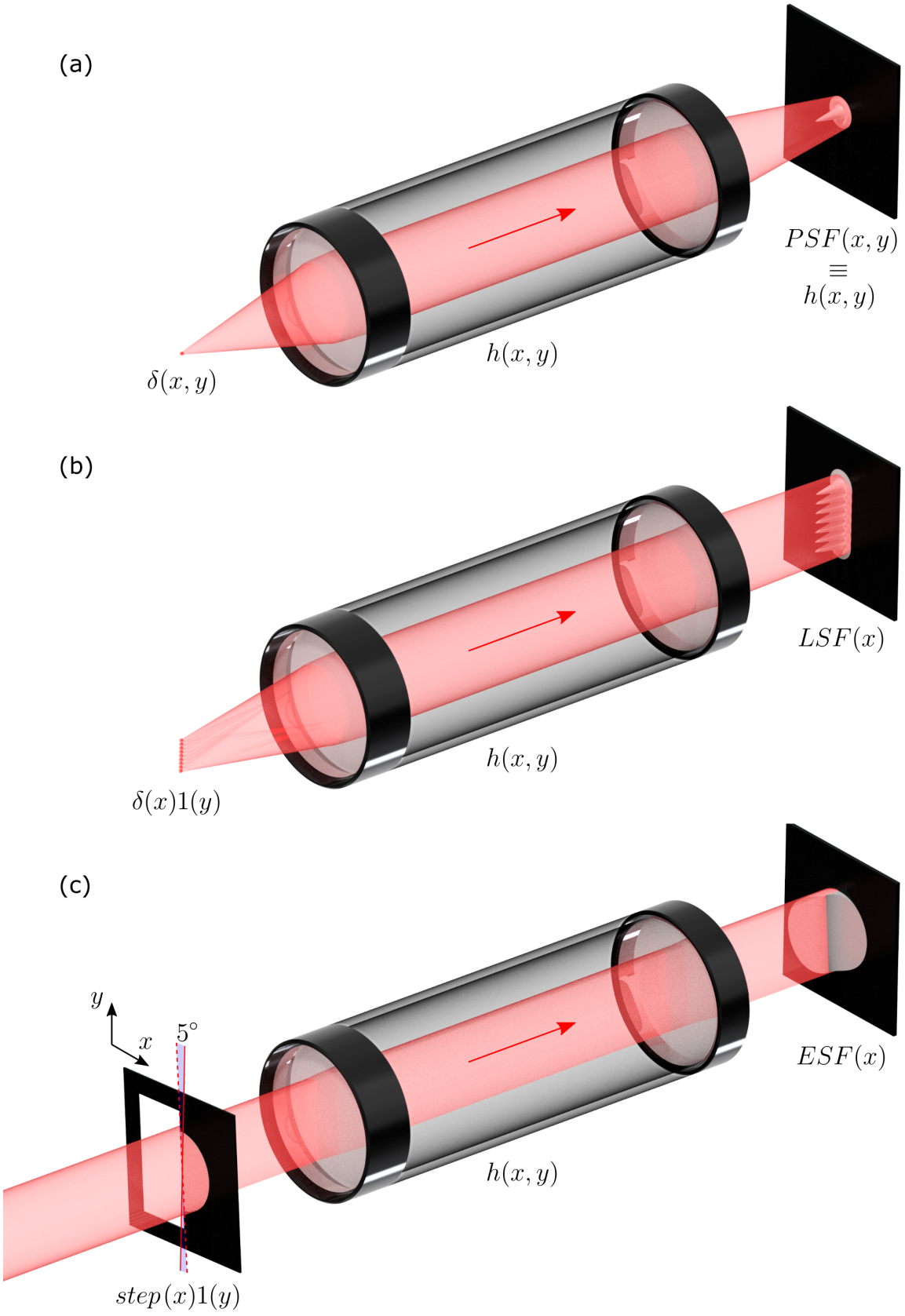

FIGURE 2.5: **The PSF, LSF, and ESF.** The two-dimensional convolution of a point-source, line-source, or edge-source with the impulse response of an imaging system (i.e. with the PSF) produces respectively the PSF, LSF or the ESF output images. The LSF is equivalent to an integration of the PSF over the y direction, whereas the ESF is equivalent to a cumulative integration of the LSF over the x direction. Note that in (c) the edge-object is shown oriented at a small angle with respect to the y-axis, like in the case of a slanted-edge MTF measurement.

of multiple point-sources, the produced MTFs can be affected by interference, in the case of spatially coherent light-sources, in which defined phase-relationships may exist between different portions of the source. However, in the current context this is not an issue due to the spatial incoherent nature of SPDC light [42].

Thus, it is possible to employ the ESF method to accurately quantify the spatial resolution (and more generally the overall performance) of the quantum-enhanced imaging system presented in this chapter. Specifically, I employ the freely-available 'sfrmat3' package [197], to compute the MTF from the acquired image of a slanted-edge. The ISO-standard slanted-edge method has been shown to be a reliable and robust assessment tool for the resolution assessment of images [198–201].

2.3.2 Quantification of the spatial resolution of an image using the slanted-edge MTF

In this work the slanted-edge MTF method is used to assess the spatial resolution of reconstructed images. This method uses the ESF route to computing the MTF discussed in section 2.3.1; however, it represents a more robust implementation, less affected by the limited spatial sampling of the detector used to capture the image of the resolution-target. This is achieved by rotating the edge by a few degrees around the optical axis , as shown in Fig. 2.5(c), allowing the measurement of an oversampled ESF [202]. For example, in the case of an edge aligned along either direction of the pixel-grid of the sensor, the ESF transition would effectively be sampled by σ_{PSF}/p, where p is the width of a detector element or pixel, and in most cases, the size of the pixel would not be small enough to allow sufficient sampling. If however, the edge is aligned at a few degrees with respect to the pixel-rows of the detector (or columns), it is possible to reproject and bin the two-dimensional edge image-data into a one-dimensional trace perpendicular to the edge. In other words, it is possible to combine

multiple linear transitions, by reprojecting the grey-level data of the original image along the direction of the shallow angle, into a one dimensional array of sub-pixel elements, thus obtaining the oversampled edge-spread function ESF(s), as shown in Fig. 2.6.

According to the picture described in Fig. 2.6, the N re-projected rows of an image array for pixels in the ith row and jth column at a distance $s(i,j) = p(j \cdot cos(\theta) - i \cdot sin(\theta))$ from the edge aligned at an angle θ, form the set of discrete samples E_{ij} of the true ESF(s) of the system. The set of discrete samples E_{ij} is defined as [198]:

$$E_{ji} = \int \mathrm{ESF}(s)\delta(s + ip \cdot sin(\theta) - jp \cdot cos(\theta))ds, \tag{2.40}$$

where s is the axis perpendicular to the edge, and p is the dimension of pixels (which are assumed to be square). The ESF as computed from pixels of the image dataset delimited by a k number of pixels (see below) is defined as [198]:

$$\mathrm{ESF}_k = \frac{1}{n_k} \sum_{ij} E_{ij} \mathrm{bin}(s(i,j) - k\Delta s), \tag{2.41}$$

where $s(i,j)$ defines the edge, n_k is the number of pixels whose distance from the edge falls within $(k - \frac{1}{2}\Delta s)$ and $(k + \frac{1}{2}\Delta s)$, Δs is the spatial width of the bins at which the E_{ij} samples of the ESF(s) are reordered, and $\mathrm{bin}(s(i,j) - k\Delta s)$ is a rectangle function defined to have a value of 1 for $|s(i,j) - k\Delta s)| \leqslant \Delta s/2$, and zero everywhere else.

The slanted-edge MTF method allows to reliably measure a one-dimensional cross-section of the MTF using a single image produced by a system. The edge can then be translated and/or rotated by 90° to retrieve other desired cross-sections of the MTF.

The ability of the slanted-edge MTF method to accurately quantify the resolution

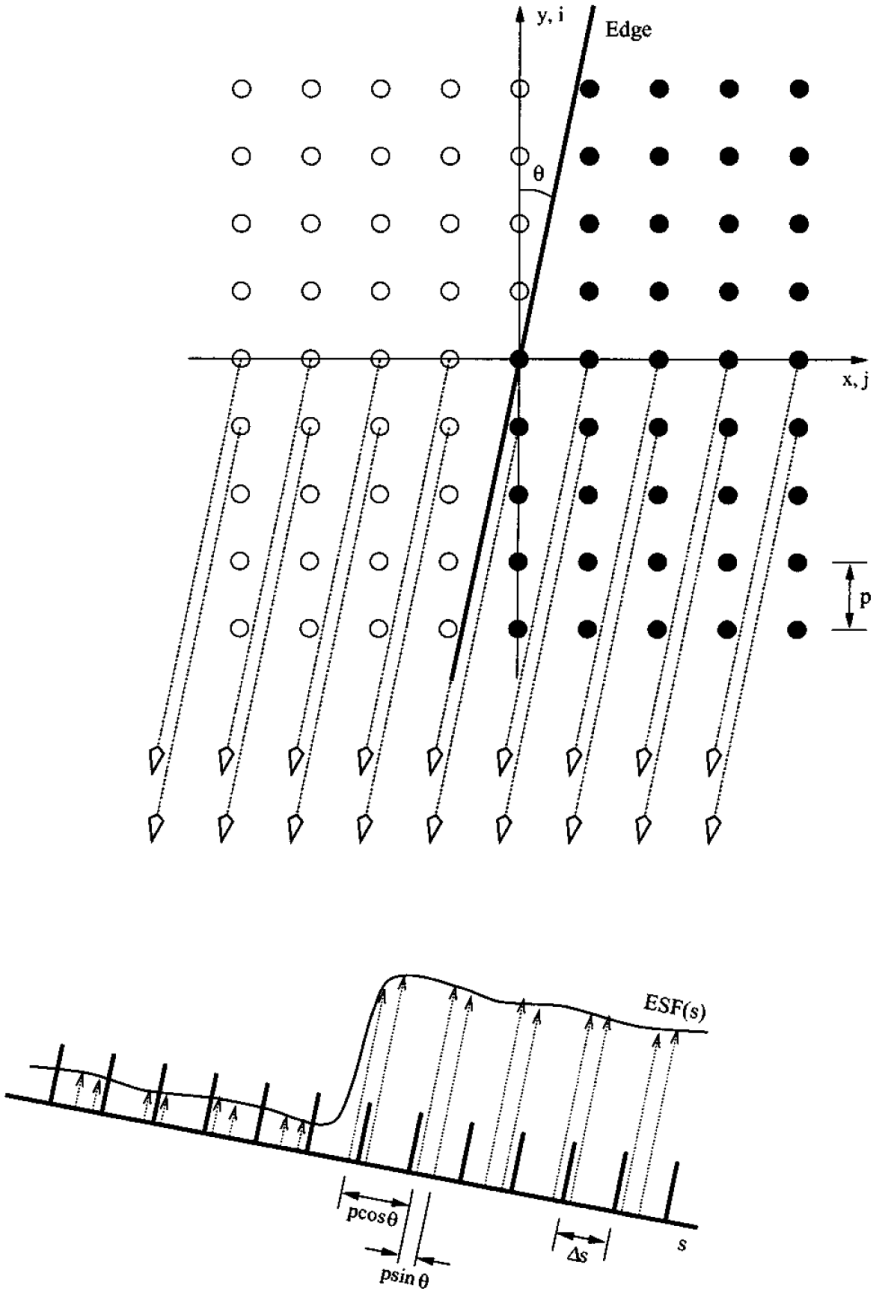

FIGURE 2.6: **Reprojection of the slanted-edge into the ESF.** The two-dimensional slanted-edge image data is re-projected and binned into a one-dimensional trace perpendicular to the edge, constituting the oversampled ESF. The angle at which the slanted-edge is oriented is shown as θ, i and j indicate the row an column number respectively, and p is the pixel dimension. Reproduced from [198].

performance of an imaging system was tested, as shown in Fig. 2.7. The modelled slanted-edges, shown in the first column of Fig. 2.7(a-c), are the output images of imaging systems whose impulse response (i.e. PSF) is shown in the central column. As expressed in Eq. 2.29, the output images are the results of the two-dimensional convolution between the impulse responses of the system and the input function of the slanted-edge (shown in the right column of Fig. 2.7). The measured MTFs for the three cases are shown at the bottom of Fig. 2.7, where the full-width-half-maxima (FWHM) are highlighted by a dotted-line. It can be seen that as the size of the PSF, σ_{PSF} is increased, the corresponding FWHM of the MTF decreases by a proportional amount. This quantity is known as the MTF50 parameter, which is typically associated with the degree of sharpness of an image [203]. Therefore, it is possible to perform a quantitative comparison between the resolution of images produced by imaging systems, simply by computing the ratio of the corresponding MTF50 values.

As a general approximation, the cut-off frequency of an MTF curve ξ_{max} (defined as the maximum spatial frequency at which the MTF goes to zero or reaches the noise-floor) can be used for a back-of-the-envelope calculation of σ_{PSF}, according to the following relation [83]:

$$\sigma_{PSF} = 1/\xi_{max}. \tag{2.42}$$

A quick check of the ξ_{max} values from the MTFs shown at the bottom of Fig. 2.7 and of the corresponding σ_{PSF} values shows that the values are indeed related according to Eq. 2.42.

Another approach to assessing the resolution of an imaging system from the MTF is computing the area of the MTF (MTFA) over a frequency range of interest [204]. This approach is quite robust as in some cases the change in the modulation may

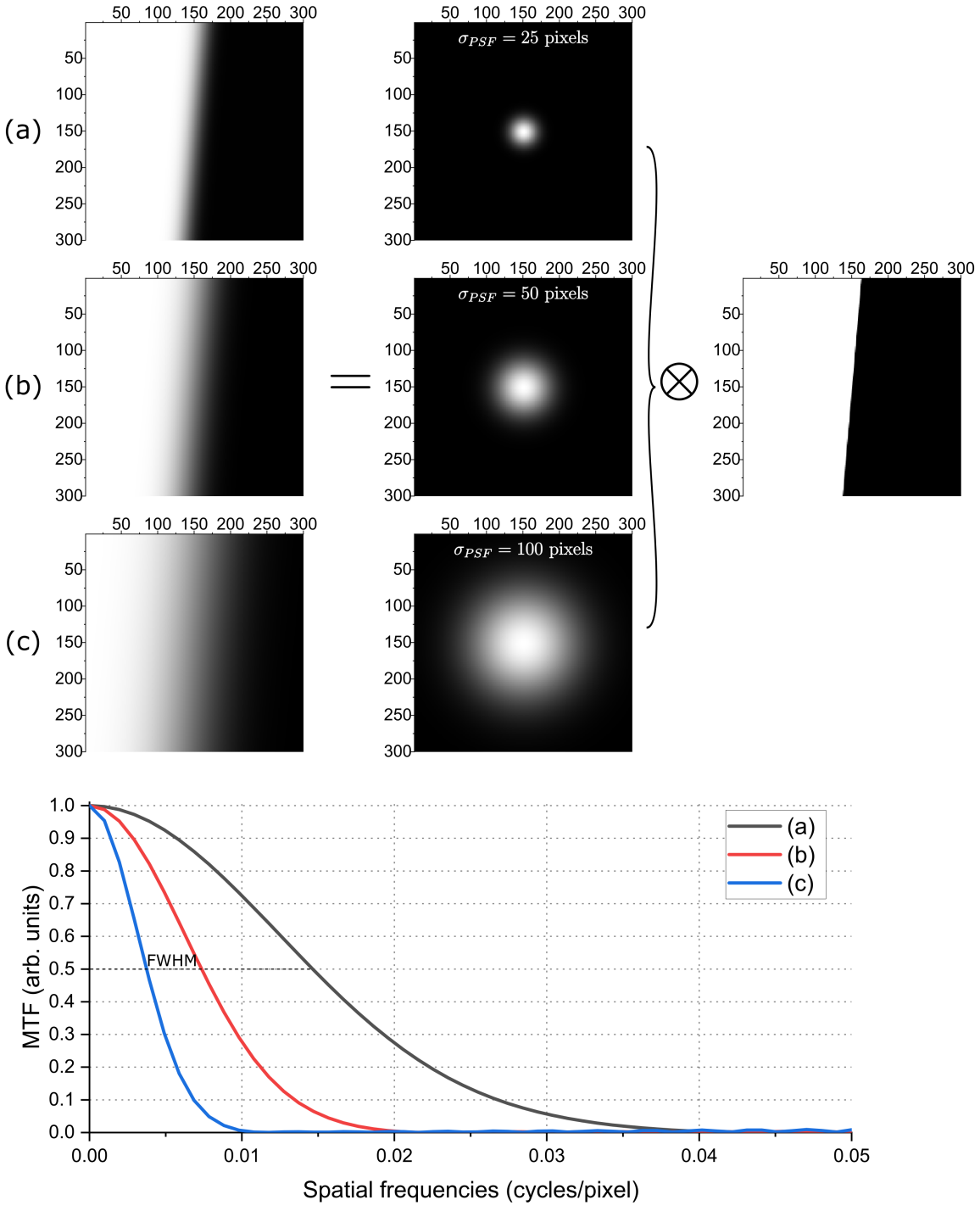

FIGURE 2.7: **Spatial-resolution and size of the PSF.** As the size of the PSF is increased, the spatial-resolution and thus sharpness of the images decreased. The spatial resolution (and thus sharpness) of the slanted-edge decreases from top to bottom (left column), as the size of the PSF is increased from 25 pixels (a) to 50 pixels (b) and 100 pixels (c) (central column). The shape of the PSF has been approximated to a Gaussian. Due to the properties of the Fourier transform, an increase in the FWHM of the PSF corresponds to a decrease in the FWHM of the MTF, as shown in the MTF curves plotted at the bottom.

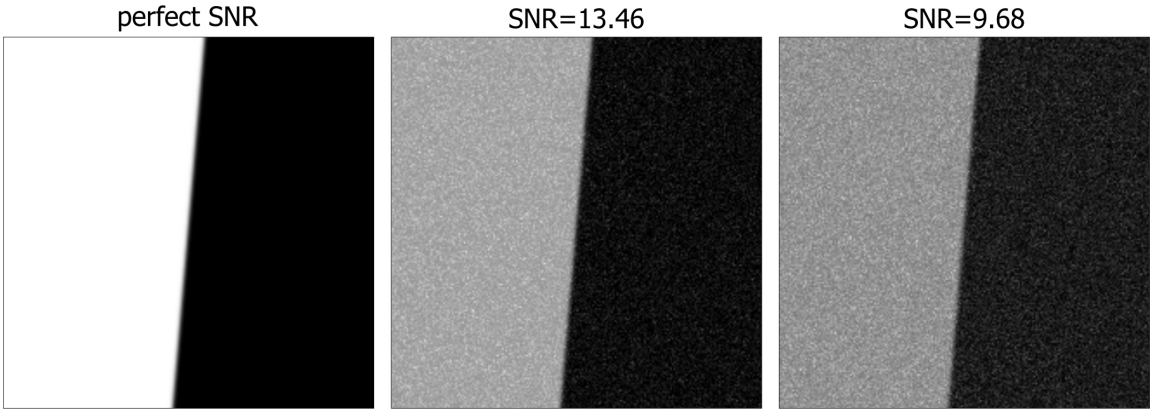

FIGURE 2.8: **Slanted-edge images for different levels of SNR.** The SNR of the modelled images of a slanted-edge was deteriorated by adding increasing amounts of pixel-to-pixel intensity fluctuations. Reproduced from [10].

be different for different spatial frequencies. This method is used to compute the resolution-enhancement achieved with the CEBs scheme over the theoretically available $\sqrt{2}$ standard-quantum-limited advantage, as discussed in section 6.4.

As a final remark, it should be noted that the slanted-edge MTF method (and more generally the ESF route to the measurement of the MTF) can be affected by poor signal-to-noise-ratio of the tested image, which causes a degradation in the noise-equivalent modulation of the MTF (i.e. in the noise-floor of the MTF). For this reason care must be taken in acquiring high signal-to-noise ratio (SNR) images of the test-target. The effect of low SNR in the images of the test-target was investigated with the aid of a simple numerical model. Accordingly, different levels of shot-noise were added to the image of a slanted-edge resulting in decreasing levels of SNR, as shown in Fig. 2.8.

The reported SNR-values were computed over a 100×100 pixel region of interest (ROI) defined in the dark region of the slanted-edge, by taking the ratio between the mean and the standard deviation (SD) of the pixel intensities. Increasing levels of noise were achieved by iteratively incrementing the intensities of randomly chosen pixels. The MTF curves for the three SNR-scenarios are shown in Fig. 2.9, confirming a degradation in the noise-equivalent modulation of the MTF for decreasing SNR

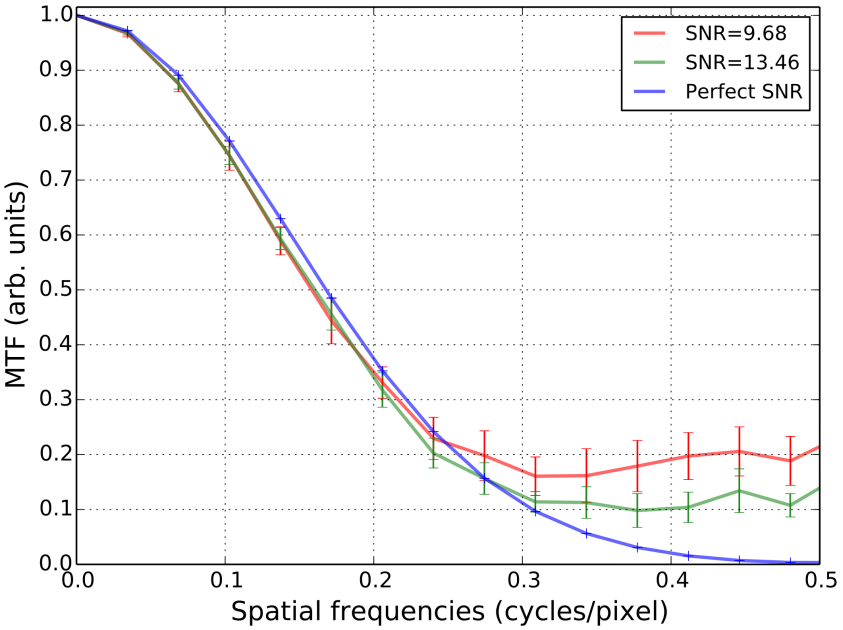

FIGURE 2.9: **Worsening of the noise-equivalent modulation of the MTF as a consequence of increasing levels of shot-noise.** As the amount of shot-noise is increased in the modelled images of a slanted-edge (shown in Fig. 2.8) the corresponding worsening of the computed SNR values is accompanied by increasingly higher levels in the noise-floor of the measured MTF curves. The error-bars were computed over 10 runs of the modelled noise-polluted edges and slanted-edge MTF measurements. Reproduced from [10].

levels (i.e. for increasing levels of noise). This dependence of the noise-equivalent-modulation on the shot-noise of the image of the slanted-edge is particularly relevant to the photon-sparse quantum imaging scheme featured in this thesis, as discussed later in chapter 6 section 6.4.2.

Chapter 3

Experimental details

In this chapter I address the common experimental details of the quantum enhanced sensing and imaging schemes featured in thesis. I will specifically discuss the following topics in depth:

1. The production of quantum-correlated biphotons via the SPDC process,
2. The general experimental set-up used to produce spatially correlated biphotons,
3. The single-photon sensitive detection of biphotons using an EMCCD camera detector.

3.1 Production of quantum-correlated biphotons via the SPDC process

Early quantum optics experiments relied on cascaded two-photon emission processes from single atoms to produce illuminating photons in a desired quantum state [205–207]. With the advent of modern nonlinear optics in the second-half of the 20th

century technically simpler ways of producing quantum entangled biphotons became available and were used in EPR and Bell inequality violation experiments [208–210].

Nonlinear optics phenomena arise from the modification of the properties of a material, as a consequence of the presence of sufficiently intense light (typically laser light). Specifically, the nonlinearity of these phenomena depends on the response of a material system that varies *nonlinearly* to the strength of an applied optical field. Consequently, the intensity of the nonlinear phenomenon tends to increase as the square, cube, etc. of the intensity of the applied laser light.

In the case of linear optics, the dependence of the dipole moment per unit volume of a material system $P(t)$ on the strength of an applied optical field $E(t)$, can be expressed as:

$$P(t) = \epsilon_0 \chi^{(1)} E(t), \tag{3.1}$$

where $\chi^{(1)}$ is known as the linear susceptibility and ϵ_0 is the permittivity of free space. The induced electrical polarisation is due to the forces exerted by the electromagnetic field of the applied light onto the loosely bound valence electrons of the medium. Thus, when the intensity of the applied electrical field is low, the induced electrical polarisation of the medium will be harmonic, and P will be linearly proportional to E.

If however, a very intense optical field is applied, the induced polarisation of the medium will become saturated and a gradual increase of its ever-present (but usually insignificant) nonlinear response will occur. Under such circumstances, the induced polarisation $P(t)$ of the medium is generalised as a power series in the strength of the applied field $E(t)$ as follows:

$$P(t) = \epsilon_0[\chi^{(0)}E(t) + \chi^{(2)}E^2(t) + \chi^{(3)}E^3(t) + ...], \tag{3.2}$$

where the quantities $\chi^{(2)}$ and $\chi^{(3)}$ are known as the second- and third-order nonlinear optical susceptibilities [211].

Spontaneous parametric downconversion is a $\chi^{(2)}$ nonlinear process, which depends on the three-wave interaction between a high energy 'pump' beam and two lower energy 'signal' and 'idler' beams within a nonlinear birefringent crystal.

This process was chosen as the illuminating light-source in the imaging and sensing experiments featured in this thesis, consisting of 710nm downconverted biphotons, produced from the spontaneous decay of 355nm UV photons. An exhaustive quantum-mechanical description of the process can be found in the following works [212–216].

Generally speaking a distinction is made between type-I and type-II phase-matched SPDC. In the former case the planes of polarisation of the signal and idler beams are the same as each other and orthogonal to the polarisation of the pump photons. In the latter, the planes of polarisation of the signal and idler beams are orthogonal to each other (with one being the same as the pump's). Moreover, whereas for type-I the signal and idler beams are superimposed, in type-II the beams are spatially separated. Thus, it is possible to produce a stream of quantum correlated signal and idler biphotons by shining a UV pump laser on a carefully aligned nonlinear crystal, as schematically represented in Fig. 3.1(a) in the case of type-I and type-II phase matching. The captured far-field intensity distributions of the downconverted field are shown in Fig. 3.1 (a) in the case of type-I phase-matching (top) and in the case of type-II phase-matching (bottom).

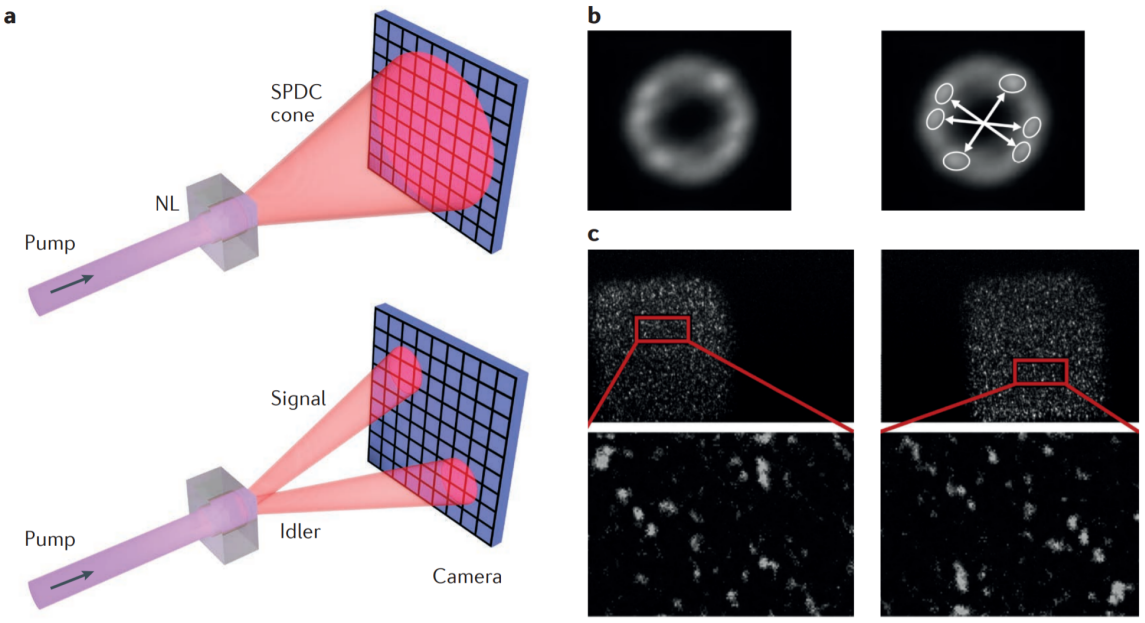

FIGURE 3.1: **Quantum correlated SPDC illumination.** The generation of quantum-correlated downconverted photons using a UV-pumped nonlinear crystal (NL) is represented in (a), both in the case of type-I (top) and type-II (bottom) phase-matching conditions. Spatial correlations within the downconverted beam can be detected using a single-photon sensitive camera, as shown in (b), in the case of the far-field of a non-collinear type-I beam. In this case both signal and idler beams (SPDC cone) reach the detector at the same region, within which spatially anticorrelated features are present, as highlighted by the white arrows. Similarly, spatial anticorrelations are also visible in the far-field of a type-II phase-matched crystal, as show in (c). In this case the signal and idler beams reach the detector at two separate regions, within which spatially anticorrelated features are present, as highlighted by the red boxes. Overall figure reproduced from [159]; panel (b) reproduced from [217], and panel [c] reproduced from [52].

Common nonlinear crystal materials are potassium titanyl phosphate (KTP), periodically poled lithium niobate (PPLN), lithium triborate (LBO), and β-barium borate (BBO) [218].

3.1.1 Type-I phase-matching

In the rest of this section I focus the discussion on BBO in the case of type-I phase-matching, since all experiments featured in this thesis were based on a BBO-crystal[1] pumped by 355nm photons and cut for type-I, wavelength degenerate and collinear

[1]Details about the crystal are provided in section 3.2.2.

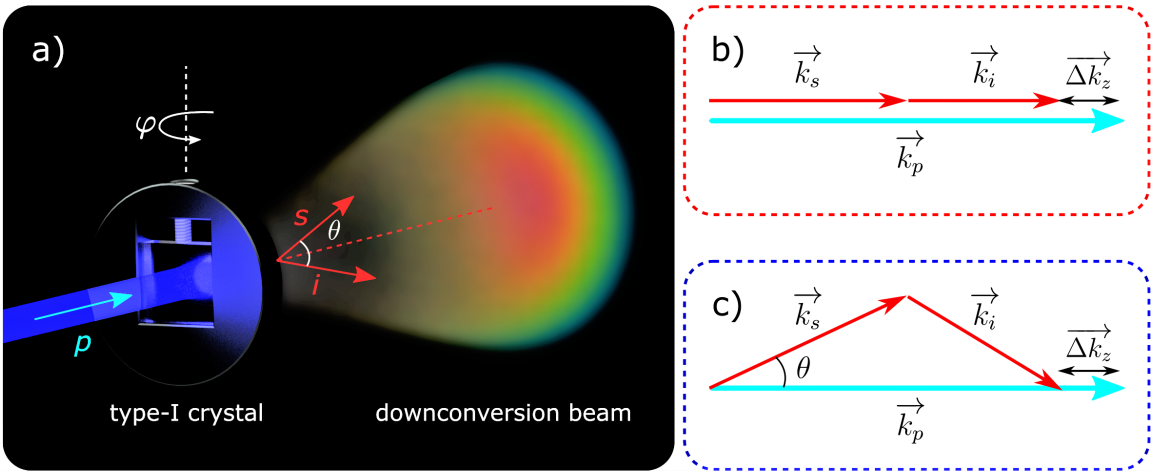

FIGURE 3.2: **Type-I phase-matching.** The SPDC process for a type-I nonlinear crystal, as employed in the experiments featured in this thesis, is represented in (a). 355nm pump photons (blue beam) decay into longer wavelength photons (chromatic cone). The spectral range of the downconverted photons arising from the longitudinal phase-mismatch term $\overrightarrow{\Delta k_z}$ is highlighted. Narrow interference band-pass filters are typically used to select degenerate signal and idler photons at 710nm. As the angle φ between the optic axis of the nonlinear crystal and the direction of propagation of the pump is changed, so are the angle θ and the transverse momenta components of the downconverted photons. Collinear phase-matching is achieved when the signal and idler photons propagate in the same direction as the pump photon (i.e. $\theta = 0$), as represented in (b). Near-collinear or non-collinear phase-matching is achieved when the directions of the momenta differ from each other (i.e. $\theta > 0$), as represented in (c). The phase-mismatch term is also responsible for the efficiency of the downconversion process, which is maximum when $\overrightarrow{\Delta k_z} = 0$. The image shown in (a) is a computer rendered composite in which the far-field intensity distribution of a type-I collinear phase-matched BBO crystal was experimentally captured, using a digital camera (also shown in Fig. 3.3 for a range of φ angles).

downconversion at 710nm, as schematically represented in Fig. 3.2(a). Interference filters (not shown in the figure) are typically used to select the wavelength degenerate signal s, and idler i, photons, such that $\lambda_s = \lambda_i = 2 \cdot \lambda_p$, where λ_p is the wavelength the pump photons. Under conservation of energy and momentum, a pump photon is instantaneously converted into two lower energy photons (typically named signal and idler) according to the following phase-matching conditions [210]:

$$\omega_p = \omega_s + \omega_i \tag{3.3}$$

$$\overrightarrow{k_p} = \overrightarrow{k_s} + \overrightarrow{k_i}, \tag{3.4}$$

where ω_p, ω_s, ω_i and $\overrightarrow{k_p}$, $\overrightarrow{k_s}$, $\overrightarrow{k_i}$ are the angular frequencies and wavevectors of the pump, signal and idler photons. The conservation of energy and momentum, according to which the initial and final state of the system are the same, is what makes SPDC a parametric process. The repartition of momentum from the pump photon to the two 'daughter' photons can be tuned by changing the angle between the optic axis of the crystal and the direction of propagation of the pump, as shown in Fig. 3.2(b) and (c) in the case of collinear (three momenta aligned) and non-collinear (three momenta misaligned) phase-matching.

The nonlinear nature of this $\chi^{(2)}$-process means that it is a very inefficient one, and typically only one pump photon in 10^8 to 10^{10} is converted into a pair of low-energy photons [219]. The pair-production rate can be increased by either raising the power of the pump laser or by choosing a longer crystal (at the expense of the strength of spatial correlations, as expressed in Eq. 3.7), thus increasing the chances of nonlinear interactions occurring.

Moreover, like in the case of optical parametric amplification where the gain coefficient depends on the momentum or phase mismatch between the three interacting waves, the efficiency of SPDC is also affected by $\overrightarrow{\Delta k}$. The phase-mismatch term is simply defined in terms of the momenta of the three interacting photons as follows [220]:

$$\overrightarrow{\Delta k} = \overrightarrow{\Delta k_p} - \overrightarrow{\Delta k_s} - \overrightarrow{\Delta k_i}. \tag{3.5}$$

The longitudinal component is shown in the phase-matching diagrams in Fig. 3.2, in the case of non-ideal downconversion efficiency. Moreover, the phase-mismatch term is also responsible for the spectral bandwidth of the SPDC beam [221].

The optimal phase-matching angle θ (i.e. the angle between the propagation direction and the optic axis) for which $\overrightarrow{\Delta k} = 0$ can be calculated in terms of the principal value

of the extraordinary n_e and ordinary n_o refractive indices. In the case of a negative uniaxial BBO crystal (i.e. for $n_e < n_o$), θ is defined as follows [222]:

$$sin^2(\theta) = \frac{(n_o^{\omega})^{-2} - (n_o^{2\cdot\omega})^{-2}}{(n_e^{2\cdot\omega})^{-2} - (n_o^{2\cdot\omega})^{-2}}, \tag{3.6}$$

where the refractive indices at the different wavelength due to dispersion are indicated by the ω and $2 \cdot \omega$ superscripts for the downconverted and pump waves. The indices of refraction for ordinary and extraordinary rays in BBO are readily available in the literature [223].

As an effect of angle-tuning, the overall far-field intensity distribution of the down-converted beam can be changed from a sinc^2 profile to a ring, by changing φ as shown in Fig. 3.1. In order to illustrate this effect, a digital camera[2] was placed in the far-field of a type-I BBO crystal. Care was taken in removing the UV-pump after the crystal by means of dichroic mirrors[3] and the exposure time of the digital camera was set to 30 seconds. The resulting pictures of the downconverted beam are shown in Fig 3.3 for a range of φ. The red and blue boxes highlight the far-field intensity distributions for collinear and non-collinear phase-matching.

As can be seen, in type-I downconversion signal and idler photons are arranged concentrically according to their wavelength. Accordingly, low-energy photons (red) can be seen at the centre, and higher energy photons (green and blue) are distributed over larger diameters. It should be noted that whereas in the case of BBO phase-matching is achieved by angle-tuning, other nonlinear materials such as KTP and PPKTP can be phase-matched by tuning their temperature.

[2]NIKON D610, ISO 100, 30 seconds exposure, lensless (i.e. sensor exposed)
[3]Details about the used dichroic filters are reported in appendix A.1.2.

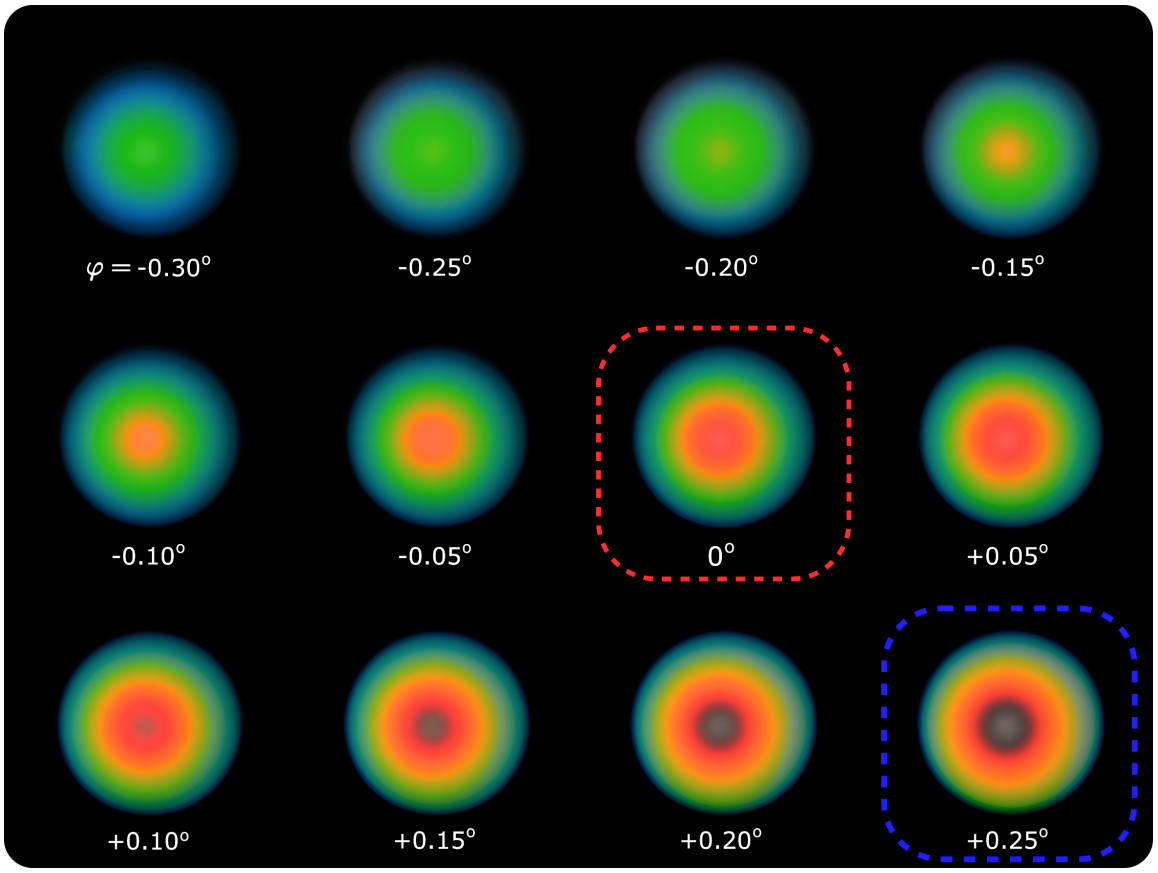

FIGURE 3.3: **Phase-matching by angle-tuning of a type-I BBO crystal.** The phase matching by angle-tuning of a type-I BBO crystal is shown, highlighting the spectral range of the downconverted photons. As the angle φ between the optic axis and the direction of propagation of the pump is changed, the transverse momenta components of the downconverted photons increase. Collinear phase-matching is achieved when the signal and idler photons propagate in the same direction as the pump photon, as highlighted by the red-dotted box. Near-collinear or non-collinear phase-matching is achieved when the directions of the momenta differ from each other, as highlighted by the blue-dotted box. The phase-mismatch term is responsible for the efficiency of the downconversion process, which is maximum when $\overrightarrow{\Delta k_z} = 0$. Each raw colour-image (as shown) was captured using a digital camera placed in the far-field of the crystal using a single $f = 600$mm lens, placed $1f$ away from both the crystal and the detector. The pump beam was removed after the crystal by means of two dichroic filters. The white spot at the centre of the downconverted field is caused by residual UV-pump photons reaching the camera. The field of view of the beam is limited by the diameter of the lens used to access the far-field of the crystal.

3.1.2 Transverse correlation width in type-I phase-matching

The biphotons produced by SPDC are strongly correlated. As a consequence, signal and idler photons of a biphoton packet are born within tens of femtoseconds[4] and in close proximity of each other in a volume within the nonlinear crystal known as the 'birth-zone' [5] [219]. This gives rise to both temporal correlations and spatial correlations. Thus, in order to exploit the quantum correlations of SPDC light it is necessary to design a scheme that for instance may take advantage of the temporal or spatial correlations of the downconverted field (or both as in the case of quantum ghost imaging [5, 143]). If it is not possible to trigger the detection of photons (as in the case of continuous-wave pump lasers or in the absence of either a single-photon avalanche photodiode or intensified CCD) it is still possible to take advantage of the spatial correlations of the downconverted photons.

In the experiments featured in this thesis the temporal correlations between biphotons are only indirectly exploited. That is to say that the nearly simultaneous production of signal and idler photons simply ensures that both photons of each photon-pair is jointly detected within the same exposure time of the employed camera detector. The spatial correlations, however, play a crucial role in achieving better-than-classical performance (as later explained in the context of each individual experiment).

Considering a detection plane oriented transversely to the beam propagation (i.e. a transverse plane) the spatial correlations in the pairs produced from SPDC depend on the energy and momentum conservation of the three interacting fields [224]. The sign of the transverse spatial correlations changes going from the image- to the Fourier-plane of the crystal. Accordingly, the detected positions of signal and idler photons are spatially correlated in the plane (or image-plane) of the crystal (i.e. in the position

[4] An intuitive estimation of the order of magnitude of the time correlation is provided in Eq. 3.23.

[5] The volume of the birth-zone can be approximated to the volume of a sphere of radius σ_x, where σ_x is the transverse correlation width in the plane of the crystal, as expressed in Eq. 3.7 and Eq. 3.17.

basis), and spatially anticorrelated in the far-field (or Fourier-plane) of the crystal, i.e. in the momentum basis [104].

The strength of the correlation as measured in the image plane of the crystal, σ_x, is expressed in terms of the length of the crystal L, the wavelength of the UV-pump λ_p, and an adjustment constant $\alpha = 0.455$ (used to compensate various approximations in the formulation of the mode function of collinear signal and idler photons [225]), as follows [4]:

$$\sigma_x = \sqrt{\frac{\alpha L \lambda_p}{2\pi}}. \tag{3.7}$$

In the case of momentum anticorrelations, it is necessary to include the effective focal length f_e of the lens used to access the far-field of the crystal. The strength of the momentum anticorrelations, σ_p, depends on the width of the Gaussian pump laser beam, and can be expressed as follows [226]:

$$\sigma_p = \frac{f_e}{k \cdot \mathrm{SD}_p}, \tag{3.8}$$

where SD_p is the standard deviation of the Gaussian pump beam, measured from the beam axis, and k is the wave number of the downconverted fields. In the next chapters σ_c is used to indicate the *detected* transverse correlation width in the image or momentum plane of the crystal, as explicitly stated.

A comprehensive derivation of Eq. 3.7 and Eq. 3.8 starting from the quantum biphoton state in SPDC, the biphoton wavefunction, its degenerate, collinear, and paraxial regime, as well as its further approximation to a double-Gaussian wavefunction, and finally the calculation of the transverse correlation width, defined as the standard deviation of the transverse distance between the signal and the idler photons, can be found in the tutorial paper by J. Schneeloch et al. [219].

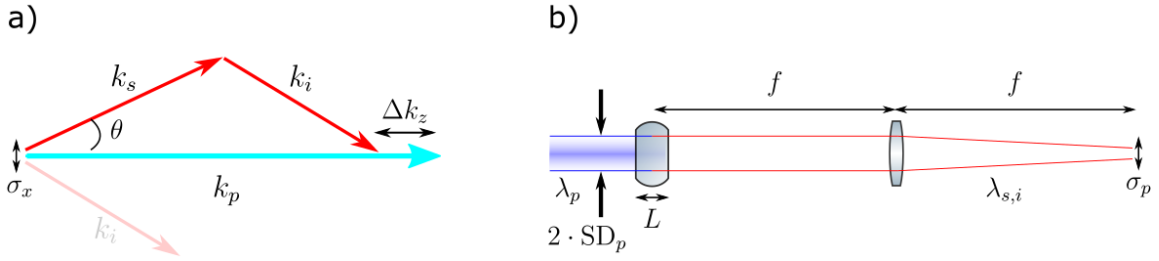

FIGURE 3.4: **Transverse correlation width in type-I phase matching.** Schematic representation of position (a) and momentum (b) transverse correlation widths in a simplified collinear and degenerate type-I phase matching process.

Here I provide a less sophisticated, though perhaps more intuitive, derivation of the transverse correlation width, both in the case of the image and Fourier planes of the crystal, as represented in Fig. 3.4 (a) and (b) respectively, and in the case of degenerate and nearly-collinear Type-I phase-matching.

In the case of the position correlation in the plane of the crystal, optimal phase-matching occurs when $\Delta k_z = 0$. However, if $\Delta k_z \neq 0$ SPDC occurs for:

$$\Delta k_z L \lesssim \pi, \tag{3.9}$$

where L is the length of the nonlinear crystal along the propagation of the pump.

For the degenerate case (i.e. $k_s \approx k_i$) and according to Fig. 3.4(a), Δk_z can be expressed in terms of k_s, k_i, k_p and the angle θ, according to:

$$\Delta k_z = k_p - 2\cos(\theta \cdot k_{s,i}) \tag{3.10}$$

$$= k_p(1 - \cos\theta) \tag{3.11}$$

$$= k_p \frac{\theta^2}{2}. \tag{3.12}$$

Combining Eq. 3.9 with Eq. 3.12 one finds:

$$\frac{\pi}{L} \approx \frac{k_p \theta^2}{2}. \tag{3.13}$$

Re-arranging Eq. 3.13, the angle θ can be expressed as:

$$\theta \approx \sqrt{\frac{\lambda_p}{L}}. \tag{3.14}$$

Equation 3.14 implies the position uncertainty of the photon in the plane of the crystal, i.e. σ_x.

The angular divergence θ of a beam of diameter D is approximately defined as:

$$\theta = \frac{2\lambda}{\pi D}. \tag{3.15}$$

By considering Eq. 3.15 in the case of the signal and idler beams and combining it with Eq. 3.14 one obtains:

$$\frac{2\lambda_{s,i}}{\pi D} = \sqrt{\frac{\lambda_p}{L}}, \tag{3.16}$$

and since $\lambda_{s,i} = 2\lambda_p$, by interpreting D as the position uncertainty of the photon, the transverse correlation width σ_x in the SPDC picture can be obtained by re-arranging Eq. 3.16 as follows:

$$\sigma_x \approx \sqrt{L\lambda_p}, \tag{3.17}$$

where D was substituted by σ_x and the $\approx$ sign is used to omit numerical coefficients. This expression for the transverse correlation width in the plane of the crystal reproduces the physical picture described by the previous cited definition in Eq. 3.7.

In the case of the far-field of the crystal, the transverse correlation width σ_p can be derived according to the simplified picture shown in Fig. 3.4 (b). In this situation the transverse momentum uncertainty of the signal and idler photons is effectively the transverse momentum uncertainty of the pump.

By considering the width of the pump $2 \cdot \mathrm{SD}_p$ (i.e. the transverse extent over which SPDC occurs within the crystal) as the transverse position uncertainty of SPDC and the range of momenta of the pump Δp as the transverse momentum uncertainty, according to the uncertainty principle one has:

$$\cdot \mathrm{SD}_p \cdot \Delta p \simeq \hbar/2, \tag{3.18}$$

from which Δp is expressed as:

$$\Delta p = \frac{\hbar}{2 \cdot \mathrm{SD}_p}. \tag{3.19}$$

In the far-field of the crystal, the longitudinal momentum p_z can be expressed as:

$$p_z = \hbar k_{s,i} \Delta p \approx \frac{\hbar}{2 \cdot \mathrm{SD}_p}, \tag{3.20}$$

where the $\approx$ sign is used to omit numerical coefficients. Thus the angular uncertainty $1/(2\ \mathrm{SD}_p \cdot k_{s,i}) = 1/(\mathrm{SD}_p \cdot k_p)$ determines the position uncertainty in the far-field of the crystal, or the momentum transverse correlation width σ_p, as follows:

$$\sigma_p \approx \frac{f \lambda_p}{\mathrm{SD}_p 2\pi} \approx \frac{f}{k \cdot \mathrm{SD}_p}, \tag{3.21}$$

where f is the focal length of the lens used to access the far-field of the crystal and k is the wavenumber of the pump. Therefore σ_p can be interpreted as the diffraction limited spot-size of the pump in the case of perfect focussing. This expression reproduces the physical picture described by the previous cited definition in Eq. 3.8.

At this point it may be useful to consider the magnitudes of the diffraction limited spot-size, the position transverse correlation width, and the PSF of an imaging system based on an SPDC light-source. As highlighted in the derivations of Eq. 3.17 and

Eq. 3.21, in the case of an ideal imaging system, the transverse correlation width in the near- or far-field of the crystal is fundamentally limited by diffraction. This means that, in the case of perfect focussing, the transverse correlation width in an image or far-field planes of the crystal corresponds to the diffraction limited spot-size of the SPDC illumination. Incidentally, under the same conditions this transverse extent also corresponds to the PSF of the system.

However, in the case of a limited numerical-aperture imaging system, the detected transverse correlation width of the SPDC photons is increased, becoming the convolution of the PSF of the imaging system (now greater than the diffraction limited spot-size) with the original transverse correlation function of the biphotons.

The detected transverse correlation width will define the width of an SPDC spatial mode as determined by the imaging system in question. The transverse size of a mode S_m as detected in the near- or far-field of the crystal can thus be approximated to the area of a circle of radius $\sigma_{x,p}$, according to:

$$S_m \approx M \cdot \pi \sigma_{x,p}^2, \tag{3.22}$$

where M is the magnification of the imaging system.

For a spatially resolved detector that is able to capture all of the transverse extent of the downconverted beam S_b, the number of permitted modes is given by S_b/S_m, given that the pixel-size of the detector is smaller than $M \cdot \sigma_{x,p}$, or in another words that the detector is not spatially undersampled with respect to the size of a mode.

3.2 General experimental set-up used to produce spatially correlated biphotons

Here I discuss the general experimental set-up used to produce spatially correlated biphotons. For the quantum-enhanced sensing and imaging schemes at the single-photon level featured in this thesis, isolation of the experiment from stray light was of paramount importance. Apart from fluorescence induced by the high energy pump photons, unwanted environmental light-sources also needed to be addressed.

3.2.1 Light-tight enclosure

Both issues of UV-induced fluorescence and stray-light were tackled by a custom-built light-tight enclosure, shown in Fig. 3.5.

The enclosure consisted of an assembled metal frame and blackened wooden panels on four sides. Apart from the bottom optical bench, the remaining front side could be sealed by means of removable lids. Care was taken to light proof all junctions and joints, using adhesive foam tape between the metal frame and the wooden panels. Additionally, the removable lids were designed so that they would fit into two recesses, introducing three ninety-degrees turns that stray light would need to propagate through in order to leak from the laboratory into the enclosure. Similarly, all input/output connections were realised using rapid-prototyped light-tight through-wall links. In order to further minimise contamination of the optical signal, the free-space optics in the EMCCD side of the enclosure was linked by light-tight rubber bellows, thus completely isolating the optical channel.

Due to the enclosure being effectively hermetically sealed to the outside, the heat produced by both the laser and the camera was extracted using air- and water-heat pipes. In the case of the laser I designed and 3D-printed a manifold to which

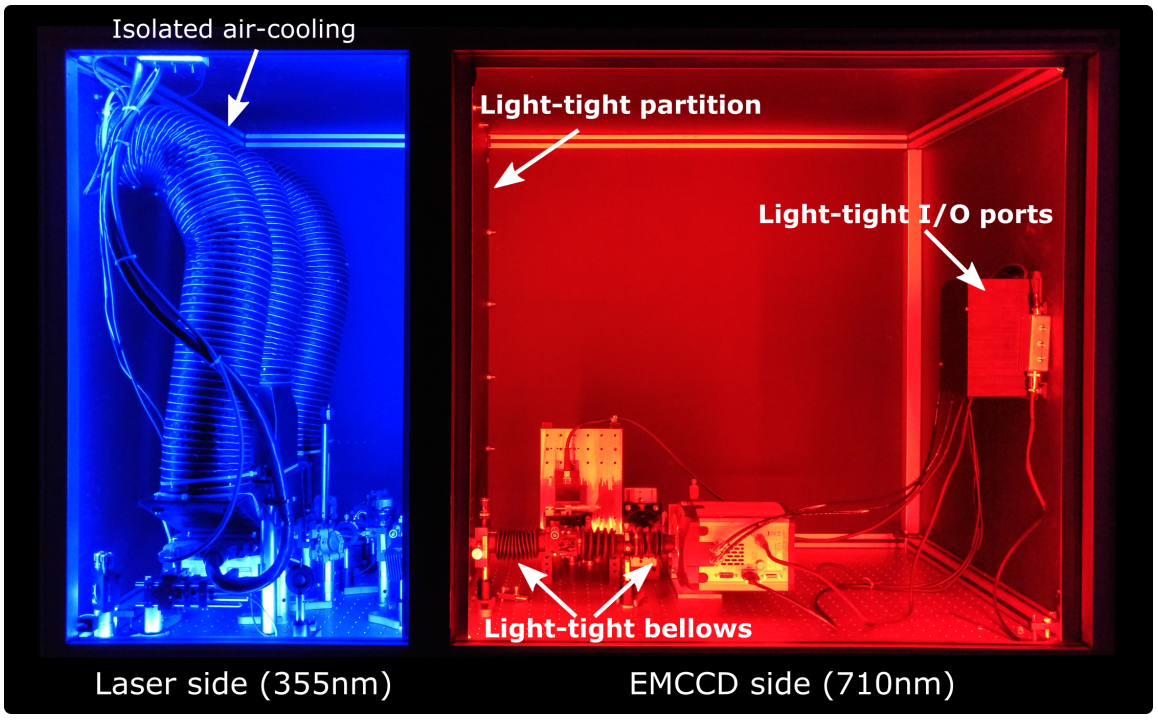

FIGURE 3.5: **Light-tight enclosure.** A light-tight enclosure was designed and built to minimise the number of detected spurious photons by the EMCCD camera (EMCCD side, highlighted in red), both originated from the surroundings and from fluorescence induced by the 355 nm UV pump (laser side, highlighted in blue). The enclosure was realised by attaching blackened wooden panels to a metal frame cladding. Tight-fit interlocking doors, 3D-printed air-cooling funnels and I/O through-wall connectors were used to eliminate stray light. Adapted from [9].

inlet and outlet air-ducts were attached, allowing the cooling to occur in isolation from the air inside the enclosure, thus both extracting the heat produced by the laser and preventing air-flow induced turbulence inside the enclosure. In the case of the EMCCD camera the built-in air-cooling fan was disabled and an external recirculating water chiller was used instead to extract the heat produced by the camera's thermoelectric cooler.

3.2.2 The pump and the crystal

The optics and equipment used produce spatially correlated biphotons by SPDC is shown in Fig. 3.6. Here I discuss each component, starting from the 355 nm UV pump-laser and finishing with the 710 nm interference filter placed in in front of the

EMCCD camera. The set-up is divided by means of a light-tight partition into laser side and EMCCD side, highlighted in blue and red respectively.

The pump consisted of a 150 mW, quasi-continuous wave (CW) (100 MHz±10 MHz repetition rate), 355 nm laser (Lumentum, Xcyte series, model: CY-SM150), $> 99\%$ spectral purity, 0.9 mm waist diameter, polarisation $> 100:1$ horizontal, and pulse-width > 10 ps.

The output 355 nm UV-photons of the pump are the product of a passively mode-locked, frequency tripled Nd:YAG laser. Therefore, a cold-mirror (Thorlabs, M254C45) was placed in front of the output of the laser at a 45-degree angle, letting the residual unwanted long-wavelength laser lines transmit to a beam bump, while directing via reflection the lower wavelength 355 nm output to the rest of the optical channel.

An interference filter centred at 355 nm was then employed to further filter out unwanted spectral components.

Subsequently, the combination of a 50 mm focal length lens, a 50 μm pinhole, and a 300 mm focal length lens was used to produce a collimated and spatially filtered beam used to pump the BBO crystal. A zero-order half-wave-plate (HWP) placed before the 300 mm lens could be used to tune the downconversion efficiency, by rotating the angle of polarisation of the pump with respect to the optical-axis of the nonlinear crystal.

A BBO crystal purchased from Newlight Photonics Inc. (part number NCBBO10300-355(I)-AP) was used to produce SPDC biphotons. The size of the crystal was 10 mm×10 mm×3.0 mm. The crystal was cut for type-I collinear phase-matched SPDC. One side of the crystal was treated with antireflection coating at 355nm, while the other side was treated with a single layer of MgF_2 protective coating, to avoid humidity causing deterioration of the crystal.

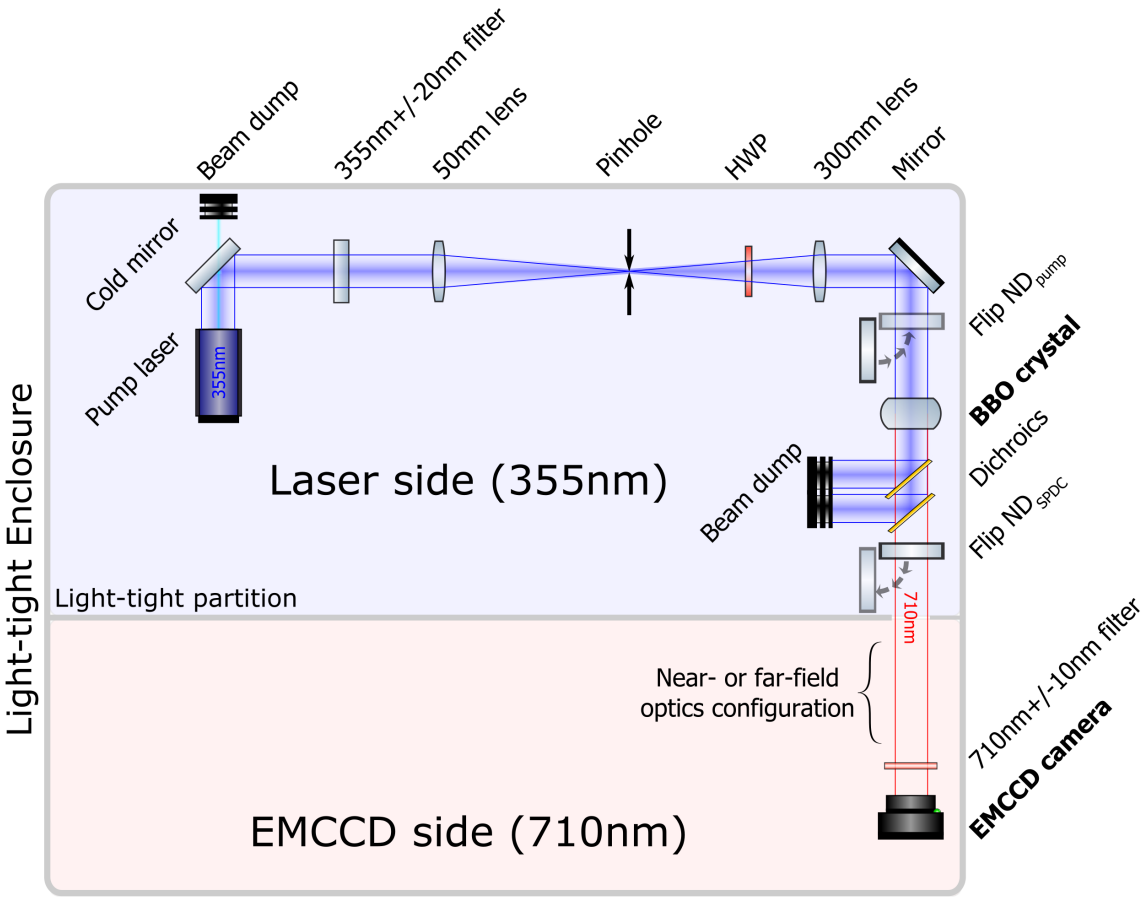

FIGURE 3.6: **Typical setup for the production and detection of quantum correlated biphotons.** (a) shows the optics required to condition the output of a frequency tripled Nd:YAG laser, used for the pumping of a BBO crystal and the production of quantum correlated biphotons. The laser side (highlighted in blue) and the EMCCD side (highlighted in red) are isolated in dedicated compartments by a light-tight partition within an enclosure. Depending on the experiment at hand, the near-field or far-field of the crystal may be accessed allowing one to detect spatially correlated biphotons or spatially anticorrelated biphotons.

Care was taken in removing the UV-pump from the downconverted 710 nm photons by means of two cascaded dichroic mirrors (Chroma, T365lptx), details of which can be found in the appendix A.1.2, and the discarded pump was collected by two beam dumps.

Two ND-filters (ND_{pump}=ND_{SPDC}=2.0 optical density) were used to switch the spatial properties of the downconverted field from spatially correlated to spatially uncorrelated, by alternatively introducing optical loss either before the nonlinear crystal (ND_{pump} flipped-in and ND_{SPDC} flipped-out) or after (ND_{pump} flipped-out and

ND_{SPDC} flipped-in). This allowed the same number of detected events to be maintained for both configurations. By introducing an ND filter after the nonlinear crystal, the chance of jointly detecting both photons of a photon-pair is reduced by a factor of $10^{-2 \cdot OD}$, where OD is the optical density of the ND filter, effectively destroying the quantum correlations. The switching between spatially correlated and spatially uncorrelated light under constant illumination is used to estimate the performance of the quantum enhanced schemes featured in this thesis, as discussed in more details in the next chapters.

A 10 nm wide band-pass interference filter (Chroma, ET710/10BP) centred at 710 nm and mounted in front of the EMCCD camera, was used to select the wavelength degenerate biphotons. Details about the interference filter can be found in appendix A.1.1. Intuitively, the inverse of the fractional bandwidth (FBW) of the detected biphotons can be used to estimate the order of magnitude of the correlation time σ_t between signal and idler photons, as follows:

$$\sigma_t = (\text{FBW})^{-1} = \left(\frac{10 \text{ nm}}{700 \text{ nm}} \cdot \frac{c}{700\text{nm}} \right)^{-1} \approx 160\text{fs}, \tag{3.23}$$

where 10 nm/710 nm is the ratio between the width of the interference filter placed in front of the detector and the degenerate wavelength of the downconverted biphotons, c is the speed of light, and $c/710$ nm is the frequency of the downconverted photons. Lastly, the coherence length l of the laser can be calculated by multiplying the speed of light by the pulse-width of the pump τ_p, according to:

$$l = c \cdot \tau_p \approx 3 \text{ mm}. \tag{3.24}$$

Since the pulse-width of the laser is specified by the manufacturer as being greater than 10 ps, it means that in turn $l > 3$ mm. Given that the width of the chosen BBO crystal for all experiments featured in this thesis is also 3 mm and given that the

pump, signal, and idler photons are all propagating nearly the same direction and thus at the same velocity within the crystal, the coherence length of the pump is non-influential to the resulting transverse correlation length of the produced biphotons.

EMCCD technology and the EMCCD cameras used in the quantum enhanced sensing and imaging schemes featured in this thesis are discussed in the next section.

3.3 Single-photon sensitive detection using an EM-CCD camera detector

Being able to produce single-photons in a certain quantum state is not enough for a quantum-enhanced scheme to work and a suitable single-photon sensitive detector is thus required. In other words, the generation of quantum states of light is not enough alone, and a single-photon detector is required to measure them. The single-photon imaging and sensing experiments discussed in the next chapters rely on the single-photon sensitive detection of biphotons by an EMCCD camera.

Single-photon resolved detection is challenging due to the electronic noise of photo-sensitive devices being typically larger than one electron. In this case the electrical charge produced by an incident photon (i.e. a photoelectron) is mixed with other electrons added by the readout electronics, enabling a distinction between signal (incident single-photons) and noise. This consideration is separate from the QE or detection efficiency of the detector, which may be quite high as in the case of high-responsivity photodiodes. Thus, even if most of the times an incident photon results in the production of a photoelectron in the semiconductor material of the detector, it is still not possible to detect its signal in the presence of electronic noise.

In order to achieve single-photon detection the avalanche effect is typically used to amplify the electrical charge produced by an incident photon [227]. Accordingly,

an avalanche of electrons is produced by impact ionisation, starting from one photo-electron placed in an accelerating electric field. As the kinetic energy of the electron becomes greater than the bandgap of the bulk material, a secondary electron and hole are generated. For enough amplification, the resulting 'lump' of electrons is greater than the electronic noise of the detector, and the signal associated with one incident photon becomes separable from the noise [228].

The mechanism by which EMCCD cameras are able to detect single-photons also relies on the avalanche effect. A schematic representation of the functional components of an EMCCD camera is shown in Fig. 3.7, in which the avalanche multiplication process is also highlighted. In simple terms, an EMCCD is nothing more than a high efficiency, low-noise CCD camera, with the addition of a solid-state gain register placed before the conventional readout electronics. The gain register is used to stochastically amplify the charge produced by one or more photons incident on a detector element (i.e. pixel) by avalanche effect. The resulting signal for each pixel is on average much greater than the noise introduced by the on-chip charge to voltage conversion. Thus, the signal is boosted above the noise floor of the output amplifier.

Specifically, the gain register a typical EMCCD sensor produced by e2v (Teledyne) and used in scientific cameras consists of 600 elements. Each element, as represented in the dashed-box in Fig. 3.7, in turn consists of two gates $\phi 1$ and $\phi 3$ which are clocked using voltage pulses similar those used in the readout register, and a higher voltage gate $\phi 2$ used to accelerate the charges in the preceding gate $\phi 1$ to ballistic speeds. Approximately once in a hundred, the accelerated electron gains enough kinetic energy to produce a secondary electron and a hole. The process is repeated over as many additional stages as the number of the gain elements. Thus, the combined multiplication over 600 stages results in average on a large total gain [230].

From the perspective of single-photon quantum imaging applications, the stochastic nature of the multiplication process is a very important one. This causes the final

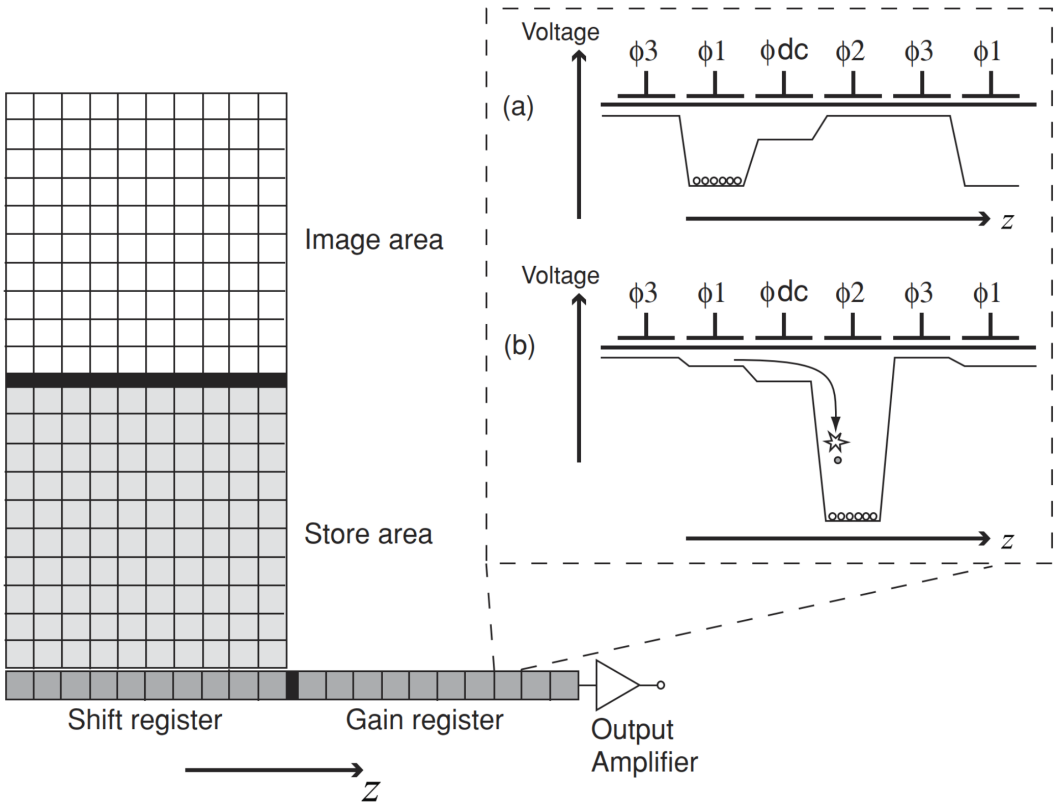

FIGURE 3.7: **Functional components of an EMCCD sensor.** A schematic representation of a typical EMCCD sensor is shown on the left, together with a representation of the gates involved in one multiplication step (dashed-box). Specifically, the frame-transfer sensor consists of an exposed half (Image area) where photoelectrons are produced from incident photons, and a shielded half (Store area) where the photoelectron charges of a frame are shifted awaiting the electronic multiplication and readout. Both vertical and horizontal transfer of photoelectron charges is achieved by clocked electric fields. Before reaching the noise-introducing CCD-readout electronics (Output Amplifier), each photoelectron is shifted horizontally (Shift register) to a dedicated register (Gain register) where avalanche multiplication takes place several hundred times, resulting in typical effective gains of 1000. The voltage phase diagram of one of these avalanche steps is shown in the dotted box. A series of gates (ϕ) are activated according to a specific sequence. The voltage potentials associated with the clocked electric fields cause the photoelectrons to accelerate to ballistic speeds, eventually resulting in the production of a considerable amount of secondary electrons. The amplified 'lump' of charge is then processed by the readout electronics (Output electronics). Reproduced from [229].

output signal in analogue counts associated with one or more incident photons to be affected by excess noise, which in the case of several hundred multiplication steps corresponds to a factor of $\sqrt{2}$ [230].

For this reason EMCCD cameras cannot be used as reliable photon-number resolved detectors [231]. Instead, the light level is typically reduced such that at most only one photon per frame per pixel is detected and a single discriminating photon-counting threshold is employed. Thus, if the signal of a pixel is found to be greater than a specified value (i.e. a threshold in analogue counts), the detection of one photon is assigned for that pixel. If on the other hand the signal does not exceed the threshold then no detection is assigned. Such a process gives rise to a binary detection scheme, according to which the value of each pixel of a single acquired frame is either 0 (no detection) or 1 (one detected photons). In such a photon-counting regime, the frames produced by an EMCCD camera are free of excess noise. That is to say that the variance of the number of detected events is not affected by the excess noise associated with the avalanche multiplication gain, although noise events (i.e. dark-events) are still present.

3.3.1 Optimal settings

Scientific EMCCD cameras are sophisticated measurement devices with many adjustable settings. In the case of Andor EMCCD cameras, it is possible to adjust many acquisition parameters, some of which can have a considerable impact on the noise performance of the detector. These are: 1) cooling, 2) EM-gain, 3) pre-amplifier gain, 4) exposure time, 5) shift speeds and voltage amplitude, and 6) crop-mode.

Some of these important parameters can be easily determined from the working principle of EMCCD cameras, some however, require ad-hoc characterisation. Below

I discuss the tuning of each parameter in relation to single-photon detection performance.

1) Cooling. In the case of cooling, the lower the temperature the better in terms of thermalised dark-noise. In fact, it is possible to half the amount of thermalised photoelectrons (i.e. exposure-time dark-noise) for every 7° to 9°C of extra cooling [232]. At the same time however, impact ionisation is found to increase at lower temperatures, and with it the amount of produced clocked-induced-charge. Moreover, the quantum efficiency of the camera-chip is found to be negatively affected by cooling, especially in the near infrared, due to silicon becoming more transparent as a consequence of a lower photon absorption-depth [233]. In the case of the employed Andor ULTRA 888 and ULTRA 897 cameras fitted with a 'BV' optical window, the QE decreases from 88.57% (710nm) at room temperature to 77.75% (710nm) at $-100°C$ [234]. However, deep-cooling of the sensor is still paramount in ensuring an overall optimal noise performance [235], and a value of $-100°C$ was found to be a good one in most cases.

2) EM-gain. The EM-gain is the determining feature in an EMCCD camera. The highest setting ensures the maximum probability of detection. More specifically, it enables the photoelectron produced by an incident photon to be multiplied to a sizeable enough current to be discernible from the electronic noise of the readout electronics. It should however be noted that as impact ionisation increases so does the chance of producing clock-induced charge (CIC). Nevertheless, the maximum allowed EM-gain was found to be the optimal compromise considering QE and CIC.

3) Pre-amplifier gain. The pre-amplifier gain is simply used to proportionally increase the number of signal electrons produced after the EM multiplication stage [236]. It therefore consists of a deterministic multiplication factor. A value of 1 was found to be optimal.

4) Exposure time. The exposure time controls the electronic global shutter of the EMCCD. Generally speaking, the shortest the exposure time the better in terms of noise performance, as more dark-counts can be accumulated for longer times. However, this time is usually automatically set when using the camera in frame-transfer mode. In this readout mode, each frame captured by the light-exposed half of the chip is completely shifted along the vertical direction and stored in the light-shielded half of the chip. The exposure time is set to match the time to vertically shift the charges, resulting in the fastest continuous acquisition rate. Thus, the exposure time was set to the shortest allowed value for the chosen ROI of the chip and using the frame transfer readout mode.

5) Shift speeds and voltage amplitude. The remaining parameters (horizontal readout speed, vertical readout speed, vertical-clock voltage amplitude) are interlinked in terms of the resulting cycle time (i.e. the overall time required to both acquire and digitise a frame). These settings are adjusted as to achieve the best noise performance in terms of dark-events per pixel per frame.

Specifically, the readout speed was set to 10MHz for the Andor ULTRA 888, corresponding to the second slowest speed, and 1MHz for the Andor ULTRA 897. The reason for wanting a slow horizontal speed is to reduce impact ionisation and the resulting CIC generated during the transfer of charges. Moreover, the faster the readout speed the hotter the chip gets and the more thermalised photoelectrons are produced. Similarly, the vertical readout speed was also set to the second slowest speed for both camera models.

The vertical-clock voltage amplitude was set to its normal level. This parameter controls the amplitude of the electric field used to sweep the generated photoelectrons during charge transfer. Typically it can be increased by a up to a few Volts during fast readout of the sensor. This ensures that no charges are left behind in the pixel potential wells, avoiding artefacts in subsequent frames. In the case of both the

Andor ULTRA 888 and ULTRA 897 featured in this thesis, high voltage amplitudes caused more noise events in the acquired frames.

6) Crop-mode. Andor EMCCD cameras support a 'crop-mode' that allows to selectively address a smaller portion of the sensor. In this acquisition mode the camera only addresses a smaller portion of the sensor, completely bypassing the discarded pixels, thus achieving faster readout speeds without compromising the noise performance [237]. Care must be taken in shielding the unaddressed portions of the sensor from incident light, in order to avoid photoelectrons unintentionally leaking into the acquired frames. Using this readout mode it is therefore possible to drastically speed-up acquisition rates, beyond what is normally achieved using a ROI. Whereas conventional acquisition ROIs still require all the pixels to be vertically shifted, crop-mode allows to redefine the number of addressable pixels, such that only the chosen pixels are vertically and horizontally shifted [238].

It should be noted that faster acquisition rates may result in greater heat being produced in the sensor. This needs to be considered in the case of prolonged acquisitions (many thousands of frames), especially if water cooling is not available.

Finally, a summary of the setting for both the Andor ULTRA 897 and 888 cameras as used in the experiments featured in this thesis is provided in table 3.1.

TABLE 3.1: **EMCCD camera settings.** Summary of the EMCCD cameras settings for each experimental investigation.

	Experimental investigations:		
	Chapter 4, Sec. 4.2	Chapter 5	Chapter 6
Camera model:	ULTRA 897	ULTRA 888	ULTRA 888
Full frame pixels:	512×512	1024×1024	1024×1024
Utilised pixels:	512×512	512×512	356×356
Pixel size:	$16\mu m$	$13\mu m$	$13\mu m$
Chip cooling:	$-100°C$	$-90°C$	$-95°C$
Liquid cooling:	$10°C$	$15°C$	$15°C$
Exposure time:	57.75 ms	56.795 ms	39.733 ms
EM-Gain:	1000	1000	1000
Vertical speed:	$0.5\,\mu s$	$1.13333\,\mu s$	$1.13333\,\mu s$
Readout rate:	1 MHz	10 MHz	10 MHz
Pre-amp. gain:	1.0	1.0	1.0
Baseline-offset:	0 electrons	0 electrons	0 electrons
Baseline-clamp:	Enabled	Enabled	Enabled
Clock-amplitude:	0V	0V	0V
Frame transfer:	Enabled	Enabled	Enabled

3.3.2 Estimation of the optimal photon-counting threshold from dark-frames

Since the number that is used to threshold the acquired frames effectively defines a photon, great care must be taken in choosing this number. Whereas it is possible to choose the optimal threshold based on acquired bright frames of quantum correlated biphotons (as discussed in chapter 4, section 4.2.4), it is also possible to choose the threshold based on the count statistics of dark frames [231, 239]. The count statistics of dark frames can be conveniently visualised by plotting the histogram of dark-counts on a logarithmic scale, as shown in Fig. 3.8 in the case of 500 dark-frames (512×512 pixels) acquired by an Andor ULTRA 888 EMCCD camera. If the chosen photon-counting threshold falls within the (a) range in Fig. 3.8, the Gaussian contribution due to the electronic noise of the camera will take over the signal associated with the actual detection of photons. This low-threshold situation effectively invalidates the benefit of the gain register and the photons' signal can only be detected in the

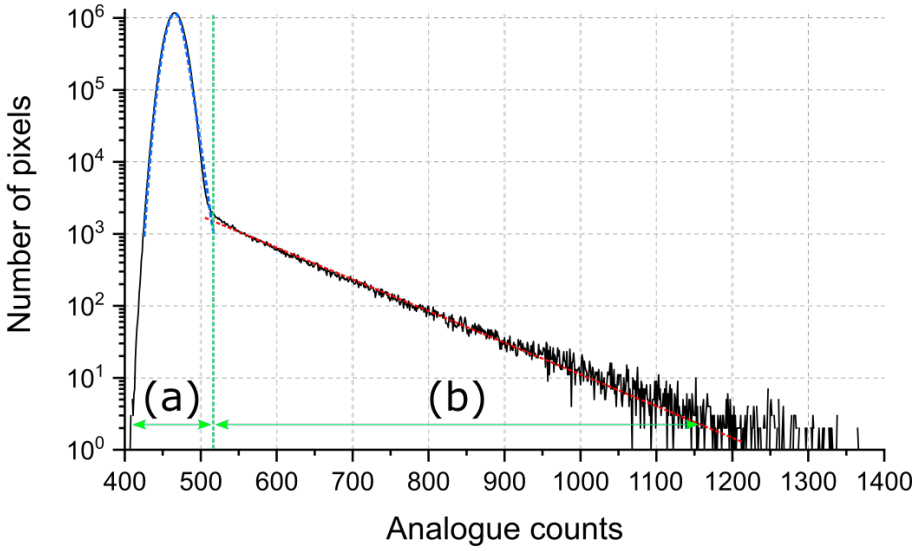

FIGURE 3.8: **Histogram of dark-counts for an Andor ULTRA 888 EM-CCD camera.** 500 dark-frames (512×512 pixels) were used to produce a histogram of dark-counts, here shown on a logarithmic scale. The Gaussian contribution due to the electronic noise of the readout amplifier extents over the (a) range of counts. The linear contribution due to amplified dark-events (thermalised electrons and clock-induced-charge) extends over the (b) range of counts, as highlighted by the red linear-fit. In case of deep-cooling of the sensor A photon-counting threshold can be chosen based on the mean and standard deviation of the fitted blue-Gaussian curve.

case of high-intensity illumination.

On the other hand, if the chosen photon-counting threshold falls within the (b) range in Fig. 3.8, the resulting signal will be free of the contribution due to the electronic noise of the camera. Nevertheless, an unnecessarily high threshold will result in the loss of photon-events, due to the stochastic nature of the gain register. In fact, the multiplied value in analogue counts for one incident photon can take any value within the range (b). Naturally, lost photon detections mean lower QE. Thus the 'sweet-spot' for the threshold is as low as possible, without falling within the range of the Gaussian electronic noise. Typically, the threshold T is specified based on the mean μ_{readout} and standard deviation $\text{SD}_{\text{readout}}$ of the Gaussian curve fitted to the electronic noise contribution, i.e. the blue-dotted curve in Fig. 3.8 as follows [231, 239]:

$$T = \mu_{\text{readout}} + 2 \cdot \text{SD}_{\text{readout}}. \tag{3.25}$$

Lantz et al. found that a light-level of 0.15 photons per pixel per frame is typically associated with the best signal to noise ratio for Andor EMCCD cameras [239]. On the other hand, Tasca et al. found that the best detection efficiency in the case of quantum spatial correlations is achieved when the number of bright events matches the number of dark events of the detector [226]. Both regimes are used in this thesis: the former to achieve sub-shot-noise performance in the optical measurement of the position of a shadow (as discussed in chapter 5) and the latter to achieve a resolution-enhancement by CEBs (as discussed in chapter 6).

In terms of detection efficiency, two factors play an important role in the case of EMCCD cameras: dark-noise and QE.

Dark-noise is the signal per pixel per frame as produced when no light is allowed to reach the detector. In the photon-counting regime (i.e. when a threshold is used to binarise the frames) the resulting dark-events constitute false detections, which based on their binary nature are effectively indistinguishable from actual photon events. Dark-events can be caused by thermalised electrons and CIC. The former can effectively be remedied by deep cooling of the sensor, whereas the latter is linked to the accidental production of secondary electrons by impact ionisation during the transfer of charges within the sensor. For this reason CIC cannot be completely remedied and can only be minimised by choosing slow vertical and horizontal shifting speeds, and to some extent by limiting the cooling of the detector which affects the probability of generating secondary electrons. Both approaches can however result in unwanted effects, such as slow acquisition rates and greater levels of thermalised electrons.

The QE of scientific-grade EMCCD cameras is the same as for high-performance CCDs and at room temperature can reach values up to 98% in the visible range. However, this does not mean that up to 98 times in 100 it is possible to retrieve an unambiguous signal for an incoming photon, since both noise events and the

stochastic nature of the gain register need to be considered. The high quantum efficiency stated by EMCCD manufactures simply means that up to 98 times in 100, a photoelectron is generated in the chip as a result of an incoming photon. The actual detection in terms of a digitised signal (including photon-counting by thresholding the frames) results in a much lower detection efficiency. When the overall losses of an imaging or sensing scheme are also considered, the total effective QE of detection channel based on a deep-cooled, photon-counting EMCCD detector is typically measured to be less than 40%, as reported in a number of works where a source of quantum correlated photons was used as a reference [7, 10, 240, 241].

The detection efficiency of EMCCD cameras is revisited later in each chapter, in the specific context of the sensing or imaging scheme at hand.

3.3.3 Spurious light

The availability of a high QE, single-photon sensitive detector means that great care must be taken in avoiding spurious sources of unwanted luminous signal. In the low-light regime at which the experiments featured in this thesis were carried out, small imperfections such as a fingerprint or a speck of dust on an optical surface may be enough to compromise the ability of the scheme to achieve a quantum enhancement.

In practical terms this simply means that optics needs to be handled with care and that dust and fingerprints are to be avoided, especially in the optics placed before the nonlinear crystal where UV-light can cause fluorescence. Although good experimental practice does not need a lengthy discussion, I will report an example in which three specks of dust and a partial fingerprint caused the production of ≈800 spurious photons. Results highlighting the effects of spurious fluorescent photons are shown in Fig. 3.9. The EMCCD was set up to image the plane of the BBO nonlinear crystal, using a $4f$ imaging system. The downconverted field was extinguished by

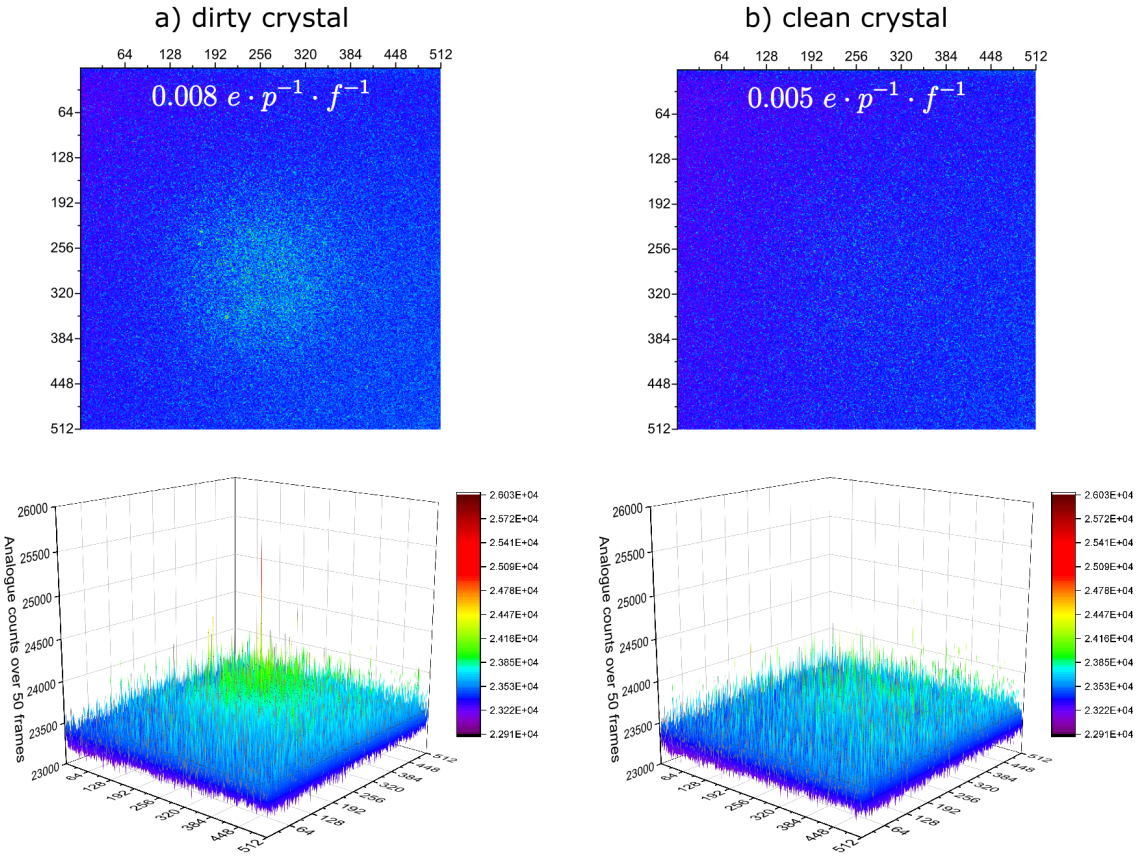

FIGURE 3.9: **Spurious noise induced by fluorescence.** The sum of 50 frames is shown to highlight spurious fluorescence due to the interaction of the UV-pump and dirty optics. The EMCCD camera was set up to image the plane of the BBO nonlinear crystal. In order to acquire only spurious photons, the downconversion efficiency was minimised by turning the plane of polarisation of the UV-pump. Under this condition, the only events detected by the camera should be dark-events, as no downconverted light can be produced and the UV-photons of the pump are removed by two dichroic mirrors placed immediately after the crystal. However, ≈800 spurious fluorescent photons were still detected. This number was found by taking the difference of the mean number of photon-counted events in a) and b). This noise was caused by three specks of dust and a partial fingerprint on the facet of the nonlinear crystal. The number of dark events per pixel per frame using a typical photon-counting threshold $T = 510$ is shown. The bottom 3D representations of the summed frames (not photon-counted in this case) are shown to highlight the presence of spurious photons.

minimising the efficiency of SPDC, allowing one to measure the amount of spurious 710nm light. In the case of fluorescent photons caused by dirty optics placed in the UV-pump, the number of dark events was measured to be 0.008 events per pixel per frame, as shown in Fig. 3.9(a). The unwanted fluorescence consisted of 790 photons (710nm), quantified using a photon-counting threshold of 510 analogue counts. More specifically, the number of unwanted fluorescent photons was computed by taking the difference of the number of events detected before cleaning the crystal ($0.008\ e \cdot p^{-1} \cdot f^{-1}$) and after cleaning the crystal ($0.005\ e \cdot p^{-1} \cdot f^{-1}$), i.e. $2100\ e - 1310\ e = 790$ photons. Note that this last value can be assumed to represent the number of detected photons, since the the dark-events cancel-out when taking the difference.

Once the optics were carefully cleaned the number of dark events measured 0.005 events per pixel per frame, corresponding to the typically measured number of dark events for dark-frames acquired with the shutter of the EMCCD camera closed, as shown in Fig. 3.9. The minute amount of fluorescence (790 photons) would be enough to completely neutralise the quantum enhancement of the schemes reported in both chapter 5 and 6.

Chapter 4

A model for the spatially resolved detection of biphotons

In this chapter I first describe a simple yet powerful model for the spatially resolved detection of biphotons produced by SPDC. Additionally I validate the accuracy of the model via an experiment, in which under different levels of optical loss the numbers of predicted and experimentally detected biphotons are compared.

In the next experimental chapters, this model is used to characterise the performance of the sub-shot-noise shadow sensing and of the resolution-enhanced quantum imaging schemes.

4.1 A simple model for the spatially-resolved detection of biphotons

The model here described produces photon-counted frames, like those acquired by an EMCCD camera illuminated by downconverted photons. Specifically, starting

from user-defined parameters which can be experimentally measured or estimated, the model produces pixel-coordinates of detected events in a frame, which consist of either bright N_B or dark events N_D, whose sum must add up to the total number of detected events in a frame, N, as follows:

$$N = \frac{N_B}{\eta_{\text{total}}} + N_D. \tag{4.1}$$

Thus, in order to maintain a certain mean number of detected events N, as the η_{total} of a detection scheme decreases, the number of bright events N_B needs to increase (i.e. by increasing the intensity of the light source). Note that according to Eq. 4.1 the model works for $0 < \eta_{\text{total}} \leq 1$.

The bright-events in a frame can either be single photons arising from partial absorption of a photon-pair, or actual biphotons. Both the detected 'unpaired' photons and biphotons are distributed according to the Gaussian intensity profile of the downconverted beam. However, in the case of biphotons, the detected positions of the signal and idler photons will be either spatially correlated or anticorrelated. In order to account for the total effective QE η_{total}, the model 'throws the dice' for each bright-event, checking the randomly generated value against a user defined parameter, thus mimicking the quantum behaviour of photo-detection [242].

The dark events are due to either thermalised photoelectrons or clock-induced-charge and are detected in a frame at random positions. The total number of dark-events N_D can be set to the number of dark events of the camera, which is easily measured by thresholding dark-frames, acquired in darkness and with the shutter of the camera in the closed position. Since fluctuations in the number of dark-events from frame to frame is Poissonian, it is possible to easily incorporate this feature in the model, using a Poissonian distribution of mean N_D. Charge-smearing, non-linearity in the pixel response, and other subtle imperfections of the sensor are ignored.

Therefore, each frame produced by the model corresponds to a distribution of detected pixel-coordinates $F(x, y)$, defined as the sum of the bright- and dark-events coordinates, $B(x, y)$ and $D(x, y)$, as follows:

$$F(x, y) = B(x, y) + D(x, y), \tag{4.2}$$

where $0 \leq x, y \leq d$ are the pixel-coordinates of a square frame of width d. This is illustrated in Fig. 4.1, in which the individual contributions due to dark-events and bright-events were produced using the model, for the photon-counted detection of type-I downconversion by an EMCCD placed in the far-field of the crystal.

More specifically, the bright pixel-coordinates of signal and idler photons (indicated by the s and i subscripts respectively) are defined as follows:

$$B(x, y) = \sum_{n=0}^{N_B/2} \Omega(f_s(x_n, y_n)) + \Omega(f_i(x_n, y_n)), \tag{4.3}$$

where Ω is the detection operator that determines whether a photon is detected or missed by acting on a function $f(x, y)$ as follows:

$$\Omega(f(x, y)) = \begin{cases} 0, & \text{if } u(0,1) > \eta_{\text{total}} \text{ (missed event)} \\ f(x, y), & \text{if } u(0,1) \leq \eta_{\text{total}} \text{ (detected event).} \end{cases} \tag{4.4}$$

where $0 < \eta_{\text{total}} \leq 1$ is the user-defined total effective QE and $u(0, 1)$ is a uniform distribution used to computationally generate pseudo-random numbers between 0 and 1.

The x and y pixel-coordinates of the bright-events are produced starting from two user-defined parameters: σ_m and σ_c. These account for the overall transverse spatial extent of the downconverted beam, as measured in plane of the detector, and for the detected correlation-width of the spatially correlated biphotons. Both intensity

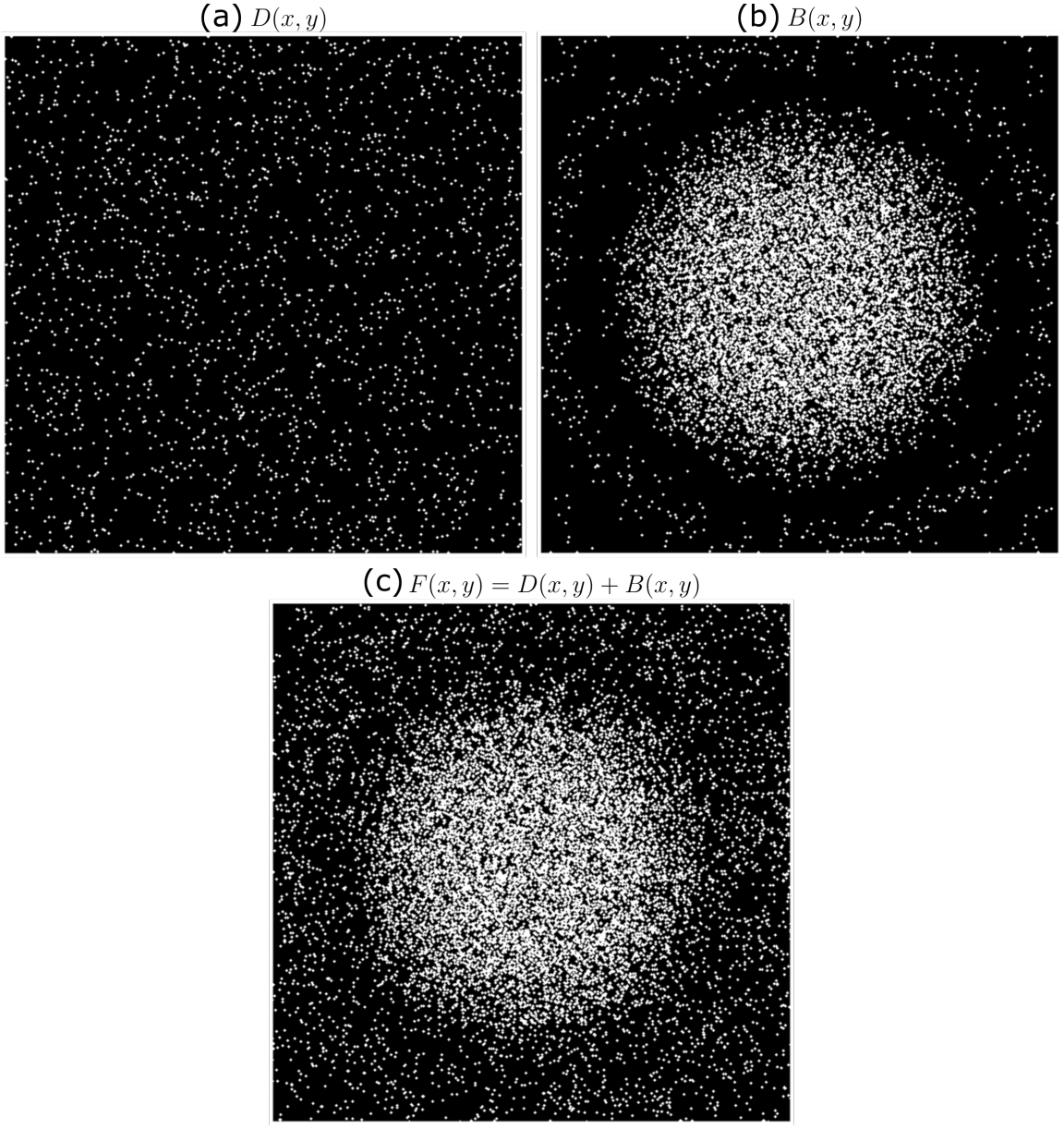

FIGURE 4.1: **Modelled pixel-coordinates of detected events for a photon-counted frame.** The pixel-coordinates $F(x, y)$ of detected events for each modelled frame consists of two contributions: 1) randomly distributed dark-events due to thermalised photoelectrons and clock-induced-charge (a), and the pixel-coordinates of the detected downconverted light (b). The sum of these contributions is shown in (c) and corresponds to the typical photon-counted output produced by an EMCCD camera illuminated by downconverted light.

profile of the downconverted beam and the intensity profile of the correlation peak are approximated to Gaussian curves, $g_m(x)$ and $g_c(x)$ respectively, defined as follows:

$$g_m(x \mid \sigma_m) = \frac{1}{\sqrt{2\pi\sigma_m}} e^{-\frac{x^2}{2\sigma_m^2}} \tag{4.5}$$

$$g_c(x \mid \sigma_c) = \frac{1}{\sqrt{2\pi\sigma_c}} e^{-\frac{x^2}{2\sigma_c^2}}. \tag{4.6}$$

In the case of spatially anticorrelated photons produced by a type-I nonlinear crystal and detected by a photon-counting camera placed in the far-field of the crystal, the sum of the x and y coordinates for all signal photons in a frame is defined as follows:

$$f_s(x,y) = \sum_{n=0}^{N_B/2} \left(x_n = x_m + x_c + \frac{d}{2}, y_n = y_m + y_c + \frac{d}{2} \right), \tag{4.7}$$

and the sum of the x and y coordinates for all the corresponding spatially anticorrelated idler photons (located at the 180-degree reciprocal positions with respect to their partners) are defined as follows:

$$f_i(x,y) = \sum_{n=0}^{N_B/2} \left(x_n = -x_m + x_c + \frac{d}{2}, y_n = -y_m + y_c + \frac{d}{2} \right), \tag{4.8}$$

where x_m, y_m and x_c, y_c are the computer-generated pseudo-random values generated from the $g_m(x)$ and $g_c(x)$ Gaussian distributions described in Eq. 4.5 and 4.6, and $d/2$ is used to locate the beam at the centre of the frame.

In the case of spatially correlated photons produced by a type-I nonlinear crystal and detected by a photon-counting camera placed in the near-field of the crystal, the sum of the x and y coordinates for all signal or idler photons in a frame is defined as follows:

$$f_{s,i}(x,y) = \sum_{n=0}^{N_B/2} \left(x_n = x_m + x_c + \frac{d}{2}, y_n = y_m + y_c + \frac{d}{2} \right), \tag{4.9}$$

where each pair of pixel-coordinates $f(x_n, y_n)$ is unique, depending on the generated pseudo-random values for x_m, x_c, y_m, and y_c.

It should be noted that the pixel-coordinates defined in Eq. 4.7, 4.8, and 4.9 include all of the detectable downconverted photons, as produced by the nonlinear crystal. These are then reduced upon detection according to the value of η_{total} (i.e. due to the effect of optical and detector losses), as defined in Eq. 4.3.

Finally, the sum of the x and y coordinates of the randomly distributed dark-events in a frame $D(x, y)$, is defined as follows:

$$D(x, y) = \sum_{n=0}^{N_D} f_D(x_n, y_n), \tag{4.10}$$

where x_n and y_n are pseudo-random numbers between 1 and d generated from the uniform distribution $u_D(1, d)$.

The modelled pixel-coordinates for spatially correlated and anticorrelated photons are shown in Fig. 4.2(a) and (b) respectively.

The model was calibrated using the following parameters: $\langle N_D \rangle = 0$ events, $\langle N_B \rangle = 50$ events, $\eta_{\text{total}} = 1$ (i.e. lossless detection), $\sigma_m = 60$ pixels, and $\sigma_c = 0$ pixels (i.e. perfect correlation).

It may be useful to note that, in the case of type-I downconversion, the intensity distribution of the downconverted beam changes from a Gaussian to a *sinc*-like, going from the image-plane to the Fourier-plane of the crystal [241]. In the Fourier-plane, the distribution is *sinc*-like, depending on the phase-matching, and becomes a ring in the case of non-collinear phase-matching.

The basic model presented in section 4.1 can be augmented in a number of ways, taking advantage of the flexibility provided by computational implementations. In

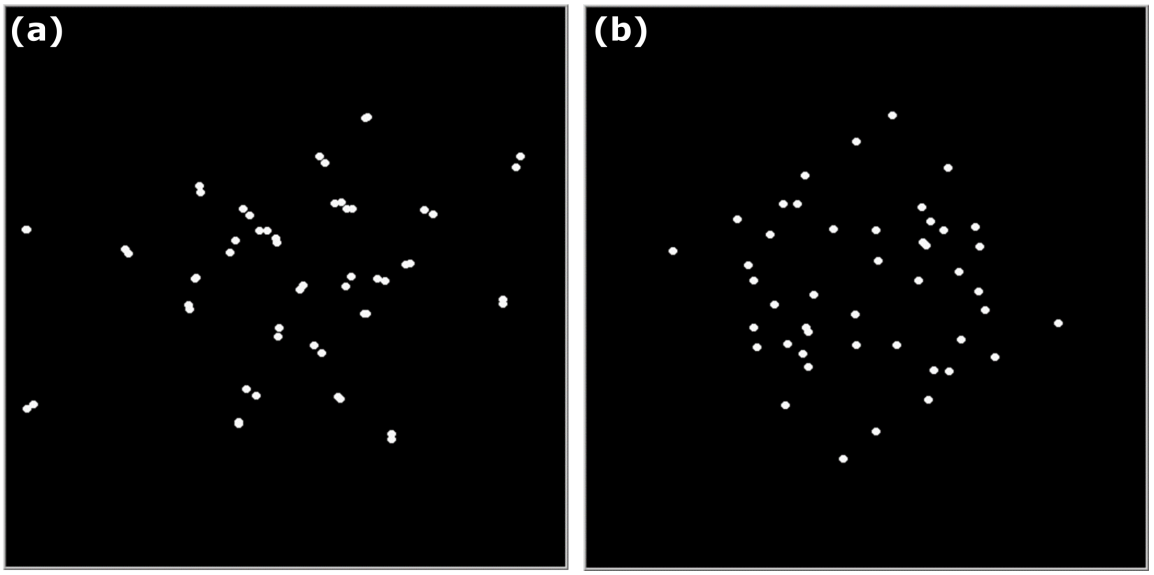

FIGURE 4.2: **Modelled pixel-coordinates of position correlated and position anticorrelated biphotons.** The modelled pixel-coordinates of 50 photon-pairs are shown, reproducing the detection of biphotons by a photon-counting camera placed in the image plane (a) or Fourier plane (b) of a type-I nonlinear crystal, in the case of perfect spatial correlations ($\sigma_c = 0$) and total effective QE ($\eta_{\text{total}} = 1$).

the next three sections I will discuss the modelling of the detection of wavelength-degenerate biphotons, in the case of photon-tagging, type-II downconversion, and non-collinear type-I downconversion.

4.1.1 Modelling the photon-tagged detection of biphotons

To begin with, it is possible to implement true photon-number resolved detection of events, by keeping track of multiple events detected by the same element (i.e. pixel) of the spatially-resolved detector array. This mode of detection is beneficial when coincidence losses (i.e. when more than one photon is recorded per pixel per frame) have an adverse effect on the performance of a scheme. An example of the photon-number resolved implementation of the model for the detection of spatially anticorrelated biphotons is discussed in section 4.2.3.

Similar to how photon-number resolved detection of events can be achieved by simply keeping track of the total number of photons detected per pixel per frame, it is also possible to tag each detection, thus keeping track of each individual dark and bright-event. Computationally, this can be easily achieved if for example each event is associated with a unique number, in addition to the two required for its x and y coordinates. This tag-number, which is used to label each event, can be set to be the same for all dark-events, since the spatial information of the noise of the detector may not be of use for a certain modelled scheme. In the case of the signal and idler detected events of a biphoton packet, the tag-number can be set to be the same, as shown below in the case of position correlated photons:

$$f_{s,i}(x,y,n) = \sum_{n=0}^{N_B/2} \left(x_n = x_m + x_c + \frac{d}{2}, y_n = y_m + y_c + \frac{d}{2}, n \right), \tag{4.11}$$

where n is the tag-number, associated with the pair of pixel-coordinates of each bright-event. A representation of this photon-tagging is shown in Fig. 4.3 for both position correlated and position anticorrelated photons.

In the case of non-unitary total effective QE, it is also possible to separate single bright-events from jointly-detected event-pairs, since in the former case only one event with the same tag is left after detection.

4.1.2 Modelling the detection of type-II downconverted biphotons

Another extension of the model allows to reproduce the detection of downconverted events in the case of type-II downconversion. In this phase-matching condition, the signal and idler beams are spatially separated in the plane of a detector placed in the far-field of the nonlinear crystal [243, 244]. In this case, the pixel-coordinates

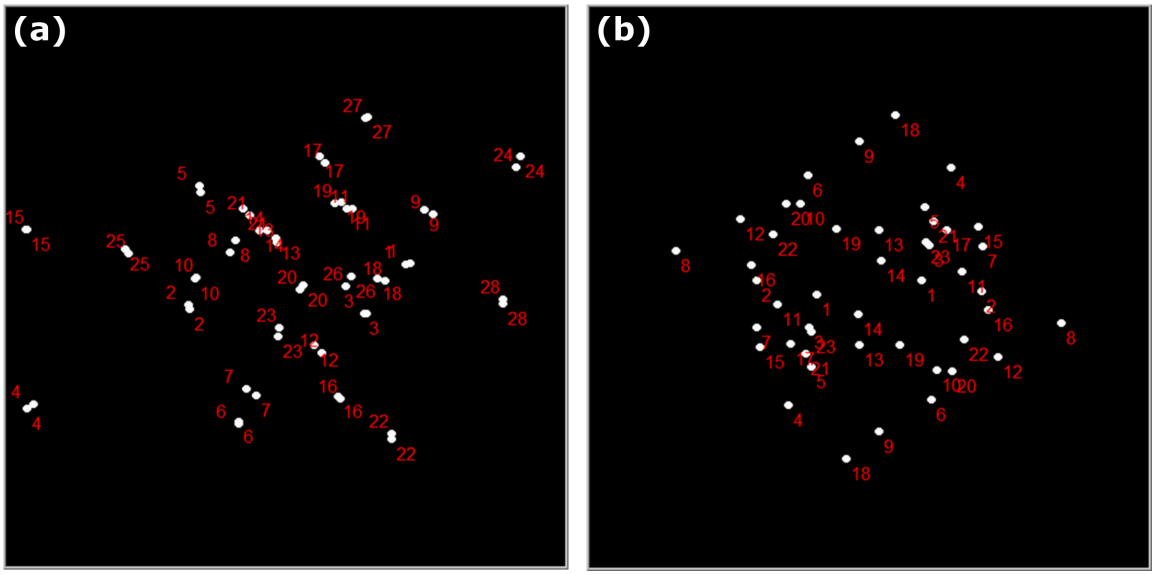

FIGURE 4.3: **Photon-tagged detection of modelled biphotons.** In this implementation of the model, a tag is created for each detected event (here pictorially represented by the red-numbers), identifying the photons of different biphoton packets. Computationally it is possible to implement tagging in the form of a third number, associated with each detected event, in addition to the two numbers required for the x and y coordinates.

of collinear signal and idler biphotons in the plane of the detector, are defined as follows:

$$f_s(x,y) = \sum_{n=0}^{N_B/2} \left(x_n = x_m + x_c + X_s, y_n = y_m + y_c + Y_s\right), \tag{4.12}$$

$$f_i(x,y) = \sum_{n=0}^{N_B/2} \left(x_n = -x_m + x_c + X_i, y_n = -y_m + y_c + Y_i\right), \tag{4.13}$$

where $X_{s,i}$ and $Y_{s,i}$ are offsets in pixels in the x and y directions that determine the positions of the type-II signal and idler beams within the frame, as well as their separation. A representation of the modelled detection of type-II downconversion is shown in Fig. 4.4, in the case of spatial anticorrelated biphotons. Again it is possible to implement photon-tagging, by adding a tag-number to each signal and idler photon of a biphoton packet, as shown in Fig. 4.4(b).

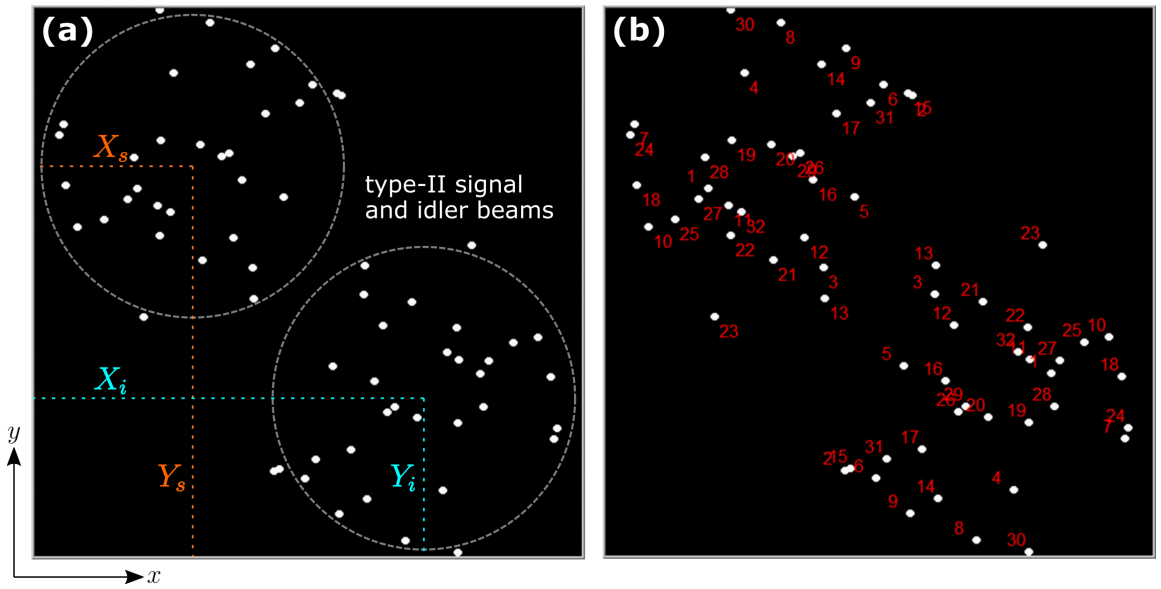

FIGURE 4.4: **Modelled detection of type-II downconverted biphotons in the far-field.** The modelled type-II downconverted signal and idler beams are detected in separate positions in the far-field of the crystal (a). The positions and the separation between the detected signal and idler beams are specified by the $X_{s,i}$ and $Y_{s,i}$ offsets. The modelled pixel-coordinates of the position anticorrelated signal and idler photons are highlighted in (b). Each photon of a biphoton packet is associated with a different tag-number (shown in red).

4.1.3 Modelling the detection of non-collinear, type-I downconverted biphotons

When considering the image-plane of the crystal where downconverted photons are born, the transverse intensity distribution of downconverted light is found to match that of the pump beam, and in most cases, this intensity-envelope can be approximated to a Gaussian. This approximation was applied for example in Eq. 4.5 to define the x_m and y_m pixel coordinates of bright-events. However, in the case of noncollinear phase-matching where the downconverted envelope is not a Gaussian, a different approach is required. Here I show how it is possible to model the detection of biphotons for arbitrary intensity profiles. In this example I show how a measured intensity cross-section of the downconverted beam can be used to accurately model a *sinc*-like intensity distribution of the downconverted beam, as detected in the far-field of a type-I nonlinear crystal, aligned for nearly-collinear downconversion.

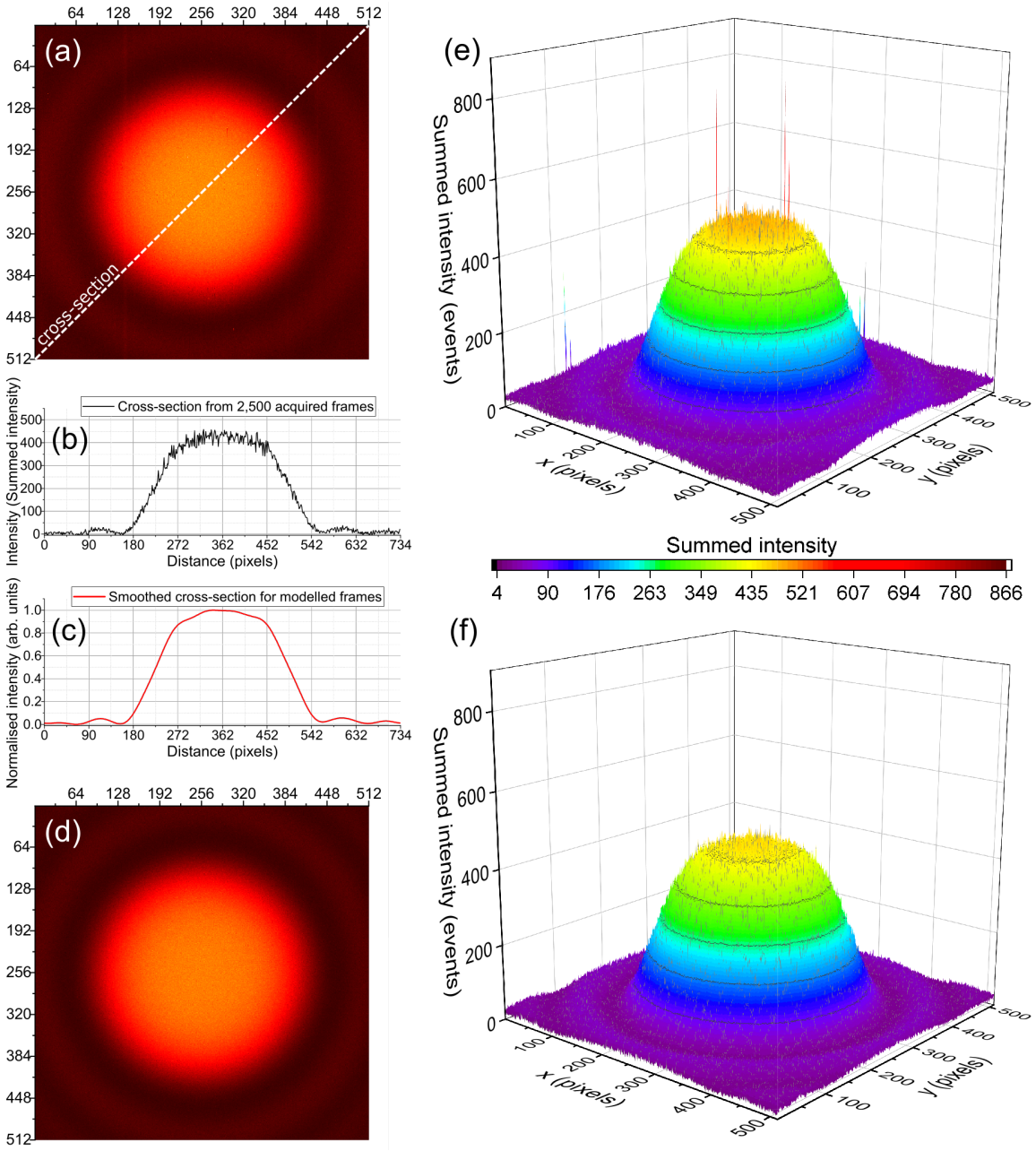

FIGURE 4.5: **Modelled detection of biphotons for a *sinc*-like intensity distribution.** The workflow used to model the detection of biphotons produced by a type-I crystal aligned for almost-collinear downconversion is shown. 2,500 frames acquired by an EMCCD camera placed in the far-field of the crystal are averaged together (a), in order to extract a low-noise intensity cross-section of the downconverted beam (b). The *sinc*-like intensity cross-section is normalised and smoothed by applying a low-pass filter (c). The average of modelled frames using the measured intensity cross-section is shown in (d). Whereas the non-linear response of the EMCCD chip causes signal spikes to be seen in the 3D-representation of the averaged intensity (e), in the case of the modelled frames, the averaged intensity is free of artefacts (f).

Firstly, a number of photon-counted frames (2,500 in this case) is acquired to produce an averaged image of the downconverted beam, as shown in Fig. 4.5(a). Next, an intensity cross-section along the diagonal is extracted, so as to include the peripheral lobes of the *sinc*-like profile, as shown in Fig. 4.5(b). This is used to compute a smoothed and normalised cross-section, obtained for example by applying a low-pass filter, as shown in Fig. 4.5. This smoothed cross-section, $f_{\text{mes.}}(x)$, is the measured intensity-profile used in the model to determine the overall intensity distribution of the bright-events.

In the case of an arbitrary one-dimensional distribution, like for the extracted *sinc*-like intensity cross-section, a probabilistic approach can be used to retrieve the x and y pixel-coordinates of modelled signal and idler photons. Here I show how it is possible to compute these coordinates in the case of spatially anticorrelated photons. The pixel-coordinates for a signal photon can be retrieved from the smoothed and normalised intensity cross-section $f_{\text{mes.}}(x)$, by satisfying the following inequality:

$$f_{\text{mes.}}\left(\sqrt{\left(x_s-\frac{d}{2}\right)^2+\left(y_s-\frac{d}{2}\right)^2}\right) > u(0,1), \tag{4.14}$$

where $x_s = y_s = u(0,d)$ is a pseudo random integer number between 0 and the width of the frame, and u(0,1) is also a pseudo-random number used to define whether the chosen combination of x and y coordinates falls within the measured intensity cross-section. As soon as Eq. 4.14 is satisfied, the x and y coordinates of the partner idler photon are retrieved simply as follows:

$$x_i = -x_s + d + \sigma_c \tag{4.15}$$

$$y_i = -y_s + d + \sigma_c \tag{4.16}$$

The detection operator Ω is then separately applied to the found signal and idler coordinates, to account for the total effective QE of the scheme, as discussed in

section 4.1. Definitions of the other terms appearing in Eq. 4.14 and 4.15 can be found earlier in the chapter, in section 4.1. It should be noted that the method described in Eq. 4.14 can be computationally expensive, as many pairs of coordinates may be wasted while trying to satisfy the inequality. Additionally, even if a satisfactory pair of coordinates is found, the corresponding event may not be committed to the frame, according to the outcome of the detection operator.

The average of 2,500 modelled frames generated using the measured intensity cross-section is shown in Fig. 4.5(d). Due to the non-linear response of some of the pixels of the EMCCD chip, spikes are noticeable in the averaged frame, as highlighted by the 3D representation in Fig. 4.5(e). These artefacts are missing in the 3D representation of the modelled frames, shown in Fig. 4.5(f).

4.2 Validation of the model

In this section the accuracy of the model is validated. This is done by comparing the number of detected biphotons for both modelled and experimentally acquired frames, retrieved using the properties of the autocorrelation function discussed in section 2.1.4. The σ_m, σ_c, N_D, N_B, and d parameters of the model (discussed in section 4.1) are specified to match the experimental counterparts.

More specifically, the number of detected photon-pair events N_{pe} [1] per frame was computed from acquired frames, for different levels of optical loss, and under constant photon flux conditions (i.e. for the same mean number of detected events per frame). The proportion of quantum correlated biphotons and uncorrelated biphotons was changed by placing neutral density filters between the crystal and the detector,

[1] Note that N_{pe} is the number of detected biphoton-events or photon-pair events. This value is different from the number of generated photon-pairs or biphotons N_p, discussed in chapter 2 section 2.1.4.

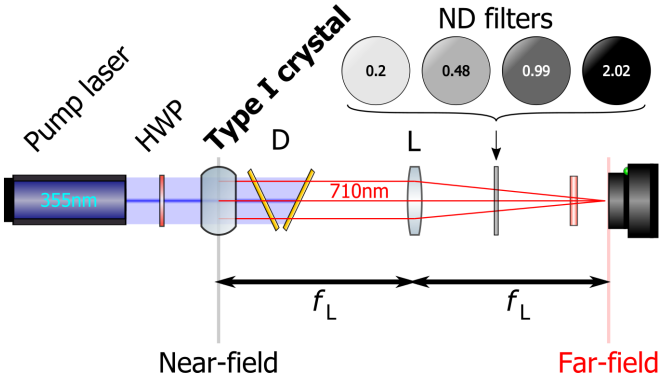

FIGURE 4.6: **Experimental apparatus to detect spatially anticorrelated biphotons.** A source of 710nm degenerate biphotons was realised by pumping a BBO crystal cut for degenerate downconversion with a 355nm laser. A half-wave plate (HWP) was used to tune the intensity of the downconverted beam. Two dichroic mirrors (D) were used to remove the pump. A 250 mm Fourier lens (L) was used to access the far-field of the crystal. Multiple datasets consisting of 2,500 frames were acquired for different levels of optical loss, under constant illumination conditions achieved by balancing the optical loss with a higher intensity of downconverted light. In this way, the attenuation introduced by various neutral density filters was compensated by tuning the downconversion efficiency by means of the HWP. The optical density at 710nm is reported for the different ND filters, as specified by the manufacturer.

while the mean number of detected photons was maintained, by increasing the intensity of the downconverted beam (achieved by rotating the plane of polarisation of the pump and thus the downconversion efficiency). The number of quantum correlated biphotons extracted from the acquired frames under different levels of optical loss was used to compute the total effective QE, starting from the measured number of dark events of the detector, the number of detected biphotons, and the average number of detected events per frame.

The experimental set-up used to capture photon-counted frames of downconverted biphotons is shown in Fig. 4.6. Details about the experimental set-up used to produce spatially correlated biphotons by SPDC can be found in chapter 3, section 3.2.2. This consisted of a type-I downconversion source (labelled 'Type I crystal'), a series of selectable neutral density (ND) filters (introduced between the source and the detector), and a single-photon sensitive, spatially resolved EMCCD

camera (Andor ULTRA 897). A 250 mm focal length planoconvex lens, was used to access the far-field of the crystal. The acquired frames of the far-field of the crystal were photon-counted by applying a single event-discriminating threshold in analogue counts, above which the detection of a photon (or a noise event in the case of dark counts) could be determined. In the first instance (i.e. before analysing the frames and producing the results shown in section 4.2.4) a threshold was chosen starting from a statistical analysis of dark-frames [226, 239]. An ad-hoc value was then measured by analysis of the acquired bright-frames, allowing one to maximise the ability to detect quantum correlations of the scheme.

4.2.1 Qualitative comparison between modelled and acquired photon-counted frames

Photon-counted frames of downconverted light in the far-field of a type-I crystal are shown in Fig. 4.7, as produced by the model and as acquired by the EMCCD camera. Samples of individual frames are shown in Fig. 4.7(a) and (d), whereas the sum of 250 frames is shown in Fig. 4.7(b) and (e). As visible from the *sinc*-like intensity distribution of the frames, the modelled pixel-coordinates of the detected bright-events were computed using the experimentally measured intensity cross-section discussed in section 4.1.3. The average cross-correlation for 250 frames is also shown in Fig. 4.7(c) and (d), highlighting that the square-root of the integral of the correlation function, $\sqrt{\mathcal{C}}$, is equal to the mean number of events in a frame [2], $\langle N \rangle$, as predicted by Fubini's theorem in Eq. 2.16.

As can be seen, the model generated frames accurately reproduce the spatial features of the acquired frames. Moreover, both kinds of data, the modelled and experimental, display the presence of spatial correlations, as visible in the correlation peaks in the

[2] Note that the mean number of detected events $\langle N \rangle$ is different from $\langle N_t \rangle$, which is the total number of generated photons.

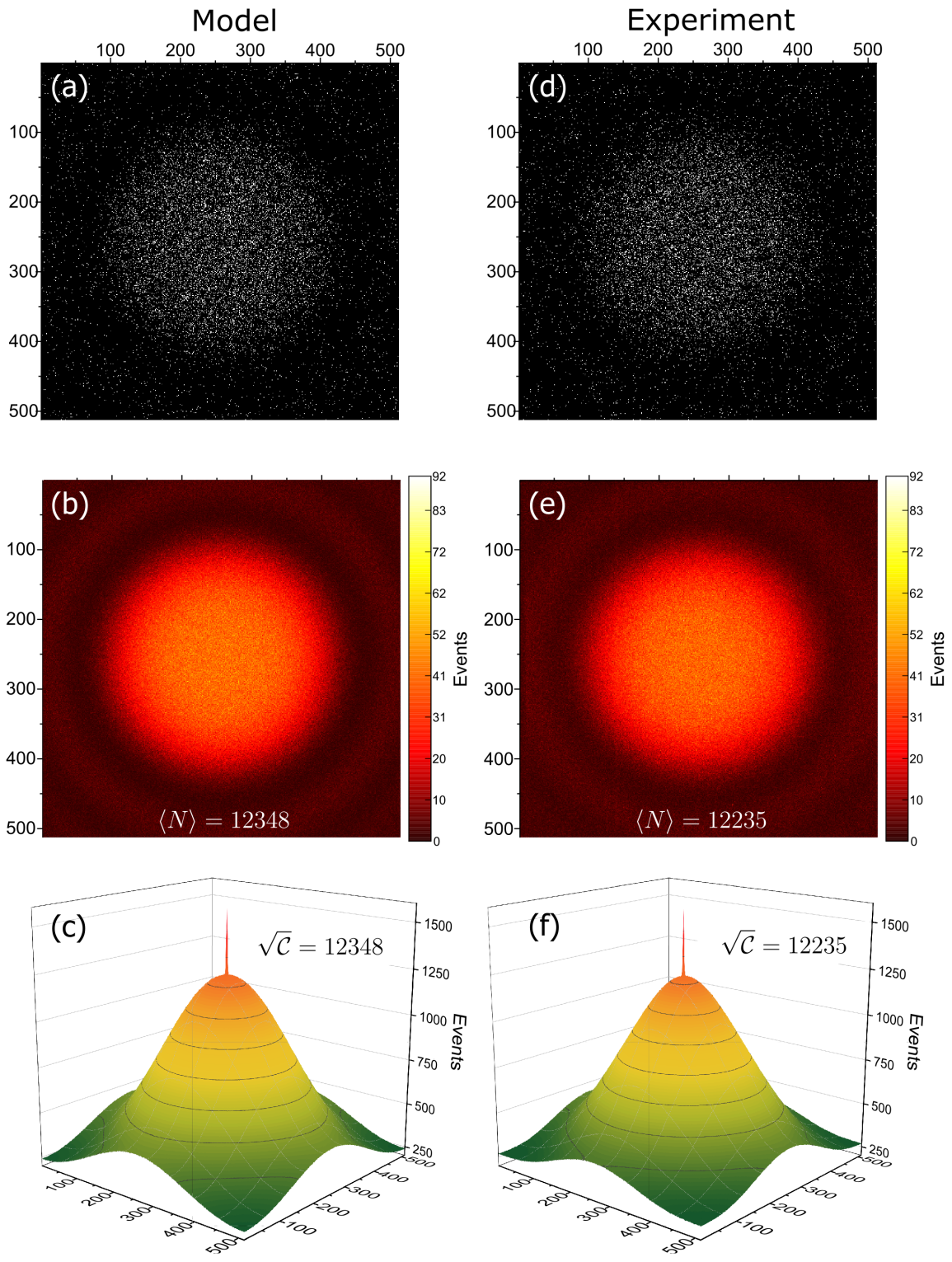

FIGURE 4.7: **Qualitative comparison of modelled and acquired frames showing both noise and downconverted photons, as detected in the far-field of a type-I nonlinear crystal.** Individual photon-counted frames as shown for modelled (a), and acquired frames (b). The average of 250 such frames is shown in (b) and (e). The average autocorrelations of 250 frames are shown in (c) and (f). According to Fubini's theorem (see Eq. 2.16) the square root of the integral of the autocorrelation function $\sqrt{\mathcal{C}}$ is the same as the average number of detected events $\langle N \rangle$. Reproduced from [162].

3D-representations of the averaged correlation functions in Fig. 4.7(c) and (f). The experimentally measured width of correlations was retrieved by curve-fitting of the correlation peak visible in Fig. 4.7(f). This value was used in the model to specify the correlation width of the modelled biphotons. Similarly, the detected number of dark-events N_D and the total number of bright-events N_B, were also experimentally measured and used in the model accordingly. As discussed in section 4.1.3, the beam waist parameter σ_m is not used if the overall intensity distribution of the downconverted beam is determined by an experimentally generated intensity cross-section.

4.2.2 Quantitative comparison of the number of detected biphotons for both modelled and acquired frames

The accuracy of the model was further tested by comparing the number of jointly-detected photon-pair events N_{pe}, extracted by computing the integral of the background-subtracted correlation function for both modelled and acquired frames.

More interestingly, the measurement of N_{pe} was repeated for different levels of extra optical loss, introduced in the form of ND-filters placed between the crystal and the detector, as shown in Fig. 4.6. Accordingly, 2,500 frames were acquired for each ND-filter. It is important to note that the total number of detected events per frame was kept constant throughout the experiment, by increasing the intensity of the downconverted light according to the value of optical loss of each ND filter. Under this constant illumination condition for which the average number of detected events was maintained, it was still possible to extract the number of detected biphoton - events, using the properties of the autocorrelation function discussed in section 2.1.4, Eq. 2.21. The intensity cross-sections of the background-subtracted correlation peaks, as computed for 2,500 frames and for each ND-filter are shown in Fig. 4.8. The

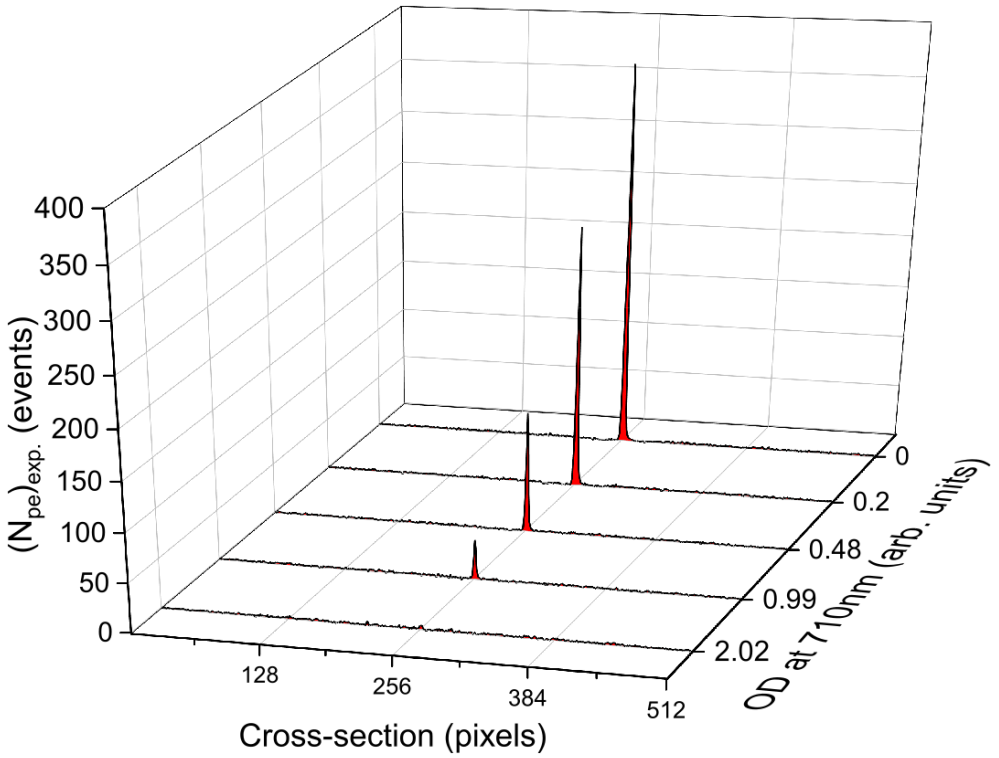

FIGURE 4.8: **Background-subtracted correlation peaks.** The intensity cross-sections of temporally subtracted autocorrelation functions are shown for different values of optical density of ND-filters introduced between the crystal and the EM-CCD camera. As expected, the number of detected biphotons extracted from the acquired frames (N_{pe})$_{exp.}$, is inversely proportional to optical density. Reproduced from [162].

background subtraction of the autocorrelation function was performed according to the method adopted by M. Edgar et al. [4] by subtracting the autocorrelations of subsequent frames (i.e. by temporal subtraction). Alternatively, it is also possible to extract the correlation peak of the autocorrelation function by subtracting the 2D-fitted uncorrelated pedestal [241]. As can be seen from the cross-sections shown in Fig. 4.8, the number of detected biphotons is adversely affected by optical loss. In fact, as the optical density of the ND-filter is increased, there is a greater probability of photons being absorbed, resulting in a higher number of 'broken' pairs, and thus single, spatially uncorrelated bright-events.

In addition to the analysis of acquired frames, a new batch of 2,500 modelled frames was produced for different values of the η_{total} parameter, chosen as to match the

TABLE 4.1: **Detected biphoton -events for modelled and acquired frames for different levels of optical loss, and for the same mean total number of detected events.** The nominal values of optical density and percentage transmission at 710nm for the various ND-filters are reported in the first and second columns. The measured number of photon-pair events for both the modelled data and the acquired frames are reported in the 3rd and 4th columns. The number of detected photon-pair events in the absence of extra optical loss was chosen as a reference, allowing one to estimate the values of neural density for the other filters, simply by taking the ratio of the reference number of photons-pair events with the detected number of photon-pair events for each filter. The experimentally estimated values of optical density are reported in the last column. Adapted from [162].

$\mathbf{ND}_{710\mathbf{nm}}$	$\mathbf{T}_{710\mathbf{nm}}$ (%)	$(\mathbf{N}_{pe})_{\mathbf{model}}$	$(\mathbf{N}_{pe})_{\mathbf{exp.}}$	$\mathbf{OD}_{\mathbf{exp.}}$
0.00	100	1608 ± 24	1612 ± 19	0.00
0.20	63.1	1015 ± 14	1083 ± 20	0.17 ± 0.01
0.48	33.1	505 ± 16	527 ± 24	0.49 ± 0.02
0.99	10.2	174 ± 17	172 ± 30	0.97 ± 0.08
2.02	0.95	15 ± 19	21 ± 12	1.88 ± 0.28

number of experimentally measured N_{pe} for each ND-filter. The estimated value of optical density $\mathrm{OD}_{\mathrm{exp.}}$, together with the computed values of detected biphotons for modelled $(\mathrm{N}_{pe})_{\mathrm{model}}$ and acquired frames $(\mathrm{N}_{pe})_{\mathrm{exp.}}$, are shown for each neutral density filter in table 4.1.

The nominal optical density at 710 nm and corresponding percentage-transmission, as stated by the manufacturer, are listed in the first and second columns, under the $\mathrm{ND}_{710\mathrm{nm}}$ and $\mathbf{T}_{710\mathbf{nm}}$ (%) headers respectively. The experimentally estimated OD values $\mathbf{OD}_{\mathbf{exp.}}$ were computed according to:

$$\mathrm{OD}_{\mathrm{exp.}} = -log\left(\frac{(N_{pe})^{ND\neq 0}_{(\mathrm{exp.})}}{(N_{pe})^{ND=0}_{(\mathrm{exp.})}}\right), \tag{4.17}$$

where $(N_{pe})^{ND=0}_{(\mathrm{exp.})}$ is the number of detected photon-pair events in the absence of extra optical loss (i.e. for ND=0), and $(N_{pe})^{ND\neq 0}_{(\mathrm{exp.})}$ is the number of detected photon-pair events in the presence of extra optical loss (i.e. for ND$\neq$ 0). As an example, the OD value for ND=2.02 was found using Eq. 4.17 according to: $\mathrm{OD}_{\mathrm{exp.}}(\text{for ND=2.02}) = -log\left(\frac{21}{1612}\right) = 1.88$.

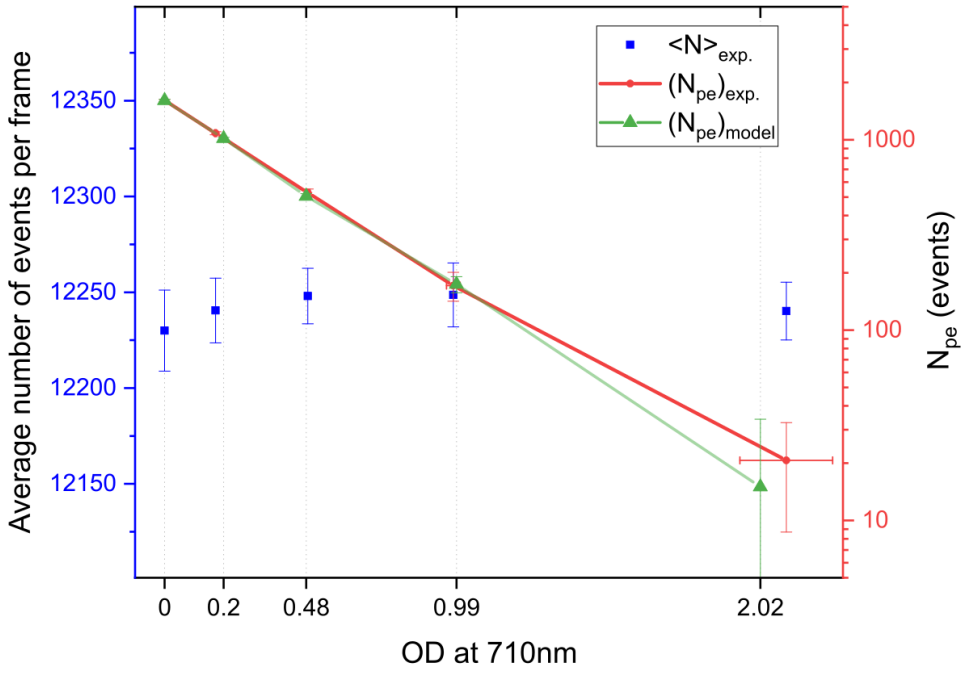

FIGURE 4.9: **Detected biphoton -events for different values of optical loss.** The number of detected photon-pair events computed from the integral of the background-subtracted correlation peaks for acquired $(N_{pe})_{exp.}$ (red-series) and modelled frames $(N_{pe})_{model}$ (green-series), is shown for different levels of optical loss achieved by increasing levels of optical density introduced between the crystal and the EMCCD camera. The fact that the number of detected photon-pair events decreases in spite of a constant number of detected events $\langle N \rangle_{exp.}$, is the key result of the property of the autocorrelation function discussed in section 2.1.4. Both green and red series are shown on a logarithmic scale.

The results reported in table 4.1 are plotted in Fig. 4.9, together with the average number of experimentally detected events per frame $\langle N \rangle_{exp.}$ measured from acquired frames.

4.2.3 Jointly-detected biphoton events: binary detection VS. photon-number resolved detection

At present, true photon-number resolved detection remains a challenge, with the QE of the detector elements playing a crucial role in the ability to resolve more than a few photons [245], since the probability of detecting the n_{th} photon $P(n_{th})$ decreases rapidly according to $P(n_{th}) = (\text{QE})^{n_{th}}$, and so does the quality of the photon-number

measurement. In the case of EMCCD cameras the difficulty of photon-number resolved detection in the presence of stochastic amplification was highlighted in the works by A. G. Basden et al [246] and E. Lantz et al. [239].

While photon-number resolved detection remains an experimental challenge, it is possible to achieve this goal with a model. Here I investigate the effects of binary detection on the number of detected biphotons, using the photon-number resolved extension of the model discussed in section 4.1.1. Specifically I show how the number of detected biphoton -events (and thus the total effective QE of the scheme) is adversely affected by an increasing number of detected bright-events (expressed in events per pixel per frame). Accordingly, modelled frames were produced using the experimentally computed parameters identified in the previous section, to investigate the role of the level of illumination on the number of detected biphoton -events, in the case of binary and photon-number resolved detection. The results are shown in Fig. 4.10. The number of events per pixel per frame associated with the different light-levels was computed within the lateral extent of the modelled beam ($\sigma_m \approx 142$ pixels), where the majority of events are detected. The grey-series in Fig. 4.10 represents the designed number of generated biphotons, as specified in the corresponding parameter of the model, whereas the green-series represents the photon-number resolved detection of biphoton -events, measured using Eq. 2.21. The yellow series represents the photon-counted (i.e. binary) detection of biphoton -events, for which at most one event is counted for each bright pixel, regardless of the actual number of detected photon -events per pixel. The difference in the number of detected events between the binary and photon-number resolved detection schemes highlights the loss of photons associated with binary detection in the light-intense regime. This is due to the an increasing probability of coincident detection, for which more than one photon -event 'lands' on the same detector-element within one exposure time, resulting in the loss of all but one event. This effect is exacerbated in the case of

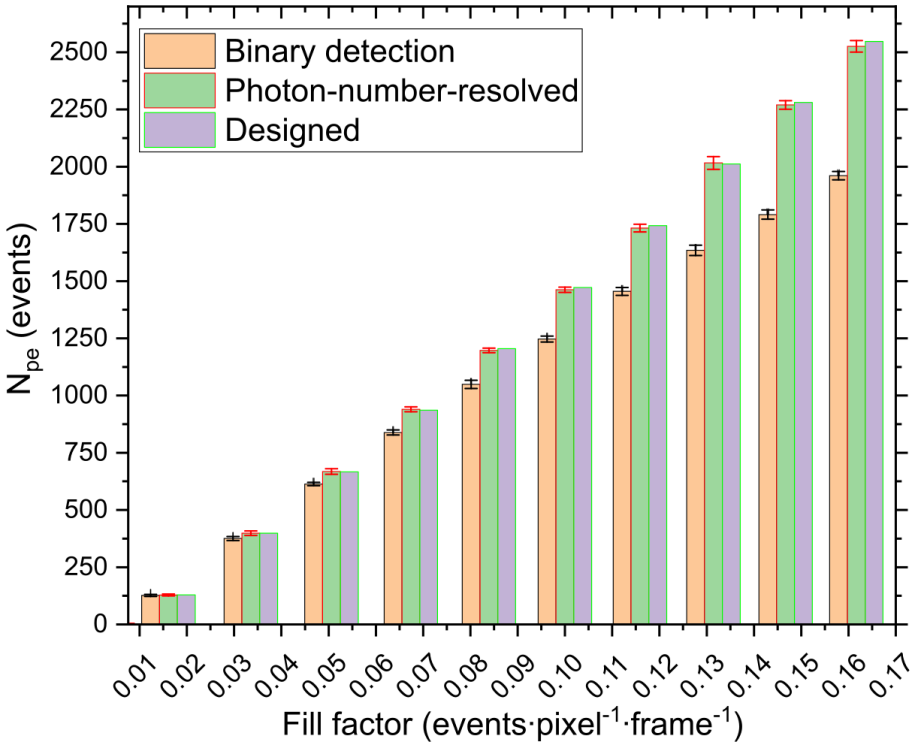

FIGURE 4.10: **Comparison in the number of detected biphoton -events for binary- and photon-number resolved detection strategies.** The number of detected biphoton -events N_{pe} was modelled in the case of binary detection (yellow-series) and photon-number resolved detection (green-series). Both numbers were extracted from the background-subtracted cross-correlation function, by computing the integral of the correlation peak. The actual number of generated biphotons, as defined by the corresponding parameter of the model, is shown in the grey-series. The level of illumination was defined in terms of the total number of detected events per pixel per frame, as detected at the centre of the beam, within a circular ROI of radius=$\sigma_m \approx 142$ pixels. 2,500 modelled frames were produced for each level of illumination. Reproduced from [162].

many events per pixel per frame, which correspond to high-levels of illumination.

In spite of these challenges, it can be seen that the model is able to accurately reproduce the photon-number detection of biphoton -events, as shown by the grey- and green-series in Fig. 4.10, by keeping track of coincident detections and thus producing photon-number resolved frames.

4.2.4 Optimised detection of quantum correlations

In this section I show how the ability to accurately measure the number of detected biphotons can be used to optimise the performance of a quantum-enabled scheme. For instance, I show here how even the choice of the event-discriminating threshold for an EMCCD camera can be guided by this quantity. Similarly, other experimental parameters can also be optimised using the number of detected biphoton -events as a metric. The validity of this metric is justified since the number of detected biphoton -events is linked to the total effective QE of the detection scheme.

The total effective QE can be useful to characterise the overall efficiency of a quantum imaging or sensing scheme. Unlike QE, η_{total} includes both the optical losses of the detection channel (which can be found by multiplying the individual QE of the optical components) and also the overall losses associated with the detector operated in a certain acquisition mode, as defined below [169]:

$$\eta_{\text{total}} = \eta_{\text{optical}} \times \eta_{\text{EMCCD}} \tag{4.18}$$

The QE of the detector η_{EMCCD}, in turn comprises the QE of the optical window placed before the sensor, the wavelength and temperature dependent response of the camera-chip (which is found to decrease in the case of deep-cooling of the sensor), and importantly the extra losses introduced by operating the camera in the photon-counting regime (i.e. by applying a single event-discriminating threshold in analogue counts, above which the signal of a pixel is considered to represent the detection of a photon) [241].

Intuitively, the total effective QE η_{total} can be defined as the ratio between the mean number of spatially correlated events $\langle N_c \rangle$, and the total number of events in a frame, $\eta_{\text{total}} = \langle N_c \rangle \,/\, \langle \text{N} \rangle$, where the total number of events is the sum of both spatially correlated and uncorrelated events. In the case of a real detector affected by noise

and losses, the spatially uncorrelated events include two contributions: one due to partially detected photon-pairs and spurious single-photons N_u, and one from the detector's dark-events N_D.

Thus, the mean number of events $\langle N \rangle$ can be expressed as follows:

$$\langle N \rangle = \langle N_c \rangle + \langle N_u \rangle + \langle N_D \rangle \tag{4.19}$$

$$= \frac{2 \langle N_{pe} \rangle}{\eta_{\text{total}}} + \langle N_D \rangle , \tag{4.20}$$

where the sum of correlated and uncorrelated bright-events has been substituted according to $\langle N_c \rangle + \langle N_u \rangle = 2 \langle N_{pe} \rangle / \eta_{\text{total}}$ and for $0 < \eta_{\text{total}} \leqslant 1$ [3]. Note that $\langle N_{pe} \rangle$ is the mean number of biphoton-events, which depends on the number of biphotons generated by the SPDC source $\langle N_p \rangle$. Thus $2 \langle N_{pe} \rangle$ is the mean number of detected bright-events. Equation 4.20 states that if the number of detected events $\langle N \rangle$ is to be kept the same and extra optical loss is inserted in the detection channel (for example by introducing an ND filter before the detector), then the intensity level of the SPDC light-source needs to be increased. The addition of optical loss corresponds to decreasing η_{total}, whereas making the SPDC light-source brighter corresponds to increasing the number of generated biphotons $\langle N_p \rangle$ and thus the number of detected photon-pair events $\langle N_{pe} \rangle$.

A diagram showing photon-pair generation and detection, as well as a summary of the definitions used in this chapter is provided in Fig. 4.11. Given a non-perfect total effective QE introduced by the losses of the optical system and the detector, starting from a number of generated photon-pairs N_p, a lower number of detected photon-pair events N_{pe} is found in a photon-counted frame [4]. The sum of the detected biphoton-events and partial biphoton-events makes up all of the detected bright-events N_B.

[3] This condition implies a non-zero probability of bright events.
[4] Note that in this context photon-pairs and biphotons are used interchangeably.

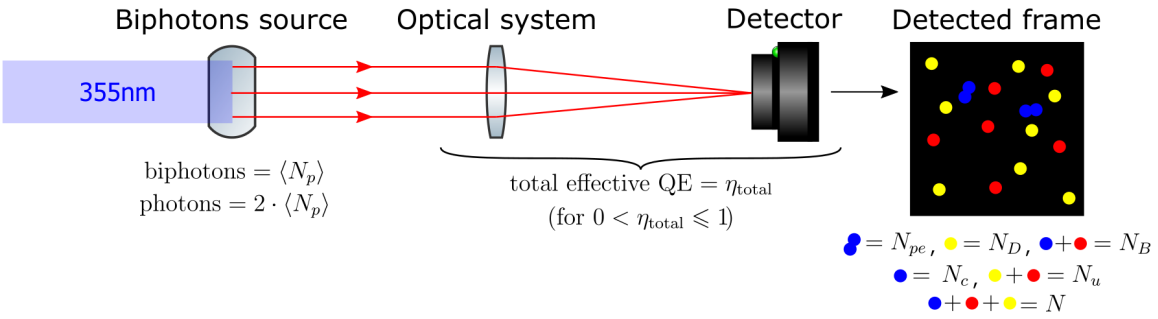

FIGURE 4.11: **Summary of definitions for pair-production and detection.** Pair-production occurs at the biphotons source, where N_p photon-pairs are generated, equal to $2N_p$ photons. The combination of an optical system and of a detector introduces losses which determine the η_{total} of the detection scheme. Detected photon-pair events N_{pe} are shown in blue, the detector's dark-events N_D are shown in yellow, and partially detected photon-pairs are shown in red.

The detected biphoton-events constitute the detected spatially-correlated events N_c, whereas the sum of the partially-detected biphoton-events and of the detector's dark-events N_D makes up the detected uncorrelated-events N_u. Finally, the total number of detected events N is made up by the sum of all events.

By re-arranging Eq. 4.20 one can find the following definition for η_{total}, in terms of experimentally measurable parameters:

$$\eta_{\text{total}} = \frac{2\,\langle N_{pe} \rangle}{\langle N \rangle - \langle N_D \rangle}. \tag{4.21}$$

It is possible to use the definition of η_{total} to maximise the detection of quantum correlations, and so optimise the performance of a quantum-enabled scheme. In Fig. 4.12 I use this method to optimise the choice of the photon-counting threshold for the EMCCD camera, based on acquired bright-frames of the downconverted beam.

It can be seen that, in the case of the used Andor ULTRA 897 EMCCD camera, the total effective QE reaches a well-defined 31% maximum value. This corresponds to a threshold T=208 analogue counts, for which the terms in Eq. 4.21 were measured as follows: $\langle N_{pe} \rangle = 1612$, $\langle N \rangle = 12240$, and $\langle N_D \rangle = 1985$.

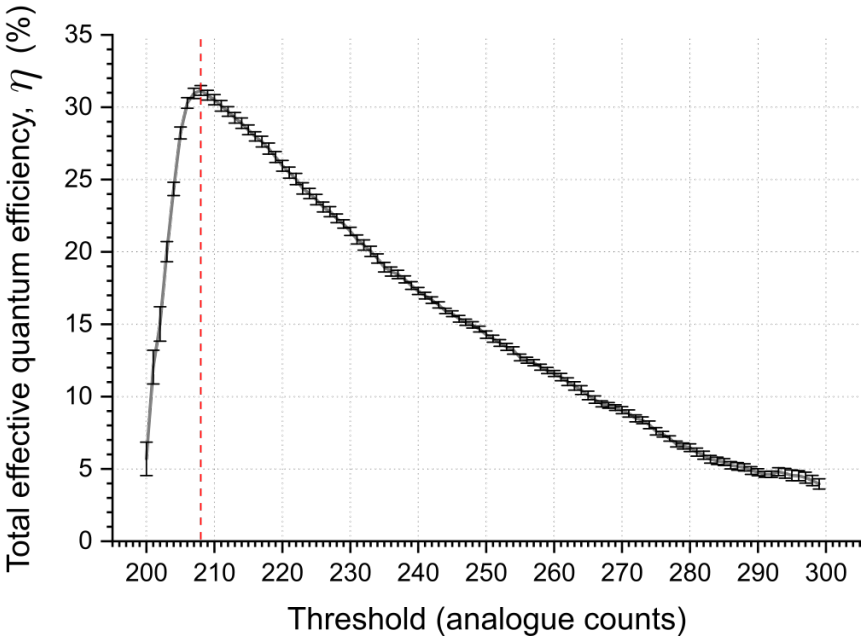

FIGURE 4.12: **Optimal detection of quantum correlations based on the measured number of detected biphoton -events: optimisation of the photon-counting threshold.** The detection of quantum correlations can be optimised by computing the η_{total} of the detection scheme, from experimentally measured quantities such as the number of detected biphoton -events, the detected dark-events, and the total number of detected events, as defined in Eq. 4.21. Accordingly, the optimal photon-counting threshold for the Andor ULTRA 897 EMCCD camera was found to be $T = 208$ (red-dotted line), corresponding to a well-defined maximum efficiency $\eta_{\text{total}} = 31\%$. Reproduced from [162].

4.3 Conclusion

In this chapter I have discussed the detection of quantum correlated biphotons produced by a nonlinear crystal using a photon-counting EMCCD camera.

The properties of the autocorrelation function discussed in chapter 2, section 2.1.4 were used to generate photon-counted frames like those acquired by an EMCCD camera illuminated by SPDC light. Extensions to the model to accurately reproduce position- momentum-correlations, type-II downconversion, non-collinear downconversion, photon-number resolved detection and photon-tagged detection, were also discussed. The validity of the model was then confirmed by both qualitative and quantitative comparison of the synthetic frames with those acquired by an EMCCD

placed in the far-field of a type-I nonlinear crystal, arranged for collinear and wavelength degenerate downconversion. Additionally, an experiment involving the measurement of the number of detected biphotons, for different levels of optical loss introduced between the crystal and the EMCCD camera, and under constant illumination, was investigated. Finally the optimal detection of quantum correlation aided by the measured total effective QE was shown, providing the example of the optimal choice of the photon-counting threshold for the EMCCD camera, based on acquired bright-frames of type-I downconverted light.

The simplicity of this model makes it a useful tool in the design and testing of quantum imaging and sensing schemes, since the complexity of the quantum system is reduced to a deterministic collection of detected pixel-coordinates, which can be tuned to a specific experiment by inputting easily measurable parameters of the light-source and detector.

Both experiments discussed in the later chapters take advantage of the model here presented, to explore the solution space of complex problems, for which the choice of certain experimental parameters (reproduced in the model) have a considerable effect on the performance of the corresponding quantum-enabled sensing or imaging scheme.

Chapter 5

Sub-shot-noise shadow-sensing with quantum correlations

In this chapter I discuss the experimental investigation that allowed to demonstrate the sub-shot-noise performance of the quantum-enhanced shadow-sensing scheme.

The quantum enhancement of this scheme relies on the quantum correlated spatial fluctuations of downconverted photons, in this case produced by a type-I nonlinear crystal and detected in the far-field of the crystal, to achieve sub-shot-noise precision in the estimation of the position of a shadow cast by a fully opaque object, operating at the single-photon level.

More specifically, the scheme employs an EMCCD camera as a split-detector, by integrating the detected signals over the two halves of the camera chip. The spatially-resolved detection of the EMCCD camera is also used to characterise the downconverted source, enabling the optimal detection of quantum correlations. A quantitative estimation of the quantum advantage is performed by comparing the noise reduction of the scheme measured with spatially anticorrelated light and spatially uncorrelated

light. The latter is obtained simply by introducing an ND filter between the nonlinear crystal and the detector, thus ensuring a fair comparison.

The noise-suppression of the scheme is found to be limited by optical losses, which affect the ability to jointly-detect the signal and idler photons of a biphoton packet, giving rise to uncorrelated noise.

5.1 Theoretical description

In this section I discuss the parameters used to quantify the achieved quantum-noise-reduction associated with the optical measurement of the position of a shadow, by means of a position estimator Δx and the degree of correlation (DOC).

5.1.1 The position estimator

The split-detection scheme on which the quantum-enhanced shadow sensor is based is schematically represented in Fig. 5.1, in which the width of the shadow w_{shadow}, size of the ROI w_{ROI}, and relative displacement of the shadow from the centre of the ROI Δx, are defined. It can also be seen that the ROI within which the shadow-sensor scheme is designed to operate is located at the centre of the field of view of the camera, where the downconverted beam (labelled as 'light beam' in the figure) is detected.

The Δx parameter is the position estimator, which in the case of uniform detected illumination within the ROI, can be defined as follows:

$$\Delta x = \frac{A - B}{\langle A + B \rangle} \cdot l = \frac{A - B}{\langle N \rangle} \cdot l, \tag{5.1}$$

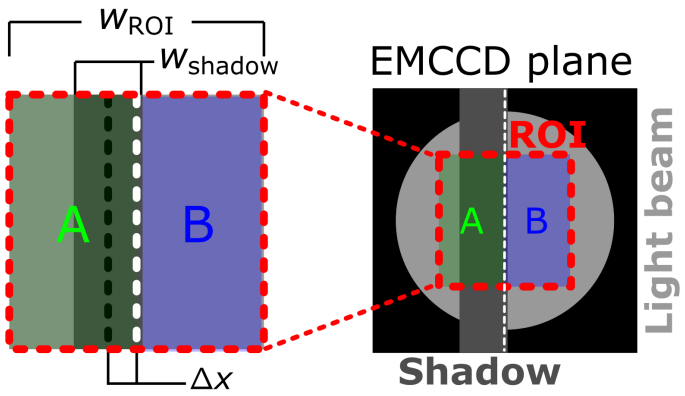

FIGURE 5.1: **Representation of the position estimator Δx.** The position estimator Δx corresponds to the relative displacement of the shadow and is computed from the sum of the left and right halves of the ROI , A and B, highlighted in the diagram in green and blue respectively. This estimator is linked to the chosen width of the ROI (w_{ROI}) and the width of the shadow (w_{shadow}). Adapted from [9].

where A and B are the summed number of photons over the two- halves of the split-detector highlighted in green and blue respectively in Fig. 5.1), defined by partitioning in half the square ROI; l is the maximum unobstructed extent of the ROI, defined as $l = (w_{\mathrm{ROI}} - w_{\mathrm{shadow}})/2$; w_{ROI} is the width of the ROI; w_{shadow} is the detected width of the shadow; N is the total number of detected photons, such that $A + B = N$ and $\langle N \rangle = \langle A \rangle + \langle B \rangle$, with $\langle\ \rangle$ indicating a temporally averaged value over a number of frames. Finally, the dimensions Δx, l, w_{ROI}, and w_{shadow} are to be intended as measured in the plane of the EMCCD camera.

It should be noted that the position estimator defined in Eq. 5.1 is only valid for $-\frac{w_{\mathrm{shadow}}}{2} \leq \Delta x \leq \frac{w_{\mathrm{shadow}}}{2}$, under which condition the shadow does not fall entirely on either half of the split-detector. This is evident in the full-characterisation of Δx shown later in Fig. 5.10, in which the *sin*-like response of Δx is revealed.

5.1.2 Quantification of quantum noise reduction using the degree of correlation

As stated in Eq. 5.1 the estimation of the position of the shadow depends upon the value of $(A - B)$. It is possible to express the noise statistics associated with the position of the shadow using the same quantity.

In the case of a coherent state, used as the benchmark representing the SNL [43], the classically best achievable uncertainty expressed in terms of the photon-number difference $(A - B)$ is given by[1]:

$$\left\langle \Delta \left(A - B\right)^2 \right\rangle = \langle A \rangle + \langle B \rangle \,, \tag{5.2}$$

where the left-hand side represents the variance of the residual difference of the detected events over the two halves of the split-detector, and the right-hand side represents the mean total number of detected events, i.e. $\langle N \rangle$.

The degree of correlation σ_{DOC} or quantum noise reduction factor is then used to quantify the noise-reduction of the shadow-sensing scheme below the SNL, in terms of the number of detected events as follows:

$$\sigma_{\mathrm{DOC}} \equiv \frac{\mathrm{Var}(A - B)}{\langle A + B \rangle} < 1, \tag{5.3}$$

where the Var( ) notation is used to indicate the variance of detected events over multiple frames. The definition of σ_{DOC} as the photon-number difference normalised to the mean number of detected photons is only valid for a low-gain downconversion regime, in which stimulated emission is effectively absent [54]. This regime is compatible to the one used in the experimental demonstration reported in this chapter.

[1] Note that in the context of direct detection of signal and idler twin-beams, the condition for quantum noise reduction, i.e. for photon-number fluctuations below the SNL, is defined by O. Aytür et al. as: $\left\langle \Delta \left(\hat{n}_1 - \hat{n}_2\right)^2 \right\rangle < \langle \hat{n}_1 \rangle + \langle \hat{n}_2 \rangle$ [43], where $\hat{n}$ is the photon-number operator.

An expression for σ_{DOC} in the case of high-gain can be found in the work by O. Aytür et al. [43].

The DOC can also be expressed in terms of the total effective QE, as follows [47, 49, 51, 247, 248]:

$$\eta_{\mathrm{total}} \equiv 1 - (\sigma_{\mathrm{DOC}})_{\mathrm{max.}} \tag{5.4}$$

A definition of the total effective QE, η_{total}, can be found in chapter 4, section 4.2.4.

The link between noise-performance and the total effective QE is not surprising, since optical losses limit the ability to detect quantum correlations, thus increasing the noise contribution due to spatially uncorrelated events, due to a smaller number of jointly-detected photon-pairs.

5.2 Experimental realisation

A representation of the experimental realisation of this scheme is shown in Fig. 5.2 (a), together with a ray-diagram, shown in (b). Details about the experimental set-up used to produce spatially correlated biphotons by SPDC can be found in chapter 3, section 3.2.2.

Two ND-filters ($\mathrm{ND}_{\mathrm{pump}}$=$\mathrm{ND}_{\mathrm{SPDC}}$=2.0 optical density) were used to switch the spatial properties of the downconverted field from spatially correlated to spatially uncorrelated.

A 200 mm lens was used to access the far-field of the nonlinear crystal, where a shadow-casting object was scanned transversely to optical-axis. This consisted of a stretched tinned-wire ($\approx$ 0.6 mm diameter) mounted on a high-precision motorised linear-stage (Newport, ESP300 controller, UE16CC motor), shown in Fig. 5.3. In

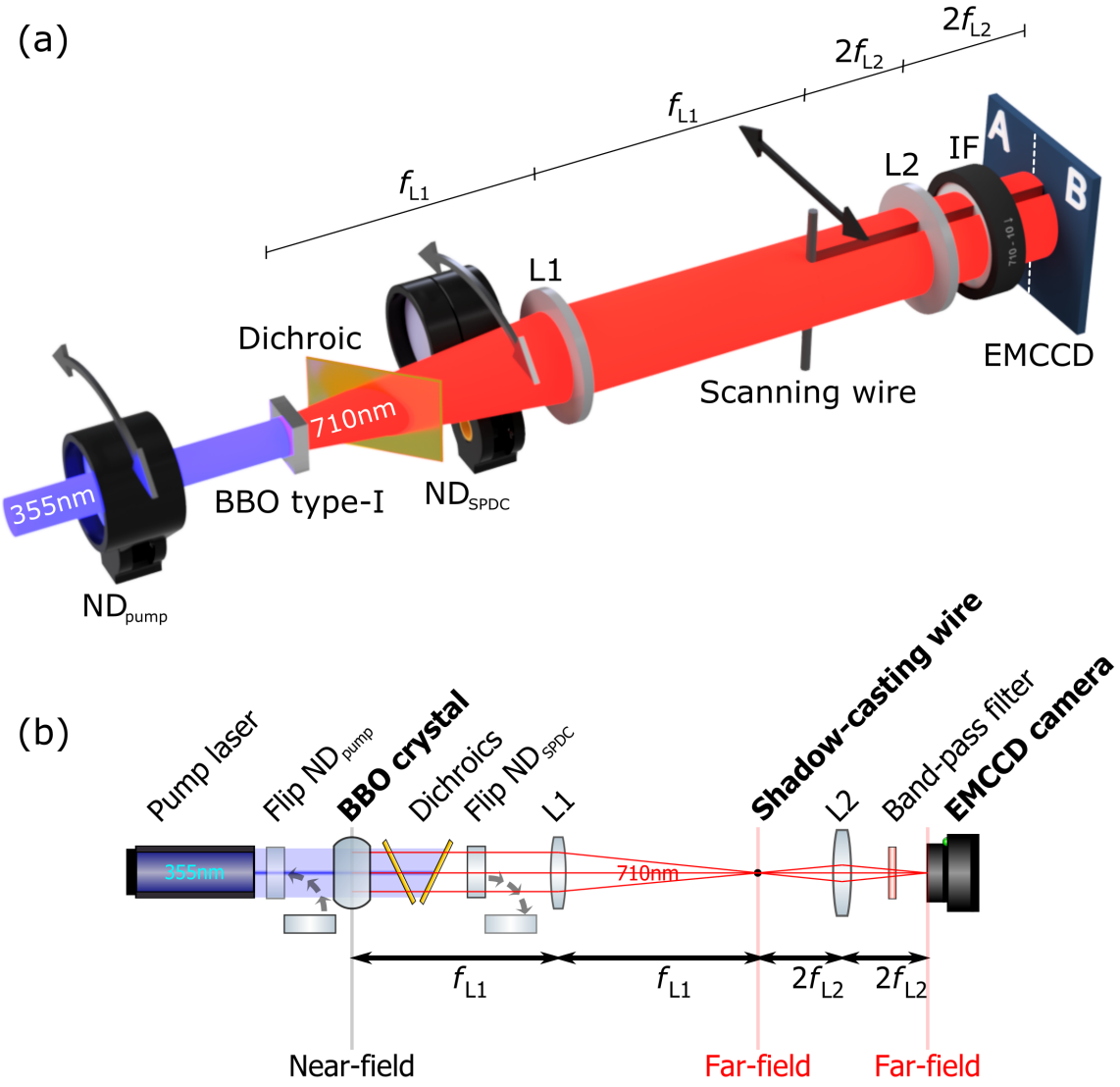

FIGURE 5.2: **Experimental realisation of the sub-shot-noise shadow sensing scheme and ray-diagram representation.** The optics used to access the far-field of the nonlinear crystal (BBO type-I) consisted of a 200 mm Fourier lens (L1) and a 50 mm relay lens (L2). L1 was placed one focal length away (i.e. 200 mm) from the nonlinear crystal, leaving another focal length distance before the shadow-casting object (stretched wire). This shadow-casting wire was re-imaged onto the plane of the EMCCD camera by L2, placed two focal lengths away from the wire and from the plane of the camera (i.e. in a 4-f) configuration. Two neutral-density filters (ND_{pump} and ND_{SPDC}) could be switched alternatively either before or after the nonlinear crystal (as represented by the two curved arrows), allowing one to change the illumination from spatially anticorrelated to uncorrelated photons. Adapted from [7].

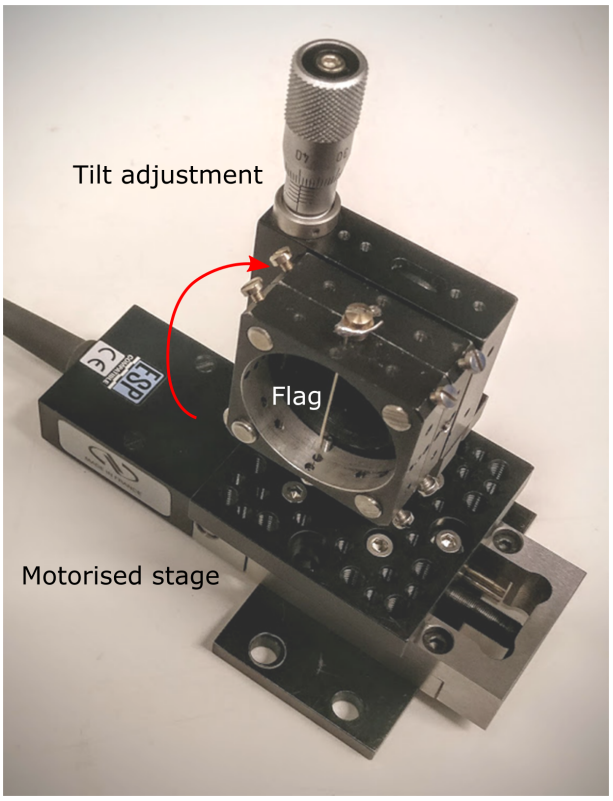

FIGURE 5.3: **Motorised linear stage holding the shadow-casting stretched-wire.** The position of the shadow was programmatically controlled using a motorised linear stage, interfaced to a PC. The direction of the shadow with respect to a row of pixels of the EMCCD camera was adjusted using an angular micrometer (labelled 'Tilt adjustment'), thus rotating the stretched-wire (labelled 'Flag').

order to ensure a symmetric detection of events over the two halves of the split-detector, the direction of the shadow-casting wire was adjusted by means of a manual rotational stage, such that its edges were aligned with the pixel-rows of the EMCCD camera.

Both the shadow-casting wire and the anticorrelated photon-pairs located in the far-field of the crystal were re-imaged onto the plane of the EMCCD camera (Andor, ULTRA 888), using a 50 mm lens placed 100 mm away from both the scanning-wire and the EMCCD camera in a $4f$ imaging configuration. The EMCCD camera was operated in the photon-counting regime, by applying a single photon-discriminating threshold T chosen from the analysis of the noise-statistics of dark-frames, according

to [226, 230, 239, 249]:

$$T \geq 2\ \mathrm{SD}_{readout} + \mu_{readout} = 520 \text{ analogue counts}, \tag{5.5}$$

where $\mathrm{SD}_{readout}$ and $\mu_{readout}$ are the standard deviation and the mean of the electronic readout noise of the EMCCD camera, measured in ADC counts. According to this experimental set-up, the shadow-sensing scheme was designed to operate at a very low-light level, with at most one photon detected per pixel per frame.

5.3 Results

In this section I first show preliminary characterisation results that were carried out to find the noise-performance of the detector and of the employed SPDC light-source.

Then I discuss the investigation used to find the optimal level of illumination and phase-matching condition, which resulted in the best sub-shot-noise performance.

Lastly the sub-shot-noise performance of the shadow-sensor is experimentally demonstrated by means of the measured DOC for a full range of positions of the scanning wire, allowing one to also compute the position estimator Δx and the resulting improvement in position estimation.

5.3.1 Noise performance of the detector

The noise performance of the detector can be a determining factor of whether or not the split-detector can reach (and hopefully beat) the SNL. For this reason, the first experimental measurement involved the characterisation of the noise of the detector, measured in terms of σ_{DOC}, as computed over the two halves of a ROI defined on the plane of the EMCCD camera. The chosen square ROI was centred on the frame and

measured 176×176 pixels^2, resulting in the two halves A and B of the split-detector measuring 88×176 pixels^2.

Accordingly, the 500 chunks of 50-frame each were acquired and used to compute the normalised variance of both the sum and the difference of the integrated signals A and B, indicated by σ_+ and σ_{DOC} respectively. It should be noted that in case of randomly distributed noise the following relation should hold true:

$$\frac{\mathrm{Var}(A+B)}{\langle N \rangle} = \frac{\mathrm{Var}(A-B)}{\langle N \rangle}. \tag{5.6}$$

Both quantities (σ_+ and σ_{DOC}) are shown in Fig. 5.4 in the case of horizontal (a) and vertical (b) orientations of the split-detector with respect to the readout direction of the EMCCD camera. The running averages and the overall average values are also shown. As can be seen from the summed images reported on the left of Fig. 5.4(a) and (b), the distribution of dark-events is not uniform, but it appears to pile-up toward the readout register. This is in accordance to the presence of charge-smearing which affects EMCCD cameras, especially for fast vertical and horizontal readout clocks [4, 230]. Moreover, streaks of hot-pixels are also visible, caused by uneven response of the camera chip. Regardless of the presence of these artefacts, the dark-frames were acquired using the optimal acquisition settings in terms of QE and dark-noise.

As shown by the variance of the normalised sum of signals (orange-series) the EMCCD camera does not operate at the SNL, and is therefore affected by excess-noise. This quantity (measured to be 1.30) is unaffected by the chosen orientation of the split-detector and is 30% worse than the SNL. Interestingly, the normalised variance of the difference of signals (green-series, corresponding to the DOC), appears to approach the SNL in case of a vertical orientation of the split-detector. This phenomenon can be understood by considering the following. From the point of view of the statistics

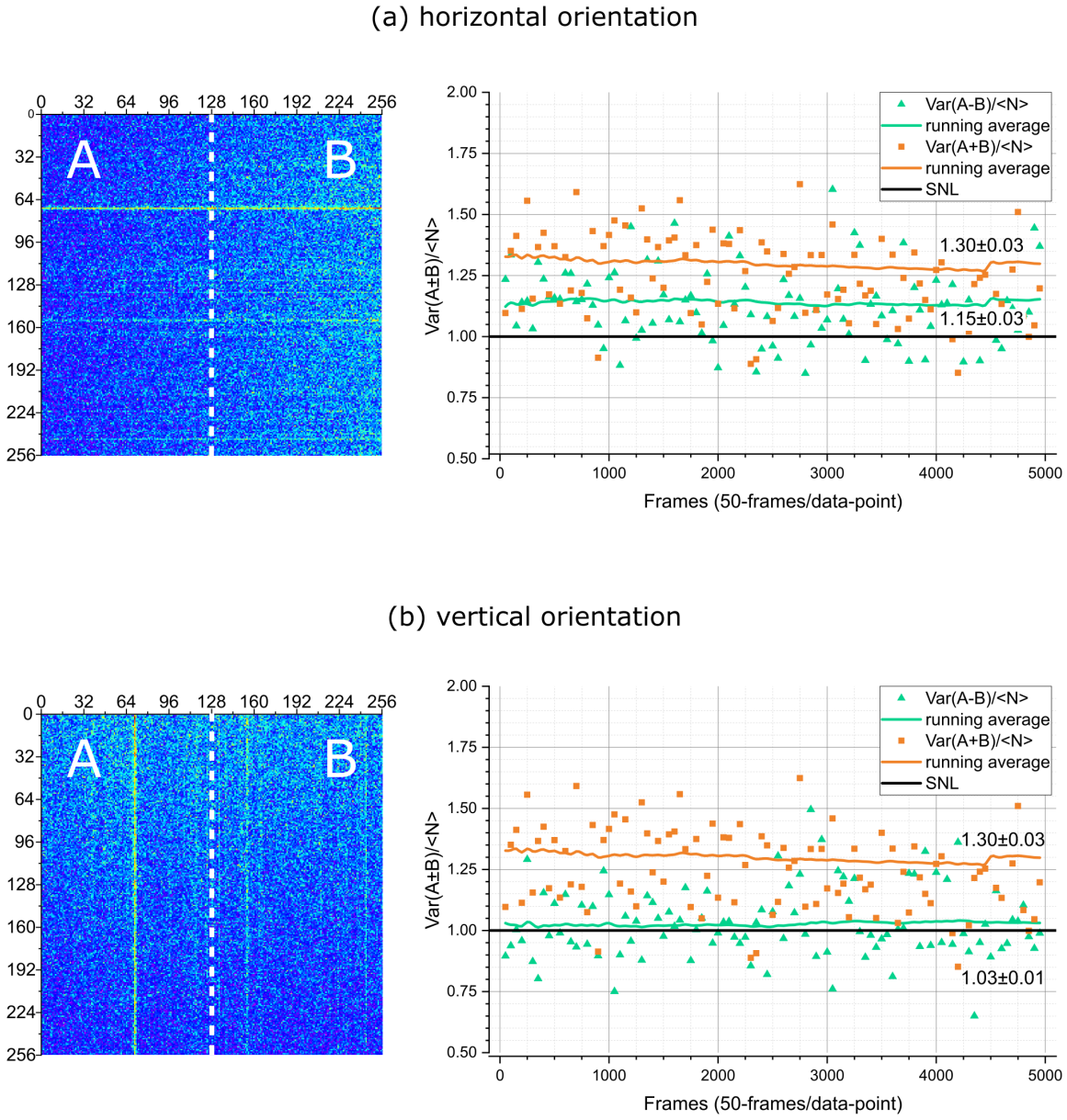

FIGURE 5.4: **Quantification of noise of the detector.** The normalised variance of the sum and difference of the integrated dark events over the two halves of the split-detector (A and B, arranged as shown in the summed images on the left) are plotted for 5,000 frames, together with their running averages for a horizontal (a) and vertical (b) orientation of the split-detection, with respect to the readout direction of the EMCCD. In the case of a horizontal orientation (a), the degree of correlation (green-series) exhibits the presence of excess noise. If using this orientation, it would be more challenging to achieve sub-shot-noise shadow sensing, due to the noise contribution of the detector. In the case of a vertical orientation (b), the degree of correlation (green-series) is close to the shot-noise-limit. The evident directional nature of the dark-events distribution along the readout direction, which becomes evident when many frames are added together, is due to charge smearing.

of detected dark-events, charge smearing is responsible for a correlation, since it is a directional phenomenon, and this correlation can affect the measured DOC (since DOC is a measure of the degree of correlation). This effect is maximised if the orientation of the split-detector is vertical, for which the correlation due to charge smearing affects both signals (A and B) the most. Accordingly, whereas in the case of a horizontal orientation the measured σ_{DOC} is 15% worse than the SNL, in the case of a vertical orientation, the measured σ_{DOC} is only 3% worse than the SNL.

The correlation due to charge-smearing was capitalised on, and the orientation of the split-detector with respect to the readout direction of the EMCCD was set to be vertical for all subsequent measurements, allowing one to operate the detector very close to the SNL.

5.3.2 Noise performance of the light-source

The second important characterisation for the noise-performance of the split-detector involved the photon-number fluctuations of the light-source. The noise-performance of the light-source was characterised choosing the spatially uncorrelated configuration of the system ($\mathrm{ND}_{\mathrm{pump}}$ flipped-out and $\mathrm{ND}_{\mathrm{SPDC}}$ flipped-in, as discussed in section 5.2) and by measuring the normalised variance of both the sum and difference of detected events. By choosing the spatially uncorrelated light-source it was possible to compare measured σ_+ with that computed from the dark-frames of the detector. The results are shown in Fig. 5.5. The values for σ_+ and σ_{DOC}, which represent the noise performance of the detector and light-source of the shadow-sensor, are summarised in table 5.1:

It is possible to use the combined noise statistics of the light-source and detector (generated by analysing bright-frames of uncorrelated light) to compute by how much

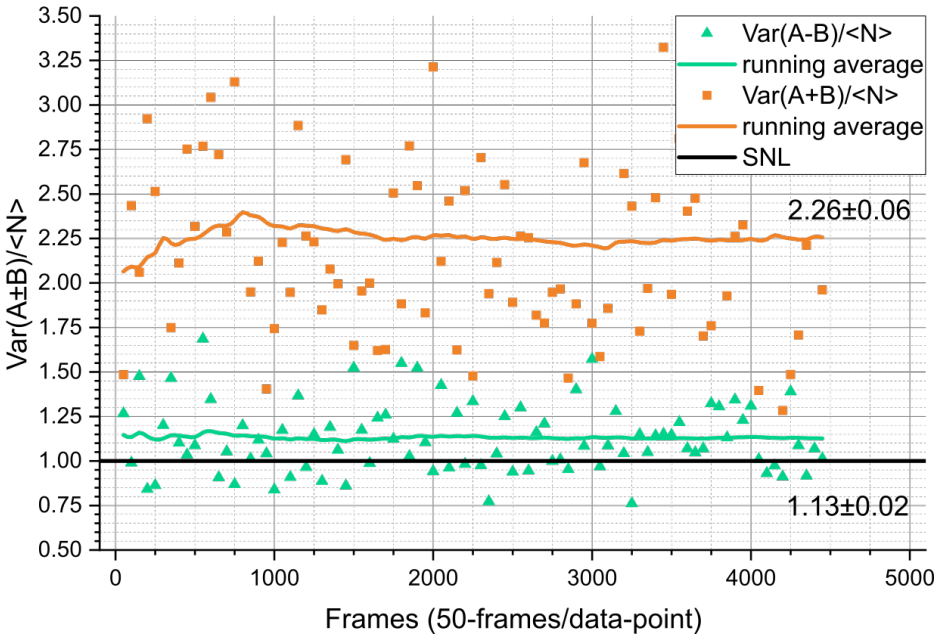

FIGURE 5.5: **Quantification of noise of the spatially uncorrelated light-source.** The normalised variance of the sum and difference of signals A and B are plotted for 5,000 frames, acquired by illuminating the EMCCD camera with spatially uncorrelated light, in the case of a vertical orientation of the split-detector with respect to the readout direction. Both data series indicate the combined noise due to the laser and the detector, which is found to exceed the SNL.

TABLE 5.1: **Summary of the noise-performance of the shadow-sensor.** The normalised variance of the sum and difference of signals A and B measured from 5,000 dark-frames and spatially uncorrelated bright-frames are reported, together with the corresponding standard errors.

	$\sigma_+ = \frac{\mathrm{Var}(A+B)}{\langle N \rangle}$	$\sigma_{\mathrm{DOC}} = \frac{\mathrm{Var}(A-B)}{\langle N \rangle}$
Detector (dark-frames)	1.30 ± 0.03	1.03 ± 0.01
Laser (uncorrelated light)	1.96 ± 0.09	1.10 ± 0.03
Total	2.26 ± 0.06	1.13 ± 0.02

the noise-performance of the detector, source, and their combination is worse than the SNL. These quantities are summarised in table 5.2.

Thus, the total excess-noise of the shadow-sensor (comprising the excess noise of the laser and of the detector) is 13% worse than the SNL. This means that in order for the quantum-enhanced shadow-sensor to be able to reach the SNL, the noise-reduction due to the detected quantum correlations needs to be at least 13%. In section 5.3 I will show that not only the quantum shadow sensor is able to compensate for the

TABLE 5.2: **Summary of the excess-noise contributions of the shadow-sensor.** The percentage by which the measured excess-noise is worse than the SNL are reported, together with their standard errors.

	Excess noise (σ_+)	Excess noise (σ_{DOC})
Detector (dark-frames)	30%±3%	3%±1%
Laser (uncorrelated light)	96%±9%	10%±3%
Total	126%±6%	13%±2%

total excess noise of the light-source and of the detector, but that its noise-reduction, enabled by a strong detection of quantum correlations, allows to achieve sub-shot-noise performance.

5.3.3 Fine-tuning of the detection of quantum correlations

The optimal detection efficiency of EMCCD cameras employed in the photon-counting regime is dependent on the number of detected events per pixel per frame [239, 249]. This quantity is also responsible for the achievable level of noise suppression, since it directly affects the proportion of detected spatially anticorrelated biphotons and spatially uncorrelated photons.

In order to find the optimal light-level, the DOC was measured in the absence of the shadow-casting object (i.e. with the unobstructed downconverted beam) and the light-level of the downconversion was progressively increased. The upper limit for the number of bright events per pixel per frame was chosen so as to ensure the validity of the employed photon-counting strategy consisting of a single discriminating threshold, thus without exceeding 0.5 events per pixel per frame [231]. The measured DOC for both spatially anticorrelated and uncorrelated light is shown in Fig. 5.6. The computed σ_{DOC} values were corrected in regard to the probability of coincident detection of more than one event per pixel per exposure [49]:

$$\sigma_{\mathrm{DOC}} = \frac{(\sigma_{\mathrm{DOC}})_{\mathrm{biased}}}{1 - \text{fill-fraction}}, \tag{5.7}$$

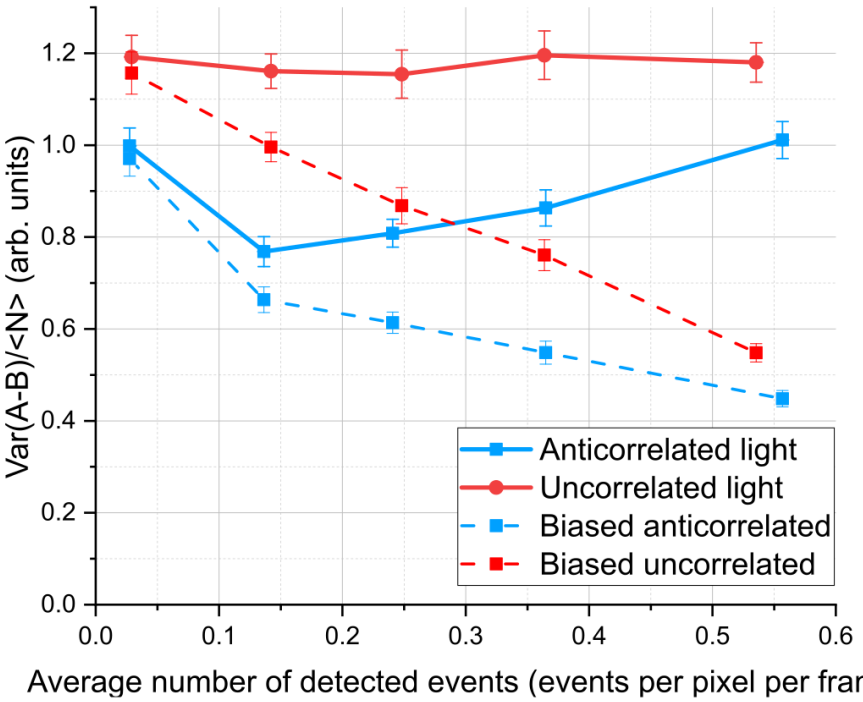

FIGURE 5.6: **The degree of correlation for the unobstructed beam as a function of light-level.** The measured normalised variance of $(A - B)$ is plotted as a function of the number of detected events per pixel per frame, for a range of intensities of the downconversion source, for anticorrelated (blue) and uncorrelated (red) light. The solid data-series represent σ_{DOC} without the correction necessary to compensate the loss in detection due to the binary nature of detection, which becomes more prominent for high levels of illumination (i.e. when coincident detection of more than one photon per pixel per exposure becomes more likely). The corrected curves (red- and blue-dashed) highlight an optimal light-level for the measured σ_{DOC}, occurring at ≈ 0.15 event per pixel per frame.

where $\sigma_{\mathrm{DOC}})_{\mathrm{biased}}$ corresponds to the biased values shown by the dotted-series in Fig. 5.6, and the fill-fraction is the number of detected events per pixel per frame. This correction is necessary to account for the losses associated with the binary detection of photons, which occur when a photon-counting strategy based on a single photon-discriminating threshold is employed. The corrected values are shown by the red- and blue-series in Fig. 5.6, for uncorrelated and anticorrelated light respectively.

Given the results of this characterisation, the light-level of the the quantum-enhanced shadow sensor was set so as to guarantee the optimal 0.15 events per pixel per frame fill- fraction. Additionally, the phase-matching of the nonlinear crystal was tuned

by slightly tilting the crystal away from its collinear position, achieving an almost-collinear phase-matching, thus increasing the transverse momentum component of the photon-pairs. As a result of this fine tuning, the *sinc*-like intensity profile of the downconverted beam (as detected in the far-field) was modified to nearly flat-top intensity profile, ensuring the optimal detection of correlated photons. The measured intensity profile is shown in Fig. 5.7. The so created uniform-intensity portion of the

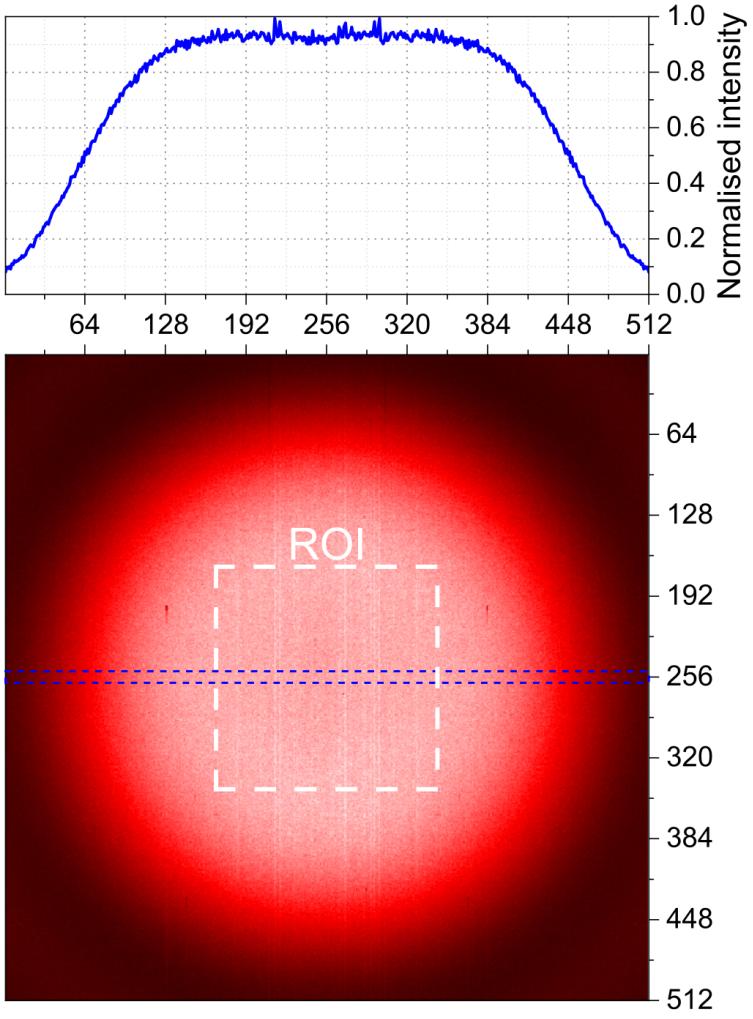

FIGURE 5.7: **Summed image over 5,000 frames and intensity cross-sections.** The summed intensity over 5,000 frames is shown, together with an intensity cross-section (averaged over 10 lines of pixels). The cross-section reveals the nearly-flat intensity-profile of the downconverted beam, achieved by tuning the angle of incidence of the UV pump on the crystal to an almost-collinear phase-matching. The chosen ROI (176×176 pixel^2)ensures that the stretched-wire is scanned over a nearly constant intensity-profile portion of the downconverted beam.

beam was used to define a ROI ($w_{\mathrm{ROI}} = 176 \times 176$ pixels or 2.29 mm × 2.29 mm,

for the 13μm pixel-pitch of the EMCCD camera) within which the split-detection scheme was operated.

Under these optimised experimental conditions the ability to detect a large number of anticorrelated biphotons was confirmed by computing the single-frame cross-correlation, revealing a promising signal-to-noise ratio of 4.34 [241, 249]. The correlation peak of spatially anticorrelated photon-pairs detected in the momentum plane of the crystal are shown in Fig. 5.8.

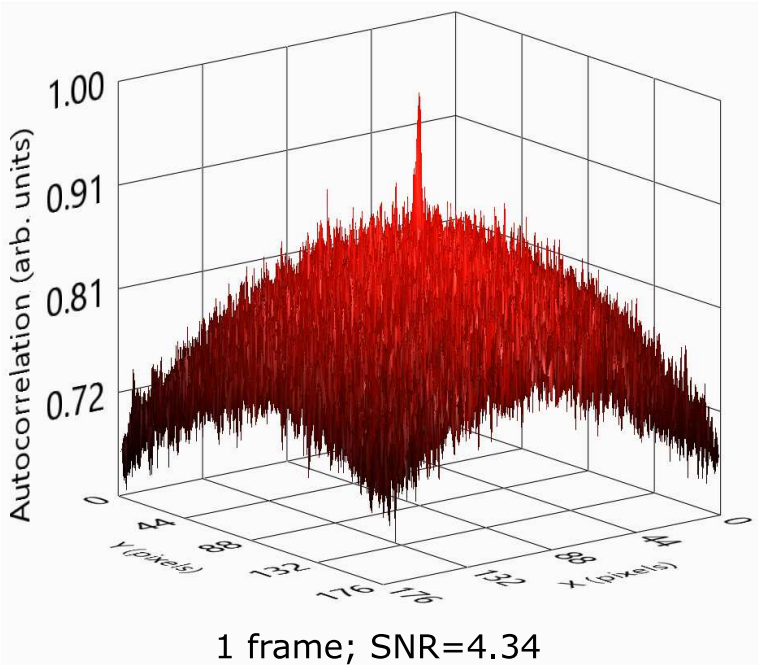

FIGURE 5.8: **Experimental evidence of strong anticorrelation of photon-pairs as detected in the far-field of the downconversion crystal.** The correlation of a single frame detected by our EMCCD camera is shown. The whole optical channel was optimised to minimise losses, resulting in a strong single-frame correlation peak ($SNR = 4.34$) at 0.15 events per pixel per frame. The SNR is computed considering the height of the correlation peak with respect to the noise of the Gaussian pedestal. Reproduced from [9].

Moreover, the σ_{DOC} for the unobstructed beam was also experimentally measured, as shown in Fig. 5.9. As observed from the distributions of σ_{DOC}, the ability of the system to achieve sub-shot-noise performance is demonstrated in the absence of a shadow-casting object for anticorrelated light (blue-series), in spite of the noise

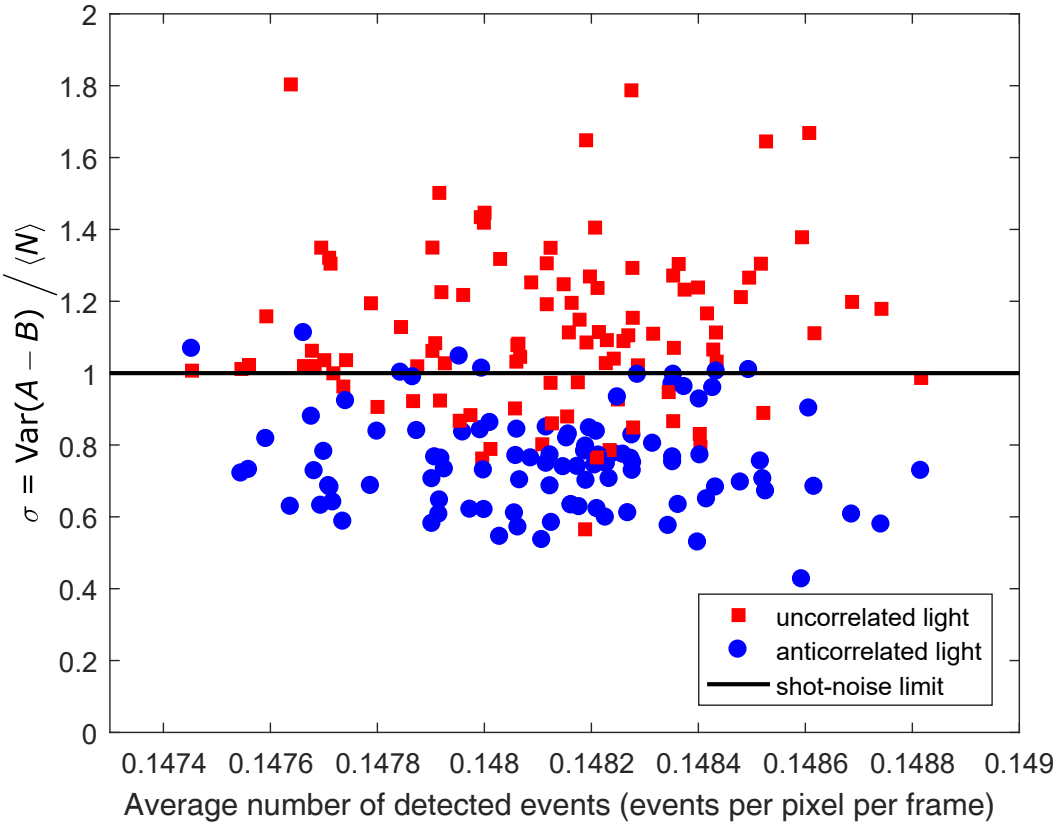

FIGURE 5.9: **Optimisation of the noise-suppression of the split-detection scheme.** The maximum achievable noise-suppression achieved by careful tuning of the experimental parameters results in an improved detection efficiency or total effective QE. This quantity can be experimentally measured by the closely related degree-of-correlation, σ_{DOC}, here computed by running the split-detection scheme in the absence of a shadow-casting object. This condition corresponds to the highest number of jointly-detectable spatially anticorrelated photon-pairs. Each point is computed for 50-frame ('chunks') of data, thus over 50 measurements. The shot-noise benchmark is highlighted by the black solid-line. As can be seen, the noise performance of the split-detection scheme achieved using spatially anticorrelated photons is better than both that of its classical counterpart (red-series) and the shot-noise-limit. The average number of detected events (dark- and bright-events) for each measured chunk of data is shown on the x-axis. Reproduced from [9].

baseline of the system (i.e. the combined noise of the laser and EMCCD camera) being worse than the SNL (red-series).

The mean σ_{DOC} was calculated to be 0.73 and used to compute the total effective QE of the system, according to Eq. 5.4, as follows:

$$\eta_{\mathrm{total}} = 1 - 0.73 = 27\%. \tag{5.8}$$

It should be noted that using the degree-of-correlation to compute the η_{total} can return a conservative value, degraded by the uncorrelated contribution of the noise of the detector and possible spurious signals (such as fluorescent photons generated by the interaction of the UV-pump with optical surfaces or accidental stray light).

5.3.4 Characterisation of the position estimator Δx

Having optimised the detection of anticorrelated photons, the response of the system was characterised by scanning the shadow-casting wire across the ROI and measuring the mean of the normalised fluctuations of the detected signals $(A - B)$, as shown in Fig. 5.10. This quantity is linked to the noise associated with the position estimator, as defined in Eq. 5.1. The central range of positions of the scanning wire, delimited by the two vertical dotted-lines in Fig. 5.10, ensures an unambiguous estimation of the position of the shadow, whereas outside this range the response of the position estimator becomes non-linear, due to part of the shadow falling outside of the split-detector. Each data-point was computed over 2,500 frames and the shaded-error bars were chosen to display a four-standard-deviation uncertainty.

The range of positions highlighted in yellow is used in Fig. 5.11 to plot the frame-to-frame fluctuations of the position estimator. As can be seen, the photon-number fluctuations are greater in the case of uncorrelated light, meaning the the sensitivity in the position estimation of the shadow is improved in the case of anticorrelated light.

5.3.5 Characterisation of the degree-of-correlation σ

The full characterisation of the noise performance of the system is shown in Fig. 5.12 as a function of the position of the shadow-casting wire. It should be noted that

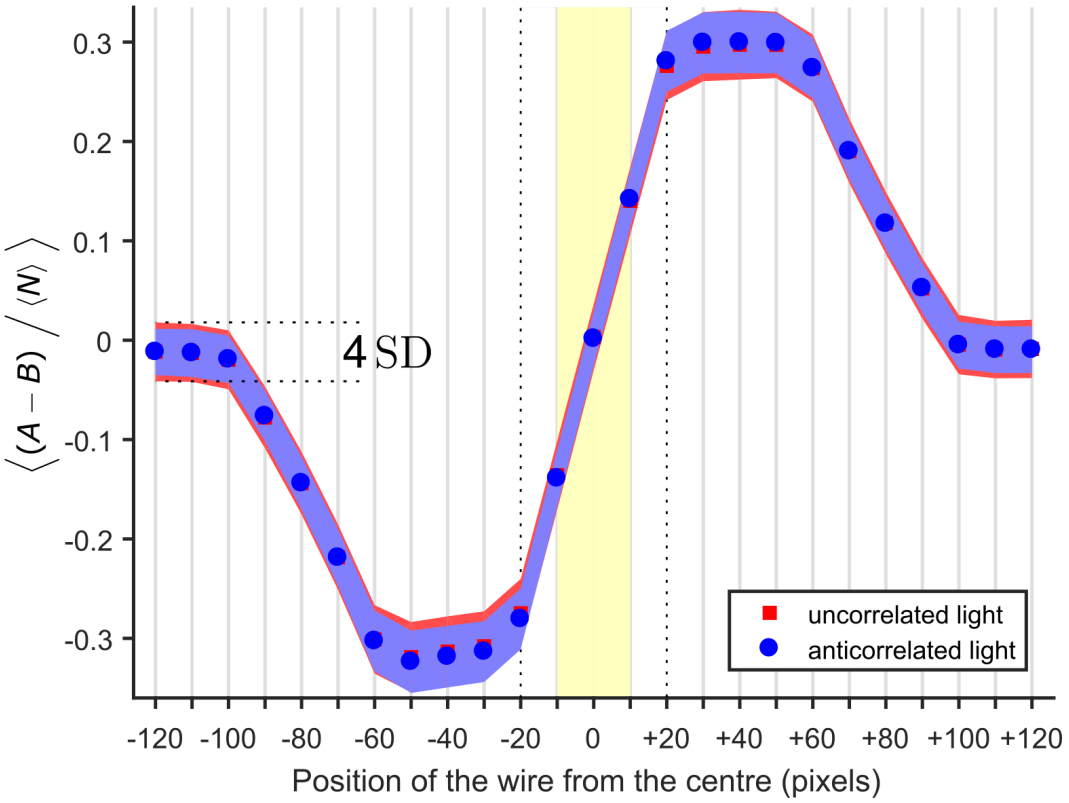

FIGURE 5.10: **Characterisation of the position estimator Δx.** The position of the shadow-casting wire can be estimated using the known physical parameters of the shadow-sensor (the width of the chosen ROI and of the detected shadow) and the summed number of photons as detected over the two halves of the split-detector, as shown in Eq. 5.1. Each data-point represents the mean of the normalised residual difference, computed over 2,500 frames at each position of the scanning-wire. The uncertainty associated with the position estimator is highlighted by the shaded error-bars (here chosen to represent four-times the standard deviation, SD). The vertical dotted-lines show the useful range over which the position estimator returns unambiguous results. The frame-to-frame fluctuations in the position estimator for the interval highlighted in yellow are shown in Fig. 5.11. Reproduced from [9].

the results shown here include the fill- fraction correction in events per pixel per frame explained in Eq. 5.7. In the case of anticorrelated light (blue-series) the noise performance appears to better than the SNL over all positions of the wire. Conversely, in the case of uncorrelated illumination, the noise performance is worse than the SNL. The fact that the system is able to beat the SNL in spite of the excess-noise of the laser and detector is testament of the presence of strong quantum correlations [52].

The noise suppression achieved by the shadow sensor depends on the position of the shadow-casting wire. On closer inspection it is possible to identify five key-positions

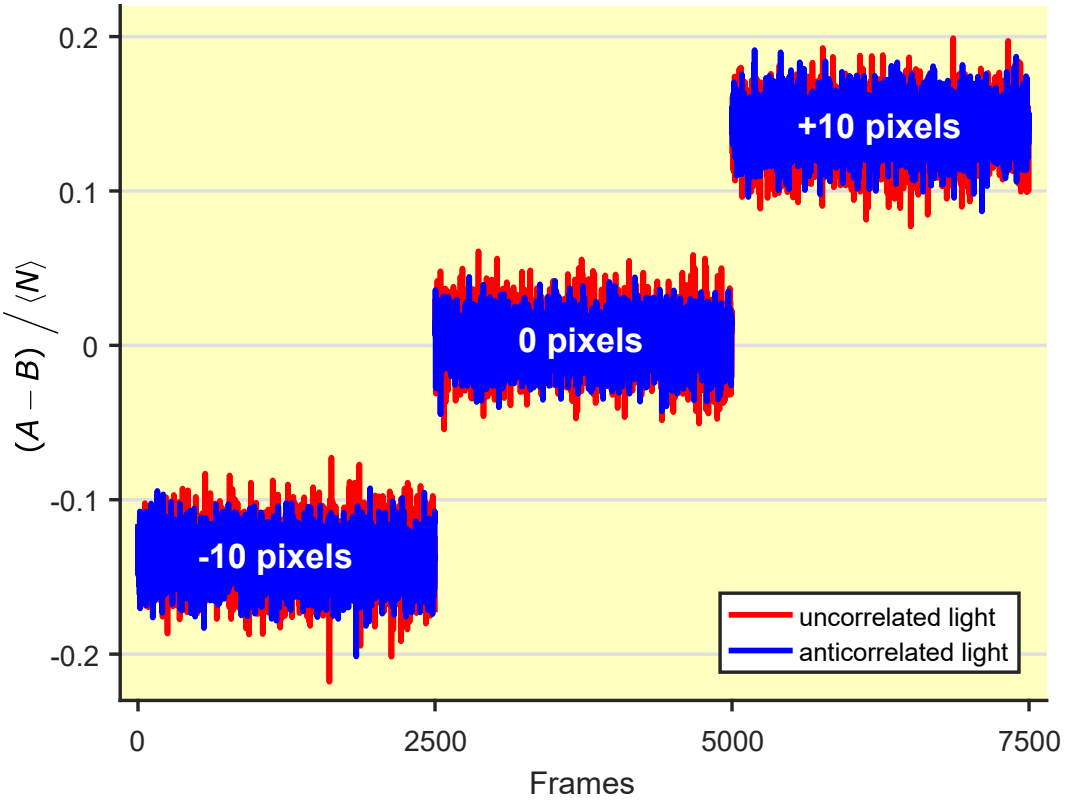

FIGURE 5.11: **Frame-to-frame fluctuations of the position estimator Δx.** The normalised residual difference of the events detected over the two halves of the split-detector (A and B) are shown for individual frames, over the three central positions of the shadow-casting wire (as highlighted by the yellow interval in Fig. 5.10. The frame-to-frame fluctuations for spatially anticorrelated light are reduced (blue-series). Noise-suppression is achieved by subtracting the detected correlated signals, since the fluctuations in the number of detected photons over A and B are correlated. Reproduced from [9].

of the wire, as highlighted by the series of summed frames, labelled (a) to (e), shown at the top of Fig 5.12. The red-dotted box shows the ROI within which the split-detection is operated and the white, vertical dotted-line defines the two halves of the split-detector, over which signals A and B are measured. The noise suppression is maximum for the unobstructed beam (a). As soon as the shadow cast by the wire starts falling within the ROI the noise suppression is affected. The quantum advantage is minimum when the full extent of the shadow falls within either half of the split-detector (b), since a maximum number of photon-pairs are intercepted generating uncorrelated events. The noise suppression is restored when the shadow falls exactly at the centre of the split-detector (c), since in this position an equal

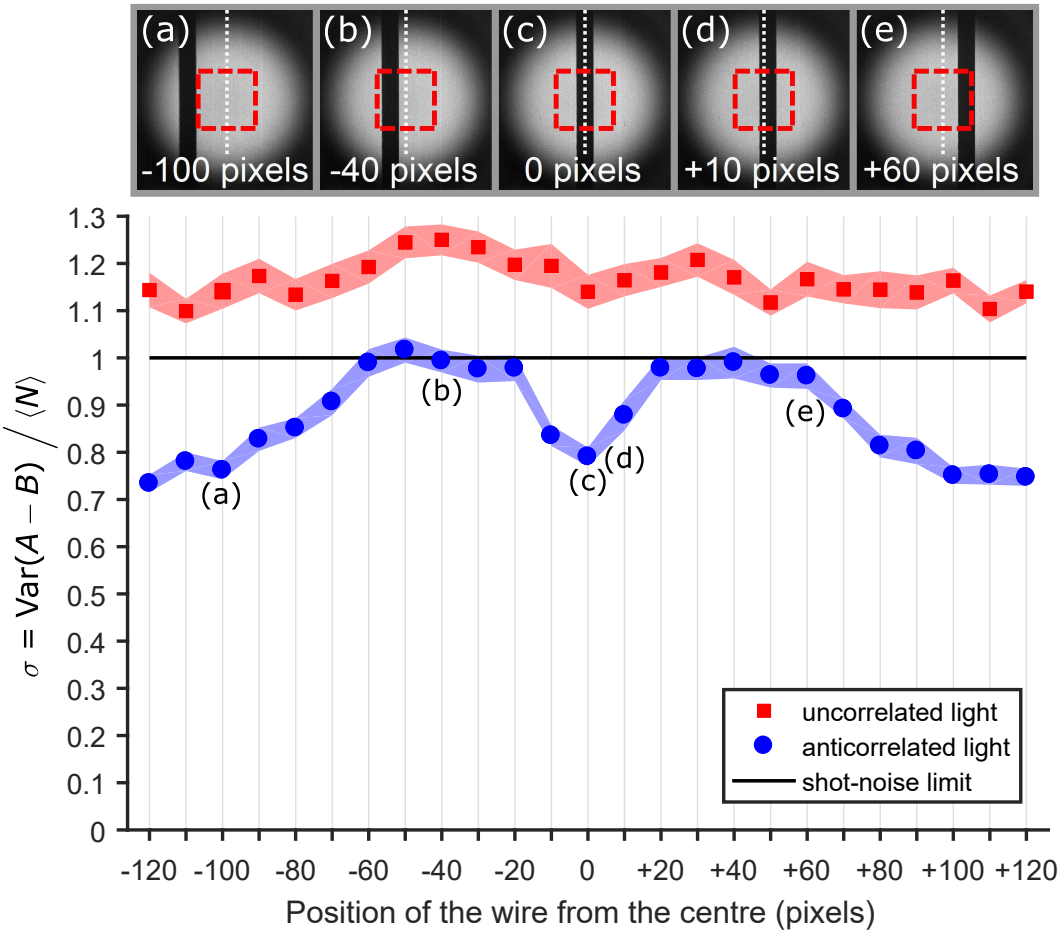

FIGURE 5.12: **Characterisation of the noise-performance of the shadow-sensing scheme using the degree of correlation for different positions of the scanning wire.** The noise-performance is measured both for spatially anti-correlated and spatially uncorrelated light, over a full-scan of the shadow-casting wire through the chosen 176×176 pixel^2 ROI, by changing the position of the wire at steps of 10 pixels each time. Each point is computed over $2,500$ frames and the uncertainty in this result is shown by the shaded error-bars in terms of the standard error of the standard deviation (i.e. the mean of the standard deviations of σ divided by the root of the number of 50-frame 'chunks' contained in each 2,500 frames data point. It can be seen that in the case of anticorrelated illumination (blue-series), the noise is reduced below both the classical-equivalent scheme (red-series) and the shot-noise-limit (black-series). The noise-reduction of the quantum-enabled shadow sensing scheme varies according to the position of the shadow with respect to the two halves of the split-detector, as defined by the chosen ROI (shown by the red-dashed box). The computed noise-reduction for the 5 positions (a-e) depends on the number of jointly-detected photon-pairs. This number changes with the position of the shadow, since the detected photons are spatially anticorrelated in the plane of the EMCCD camera. The detected position of the shadow with respect to the centre of the frame (white dotted-line) is reported below each frame in pixels. Reproduced from [9]

number of anticorrelated signal- and idler-photons are intercepted, without producing extra uncorrelated events. Considerable levels of noise suppression are also found for positions of the shadow near the centre (d). As soon as the shadow of the wire starts falling outside of the split-detector (e) the noise suppression improves again, since less and less photon-pairs are intercepted by the wire.

5.3.6 Computation of the quantum-advantage $\mathcal{E}$

The quantum-advantage in the estimation of the position of the shadow $\mathcal{E}$ is proportional to $\langle A - B \rangle$, and can be computed as follows:

$$\mathcal{E} = 1 - \frac{\mathrm{SD}(\Delta x)_{\mathrm{AC}}}{\mathrm{SD}(\Delta x)_{\mathrm{UC}}} = 1 - \frac{\mathrm{SD}(A-B)_{\mathrm{AC}}}{\mathrm{SD}(A-B)_{\mathrm{UC}}} = 1 - \frac{\sqrt{(\sigma_{\mathrm{DOC}})_{\mathrm{AC}}}}{\sqrt{(\sigma_{\mathrm{DOC}})_{\mathrm{UC}}}}, \tag{5.9}$$

where $\mathrm{SD}(A-B)$ is here defined as the square root of σ_{DOC}, the subscripts AC and UC indicate spatially anticorrelated and uncorrelated light respectively, and $\mathrm{SD}(\Delta x)$ is the uncertainty in the position estimation of the shadow.

It is possible to estimate the sensitivity advantage achieved using anticorrelated light, with respect to both a classical-equivalent scheme (here realised using spatially uncorrelated light) and to the more general SNL benchmark. This can be done using the measured σ_{DOC} (plotted in Fig. 5.12) and Eq. 5.9.

Therefore, the position advantage with respect to a classical-equivalent scheme is computed from the central position of the shadow-casting wire as follows:

$$\mathcal{E}_0 = 1 - \frac{\sqrt{0.79}}{\sqrt{1.14}} = 17\%(\pm 2\%), \tag{5.10}$$

whereas the position advantage with respect to the SNL (here represented by setting $(\mathrm{DOC})_{\mathrm{UC}}$ to one) using the central position of the shadow-casting wire is calculated

as follows:

$$\mathcal{E}_{SNL} = 1 - \frac{\sqrt{0.79}}{\sqrt{1.00}} = 11\%(\pm 1\%). \tag{5.11}$$

It should be noted that the errors associated with the values of $\mathcal{E}_0$ and $\mathcal{E}_{SNL}$ were computed at one standard-deviation.

5.3.7 Modelled results

The quantum-enhanced shadow sensing scheme was simulated using the model developed in chapter 4, section 4.1, with the addition of a modelled opaque object, whose position could be specified. It should be noted that in terms of the modelled position arrivals of biphotons, the effect of an opaque object is simply to cause the pixel-coordinates of the bright-events that fall within its transverse extent to disappear. These 'intercepted' bright-events are thus absorbed by the scanning-wire and do not add up to the detected events in a frame. However, it should be noted that the uniformly distributed dark-events of the detector are not affected by the position of the scanning wire, since they are generated directly on the plane of the detector. Additionally, it is reminded that both the detector and the scanning wire are in the far-field of the type-I nonlinear crystal, and thus the modelled detections of biphotons occur at spatially anticorrelated positions.

For simplicity, diffraction effects caused by the edges of the modelled wire were not considered. Moreover, both the detector noise-events and the bright-events were modelled with a shot-noise-limited statistics (i.e. Poissonian).

The split-detector was defined over a 172×172 pixel ROI. The modelled shadow of the object was 50 pixels wide. The shadow was moved across the field of view over 31 positions (including the central position) by 10 pixel steps. For each position of the

wire 20,000 modelled frames were analysed in chunks of 100 frames per data-point, allowing one to compute the normal-errors associated with the σ_{DOC} and σ_{+} values. Lastly, the transverse width of the biphotons' spatial correlations was set to a mean of 1.5 pixels, matching the experimental conditions.

The link between η_{total} and the achievable QNR is explored using a simulated model of the experiment (based on the work described in chapter 4 section 4.1). Under the conditions specified in the previous section, the noise-performance of the shadow sensing scheme was modelled by computing the σ_{DOC} for various positions of the scanning wire and for different values of the total effective QE, η_{total}.

This analysis was repeated for two scenarios: 1) for detector with zero-noise, to better isolate the effects of η_{total} on the measured σ_{DOC}, 2) for a number of noise events per pixel per frame matched to the experimentally measured number of dark-events per pixel per frame of the EMCCD camera. The results of both modelled scenarios are shown in Fig. 5.13. As the shadow moves from the central position, a greater number of anticorrelated events are disrupted, with the resulting unpaired events being responsible for a degradation in the noise suppression. The greatest noise suppression is shown by arrows (1) and (3), corresponding to the shadow falling outside of the split-detector, when therefore all anticorrelated events are detected in a balanced manner. According to Eq. 5.4, the achieved σ_{DOC} is directly related to the total effective QE, η_{total}. This can be observed by the ascending trend of the thick data-series (corresponding to the quantum-enabled noise reduction with anticorrelated illumination) in Fig. 5.13(a) and (d). The presence of spatially uncorrelated noise of the detector results in a degradation of σ_{DOC}, as visible by comparing the magnitude of arrows (1) and (3). Moreover, the width of the shadow (here modelled to be 50 pixels wide so as to match the experimentally measured width) affects the minimum achievable noise suppression $(\sigma_{\mathrm{DOC}})_{\mathrm{min.}}$, highlighted by arrow (2). The amount of degradation

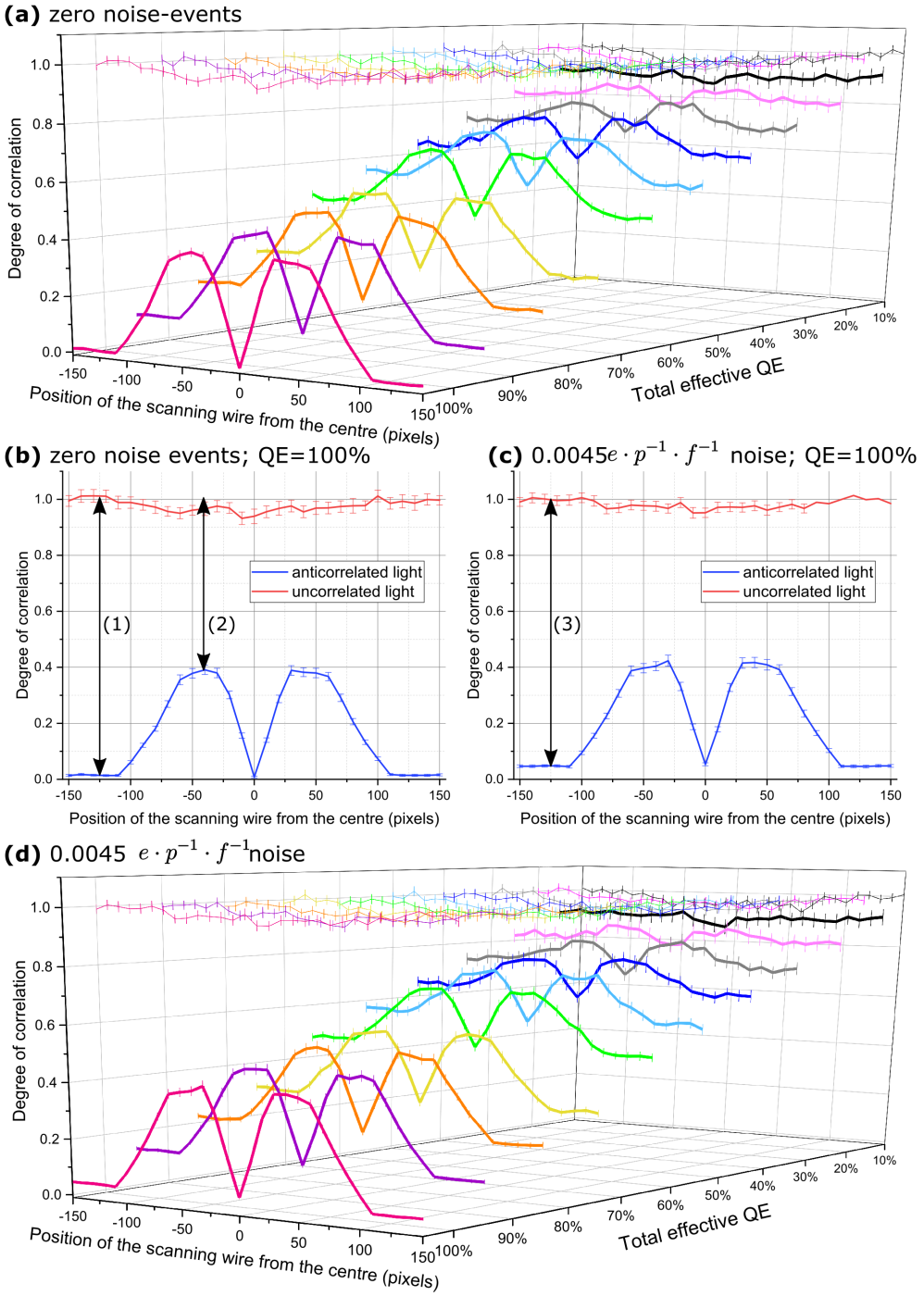

FIGURE 5.13: **Modelled noise performance for anticorrelated and uncorrelated light, as a function of η_{total} and wire position.** The degree of correlation (i.e. normalised variance of $A - B$) is computed for a range of total effective QE, $10\% \leq \eta_{\text{total}} \leq 100\%$, both in the case of a zero noise events of the detector (a), and for the experimental-like noise of 0.0045 dark events per pixel per frame (d). The thick data-series in (a) and (d) correspond to the noise performance in the case of anticorrelated illumination, while the thin data-series correspond to uncorrelated illumination. The noise performance computed for $\eta_{\text{total}} = 100\%$ is highlighted in the individual plots (b) and (c), in the case of zero-noise and typical noise respectively. The arrows indicate the maximum (1 and 3), and the minimum (2) achievable noise reduction, at different positions of the shadow-casting modelled object, from the centre of the split-detector.

is simply related to twice the ratio between w_{shadow} and w_{ROI} (here chosen to be 172 pixels), as shown below:

$$(\sigma_{\text{DOC}})_{\text{min.}} = 2 \cdot \frac{w_{\text{shadow}}}{w_{\text{ROI}}} = 2\cdot, \frac{50}{172} \approx 0.58 \tag{5.12}$$

as confirmed by visual inspection of the magnitude of arrow (2) in Fig. 5.13(b). The factor of 2 in Eq. 5.12 is due to the fact that for each unpaired event (caused by its partner being absorbed on the other side of the split-detector by the scanning wire) the degrading contribution to the measured noise influences both the event count of A and B.

Finally, it should be noted that Eq. 5.12 is only valid in case of noiseless detection and $\eta_{\text{total}} = 100\%$, since in this condition the only source of uncorrelated event is due to the absorption by the shadow-casting wire.

5.4 Conclusion

In this chapter I have discussed a quantum-enabled shadow-sensing technique, which allows to enhance beyond the shot-noise-limit the sensitivity with which the position of a shadow can be estimated, by exploiting the properties of quantum states. Specifically, the quantum shadow-sensor achieves sub-shot-noise performance by detecting the spatially anticorrelated photon-pairs produced by a type-I nonlinear crystal, pumped in the SPDC regime, and using a single-photon sensitive EMCCD camera, operated in the photon-counting regime.

The noise statistics of the shadow-sensor were characterised in terms of its main components: the employed downconversion light-source and the EMCCD camera, employed as a split-detector. The combined noise-baseline of the system (i.e. the sum of excess noise of the source and detector) was found to be 13% worse than the

SNL, by computing the normalised variance of the difference of the signals of the split-detector, meaning that the degree-of-correlation of the quantum illumination must exceed this value in order to reach sub-shot-noise operation. Modelled results of the noise performance of the system for different noise levels of the detector and a range of total effective QE were also produced and discussed.

The ability of the system to reach sub-shot-noise performance was experimentally demonstrated, reaching an overall 17% noise-reduction in the estimation of the position of the shadow with respect to a classical-equivalent scheme, and an 11% noise-reduction with respect to the SNL. The quantum advantage was shown to scale favourably with the total effective QE of the detection channel, meaning that optical loss and detector-noise are the limiting factors of the scheme. It is envisioned that with the advent of less expensive and better performing detectors (such as high-responsivity/low-noise photodiodes), the quantum-enabled shadow-sensor could be operated in a higher-flux regime, exploiting the intensity correlations of parametric downconversion, potentially enabling applications of the technique outside of the laboratory.

To my best knowledge, these findings represent the first experimental demonstration of a quantum noise reduction scheme applied to the position measurement of a shadow, able to operate at the single-photon regime, using spatially anticorrelated photon-number correlations of SPDC biphotons .

Chapter 6

Resolution-enhanced quantum imaging by centroid estimation of biphotons

In this chapter I discuss the experimental investigation that enabled the demonstration of a full-field resolution-enhancing scheme, based on the centroid estimation of spatially correlated biphotons.

6.1 Theoretical description

First I present an intuitive theoretical description of the resolution-enhancement due to the centroid estimation of detected biphotons, analytically proving its standard-quantum-limited resolution advantage, in terms of the reduction of the width of the PSF. The theoretically achievable resolution advantage of schemes based on optical centroid measurements is standard quantum limited [250]. In this section I provide a simple theoretical description of the mechanism by which the detected size of the

PSF, σ_{PSF}, is reduced by a factor of $\sqrt{2}$ in the case of an image entirely made of estimated centroids of jointly detected biphotons, thus proving the SQL nature of the CEBs imaging scheme. A complete quantum mechanical description of both SQL and HL imaging schemes can be found in the following works [1, 251, 252].

The quantum-enhanced CEBs scheme employs SPDC illumination. Thus the produced biphotons are spatially correlated in the transverse plane of the crystal. For simplicity the description of the system is reduced to a one-dimensional geometry in the transverse plane of the crystal and of the detector; also, the source (i.e. the pump) is assumed to be planar [251]. Moreover, a collinear and degenerate phase-matching condition is considered. According to this picture both signal s and idler i photons of a biphoton packet propagate through the same optical system (i.e. along the same mode), interacting first with an object (placed in the image plane of the crystal) and then with a spatially-resolved detector (also placed in the image plane of the crystal). Finally, according to a thin-crystal approximation [224], the s and i photons are assumed to be born in the same position in the plane of the crystal, as shown in fig. 6.1(a), thus illuminating the same feature of the object, as shown in Fig. 6.1(b). The distances between the detected positions of the s and i photons in the transverse plane of the detector and their original transverse positions in the plane of the object are assumed to be normally-distributed random variables, δX_s and δX_i respectively, as shown in Fig. 6.1(c).

According to the standard-quantum-limited regime of the scheme, each s and i photons of a biphoton packet interacts independently with the diffracting features of the object and optics. Thus, δX_s and δX_i can be considered to be independent quantities. Consequently, their variance can be expressed as the square of the size of the

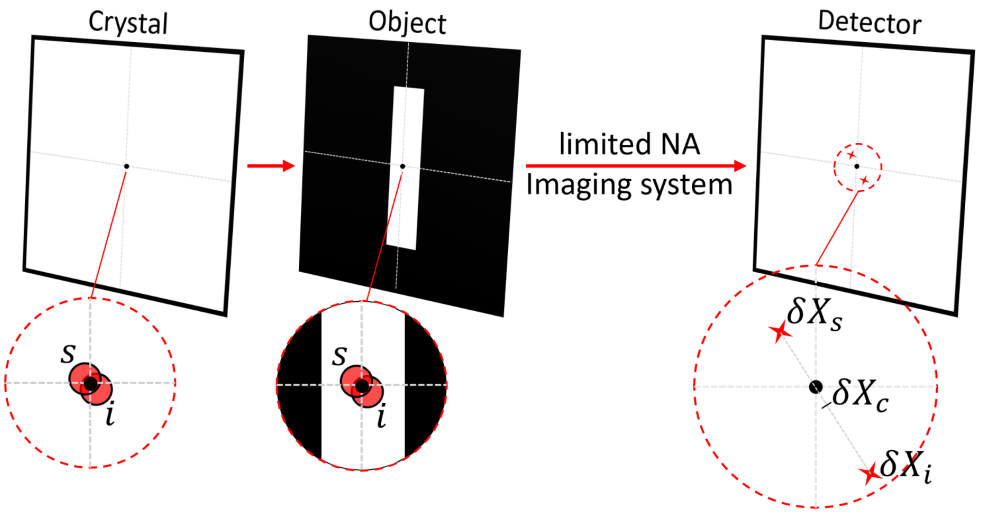

FIGURE 6.1: **Centroid estimation using the detected positions of a signal and idler photon of a biphoton packet.** The s and i photons of a biphoton packet are born in the same position in the crystal, according to the thin-crystal approximation (a). They also propagate through the same optical mode and reach the same feature of the object (b). As they propagate through a non-ideal imaging system placed between the object and the detector (e.g. a limited NA system) their transverse positions change. Their detected positions in the plane of the detector are assigned to two normally-distributed variables, δX_s and δX_i (c). The loss in resolution caused by the limited NA imaging system is represented by the difference in position between the original transverse position in the plane of the object and the middle point between the detected transverse positions of s and i, δX_c. The small black-dots indicate the transverse position where the s and i photons are born in the crystal. The red round-shapes illustrate the s and i photons. The red four-pointed stars in (c) indicate the detected transverse positions of s and i photons.

PSF, according to:

$$\mathrm{Var}\left(\delta X_s\right) = \mathrm{Var}\left(\delta X_i\right) = \left(\sigma_{PSF}\right)^2, \tag{6.1}$$

where Var indicates the variance operation, and σ_{PSF} is the transverse size of the PSF in the plane of the detector.

The mid-point between the detected position of the s and i photons is defined as the estimated centroid position δX_c, according to:

$$\delta X_c = \frac{\delta X_s + \delta X_i}{2}. \tag{6.2}$$

This quantity, as shown in Fig. 6.1(c), represents instantaneous (i.e. for one biphoton) loss in resolution due to diffraction and other PSF-broadening factors. The mean loss in resolution r, is found by considering a statistically significant number of centroid estimations and is expressed as follows:

$$r = \sqrt{\mathrm{Var}\left(\delta X_c\right)} = \sqrt{\mathrm{Var}\left(\frac{\delta X_s + \delta X_i}{2}\right)} = \frac{\sqrt{\mathrm{Var}\left(\delta X_s + \delta X_i\right)}}{2}. \tag{6.3}$$

The SQL resolution enhancement of the CEBs scheme can then be demonstrated by comparing the loss in resolution described in Eq. 6.3 to the loss in resolution of a scheme that detects the transverse positions of all incident photons (also affected by the non-ideal imaging system placed between the object and the detector).

Since the sum of normally-distributed random variables is also a normally-distributed variable, and its variance equals the sum of variances of individual variables, if follows that:

$$r = \frac{\sqrt{\mathrm{Var}\left(\delta X_s + \delta X_i\right)}}{2} = \frac{\sqrt{\mathrm{Var}\left(\delta X_s\right) + \mathrm{Var}\left(\delta X_i\right)}}{2} = \tag{6.4}$$

$$= \frac{\sqrt{2 \cdot (\sigma_{PSF})^2}}{2} = \frac{\sigma_{PSF} \cdot \sqrt{2}}{2} = \frac{\sigma_{PSF}}{\sqrt{2}}, \tag{6.5}$$

where $\mathrm{Var}\left(\delta X_s\right)$ and $\mathrm{Var}\left(\delta X_i\right)$ were substituted by $(\sigma_{PSF})^2$ according to Eq. 6.1. The spatial resolution of an image entirely made of estimated centroid positions is therefore higher than that obtained by a classical counterpart. The advantage corresponds to a $1/\sqrt{2}$ narrowing of the PSF.

6.2 Experimental realisation

In this section I discuss the experimental set-up shown in Fig. 6.2 (a) that allowed the demonstration of the resolution-enhanced quantum imaging scheme by CEBs ,

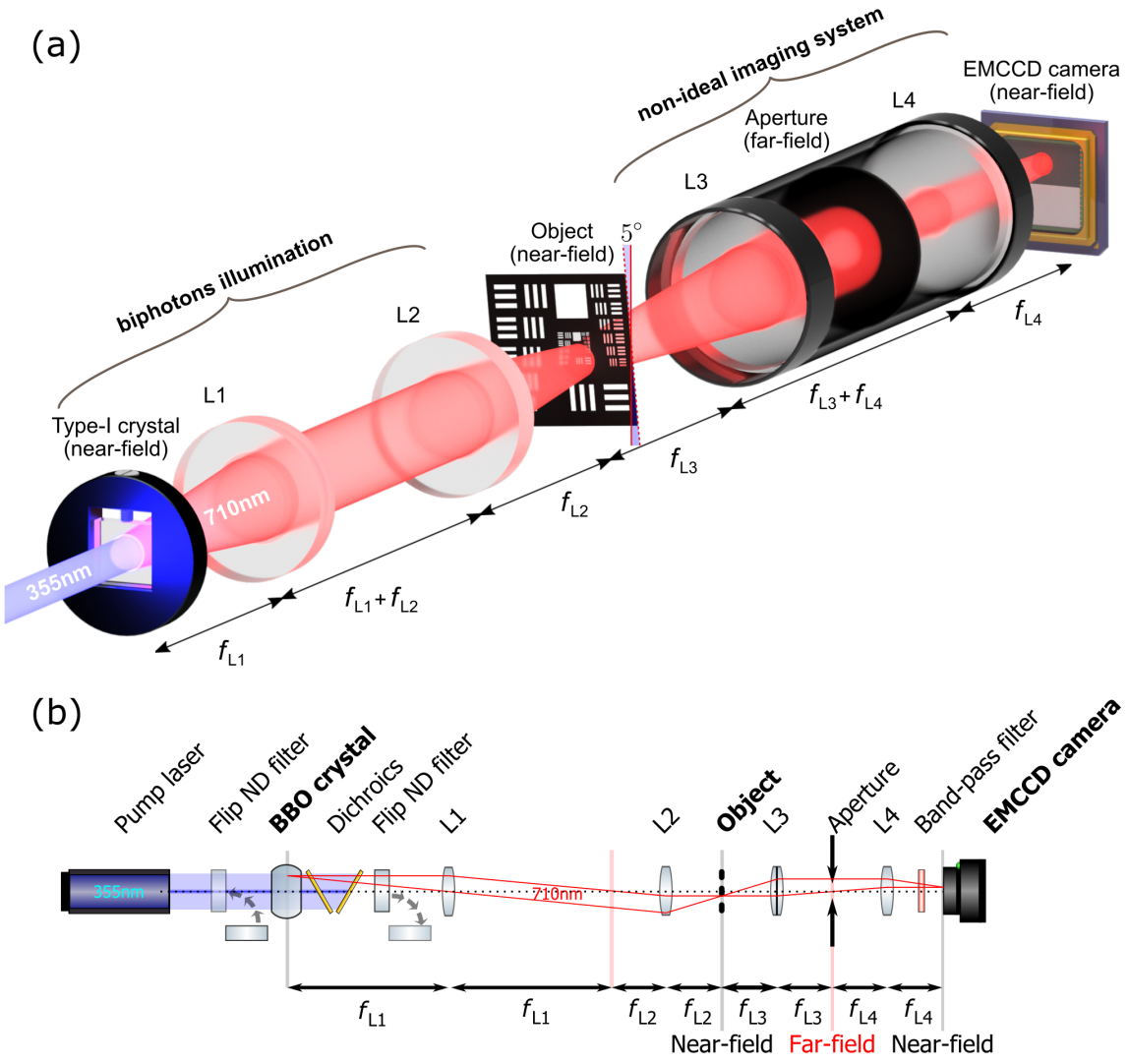

FIGURE 6.2: **Experimental realisation of the resolution-enhanced quantum imaging scheme by CEBs and ray-diagram representation..** The imaging scheme is comprised of a source of biphotons illumination, an object, a non-ideal imaging system whose optical resolution is affected by its limited numerical aperture, and an EMCCD camera operated in the photon-counting regime. Both the object and the EMCCD are placed in the image plane of the crystal, where the biphotons are spatially correlated. An aperture is placed in the far-field of the crystal, between the object and the EMCCD camera, to tune the detected size of the PSF of the system. A demagnifying telescope (i.e. the first telescope after the crystal) is used to reduce the size of the spatial correlations on the plane of the object, thus ensuring that both photons of a biphoton packet probe the same portion of the object. Reproduced from [10].

together with its ray-diagram, shown in (b). The scheme is based on four main functional parts: 1) a source of biphotons (labelled in the figure as 'biphotons illumination'), 2) the object, 3) a non-ideal imaging system (responsible for the loss in

resolution), 4) a single-photon sensitive and spatially-resolved detector.

Details about the experimental set-up used to produce spatially correlated biphotons by SPDC can be found in chapter 3, section 3.2.2. In addition to the nonlinear crystal, the illumination part of the experiment included a 0.67 magnification $4f$-telescope, achieved using two plano-convex lenses: L1 (150mm focal length) and L2 (100mm focal length). In this experiment, the spatial correlations of biphotons in the image plane of the crystal were exploited to realise the quantum-enhanced imaging scheme, using a collinear phase-matching condition.

The object consisted of a clear optical-path USAF resolution target (Edmund Optics, model number 58-402), rotated around the longitudinal optical-axis by $\approx 5°$, in order to serve as a knife-edge object for the measurement of the slanted-edge MTF.

The non-ideal imaging system was built by placing an adjustable aperture in the far-field of both the crystal and the object, thus allowing one to tune the size of the detected diffraction limited spot of the system (i.e. σ_{PSF}).

Importantly, the maximum number of detected biphoton -events N_{pe}, as described in chapter 4 section 4.2, was used to guide the accurate positioning of the EMCCD in the image plane of the crystal. Once the plane of the detector was optimally tuned by small displacements along the optical axis using a micrometer linear-stage (not shown in the figure) the position of the object was also optimised. This was simply achieved by displacing the object along the optical axis (also by means of a micrometer stage, not shown in the figure) using the sharpness of its captured image as a metric. With both the camera and the object accurately placed in the image plane of the crystal, the last step consisted in placing the adjustable iris in the far-field of the crystal and of the object. This was achieved by exchanging $L4$ with another lens of half the focal length, thus temporarily imaging both the far-field of the crystal and of the object onto the EMCCD camera. Next, the iris was centred and displaced along

the optical-axis (also by means of a linear-stage, not shown in the figure) using the sharpness of its captured image as a metric. Lastly, L4 was put back to its place, and its transverse position finely re-adjusted using the detected position of the correlation peak (which was previously set to be at the centre of the camera sensor). It should be noted that even a slight misalignment by a few μm can have detrimental effects on the strength of the detected correlation peak, which in turn is an indicator of the number of detected biphotons. For this reason great care was taken in operating the 3-axis micrometer stage of the EMCCD, finely tuning its position in the transverse plane.

In summary, the nonlinear crystal was imaged on the plane of the object, and both the crystal and the object were also imaged on the plane of the detector. The demagnification of the first telescope was used to reduce the transverse spatial correlation area of the SPDC illumination, ensuring that both s and i photons of a biphoton packet interacted with the same feature of the object. As mentioned in section 6.1 this is a requirement for the operation of the CEBs scheme.

In order to measure the resolution-enhancement of the quantum-enabled imaging scheme, the illumination was switched between spatially correlated and spatially uncorrelated, using a pair of neutral density filters alternatively placed immediately before or after the nonlinear crystal , as explained in chapter 3, section 3.2.2.

6.3 Characterisation and modelling

In this section I first describe how biphotons (i.e. event-pairs) are selected from the acquired binary frames of the EMCCD camera. Known experimental parameters (such as the number of noise events per pixel per frame of the detector and total effective QE of the system) are used to design an optimised pair-finding algorithm

and identify the optimal light-level. Lastly, I show how the achievable resolution advantage is affected by optical losses and noise of the detector.

6.3.1 Determination of the optimal kernel size from the analysis of dark-frames

As mentioned the CEBs scheme relies on the ability to find and therefore select biphoton events from all other detected binary events in a frame. This task was achieved by software post-selection of spatially correlated events, using a pair-finder algorithm. In simple terms, the algorithm tests every detected photon-counted event with nearby events that fall within a specified distance (the kernel-size). Selection rules are applied in order to minimise the number of ambiguously found pairs, thus ensuring that those event-pairs that are found and selected for the centroid estimation are real photon-pairs (i.e. detected biphotons).

The first important parameter of the pair-finder is thus the kernel-size. This quantity largely depends on the detected transverse correlation width $(\sigma_c)_{\text{detected}}$, which in the case of an NA-limited imaging system is affected by the width of the PSF σ_{PSF}, according to:

$$(\sigma_c)_{\text{detected}} = \sigma_c * \sigma_{PSF}, \tag{6.6}$$

where σ_c is the actual transverse correlation-width in the plane of the crystal, and $*$ indicates the convolution operation. In practice, this quantity is tuned by operating the variable aperture placed in the far-field of both the object and the nonlinear crystal, as discussed in section 6.2.

It is however not possible to ignore the noise of the detector, which effectively introduces unwanted randomly distributed events, which are indistinguishable from actual

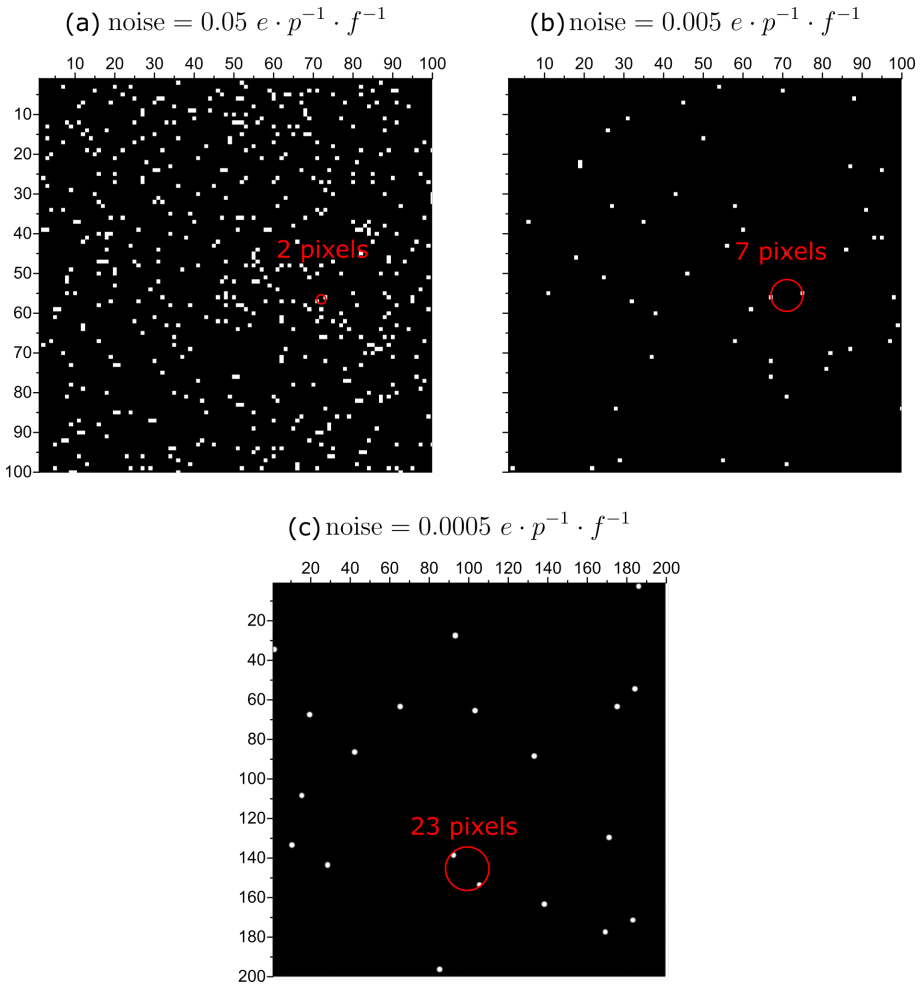

FIGURE 6.3: **Determination of the optimal kernel-size of the pair-finding algorithm.** The minimum free-path between noise-events is used to determine the optimal size of the pair-finding algorithm, ensuring a minimum number of accidentally detected event-pairs. The minimum free-path is shown to be inversely proportional to the noise of the detector, using modelled dark-frames.

photon-events. Therefore, the number of noise events per pixel per frame of the detector operated in photon-counting mode was analysed to determine the minimum free-path between noise events, defined as the average minimum distance from any event, within which another event may be found. This is represented in Fig. 6.3 in the case of decreasing levels of noise (a-c). The mean minimum free-path $\langle l_{min} \rangle$ for a binary dark-frame of size $d \times d$ pixels, can be expressed as:

$$\langle l_{min} \rangle = d/\sqrt{\langle N_D \rangle}, \tag{6.7}$$

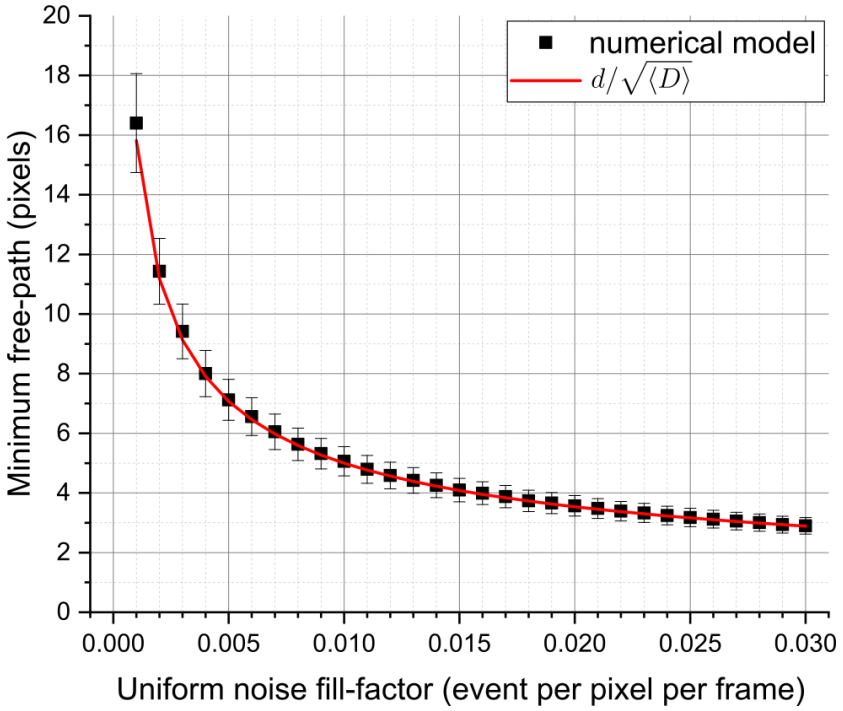

FIGURE 6.4: **Minimum free-path between dark-events.** The minimum free-path between uniformly distributed dark-events is computed both using modelled dark-frames (dark-series) and Eq. 6.7. For a number of bright events matched to the noise level of the employed EMCCD camera (i.e. 0.005 events per pixel per frame) the average minimum free-path is ≈7 pixels. The error-bars were computed over 20 iterations of the numerical model, each employing a different seed of the pseudo-random generator used to generate the coordinates of noise-events.

where N_D is the total number of uniformly distributed noise events. This can be intuitively understood by realising that $\sqrt{D}$ is the side of the square made by D pixels. Hence the ratio between the size of the square-frame and the size of the dark-events (also expressed as a square), returns the minimum free-path.

As expected, the average minimum free path $\langle l_{min} \rangle$ is inversely proportional to the noise of the detector, and thus to the number of noise-events in a dark-frame, as plotted in Fig. 6.4. The minimum free-path as a function of noise was computed using both Eq. 6.7 and modelled dark-frame (as discussed in chapter 4, section 4.1). An average minimum free-path of ≈ 7 pixels was found for the noise of the EMCCD detector used in the experimental demonstration (noise= 0.005 events per pixel per frame).

This quantity sets the upper limit to the detected transverse correlation width of spatially correlated biphotons. According to the noise-level of the used EMCCD camera, the optimal range for $(\sigma_c)_{\text{detected}}$ is defined as follows:

$$0 \leq (\sigma_c)_{\text{detected}} \leq \left(\frac{\langle l_{min}(0.005e \cdot p^{-1} \cdot f^{-1}) \rangle}{2} \approx 3.5 \text{ pixels} \right), \tag{6.8}$$

where the division by 2 is motivated by the need of establishing a safety margin between found event-pairs (shown in Fig. 6.5(a)). In fact, without enforcing a safe distance, an event could ambiguously belong to more than one event-pair.

It should be noted that $(\sigma_c)_{\text{detected}}$ is measured in terms of the FWHM of the corresponding distribution function. In the case of Gaussian distributions (and to a first approximation in the case of double-Gaussian functions) 68% of all events falls within this range. In order to 'catch' the remaining percentage it is therefore necessary to increase $(\sigma_c)_{\text{detected}}$. Following this analysis, the detected transverse correlation-width was tuned by operating the variable aperture, and set to a size of ≈2.2 pixels, leaving a safety margin of 2 pixels around found event-pairs, thus satisfying the upper limit set by Eq. 6.8.

Given the chosen 3×3 kernel-size, 11 of 12 available biphoton arrangements were captured by the pair-finder, as represented in Fig. 6.5(a-c). Specifically, these consisted of 4 skew biphotons in a 2×3 and 3×2 sub-kernel (shown in Fig. 6.5(a)), 4 long-range biphoton separated by 1 pixel in the full 3×3 kernel (shown in Fig. 6.5(b)), and 3 short-range biphotons in a 2×2 sub-kernel (shown in Fig. 6.5(c)). Vertically adjacent event-pairs were discarded in order to avoid accidental pairs caused by the camera's charge-smearing artefact [4]. Additionally, each photon-counted frame was pre-processed by removing pixel-islands of more than 2 pixels, as shown in Fig. 6.5(e).

The effect of discarding vertically adjacent pairs corresponds to removing ≈ 17% from the total number of detectable pairs, or one fourth of all detectable pairs within

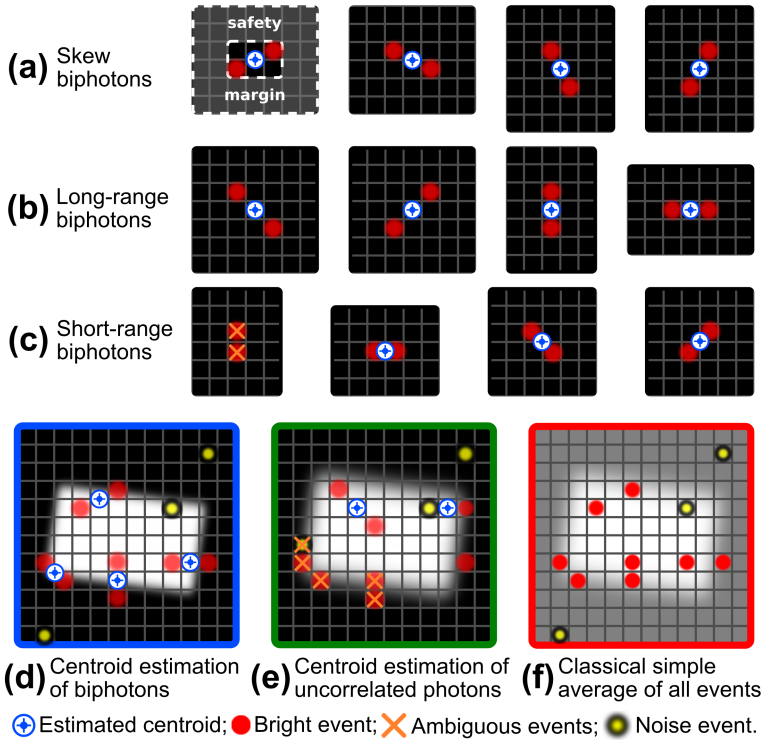

FIGURE 6.5: **Representation of the pair-finding algorithm.** The optimal size of the kernel was found to be 3×3 pixels, from analysis of the number of noise events per pixel per frame of the EMCCD. An additional 2-pixel wide safety margin is necessary to avoid ambiguity between potential event-pairs. Thus, 12 event-pairs can be detected: 4 skew (a), 4 long-range (b), and 4 short-range (c). Vertically adjacent event-pairs are discarded to avoid accidental detections due to the charge-smearing artefact of the EMCCD camera, as well as interconnected pixel-islands (both cases shown in (e)). A resolution enhanced image of the object illuminated using biphotons can be reconstructed, using the estimated centroid positions of detected event-pairs, as shown in (d). In the case of spatially uncorrelated illumination (shown in (e)), the spatial resolution is the same as that for the classical simple average of all events (shown in (f)). This is because it is not possible to reduce the spreading of the PSF caused by the non-ideal imaging system. Moreover, the background of the simple average of all events is higher than that obtained by centroid estimation, since there is no rejection of uncorrelated noise-events. Reproduced from [10].

one $(\sigma_c)_{\text{detected}}$. In more details, given that $(\sigma_c)_{\text{detected}}$ is the FWHM of the detected transverse correlation width (which was set to a size of 2.2 pixels by closing the variable aperture), within this transverse extent each of the four detectable short-range biphotons shown in Fig 6.5(c) account for approximately a fourth of all biphotons detectable within a one standard deviation range (i.e. $1/4 \cdot 68.27\% \approx 17\%$).

Both the centroid-estimation imaging scheme (applied to both spatially correlated

and uncorrelated illumination) and the classical-equivalent imaging scheme (i.e. the simple average of all events) are schematically represented in Fig. 6.5(d-e). In the case of biphotons illumination, the centroid-estimated pixel- coordinates can be used to generate a resolution enhanced image of the object, as represented in Fig. 6.5(d). In the case of spatially uncorrelated photons (obtained by introducing optical loss immediately after the nonlinear crystal by means of an ND filter), the centroid-estimated pixel-coordinates of accidental event-pairs do not produce a resolution enhancement, as represented in Fig. 6.5(e). This is also true in the case of the simple average of all events, as represented in Fig. 6.5(f). A reduction in the background (i.e. in the retained dark-events) is associated with applying a pair-finder, as a consequence of the spatially-defined coincidence-detection. Accordingly, both in the case of spatially correlated and uncorrelated centroid-estimated frames (and indeed even without computing the centroid positions of the detected event-pairs [253]) the chance of detecting a noise event is reduced with respect to the classical scheme by $1/\text{noise}^2 = 1/0.005^2$, where 0.005 is the measured noise of the EMCCD in terms of dark events per pixel frame.

6.3.2 Determination of the optimal light level

Using the optimised pair-finder algorithm discussed in section 6.3.1, the optimal level of illumination (i.e. the number of bright events per pixel per frame) was investigated. The number of unambiguously detected biphotons per frame was used as a metric to guide the optimisation. More specifically, the CEBs imaging scheme was simulated for different levels of illumination and total effective QE, using the model developed in chapter 4, section 4.1, with the addition of the pair-finder algorithm.

The results of this analysis are shown in Fig. 6.6, in terms of the number of unambiguously found event-pairs. Firstly, as a result of the safety-margin enforced by the

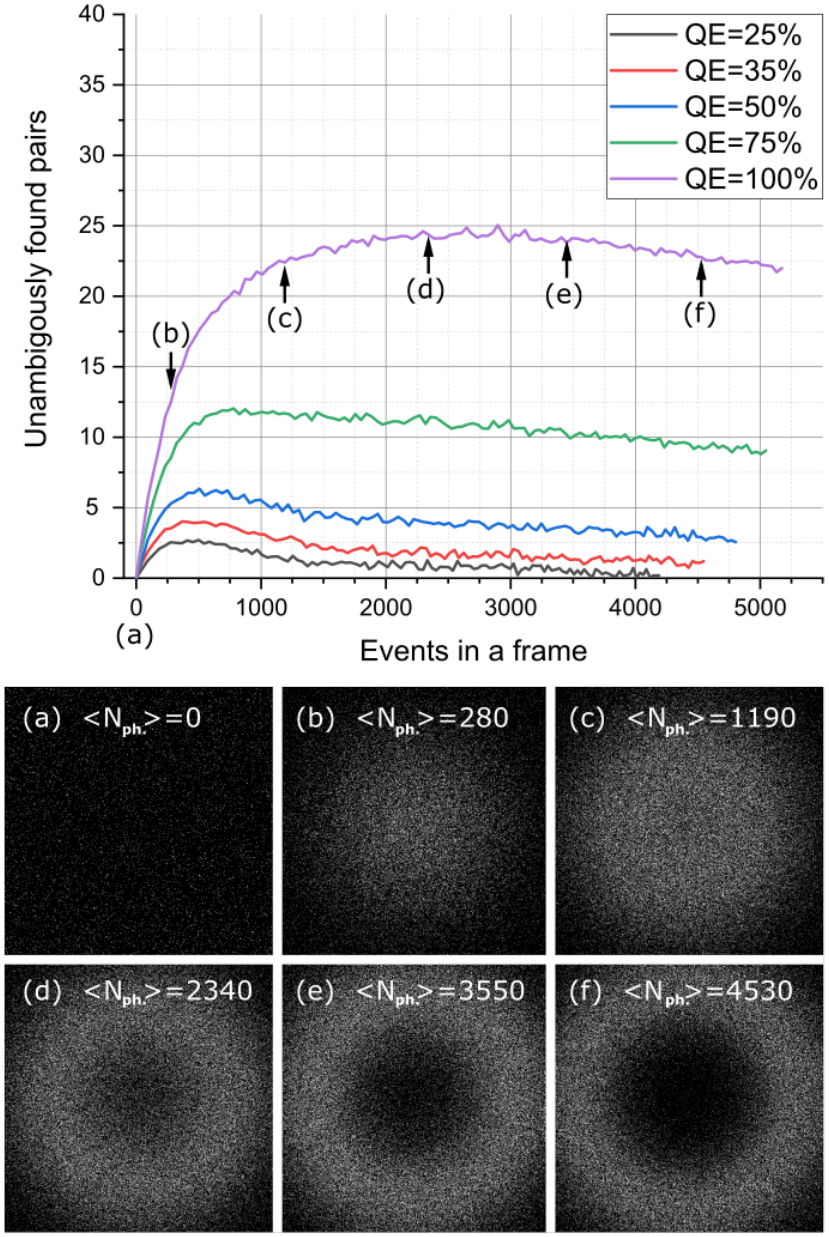

FIGURE 6.6: **Modelling of the influence of the number of detected events per pixel per frame over the number of unambiguously found pairs.** The optimal light-level corresponds to the highest number of unambiguously found event-pairs. 256×256 pixel photon-counted frames of the downconverted beam were modelled for different levels of both spatially correlated and uncorrelated illumination, and different values of the system's total effective QE. The number of noise events was matched to the experimentally measured 0.005 events per pixel per frame. The number of unambiguously found event-pairs was calculated by taking the difference of the number of detected pairs for spatially correlated and uncorrelated illumination. Due to the Gaussian intensity distribution of the downconverted beam, more and more event-pairs are rejected at the centre of the frame (i.e. where the minimum free-path is shortest) as the level of illumination is increased. The sum of pair-detections over 500 frames are shown in the case of QE=100% for 6 increasing light-levels, labelled (a) to (f). The x-axis shows the total number of events in a frame, including dark-events.

pair-finder algorithm, an increasing number of events is rejected following an increase in the light-level. This can be seen in the summed frames shown at the bottom of Fig. 6.6, where a hole appears in the central region of the beam, as clearly visible in (e-f). The fact that most events are rejected at the centre is not surprising, since the intensity-profile of the downconverted beam as detected in the image plane of the nonlinear crystal is the same Gaussian profile of the UV-pump.

The plot at the top of Fig. 6.6 highlights the optimal light-level which corresponds to the maximum number of unambiguously detected event-pairs. This quantity was found by subtracting the average number of detected event-pairs for spatially correlated and uncorrelated frames. Specifically, two sets of modelled frames were produced: one for spatially correlated bright-events, and one for spatially uncorrelated. Each set was then processed using the pair-finder, yielding the average number of detected pair events per frame for both types of illumination: $\langle N_{pe} \rangle_{\text{correlated}}$ and $\langle N_{pe} \rangle_{\text{uncorrelated}}$.

It should be noted that the number of detected pairs in the case of spatially uncorrelated illumination correspond to the number of accidental detections, whereas the number of detected pairs in the case of spatially correlated illumination corresponds to the sum actually detected photon-pairs and again the number of accidental detections. The average number of *unambiguously* detected pairs (i.e. the number of detected biphotons) was defined as follows:

$$\langle N_{pe} \rangle_{\text{unambiguous}} = \langle N_{pe} \rangle_{\text{correlated}} - \langle N_{pe} \rangle_{\text{uncorrelated}} \tag{6.9}$$

and was estimated by running the model twice, once setting the bright events to be spatially correlated (thus yielding $\langle N_{pe} \rangle_{\text{correlated}}$), once setting the bright events to be spatially uncorrelated (thus yielding $\langle N_{pe} \rangle_{\text{uncorrelated}}$), and finally by substituting the detected numbers of pairs into Eq. 6.9.

As shown in the plotted series at the top of Fig. 6.6, the number of unambiguously detected biphotons is linked to the total effective QE of the scheme. According to the total effective QE of the experiment ($\eta_{\text{total}} = 0.35$) the optimal average number of all events per frame $\langle N \rangle$ was found to be ≈ 390. This number includes both dark events $\langle N_D \rangle$ and bright-events $\langle N_B \rangle$. Given the 256×256 pixel size of the modelled frames and the specified 0.005 dark events per pixel per frame noise level, the optimal light-level in terms of bright events per frame $\langle N_B \rangle$ was found to be ≈60, according to:

$$\langle N \rangle = \langle N_B \rangle + \langle N_D \rangle \tag{6.10}$$

$$\langle N_B \rangle = \langle N \rangle - \langle N_D \rangle \tag{6.11}$$

$$\langle N_B \rangle = 390 - 0.005 \cdot 256^2 \approx 60, \tag{6.12}$$

thus ≤ 0.001 photon per pixel per frame.

As shown in the red-series of Fig. 6.6, under typical experimental conditions the mean number of unambiguously detected photon-pairs in a 256×256 frame is ≈3.5. This number compares favourably to a back-of-the-envelope calculation of jointly-detectable pair events N_{pe}, in the case of a total number of bright events $N_B = 60$ and total-effective QE $\eta_{\text{total}} = 0.35$, according to:

$$N_{pe} = \frac{N_B \cdot \eta_{\text{total}}^2}{2} = \frac{60 \cdot 0.35^2}{2} \approx 3.7, \tag{6.13}$$

where η_{total}^2 indicated the probability of joint-detection, and the division by two is done to convert the number jointly-detect events into jointly-detected pairs. This means that in the case of very low-illumination and for 0.005 dark-events per pixel per frame, the pair-finding algorithm is of adequate performance, since it does not

miss a significant number of the event-pairs detectable according to the total quantum efficiency of the detector.

However, due to the binary nature of detection (discussed in Chapter 4, section 4.2.3) the number of unambiguously detected pairs is found to decrease as the light level is increased. For example, it is possible to consider the violet-series of Fig. 6.6, where in spite of $\eta_{\text{total}} = 100\%$ and for $N_B \approx 2500$, the number of unambiguously detected pairs is found to be only 50, whereas the same back-of-the-envelope calculation shown in Eq. 6.13 suggests a number of jointly-detectable pair events of 150.

Thus, the model indicates that regardless of the level of QE and in the specific case of a binary single-photon sensitive detection scheme, the pair-finding algorithm works best for event-sparse frames, i.e. for *very* low levels of illumination. The measurement of η_{total} from photon-counted frames of SPDC illumination is discussed in chapter 4, section 4.2.4.

6.3.3 The role of η_{total} and detector's noise on the attainable resolution advantage

As seen in the previous section, the total effective QE affects the number of detected biphotons. In practice η_{total} depends on optical and detector's losses.

In the present context, the effect of losses causes a reduction in the number of detected 'true'-centroids, resulting in a stronger contribution to the reconstructed image by accidentally detected centroids. Thus, if an image entirely made by true-centroids has a $\sqrt{2}$ enhancement in resolution, in the case of accidental centroids (or the simple average of all events) the resolution of the image is not improved. Consequently, an

image *not entirely* made by true-centroids will be characterised by a lower enhancement in resolution. Similarly, uncorrelated events introduced by the noise of the detector can have a similar effect on the resolution enhancement.

First, the model of spatially-resolved detections of SPDC photons was augmented by the addition of a synthetic slanted-edge target, allowing one to simulate the whole CEBs scheme. More specifically, a pseudo-random Gaussian distribution matched to the experimentally measured size of the PSF, σ_{PSF}, was used to alter the pixel-coordinates of the transmitted events, accounting for the limited NA of the imaging system and a transmissive mask was used to define transmission or absorption of events by the slanted-edge.

This was first achieved by simply representing the slanted-edge as a rectangular binary mask within each modelled frame. The binary values of the affected pixels (1 inside the slanted-edge mask and 0 outside it) were used to determine whether an event would be transmitted or absorbed. This method resulted in unwanted pixelation of the slanted-edge, as shown in Fig. 6.7 (a). Importantly, pixelation in the slanted-edge would compromise the MTF-measurement, by introducing unwanted spatial frequencies.

In order to produce a realistically smooth edge, the transmissive part of the slanted-edge was instead defined in terms of four lines (one for each edge of the transmissive rectangle) and by retaining the fractional coordinates of each generated bright-event , as shown in Fig. 6.7 (b). In more details, the coordinates of each bright-event were substituted into the four line-equations. According on whether the resulting number was less/greater than zero, the fractional pixel coordinate would be incremented/decremented (depending on which line was tested). In the case of the altered pixel-coordinate falling outside of the transmissive area of the test-target, the tested event would be discarded. In other words, only after having accounted for the sub-pixel contributions to the coordinates of bright-events, the events were committed to

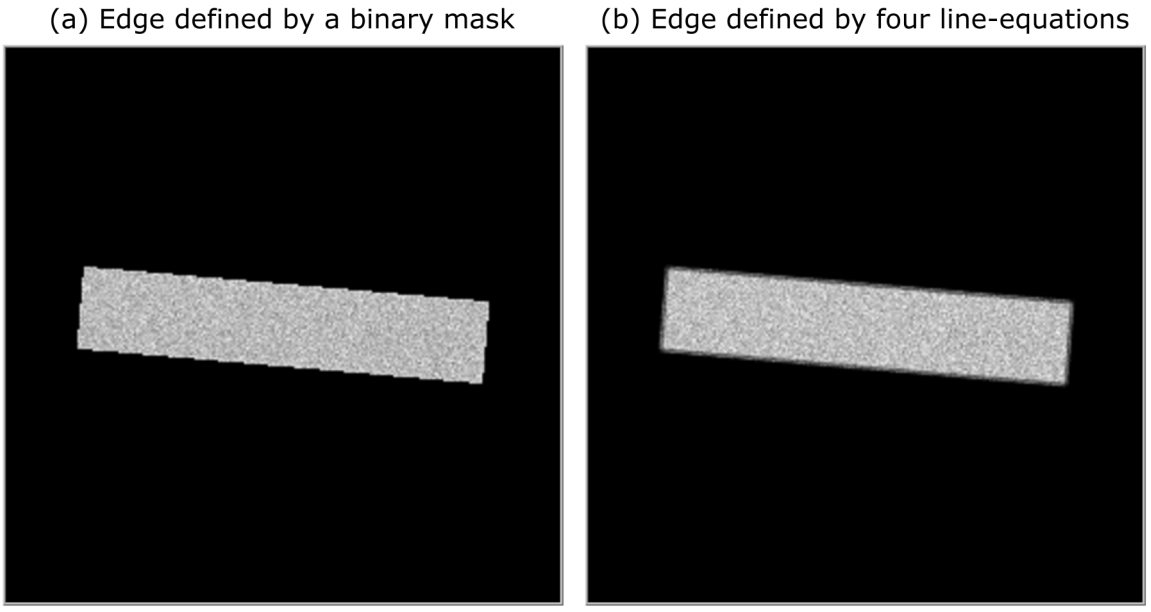

FIGURE 6.7: **Modelled frames of the slanted-edge target represented by a simple binary mask or four line-equations.** A simple binary mask used within modelled frames to define the transmission or absorption of events by the slanted-edge target resulted in visible pixelation, as shown in (a). Smooth edges of the resolution-target were obtained by considering the sub-pixel contributions , as determined using four line-equations to define the transmissive region of the slanted-edge, as shown in (b). Both (a) and (b) were simulated using 256×256 pixel frames.

the coordinate-grid of the frame, by rounding them to their nearest integer.

The model of the CEBs imaging scheme was used to investigate the influence of η_{total} and of the detector's mean number of noise events on the attainable resolution enhancement. In order to decouple the effects of losses and noise, each quantity was individually investigated, setting the other to its ideal value.

The role of η_{total} on the attainable resolution advantage. The role of losses was investigated under zero-noise conditions. MTF curves of reconstructed images using both the simple average of all events and the CEBs approach were produced, as shown in Fig. 6.8(a).

The blue solid-line shows the MTF computed for ideal QE (i.e. for η_{total}=1), whereas the blue dotted-line shows a degraded MTF, computed for a level of losses matched

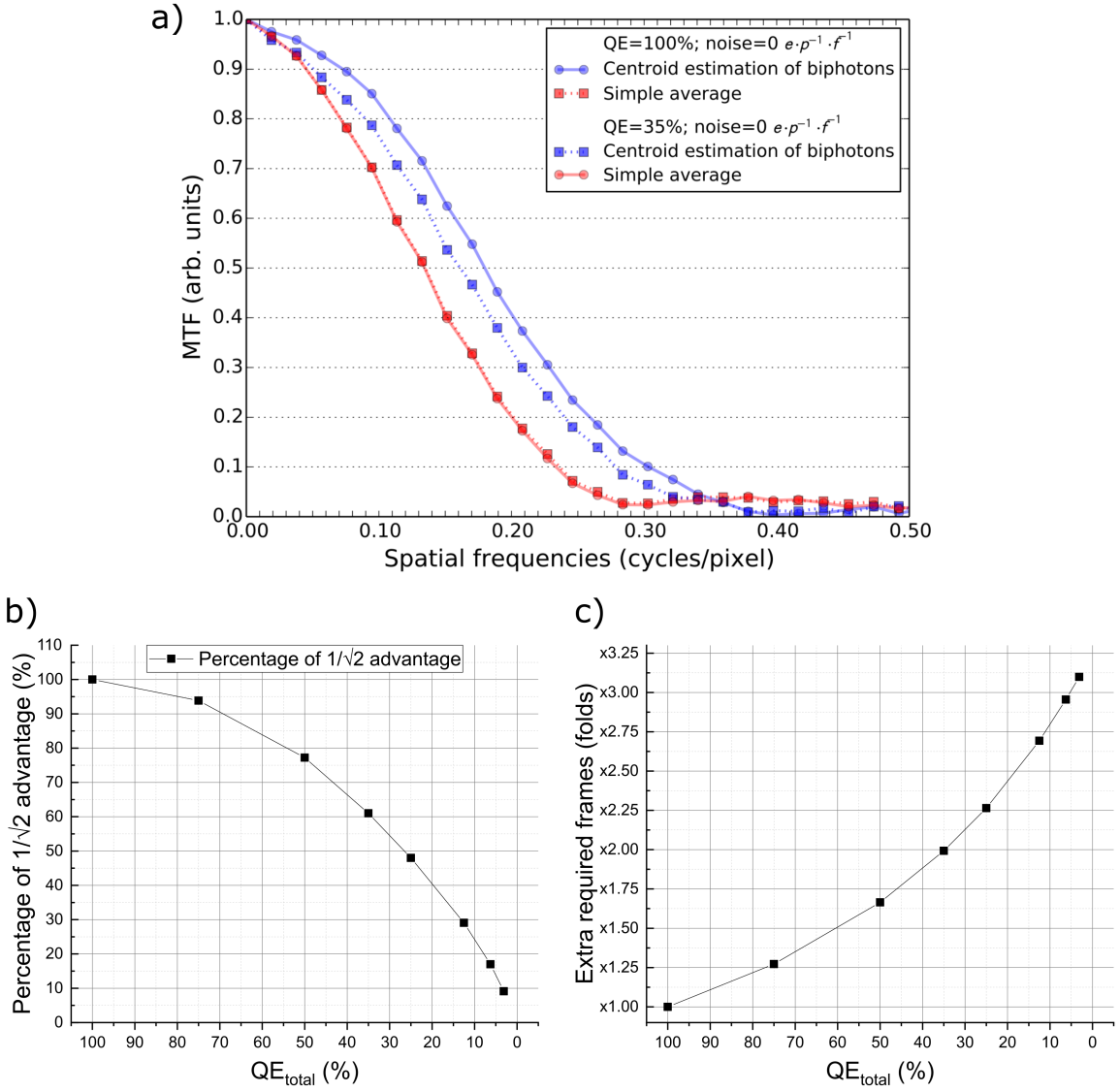

FIGURE 6.8: **The role of the total effective QE on the resolution enhancement and on the required number of frames.** The MTF curves of the modelled slanted-edge frames are plotted (a) for ideal QE (solid lines) and matching the experimental QE (dotted lines), under zero-noise conditions. A nonlinear degradation of the MTF can be observed. The resilience to optical loss achieved by the rejection of uncorrelated events of the pair-finder is better highlighted in (b), in which a 50% QE is associated with only ≈20% degradation in the resolution advantage. However, the number of frames required for a certain number of biphotons per pixel in the final reconstructed image is shown to increase as a function of optical loss (c), as the proportion of accidentally estimated centroids versus centroids of biphotons increases. Reproduced from [10].

to the experimentally measured value of η_{total}. Interestingly, the degradation in the MTF does not appear to be simply proportional to η_{total}, as expected from the ability of the pair-finder to reject uncorrelated events.

This dependence was further investigated by means of the MTFA parameter (discussed in section 2.3.2), used to quantitatively assess the achieved resolution-advantage for a range of QE spanning from 3%[1] to 100%.

The results of these simulations are plotted in Fig. 6.8(b). The total number of detected centroids in the final reconstructed image was kept constant for each value of η_{total}, requiring more and more frames to be modelled for increasing levels of optical loss. This effect is shown in Fig. 6.8(c).

Regarding Fig. 6.8 (c), it should be noted that the number of frames required to achieve the same number of detected centroids in the final reconstructed image, does not tend to infinity as the QE parameter approaches zero. That is to say that for spatially uncorrelated events (i.e. when QE≈0), the number of frames required to reconstruct an image is found to depend entirely on the number of accidental pairs detected in a single frame, which is not zero under typical noise and illumination conditions.

The role of the detector's noise on the attainable resolution advantage. The role of the noise of the detector was investigated under ideal QE conditions. MTF curves of reconstructed images using both the simple average of all events and the CEBs approach were produced, as shown in Fig. 6.9. The blue solid-line shows the MTF computed for zero-noise, whereas the blue dotted-line shows a degraded MTF, computed for the level of noise of the EMCCD camera (i.e. 0.005 events

[1] For a desired total number of bright events in a synthetic frame, as the QE parameter is reduced the model takes a longer time to populate each individual frame. This is due to the increasing number of missed events by the detection operator Ω when $u(0,1) > \eta_{\text{total}}$, where $u(0,1)$ is a uniform distribution used to computationally generate pseudo-random numbers between 0 and 1, as discussed in Chapter 4 section 4.1. In order to limit processing times, the lower QE limit in these simulations was set to 3%.

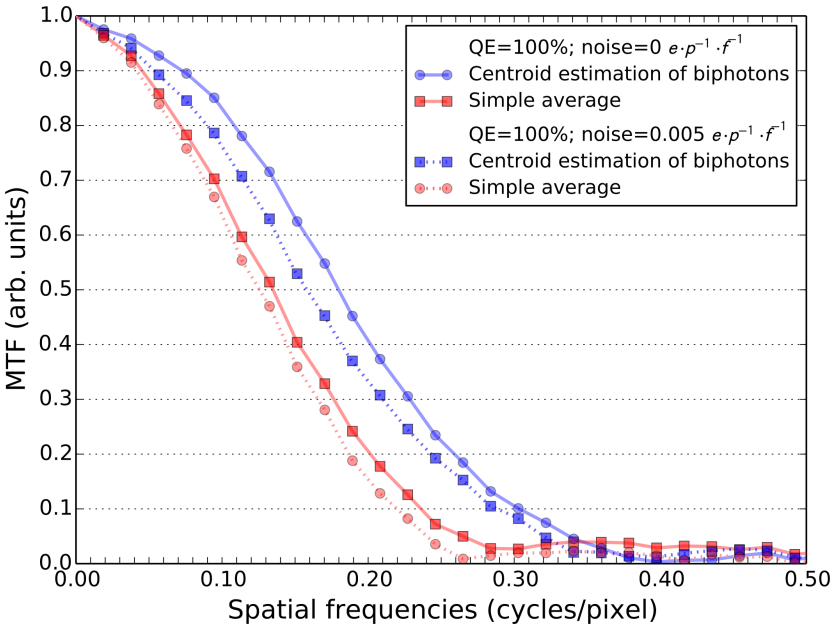

FIGURE 6.9: **The role of the detector noise on the resolution enhancement.** The MTF curves of the modelled slanted-edge frames are plotted for noise-free (solid lines) and the experimental level of noise (dotted lines), under perfect QE conditions. An increase in the noise level is accompanied by a degradation in resolution for both the simple average of all events and the centroid estimated reconstructed images. The former can be explained by a decrease in contrast of the image, due to the accumulation of noise events in the opaque portion of the slanted-edge, whereas the latter is explained by an increase in the number of accidentally estimated centroids at the expense of the number of actual centroids of biphotons. Reproduced from [10].

per pixel per frame). The presence of uniformly distributed noise events resulted in degraded MTF curves, both in the case of the CEBs and simple average of events approaches. In the case of CEBs, the degradation can be readily understood in terms of an increase in the number of accidental centroids, resulting from a greater number of spatially uncorrelated events in each frame. In the case of the simple average of all events, the worsening of the MTF is caused by a higher background intensity in the final reconstructed image, due to the summing of randomly distributed noise-events in each frame.

Finally, it should be noted that an analytical treatment of the effect of noise and detection efficiency on the attainable resolution advantage is not straightforward,

due to the various statistical distributions used in the generation of each modelled frame. For instance, in the case of the image plane of the crystal the spatial coordinates of bright events are modelled according to a Gaussian distribution, the spatial coordinates of dark events are modelled according to an uniform distribution, and the detection of each event that populates a synthetic frame depends on a uniform distribution.

6.4 Results

In this section the resolution-enhanced quantum imaging scheme by CEBs is experimentally demonstrated, using the pair-finding algorithm and optimal illumination level investigated in the previous section. The quantum-enabled resolution advantage is quantitatively measured using the slanted-edge MTF standard, and images of real-world objects are shown for visual comparison.

In order to measure the performance of the imaging scheme, 10^6 frames of the slanted-edge resolution target were acquired, using both spatially-correlated and spatially uncorrelated illumination. This data was processed to produce the blue-, green- and red-MTFs shown in Fig. 6.10. More specifically, the blue-MTF was computed from the centroid estimated image of the slanted-edge, illuminated using spatially correlated light; the green-MTF was computed from the centroid estimated image of the slanted-edge, this time illuminated by spatially uncorrelated light; and the red-MTF was computed from the image of the edge processed by averaging together all of the detected events.

Key to the demonstration of a quantum-enabled advantage is that both the red- and green-MTF curves display the same imaging performance (i.e. the two curves are almost perfectly superimposed). This confirms that the improvement in spatial

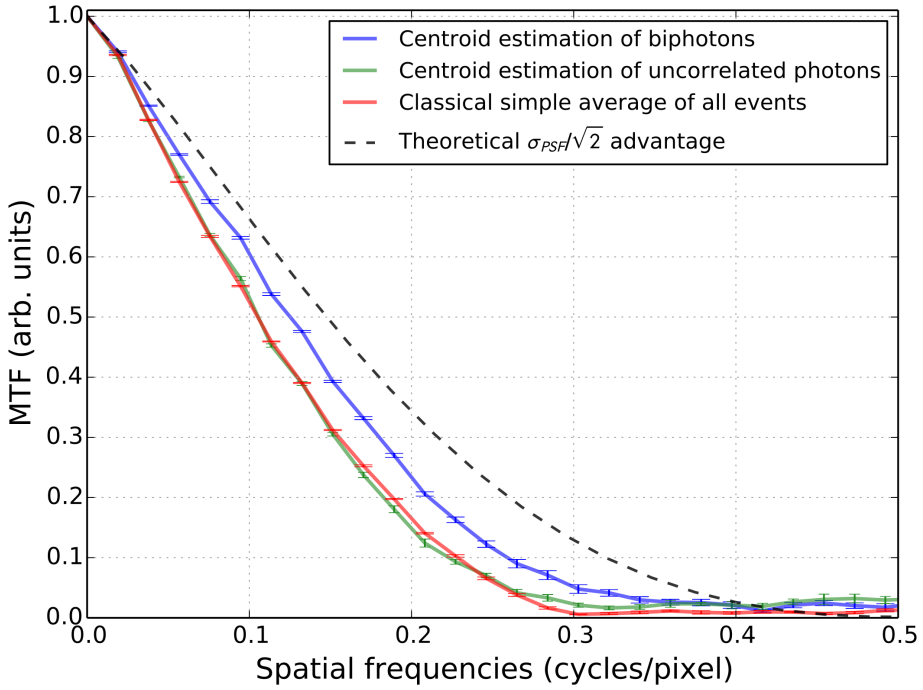

FIGURE 6.10: **Experimental demonstration of the quantum-enabled resolution-enhancement using the slanted-edge MTF method.** The imaging performance the CEBs scheme (blue-MTF) is compared against that of an equivalent classical imaging scheme (red-MTF). The centroid estimation is applied to spatially uncorrelated frames (green-MTF) to test that the resolution-enhancement is not an artefact of the pair-finding algorithm, confirmed by the almost perfectly super-imposed green- and red-MTFs. The black-MTF shows the full theoretical advantage, as given by the standard-quantum-limited reduction of the PSF by $1/\sqrt{2}$. The error-bars were computed over 10 sets of data, each comprising 10^6 frames. Reproduced from [10].

resolution highlighted by the blue-MTF is not an artefact of the pair-finding algorithm. On the contrary, the achieved resolution-enhancement is shown to be linked to the detection of spatially correlated biphotons and the estimation of their centroid pixel-coordinates.

Since the photon-counted events in the acquired frames comprise both spatially correlated and uncorrelated events, the experimentally achieved advantage was less than the theoretically available one, represented by the black-MTF in Fig. 6.10. It should be noted that within a photon-counted frame, spatially uncorrelated events may be due to partially-detected biphotons (where either the signal or idler was not detected), stray-light (such as fluorescence or unintended light from the surroundings), or noise

events of the detector (such as thermalised photoelectrons and clock-induced-charge).

In order to quantify the experimentally achieved resolution-enhancement, the MTFA values computed for the blue- red- and black-MTFs of Fig. 6.10 were compared. These represent the area under the MTF, chosen here within a range of spatial-frequencies spanning from 0.9 to the 0.3 cycles/pixel (i.e. up to the noise floor of the centroid estimated MTF curve). Accordingly, the quantum-enabled resolution advantage was found to be 41% of the theoretically available SQL advantage, corresponding to a 12% reduction in size of the PSF.

6.4.1 Images of real-world objects

Images of real-world objects were also acquired in order to illustrate the resolution-enhancement achievable by CEBs. The reconstructed images of an insect's wing and of a bundle of glass fibres are shown in Fig. 6.11 (a) and (b), together with intensity cross-sections, shown at the bottom. Reconstructed images of additional objects are shown in Fig. 6.12. The images produced by the simple average of all events are highlighted by a red-box, whereas those reconstructed using the CEBs approach are highlighted by a blue-box. In order to facilitate a resolution assessment by eye, all images in Fig. 6.11 and Fig. 6.12 were normalised and equalised according to the minimum and maximum intensity values retrieved from their histograms.

In order to avoid shot-noise in the CEBs images (which due to rejection of uncorrelated events are more prone to this type of artefact), a comfortably large number of frames was acquired and processed (i.e. 1.5×10^6 frames for each image). Given an acquisition rate of 24.445 Hz for the chosen 356×356 pixels frame-size and acquisition settings, the total time required to acquire 1.5×10^6 frames is ≈17 hours. This time may be reduced either by using a faster detector or simply by acquiring less frames.

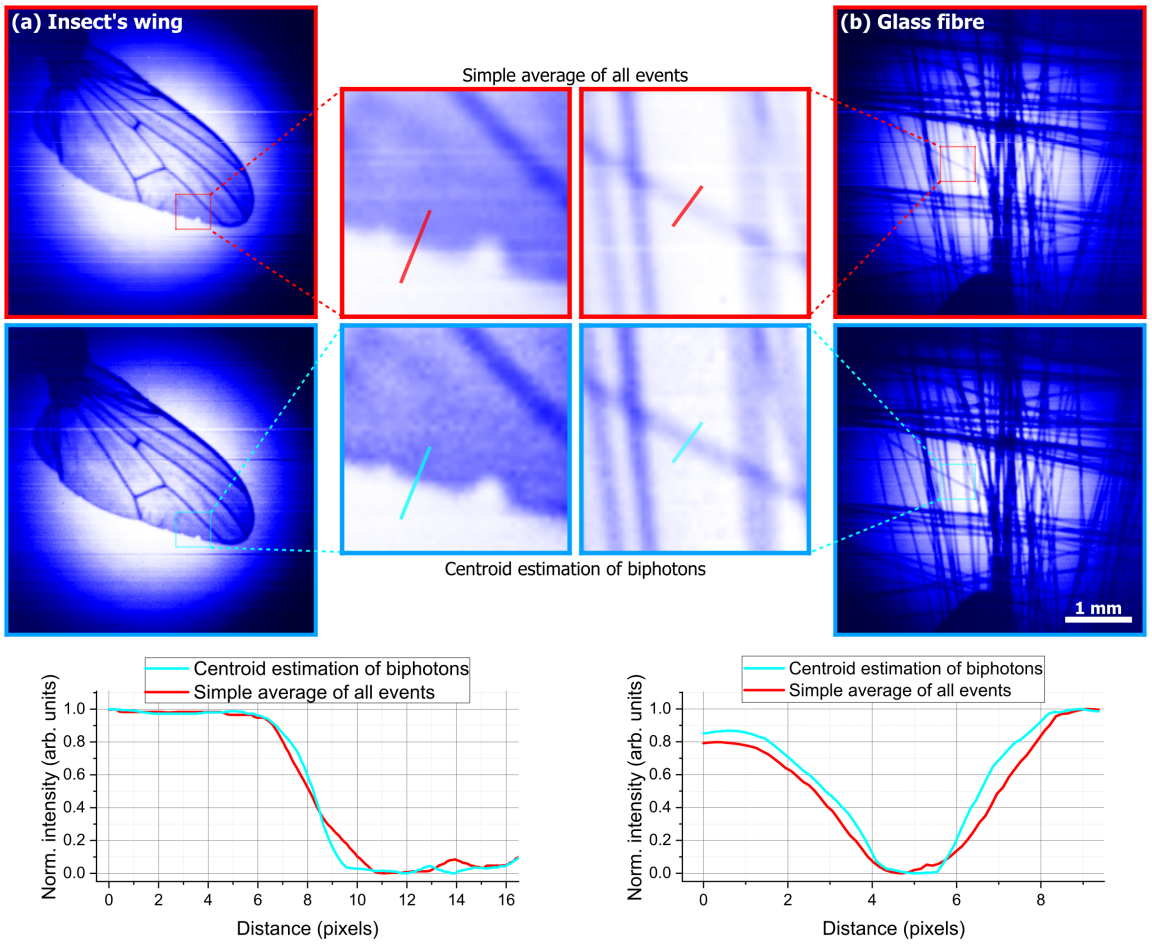

FIGURE 6.11: **Resolution-enhanced images of real-world objects.** Images of an insect's wing (a) and crossed glass fibres (b) were reconstructed using the simple average of all events (red-box) and the CEBs (blue-box) approaches. Zoomed portions of the images (obtained by linear interpolation) and intensity cross-sections are shown for visual comparison. Each 356×356 pixels image was reconstructed from 1.5×10^6 acquired frames. The horizontal streaks are due to charge-smearing of the EMCCD camera, here revealed by the large number of constituting frames. The size-bar shown at the bottom-right applies to all images. Reproduced from [10].

In the latter case, however, shot-noise in the reconstructed images may become an issue.

6.4.2 Centroid estimated images using less frames

According to the specifications of our detector, it is possible to achieve an acquisition rate of 92.7 Hz or 282 Hz, for a 256×256 or 128×128 pixels frame-size, by enabling

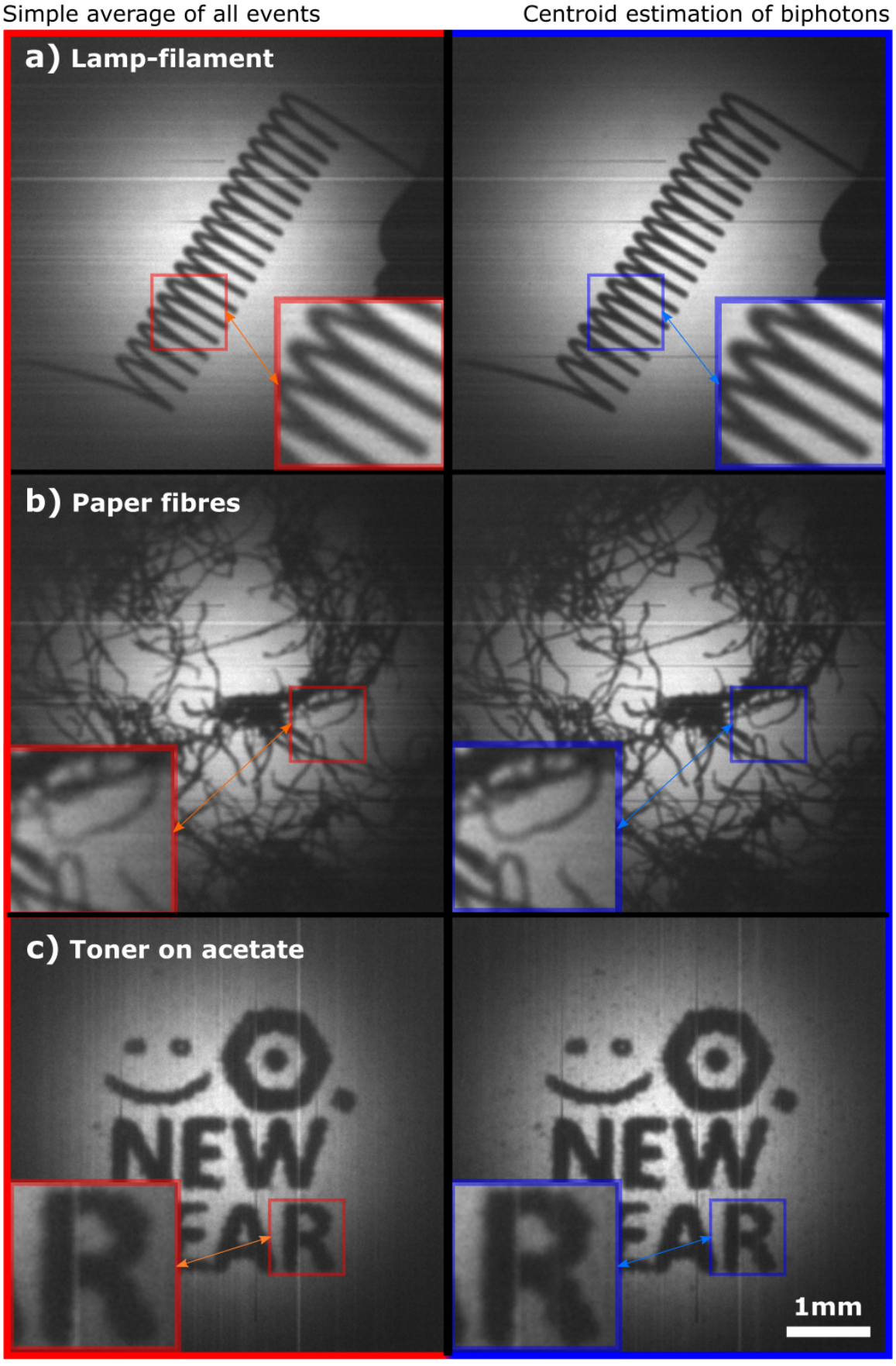

FIGURE 6.12: **Additional real-world objects.** Images reconstructed using the simple average of all events (red-box) and the centroid estimation of biphotons (blue-box) are shown for comparison, together with zoomed-portions. Each 356×356 pixels image was reconstructed from 1.5×10^6 acquired frames.

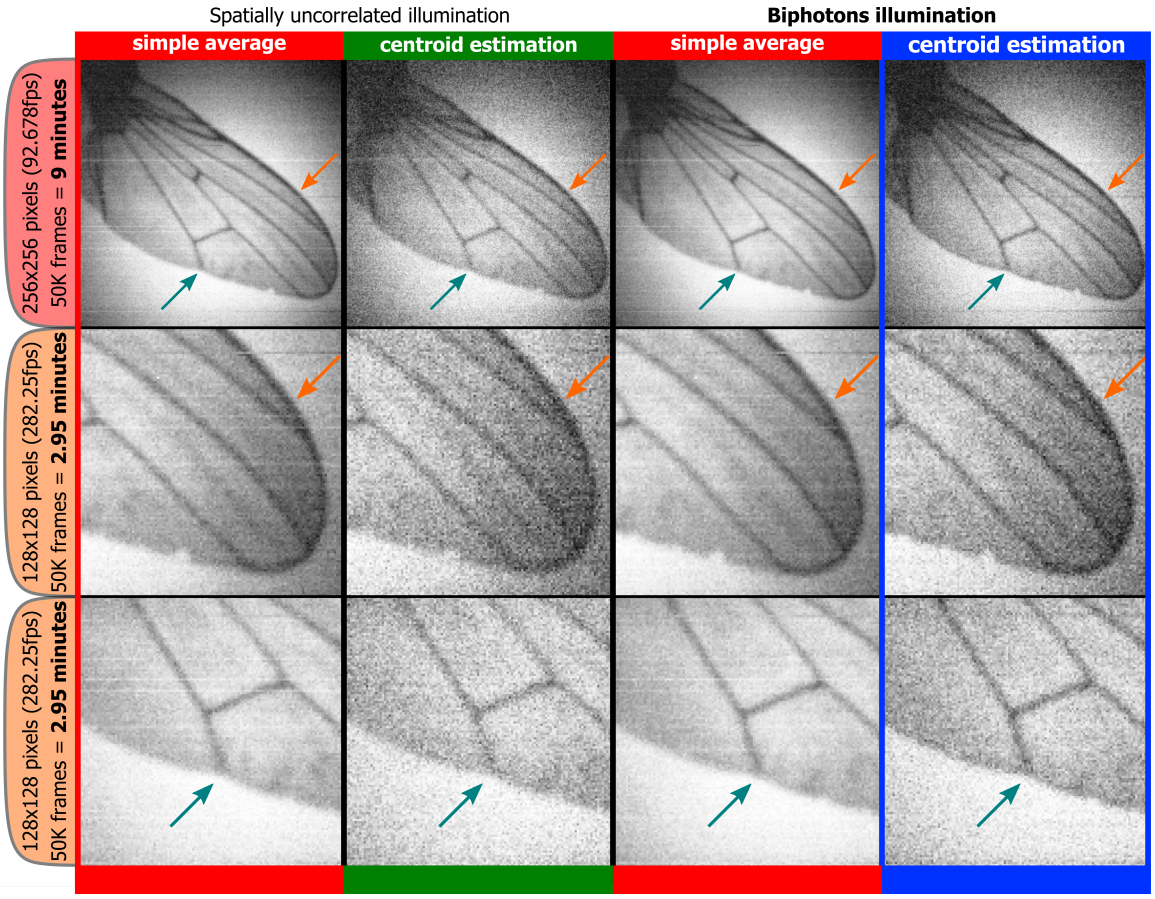

FIGURE 6.13: **Resolution-enhanced images using 5% of the data.** The arrows point to features of the object, for which a resolution-enhancement can be seen. Shot-noise is visible as a consequence of only using 50,000 frames for the reconstruction of the final images. Both acquisition rates and times are reported in the row-headers. Reproduced from [10].

the 'optically-centred' crop-mode of the EMCCD. More details about this acquisition mode can be found in chapter 3, section 3.3.1.

Images reconstructed using 50,000 frames (i.e. 5% of the originally acquired frames) are reported in Fig. 6.13, together with the corresponding acquisition rates and times. Faster acquisition times obtained by acquiring a smaller number of frames are associated with more prominent shot-noise in the reconstructed images, which scales as the square-root of the number of detected centroids per pixel. In spite of shot-noise, it was still possible to demonstrate a resolution advantage, as shown in the measured slanted-edge MTFs, plotted in Fig. 6.14.

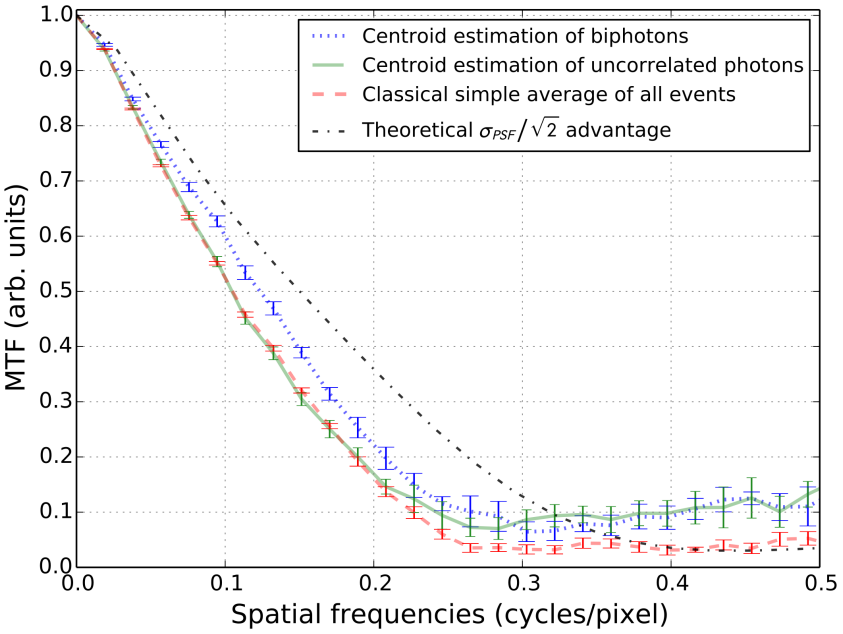

FIGURE 6.14: **Slanted-edge MTFs using 5% of the data.** The imaging performance of the CEBs scheme (blue-MTF) is compared against that of the classical imaging scheme (red-MTF). Due to a limited number of centroids per pixel in the reconstructed image of the slanted-edge, the noise-floor of both the green- and blue- MTFs display the effect of poor SNR, as discussed in section 2.3.2 and shown in Fig. 2.9. The error-bars were computed over ten datasets, each comprising 50,000 frames. Reproduced from [10].

6.5 Conclusion

In this chapter I have demonstrated a full-field, standard-quantum-limited imaging scheme for general non-fluorescing objects, operating in the photon-sparse regime (i.e. with less than 0.001 photon per pixel per frame, at 710nm). The presented imaging scheme is based on the estimation of the centroid positions of illuminating biphotons, detected by an electron-multiplying CCD camera, and used to reconstruct an image that is sharper by up to a factor of $\sqrt{N}$ (where $N = 2$ is the number of jointly detected spatially correlated photons).

Additionally, the CEBs approach to resolution-enhanced imaging allows to reduce the spreading of the PSF, in the current context induced by limited NA of the system used to image the object onto the detector. Similarly, other unwanted effects can cause a loss in resolution and thus a broadening of the PSF, such as defocus [254] or

turbulence [255]. In the case of turbulence, the resolution-enhancement produced by CEBs would rely on the sufficient detection of spatially correlated biphotons and on the fact the time scale of turbulence is typically longer than the correlation time of biphotons, i.e. $> 100fs$ [219].

It should be noted that better performing detectors, in terms of noise, quantum efficiency, and acquisition rate, could improve the feasibility of te CEBs scheme for real-world applications. For instance, a 256×256 pixel^2 and a 512×512 pixel^2 single-photon diode image sensors have recently been developed [256, 257] able to acquire binary photon-counted frames at a rate up to 100,000 frames per second. The combination of an encouraging 61% fill-factor of the 256×256 sensor and its pixel pitch similarly sized to current state-of-the-art EMCCD cameras, means that this type of detector may be compatible with existing quantum-enhanced imaging schemes, like those discussed in this thesis.

Chapter 7

Conclusion

SPDC has become one of the most useful sources of quantum states of light, allowing one to readily produce spatially correlated biphotons, as discussed in chapters 2 and 3. A model able to accurately reproduce the spatially resolved detection of biphotons by a photon-counting camera was discussed in chapter 4. In chapter 5, a sub-shot-noise shadow sensing scheme based on the detection of spatially anticorrelated biphotons was demonstrated, achieving a 17% improvement in the optical measurement of the position of a shadow over a classical equivalent scheme. Finally in chapter 6, the spatial correlations of biphotons were used to experimentally demonstrate a resolution enhanced quantum imaging scheme, achieving a 12% reduction in the size of the PSF.

In answer to the question raised at the beginning of this thesis, a quantum enhancement in real-world applications may be obtained by harnessing the spatial correlations of biphotons.

7.1 Comparison with other works

In this section I discuss the significance of the findings of this thesis for the sub-shot-noise shadow sensing scheme and for the resolution-enhanced quantum imaging schemes by CEBs, by comparing the achieved quantum enhancements with that demonstrated in other relevant works. Finally I point out peculiarities of the model discussed in chapter 4 with respect to other relevant models. The reader is redirected to the following review articles for a more comprehensive collection of achievements in the fields of quantum enhanced imaging and sensing [2, 110, 159, 258].

Sub-shot-noise shadow-sensing with quantum correlations

The quantum-enhanced shadow sensing scheme discussed in chapter 5 is based on the sub-shot-noise detection of spatially anticorrelated biphotons. Although no other previous work can be found in which the SPDC anticorrelated biphotons are used to enhance a shadow-sensor, there are a few seminal works that have demonstrated a quantum noise reduction based on the correlation measurement of the difference of the number of SPDC photons.

Jedrkiewicz et al. [52], Blanchet et al. [49], and Bolduc et al. [259] demonstrated a sub-shot-noise correlation measurements operating at 10, 0.15, up to 100 photons per pixel per frame respectively, and achieving a reduction of noise below the shot-noise limit of 25% (as gathered from visual inspection of the plotted results), 12% (as obtained by converting the employed SQL=2 value to SQL=1), and 8% respectively. In contrast, the sub-shot-noise scheme in this thesis operated at 0.14 photons per pixel per frame, achieving a reduction of noise below the shot-noise limit of 27%[1], as reported in Eq. 5.8 and shown in Fig. 5.9.

[1] The degree of correlation σ_{DOC} in the absence of a shadow casting object was chosen as the appropriate metric of sub-shot-noise performance for a fair comparison with the other cited works.

TABLE 7.1: **Comparison of sub-shot-noise schemes.** The sub-shot-noise performance achieved in relevant seminal works is compared to the one discussed in this thesis (i.e. Toninelli et al.). The QNR parameter is used to quantify the sub-shot-noise performance. *With subtraction of the noise variance of the detector. **Based on a split-detection scheme and in principle not requiring a spatially resolved detector.

	Light level $(e \cdot p^{-1} \cdot f^{-1})$	**QNR**	**Detector**
Jedrkiewicz et al.	10	25%*	CCD
Blanchet et al.	0.15	12%	EMCCD
Bolduc et al.	up to 100	8%	EMCCD
Toninelli et al.	0.14	27%	EMCCD**

Two additional important differences between these works should also be mentioned. Firstly, all of the mentioned seminal works achieve a noise reduction relying on the spatially resolved nature of the employed camera detector, whereas the shadow-sensing scheme featured in this thesis only requires a single-photon sensitive split-detector.

Secondly, all of the discussed works, with the exception of the one realised by Jedrkiewicz et al., achieve a sub-shot-noise enhancement without having to subtract the noise variance of the employed detector. When this detail is taken into consideration, it is clear that the noise reduction achieved by the shadow-sensing scheme is quantitatively greater (more than twice) than that achieved in the cited works. This may be due to the use of a newer detector with improved detection efficiency and better noise performance.

A summary of the various properties of these schemes can be found in table 7.1.

Resolution-enhanced quantum imaging by centroid estimation of biphotons

The standard quantum limited resolution enhancing scheme discussed in chapter 6 utilises the spatial correlations of SPDC biphotons, detected by a single-photon sensitive EMCCD camera, operating in a photon sparse regime. A summary of quantum

resolution-enhanced imaging schemes operating at both the SQL or HL is provided in section 1.3.1.

The CEBs scheme discussed in this thesis is related to other classical and quantum schemes that achieve a resolution advantage via a localisation or centroid measurement. Importantly, whereas localisation-based superresolution techniques operate by adding a point-like fluorescent source to the sample [260, 261], CEBs operates by projecting spatially quantum-correlated biphotons onto the sample. Both approaches, however, still rely on an optical centroid estimation measurement, with a precision that scales favourably with the square-root of the number of photons.

In terms of absolute resolution advantage, the performance of CEBs is limited by the number of spatially correlated photons involved in the centroid estimation. Due to the bipartite nature of the exploited biphoton quantum states, the maximum achievable resolution advantage is subject to the SQL and is bound to a $1/\sqrt{2}$ narrowing of the PSF, as discussed in section 6.1, Eq. 6.4.

Heisenberg limited schemes can instead produce a resolution advantage equal to a $1/N$ narrowing of the PSF, where N is the number of entangled photons per measurement. Recently, the first quantum-imaging scheme able to achieve an HL resolution-enhancement with an $N = 2$ NOON state and using a full-field scientific complementary metal oxide semiconductor (sCMOS) camera, was experimentally demonstrated by M. Unternährer et al. [262]. The scheme requires the object to be placed in the ultraviolet (UV) pump (i.e. before the nonlinear crystal) in order to produce the $N = 2$ NOON state and achieve a two-fold resolution enhancement in the image reconstructed using the infrared downconverted photons. A brief discussion of NOON states can be found in section 2.2.4.

Thus, whereas the Heisenberg limited resolution enhancement achieved by M. Unternährer et al. is $\sqrt{2}$ greater than the one achievable by the standard quantum

limited CEBs scheme, the extra advantage comes at the cost of having to illuminate the object with high energy UV photons. For this reason, the CEBs approach may be more appropriate for light-sensitive applications, due to the limited photon-dose used to illuminate the object. Specifically, even for a long time of 17 hours (as required to acquire 1M frames), the low-intensity regime of CEBs ensures that the resulting photon-dose is still only in the order of $0.1\mu J/mm^2$ (given a typical pump power of $3mW/mm^2$) [215, 263].

A model for the spatially resolved detection of biphotons

The performance of both quantum enhanced schemes featured in this thesis were further explored using the the numerical model described in chapter 4.

Previous seminal works have been concerned with the modelling of detector technology. The noise performance of ICCD and EMCCD cameras have been investigated, together with the optimisation of their signal-to-noise ratio (SNR), a description of their photon-counting statistics based on a Bayesian analysis of detected events [226, 230, 239, 249], and the absolute calibration of their detection efficiency using entangled light produced via a type-II and a type-I phase-matched crystal respectively [240, 264].

Whereas these works are concerned with the modelling of the detection mechanism of single-photon scientific cameras and their absolute calibration, the model discussed in chapter 4 is instead tailored for the simulation of entire quantum imaging and sensing schemes, based on the single-photon sensitive detection of biphotons produced by a type-I nonlinear crystal. The generality of this model, which is simple yet quantitatively accurate, was also extended to the detection of biphotons produced by a type-II crystal, as well as collinear and noncollinear phase matching conditions, as discussed in section 4.1.2 and 4.1.3.

Moreover, it was shown how the model can be used to extract quantitative information about the strength of detected quantum correlations. For example, it was shown how under constant illumination, it is possible to predict the decreased detection of spatially correlated biphotons, as a consequence of optical loss. These findings are particularly useful in the optimisation of the detection of quantum correlations, which determines the achievable quantum advantage of a certain scheme.

7.2 The 'quantumness' of the presented better-than-classical schemes

Whereas there is no doubt that the enhanced performance relies on the properties of quantum states of the employed SPDC photons, it may be useful to consider to what extent this performance relies on the 'quantumness' of the system. Entanglement and more specifically its associated 'spooky action at a distance' is often used to draw a clear distinction between classical and quantum phenomena. Below I adopt this inquisitive perspective in revisiting the experiments featured in this thesis, thus considering how *quantum* these quantum-enhanced schemes really are.

The photon-number correlations exploited in chapter 4 to achieve sub-shot-noise performance in the estimation of the position of a shadow rely on quantum correlations. These types of correlations, however, do not require the photons to be in a joint position-momentum quantum state. Thus, EPR entanglement is not a necessity. In fact, although the temporal correlations between the signal and idler photons are required to ensure photon-number correlations [265], from a spatial perspective, the transverse momenta correlations between the detected photons play a smaller role. Indeed, in the context of the shadow-sensing scheme, only transverse anticorrelations between the detected positions of biphotons and the photon-number correlations

(due to the nearly simultaneous production of signal and idler photons) are required, whereas the position correlations in the plane of the crystal not utilised.

However, sub-Poissonian photon-number correlations between two light beams (in this case between the signal and idler beams) cannot be classically achieved [160]. For this reason, the sub-shot-noise shadow-sensing scheme is a quantum-enhanced scheme, enabled by the temporal and spatial quantum correlations of its SPDC source. The fact that these same SPDC photons may well be in an EPR-entangled state is in this context redundant.

In the case of the resolution enhanced imaging scheme by CEBs in chapter 6, the advantage in resolution relies on the strong spatial correlations between signal and idler. As discussed in chapter 2 section 2.1.2 and chapter 3 section 3.1, the transverse positions of SPDC signal and idler photons of a biphoton packet are simultaneously spatially correlated and anticorrelated in the near- and far-field of the nonlinear crystal, according to the EPR inequality of their quantum state. It was also mentioned that in the classical regime such conditional correlation between position and momentum cannot be realised, meaning that a strong correlation in position would necessarily be accompanied by a less strong correlation in the momentum basis. The crucial point is thus whether the CEBs scheme requires the illuminating photons to be strongly correlated in both the position and momentum bases. In order to answer this question it may be useful to consider once more the role of these correlations within CEBs. It should also be recalled that the resolution degrading effects of diffraction on the detected transverse positions of the illuminating photons are due to both the interaction with sharp diffracting features of the object and to the limited NA of the imaging system.

Thus, according to the set-up described in chapter 6 section 6.2, the image plane of the crystal is re-imaged onto the object such that the transverse correlation width is as small as possible (achieved by using a de-magnifying telescope). This is necessary

so that both photons of a biphoton packet may probe the same feature of the object, therefore undergoing a similar diffraction process. After the interaction with the object the biphotons are once more re-imaged onto the spatially resolved detector by a resolution-degrading imaging system. In this case the loss in resolution is mainly due to the limited NA of the light collecting lenses (which in the CEBs realisation is accentuated by using a tunable aperture, placed in the far-field of both the object and the nonlinear crystal). The anticorrelated momenta of signal and idler photons mean that they propagate along 'reciprocal' spatial modes, separated by the same (although opposite) distance from the optical axis. Since a rotational symmetry around the optical axis can be assumed in the case of round lenses, it is then reasonable to also assume that both photons of a biphoton packet will be similarly affected by the limited NA of the system. It should be noted however, that in the case of aberrations that are exacerbated by non-paraxial modes (such as spherical aberration) having photons propagating through different modes (in terms of transverse distance from the optical axis) may cause some issues in the validity of the estimated centroid position. However, if the degradation in spatial resolution is mainly due to the limited NA of the imaging system, it may still be possible to achieve a resolution advantage, even in the case of photons that may only be spatially correlated in the position base.

7.3 Closing remarks and future work

The performance of the schemes featured in this thesis was shown to be limited by noise and losses, as explored by means of simulated models in each experimental chapter. However, another way of expressing this limitation is that the schemes actually manage to achieve a performance advantage *in spite* of noise and losses (albeit a proportionally smaller one).

For example, the noise performance of the shadow-sensing scheme was shown to beat the shot-noise-limit, even if both the light source and the detector suffered from excess noise, and even without subtracting the variance of these noise sources.

Moreover, in the case of CEBs, the final reconstructed image was described as the sum of two contributions: a resolution enhanced image (made of actual estimated centroids of spatially correlated events) and a classically-bound image (made of accidentally detected centroids of spatially uncorrelated events). The weighting of these contributions was shown to depend on the ratio between the number of correlated and uncorrelated events reaching the detectors, and thus on the amount of noise and losses affecting the imaging system. In terms of future work it may be interesting to investigate whether the full theoretically available SQL resolution advantage may be recovered by subtracting the uncorrelated image contribution from the final reconstructed image, leaving only the resolution enhanced contribution.

Finally, it may be possible to mimic the strong spatial correlations of downconverted photons using a structured classical light source, allowing one to exceed the $\sqrt{2}$ resolution advantage[2].

A quantum-inspired classical implementation would rely on an amplitude-only spatial light modulator (SLM) to reproduce both the multimodal properties of SPDC and the spatial correlations of the illuminating biphotons. Specifically, an intense, classical light-source would be used to illuminate an SLM, used in turn to create spatially correlated point-sources (not limited to two as in the case of biphotons), located randomly over the field of view. This realisation would rely on a Klyshko interpretation of the CEBs scheme, in which the nonlinear crystal is exchanged by a mirror and the multimode detector by a multimode light-source. Details about the Klyshko advanced wave picture can be found in his 1988 seminal paper [266].

[2]This classical implementation of CEBs was brainstormed together with colleagues P.-A. Moreau and N. Radwell.

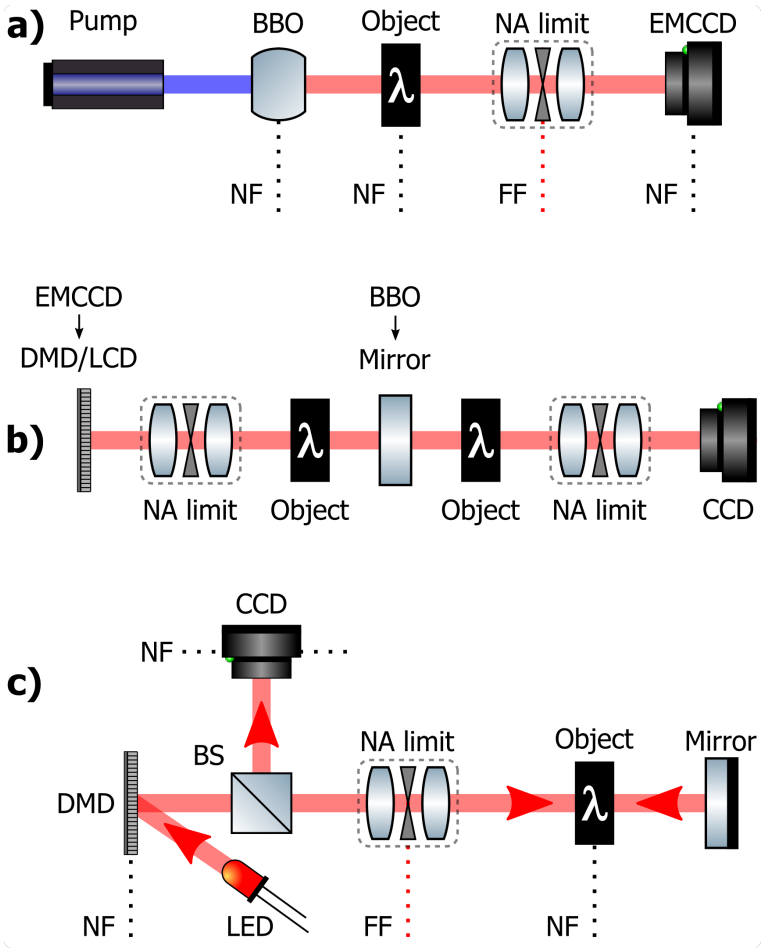

FIGURE 7.1: **Quantum inspired resolution enhanced imaging.** The near-field and far-field of the object are indicated by NF and FF respectively. An NA limited imaging system (such as a microscope) is represented by the dotted box labelled 'NA limit'. (a) Shows the configuration of the quantum imaging resolution-enhanced scheme based on CEBs; (b) is the Klyshko representation of (a) in which the BBO crystal and the spatially resolved detector have been replaced by a mirror and a multimode light-source: an LCD or a DMD. A possible realisation of the quantum-inspired scheme is shown in (c), where the spatial correlations of biphotons in the image plane of the BBO crystal are replaced by known point sources, i.e. individually activated mirrors of the DMD or lit pixels of a light-emitting LCD or LED array.

Both the original quantum implementation of CEBs and its Klyshko interpretation are respectively shown in Fig. 7.1(a) and (b).

As shown in Fig. 7.1(c) the multimodal light-source may be realised by means of a digital micromirror device (DMD) SLM or a light emitting liquid crystal display (LCD). Accordingly, a number of closely located mirrors (or pixels in the case of an LCD) would be 'switched-on', projecting on the object a number of point-like sources.

The produced intensity distributions would then be detected by a CCD camera and used to perform a centroid estimation, producing a resolution-enhanced image of the object.

This quantum-inspired scheme would aim at improving the performance of its quantum counterpart, which in the case of biphotons is bound to $1/\sqrt{N} = 1/\sqrt{2}$ reduction of the point-spread-function, where N is the number of jointly-detected photons per measurement. Unlike the quantum implementation, where it is very hard to reliably produce (and detect) multipartite systems with more than two photons, the proposed classical approach would be able to produce an arbitrary number of spatially correlated point-sources, which due to the intense light regime would also be readily detected. This ability to produce point-like sources in the plane of the object has fuelled numerous other resolution-enhanced techniques, which typically rely on optically induced fluorescence [56, 72]. For example, in the case of localisation-based super-resolution imaging techniques such as STED and GSD, the spatial correlations between photons necessary to perform a meaningful centroid measurement are realised using point-like sources, by adding fluorescent markers to the object [260, 267].

On the other hand, the proposed scheme would not rely on optically induced fluorescence of markers, since the spatially correlated point-like sources would be produced in the plane of the object using the combination of an intense source and a light-shaping SLM.

Appendix A

Extra information

A.1 Filters

Here are reported the transmission spectra of the filters used in the quantum-enhanced imaging and sensing schemes featured in this thesis.

A.1.1 Interference filter

Chroma custom-made interference filters (model: ET710/10BP) centered at 710nm with a 10nm wide transmission window were used to select the wavelength degenerate downconverted photons. The typical transmission spectrum of these filters is reported in Fig. A.1.

A.1.2 Dichroic filters

Chroma dichroic filters (model: T365lpxt) were used to remove the UV-pump after the nonlinear crystal. The typical transmission spectrum of these filters is reported in Fig. A.2.

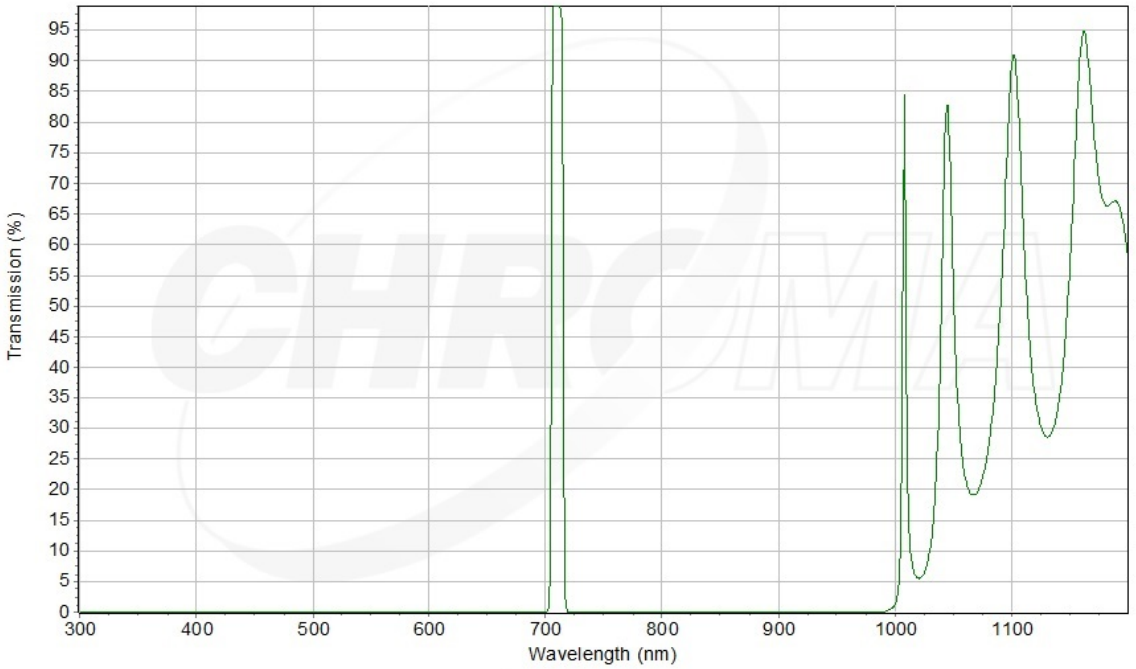

FIGURE A.1: **Typical transmission spectrum of ET710/10BP filters.**

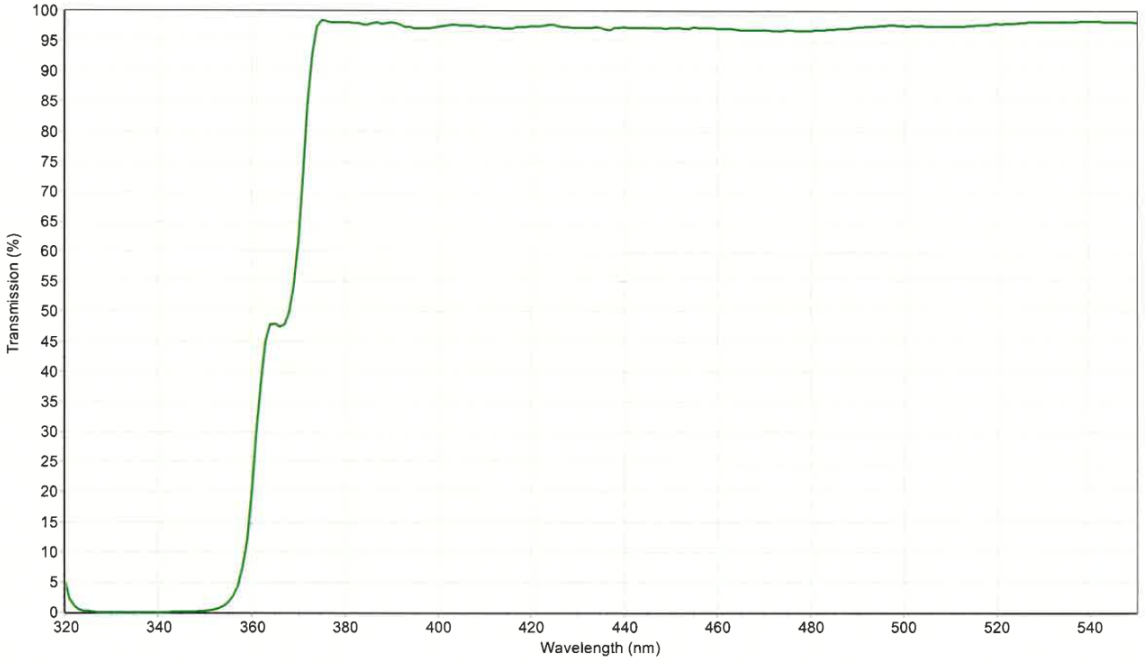

FIGURE A.2: **Typical transmission spectrum of T365lpxt filters.**

A.2 Extra derivations

Here are reported intermediate steps linking Eq. 2.17 and 2.20, as introduced and defined in chapter 2.

Starting from:

$$\begin{aligned} \langle \mathcal{C} \rangle &= \left\langle N_t^2 \right\rangle = \left\langle (N_s + 2N_p)^2 \right\rangle && \text{(A.1)} \\ &= \left\langle N_s^2 + 4N_p^2 + 4N_s N_p \right\rangle && \text{(A.2)} \\ &= \left\langle N_s^2 \right\rangle + 4\left\langle N_p^2 \right\rangle + 4\left\langle N_s N_p \right\rangle && \text{(A.3)} \end{aligned}$$

by definition it can be identified that:

$$\mathrm{Var}(N_s) = \left\langle N_s^2 \right\rangle - \langle N_s \rangle^2 \quad \text{(A.4)}$$

and:

$$\mathrm{Var}(N_p) = \left\langle N_p^2 \right\rangle - \langle N_p \rangle^2 , \quad \text{(A.5)}$$

where Var indicates the statistical variance operation.

Since both quantities follow Poissonian statistics, one has:

$$\begin{aligned} \left\langle N_s^2 \right\rangle &= \mathrm{Var}(N_s) + \langle N_s \rangle^2 && \text{(A.6)} \\ &= \langle N_s \rangle + \langle N_s \rangle^2 . && \text{(A.7)} \end{aligned}$$

The same applies for p:

$$\begin{aligned} \left\langle N_p^2 \right\rangle &= \mathrm{Var}(N_p) + \langle N_p \rangle^2 && \text{(A.8)} \\ &= \langle N_p \rangle + \langle N_p \rangle^2 . && \text{(A.9)} \end{aligned}$$

Moreover because N_p and N_s are independent (i.e. loss processes are random and no common temporal laser fluctuation are present):

$$\langle N_s N_p \rangle = \langle N_s \rangle \langle N_p \rangle . \tag{A.10}$$

Thus, using eq. (A.7),(A.9) and(A.10) in (A.3) one can find that:

$$\begin{aligned}
\langle \mathcal{C} \rangle &= \left\langle N_s^2 \right\rangle + 4 \left\langle N_p^2 \right\rangle + 4 \langle N_s N_p \rangle && \text{(A.11)} \\
&= \langle N_s \rangle + \langle N_s \rangle^2 + 4(\langle N_p \rangle + \langle N_p \rangle^2) + 4 \langle N_s N_p \rangle && \text{(A.12)} \\
&= \langle N_s \rangle + \langle N_s \rangle^2 + 4(\langle N_p \rangle + \langle N_p \rangle^2) + 4 \langle N_s \rangle \langle N_p \rangle && \text{(A.13)} \\
&= (\langle N_s \rangle^2 + 4 \langle N_p \rangle^2 + 4 \langle N_s \rangle \langle N_p \rangle) + (\langle N_s \rangle + 2 \langle N_p \rangle) + 2 \langle N_p \rangle && \text{(A.14)} \\
&= \langle N_t \rangle^2 + \langle N_t \rangle + 2 \langle N_p \rangle . && \text{(A.15)}
\end{aligned}$$

Indeed, going from (A.14) to (A.15) one finds:

$$\begin{aligned}
\langle N_t \rangle^2 &= \langle N_s + 2N_p \rangle^2 && \text{(A.16)} \\
&= (\langle N_s \rangle + 2 \langle N_p \rangle)^2 && \text{(A.17)} \\
&= \langle N_s \rangle^2 + 4 \langle N_p \rangle^2 + 4 \langle N_s \rangle \langle N_p \rangle . && \text{(A.18)}
\end{aligned}$$

Finally, as in Eq. 2.20 one has:

$$\langle \mathcal{C} \rangle = \langle N_t \rangle^2 + \langle N_t \rangle + \sum_{\boldsymbol{\rho}} \mathcal{C}_q(\boldsymbol{\rho}), \tag{A.19}$$

by using equation (A.15) here and Eq. 2.13 from chapter 2.

If one assumes that $\mathcal{C} = N_t^2$, an interesting question is whether $\langle \mathcal{C} \rangle = \langle N_t^2 \rangle$ is constant regardless of the number of pairs. Arguably, this may not be the case, since $\langle \mathcal{C} \rangle$ depends on the statistics of N_t, which determines the fluctuation in the total number of photons from one captured frame to the other.

Moreover, in the case of only singles being detected (i.e in the case of high loss), then $N_t = N_s$ and therefore the process would be described by Poissonian statistics, according to:

$$\langle \mathcal{C} \rangle = \left\langle N_t^2 \right\rangle = \langle N_t \rangle^2 + \mathrm{Var}(N_t) = \langle N_t \rangle^2 + \langle N_t \rangle \tag{A.20}$$

On the other hand, in the case of ideal detection efficiency, N_t would no longer be Poissonian because the photons would in that case arrive two-by-two. This would imply that: $N_t = 2N_p$, where N_p *only* is Poissonian, but not N_t. In this case it can be found that:

$$\begin{aligned} \langle \mathcal{C} \rangle &= \left\langle N_t^2 \right\rangle = \langle N_t \rangle^2 + \mathrm{Var}(N_t) && \text{(A.21)} \\ &= \langle N_t \rangle^2 + 4\ \mathrm{Var}(N_p) && \text{(A.22)} \\ &= \langle N_t \rangle^2 + 4N_p && \text{(A.23)} \\ &= \langle N_t \rangle^2 + \langle N_t \rangle + 2N_p. && \text{(A.24)} \end{aligned}$$

Bibliography

[1] Vittorio Giovannetti, Seth Lloyd, and Lorenzo Maccone. Quantum-Enhanced Measurements: Beating the Standard Quantum Limit. *Science*, 306(5700): 1330–1336, November 2004. ISSN 0036-8075, 1095-9203. doi: 10.1126/science.1104149. URL http://science.sciencemag.org/content/306/5700/1330.

[2] Marco Genovese. Real applications of quantum imaging. *J. Opt.*, 18(7):073002, 2016. ISSN 2040-8986. doi: 10.1088/2040-8978/18/7/073002. URL http://stacks.iop.org/2040-8986/18/i=7/a=073002.

[3] Girish Agarwal, Roland E. Allen, Iva Bezděková, Robert W. Boyd, Goong Chen, Ronald Hanson, Dean L. Hawthorne, Philip Hemmer, Moochan B. Kim, Olga Kocharovskaya, David M. Lee, Sebastian K. Lidström, Suzy Lidström, Harald Losert, Helmut Maier, John W. Neuberger, Miles J. Padgett, Mark Raizen, Surjeet Rajendran, Ernst Rasel, Wolfgang P. Schleich, Marlan O. Scully, Gavriil Shchedrin, Gennady Shvets, Alexei V. Sokolov, Anatoly Svidzinsky, Ronald L. Walsworth, Rainer Weiss, Frank Wilczek, Alan E. Willner, Eli Yablonovitch, and Nikolay Zheludev. Light, the universe and everything – 12 Herculean tasks for quantum cowboys and black diamond skiers. *J. Mod. Opt.*, 65(11):1261–1308, June 2018. ISSN 0950-0340. doi: 10.1080/09500340.2018.1454525. URL https://doi.org/10.1080/09500340.2018.1454525.

[4] M.P. Edgar, D.S. Tasca, F. Izdebski, R.E. Warburton, J. Leach, M. Agnew, G.S. Buller, R.W. Boyd, and M.J. Padgett. Imaging high-dimensional spatial

entanglement with a camera. *Nat. Commun.*, 3:984, August 2012. ISSN 2041-1723. doi: 10.1038/ncomms1988. URL http://www.nature.com/doifinder/10.1038/ncomms1988.

[5] Peter A. Morris, Reuben S. Aspden, Jessica E. C. Bell, Robert W. Boyd, and Miles J. Padgett. Imaging with a small number of photons. *Nat. Commun.*, 6: 5913, 2015. ISSN 2041-1723. doi: 10.1038/ncomms6913. URL http://www.nature.com/ncomms/2015/150105/ncomms6913/full/ncomms6913.html.

[6] Reuben S. Aspden, Peter A. Morris, Ruiqing He, Qian Chen, and Miles J. Padgett. Heralded phase-contrast imaging using an orbital angular momentum phase-filter. *J. Opt.*, 18(5):055204, 2016. URL http://stacks.iop.org/2040-8986/18/i=5/a=055204.

[7] Ermes Toninelli, Matthew P Edgar, Paul-Antoine Moreau, Graham M Gibson, Giles D Hammond, and Miles J Padgett. Quantum position measurement of a shadow: Beating the classical limit. In *Frontiers in Optics*, pages FTu5E–3. Optical Society of America, 2017. doi: https://doi.org/10.1364/FIO.2017.FTu5E.3.

[8] E. Toninelli, P.-A. Moreau, A. Mihalyi, T. Gregory, M. P. Edgar, and M. J. Padgett. Resolution-enhanced imaging with quantum correlations. In *CLEO*, Conference on Lasers and Electro-Optics, page FF1B.1. Optical Society of America, 2018. doi: 10.1364/CLEO_QELS.2018.FF1B.1. URL http://www.osapublishing.org/abstract.cfm?URI=CLEO_QELS-2018-FF1B.1.

[9] Ermes Toninelli, Matthew P. Edgar, Paul-Antoine Moreau, Graham M. Gibson, Giles D. Hammond, and Miles J. Padgett. Sub-shot-noise shadow sensing with quantum correlations. *Opt. Express, OE*, 25(18):21826–21840, September 2017. ISSN 1094-4087. doi: 10.1364/OE.25.021826. URL https://www.osapublishing.org/abstract.cfm?uri=oe-25-18-21826.

[10] Ermes Toninelli, Paul-Antoine Moreau, Thomas Gregory, Adam Mihalyi, Matthew Edgar, Neal Radwell, and Miles Padgett. Resolution-enhanced quantum imaging by centroid estimation of biphotons. *Optica, OPTICA*, 6(3):347–353, March 2019. ISSN 2334-2536. doi: 10.1364/OPTICA.6.000347. URL https://www.osapublishing.org/optica/abstract.cfm?uri=optica-6-3-347.

[11] L. Carbone, S. M. Aston, R. M. Cutler, A. Freise, J. Greenhalgh, J. Heefner, D. Hoyland, N. A. Lockerbie, D. Lodhia, N. A. Robertson, C. C. Speake, K. A. Strain, and A. Vecchio. Sensors and actuators for the Advanced LIGO mirror suspensions. *Class. Quantum Grav.*, 29(11):115005, May 2012. ISSN 0264-9381. doi: 10.1088/0264-9381/29/11/115005. URL https://doi.org/10.1088%2F0264-9381%2F29%2F11%2F115005.

[12] R. P. Middlemiss, A. Samarelli, D. J. Paul, J. Hough, S. Rowan, and G. D. Hammond. Measurement of the Earth tides with a MEMS gravimeter. *Nature*, 531(7596):614–617, March 2016. ISSN 0028-0836. URL http://dx.doi.org/10.1038/nature17397.

[13] Richard P Middlemiss, Steven G Bramsiepe, Rebecca Douglas, James Hough, Douglas J Paul, Sheila Rowan, and Giles D Hammond. Field tests of a portable MEMS gravimeter. *Sensors*, 17(11):2571, 2017. URL https://dx.doi.org/10.3390/s17112571.

[14] S. G. Bramsiepe, D. Loomes, R. P. Middlemiss, D. J. Paul, and G. D. Hammond. A High Stability Optical Shadow Sensor With Applications for Precision Accelerometers. *IEEE Sens. J.*, 18(10):4108–4116, May 2018. ISSN 1530-437X. doi: 10.1109/JSEN.2018.2818066. URL https://ieeexplore.ieee.org/abstract/document/8320787.

[15] C. L. Degen, F. Reinhard, and P. Cappellaro. Quantum sensing. *Rev. Mod. Phys.*, 89(3):035002, July 2017. doi: 10.1103/RevModPhys.89.035002. URL https://link.aps.org/doi/10.1103/RevModPhys.89.035002.

[16] J. Abadie, Benjamin P. Abbott, Richard S. Abbott, Thomas D. Abbott, Matthew Robert Abernathy, and and others. A gravitational wave observatory operating beyond the quantum shot-noise limit. *Nat. Phys.*, 7(12):962–965, 2011. ISSN 1745-2473. doi: 10.1038/nphys2083. URL https://research.monash.edu/en/publications/a-gravitational-wave-observatory-operating-beyond-the-quantum-sho.

[17] J Aasi, J Abadie, BP Abbott, R Abbott, TD Abbott, MR Abernathy, C Adams, Thomas Adams, P Addesso, RX Adhikari, et al. Enhanced sensitivity of the LIGO gravitational wave detector by using squeezed states of light. *Nat. Photonics*, 7(8):613–619, 2013. URL https://www.nature.com/articles/nphoton.2013.177.

[18] Ulrik L. Andersen, Tobias Gehring, Christoph Marquardt, and Gerd Leuchs. 30 years of squeezed light generation. *Phys. Scr.*, 91(5):053001, April 2016. ISSN 1402-4896. doi: 10.1088/0031-8949/91/5/053001. URL https://doi.org/10.1088%2F0031-8949%2F91%2F5%2F053001.

[19] Roman Schnabel. Squeezed states of light and their applications in laser interferometers. *Phys. Rep.*, 684:1–51, 2017. ISSN 0370-1573. doi: https://doi.org/10.1016/j.physrep.2017.04.001. URL http://www.sciencedirect.com/science/article/pii/S0370157317300595. Squeezed states of light and their applications in laser interferometers.

[20] L. Mandel. Physical Significance of Operators in Quantum Optics. *Phys. Rev.*, 136(4B):B1221–B1224, November 1964. doi: 10.1103/PhysRev.136.B1221. URL https://link.aps.org/doi/10.1103/PhysRev.136.B1221.

[21] David Stoler. Photon Antibunching and Possible Ways to Observe It. *Phys. Rev. Lett.*, 33(23):1397–1400, December 1974. doi: 10.1103/PhysRevLett.33.1397. URL https://link.aps.org/doi/10.1103/PhysRevLett.33.1397.

[22] James N. Hollenhorst. Quantum limits on resonant-mass gravitational-radiation detectors. *Phys. Rev. D*, 19(6):1669–1679, March 1979. doi: 10.1103/PhysRevD.19.1669. URL https://link.aps.org/doi/10.1103/PhysRevD.19.1669.

[23] Carlton M. Caves. Quantum-mechanical noise in an interferometer. *Phys. Rev. D*, 23(8):1693–1708, April 1981. doi: 10.1103/PhysRevD.23.1693. URL https://link.aps.org/doi/10.1103/PhysRevD.23.1693.

[24] J. J. Snyder, E. Giacobino, C. Fabre, A. Heidmann, and M. Ducloy. Sub-shot-noise measurements using the beat note between quantum-correlated photon beams. *J. Opt. Soc. Am. B, JOSAB*, 7(10):2132–2136, October 1990. ISSN 1520-8540. doi: 10.1364/JOSAB.7.002132. URL https://www.osapublishing.org/josab/abstract.cfm?uri=josab-7-10-2132.

[25] P. R. Tapster, S. F. Seward, and J. G. Rarity. Sub-shot-noise measurement of modulated absorption using parametric down-conversion. *Phys. Rev. A*, 44(5):3266–3269, September 1991. doi: 10.1103/PhysRevA.44.3266. URL https://link.aps.org/doi/10.1103/PhysRevA.44.3266.

[26] R. E. Slusher, P. Grangier, A. LaPorta, B. Yurke, and M. J. Potasek. Pulsed Squeezed Light. *Phys. Rev. Lett.*, 59(22):2566–2569, November 1987. doi: 10.1103/PhysRevLett.59.2566. URL https://link.aps.org/doi/10.1103/PhysRevLett.59.2566.

[27] Prem Kumar, Orhan Aytür, and Jianming Huang. Squeezed-light generation with an incoherent pump. *Phys. Rev. Lett.*, 64(9):1015–1018, February

1990. doi: 10.1103/PhysRevLett.64.1015. URL https://link.aps.org/doi/10.1103/PhysRevLett.64.1015.

[28] Yun Zhang, Hai Wang, Xiaoying Li, Jietai Jing, Changde Xie, and Kunchi Peng. Experimental generation of bright two-mode quadrature squeezed light from a narrow-band nondegenerate optical parametric amplifier. *Phys. Rev. A*, 62(2):023813, July 2000. doi: 10.1103/PhysRevA.62.023813. URL https://link.aps.org/doi/10.1103/PhysRevA.62.023813.

[29] Chonghoon Kim and Prem Kumar. Quadrature-Squeezed Light Detection Using a Self-Generated Matched Local Oscillator. *Phys. Rev. Lett.*, 73(12): 1605–1608, September 1994. doi: 10.1103/PhysRevLett.73.1605. URL https://link.aps.org/doi/10.1103/PhysRevLett.73.1605.

[30] Carlton M. Caves, Kip S. Thorne, Ronald W. P. Drever, Vernon D. Sandberg, and Mark Zimmermann. On the measurement of a weak classical force coupled to a quantum-mechanical oscillator. I. Issues of principle. *Rev. Mod. Phys.*, 52(2):341–392, April 1980. doi: 10.1103/RevModPhys.52.341. URL https://link.aps.org/doi/10.1103/RevModPhys.52.341.

[31] Min Xiao, Ling-An Wu, and H. J. Kimble. Detection of amplitude modulation with squeezed light for sensitivity beyond the shot-noise limit. *Opt. Lett., OL*, 13(6):476–478, June 1988. ISSN 1539-4794. doi: 10.1364/OL.13.000476. URL https://www.osapublishing.org/ol/abstract.cfm?uri=ol-13-6-476.

[32] S. Machida, Y. Yamamoto, and Y. Itaya. Observation of amplitude squeezing in a constant-current–driven semiconductor laser. *Phys. Rev. Lett.*, 58(10): 1000–1003, March 1987. doi: 10.1103/PhysRevLett.58.1000. URL https://link.aps.org/doi/10.1103/PhysRevLett.58.1000.

[33] W. H. Richardson and R. M. Shelby. Nonclassical light from a semiconductor laser operating at 4 K. *Phys. Rev. Lett.*, 64(4):400–403, January

1990. doi: 10.1103/PhysRevLett.64.400. URL https://link.aps.org/doi/10.1103/PhysRevLett.64.400.

[34] M. J. Freeman, H. Wang, D. G. Steel, R. Craig, and D. R. Scifres. Wavelength-tunable amplitude-squeezed light from a room-temperature quantum-well laser. *Opt. Lett., OL*, 18(24):2141–2143, December 1993. ISSN 1539-4794. doi: 10.1364/OL.18.002141. URL https://www.osapublishing.org/ol/abstract.cfm?uri=ol-18-24-2141.

[35] W. H. Richardson, S. Machida, and Y. Yamamoto. Squeezed photon-number noise and sub-Poissonian electrical partition noise in a semiconductor laser. *Phys. Rev. Lett.*, 66(22):2867–2870, June 1991. doi: 10.1103/PhysRevLett.66.2867. URL https://link.aps.org/doi/10.1103/PhysRevLett.66.2867.

[36] N. Treps, U. Andersen, B. Buchler, P. K. Lam, A. Maître, H.-A. Bachor, and C. Fabre. Surpassing the Standard Quantum Limit for Optical Imaging Using Nonclassical Multimode Light. *Phys. Rev. Lett.*, 88(20):203601, May 2002. doi: 10.1103/PhysRevLett.88.203601. URL http://link.aps.org/doi/10.1103/PhysRevLett.88.203601.

[37] Nicolas Treps, Nicolai Grosse, Warwick P. Bowen, Claude Fabre, Hans-A. Bachor, and Ping Koy Lam. A Quantum Laser Pointer. *Science*, 301 (5635):940–943, 2003. ISSN 0036-8075. doi: 10.1126/science.1086489. URL http://science.sciencemag.org/content/301/5635/940.

[38] Katherine Wagner, Jiri Janousek, Vincent Delaubert, Hongxin Zou, Charles Harb, Nicolas Treps, Jean François Morizur, Ping Koy Lam, and Hans A. Bachor. Entangling the Spatial Properties of Laser Beams. *Science*, 321(5888):541–543, July 2008. ISSN 0036-8075, 1095-9203. doi: 10.1126/science.1159663. URL http://science.sciencemag.org/content/321/5888/541.

[39] Vincent Boyer, Alberto M. Marino, Raphael C. Pooser, and Paul D. Lett. Entangled Images from Four-Wave Mixing. *Science*, 321(5888):544–547, July 2008. ISSN 0036-8075, 1095-9203. doi: 10.1126/science.1158275. URL http://science.sciencemag.org/content/321/5888/544.

[40] M. Lassen, G. Leuchs, and U. L. Andersen. Continuous Variable Entanglement and Squeezing of Orbital Angular Momentum States. *Phys. Rev. Lett.*, 102 (16):163602, April 2009. doi: 10.1103/PhysRevLett.102.163602. URL https://link.aps.org/doi/10.1103/PhysRevLett.102.163602.

[41] Henning Vahlbruch, Moritz Mehmet, Karsten Danzmann, and Roman Schnabel. Detection of 15 dB Squeezed States of Light and their Application for the Absolute Calibration of Photoelectric Quantum Efficiency. *Phys. Rev. Lett.*, 117(11):110801, September 2016. doi: 10.1103/PhysRevLett.117.110801. URL http://link.aps.org/doi/10.1103/PhysRevLett.117.110801.

[42] S.P. Walborn, C.H. Monken, S. Pádua, and P.H. Souto Ribeiro. Spatial correlations in parametric down-conversion. *Phys. Rep.*, 495(4-5):87–139, October 2010. ISSN 03701573. doi: 10.1016/j.physrep.2010.06.003. URL http://linkinghub.elsevier.com/retrieve/pii/S0370157310001602.

[43] Orhan Aytür and Prem Kumar. Pulsed twin beams of light. *Phys Rev Lett*, 65(13):1551–1554, September 1990. doi: 10.1103/PhysRevLett.65.1551. URL http://link.aps.org/doi/10.1103/PhysRevLett.65.1551.

[44] J. G. Rarity, P. R. Tapster, and E. Jakeman. Observation of sub-poissonian light in parametric downconversion. *Optics Communications*, 62(3):201–206, May 1987. ISSN 0030-4018. doi: 10.1016/0030-4018(87)90028-9. URL http://www.sciencedirect.com/science/article/pii/0030401887900289.

[45] C. D. Nabors and R. M. Shelby. Two-color squeezing and sub-shot-noise signal recovery in doubly resonant optical parametric oscillators. *Phys. Rev. A*, 42

(1):556–559, July 1990. doi: 10.1103/PhysRevA.42.556. URL https://link.aps.org/doi/10.1103/PhysRevA.42.556.

[46] P. H. Souto Ribeiro, C. Schwob, A. Maître, and C. Fabre. Sub-shot-noise high-sensitivity spectroscopy with optical parametric oscillator twin beams. *Opt. Lett., OL*, 22(24):1893–1895, December 1997. ISSN 1539-4794. doi: 10.1364/OL.22.001893. URL https://www.osapublishing.org/ol/abstract.cfm?uri=ol-22-24-1893.

[47] Maria Bondani, Alessia Allevi, Guido Zambra, Matteo G. A. Paris, and Alessandra Andreoni. Sub-shot-noise photon-number correlation in a mesoscopic twin beam of light. *Phys. Rev. A*, 76(1):013833, July 2007. doi: 10.1103/PhysRevA.76.013833. URL https://link.aps.org/doi/10.1103/PhysRevA.76.013833.

[48] Timur Iskhakov, Maria V. Chekhova, and Gerd Leuchs. Generation and Direct Detection of Broadband Mesoscopic Polarization-Squeezed Vacuum. *Phys. Rev. Lett.*, 102(18):183602, May 2009. doi: 10.1103/PhysRevLett.102.183602. URL https://link.aps.org/doi/10.1103/PhysRevLett.102.183602.

[49] Jean-Luc Blanchet, Fabrice Devaux, Luca Furfaro, and Eric Lantz. Measurement of Sub-Shot-Noise Correlations of Spatial Fluctuations in the Photon-Counting Regime. *Phys. Rev. Lett.*, 101(23):233604, December 2008. doi: 10.1103/PhysRevLett.101.233604. URL http://link.aps.org/doi/10.1103/PhysRevLett.101.233604.

[50] Jean-Luc Blanchet, Fabrice Devaux, Luca Furfaro, and Eric Lantz. Purely spatial coincidences of twin photons in parametric spontaneous down-conversion. *Phys. Rev. A*, 81(4):043825, April 2010. doi: 10.1103/PhysRevA.81.043825. URL http://link.aps.org/doi/10.1103/PhysRevA.81.043825.

[51] A. Heidmann, R. J. Horowicz, S. Reynaud, E. Giacobino, C. Fabre, and G. Camy. Observation of Quantum Noise Reduction on Twin Laser Beams. *Phys. Rev. Lett.*, 59(22):2555–2557, November 1987. doi: 10.1103/PhysRevLett.59.2555. URL https://link.aps.org/doi/10.1103/PhysRevLett.59.2555.

[52] O. Jedrkiewicz, Y.-K Jiang, E. Brambilla, A. Gatti, M. Bache, L. A. Lugiato, and P. Di Trapani. Detection of Sub-Shot-Noise Spatial Correlation in High-Gain Parametric Down Conversion. *Phys. Rev. Lett.*, 93(24):243601, December 2004. doi: 10.1103/PhysRevLett.93.243601. URL http://link.aps.org/doi/10.1103/PhysRevLett.93.243601.

[53] Kevin Lyons, Shengshi Pang, Paul G. Kwiat, and Andrew N. Jordan. Precision optical displacement measurements using biphotons. *Phys. Rev. A*, 93(4):043841, April 2016. doi: 10.1103/PhysRevA.93.043841. URL http://link.aps.org/doi/10.1103/PhysRevA.93.043841.

[54] G. Brida, M. Genovese, and I. Ruo Berchera. Experimental realization of sub-shot-noise quantum imaging. *Nat. Photon.*, 4(4):227–230, April 2010. ISSN 1749-4885, 1749-4893. doi: 10.1038/nphoton.2010.29. URL http://www.nature.com/doifinder/10.1038/nphoton.2010.29.

[55] Sung Cheol Park, Min Kyu Park, and Moon Gi Kang. Super-resolution image reconstruction: A technical overview. *IEEE Signal Process. Mag.*, 20(3):21–36, 2003. URL https://doi.org/10.1109/MSP.2003.1203207.

[56] Stefan W. Hell and Jan Wichmann. Breaking the diffraction resolution limit by stimulated emission: Stimulated-emission-depletion fluorescence microscopy. *Opt. Lett., OL*, 19(11):780–782, June 1994. ISSN 1539-4794. doi: 10.1364/OL.19.000780. URL https://www.osapublishing.org/ol/abstract.cfm?uri=ol-19-11-780.

[57] S. W. Hell and M. Kroug. Ground-state-depletion fluorscence microscopy: A concept for breaking the diffraction resolution limit. *Appl. Phys. B*, 60(5):495–497, May 1995. ISSN 0946-2171, 1432-0649. doi: 10.1007/BF01081333. URL https://link.springer.com/article/10.1007/BF01081333.

[58] Eric Betzig, George H Patterson, Rachid Sougrat, O Wolf Lindwasser, Scott Olenych, Juan S Bonifacino, Michael W Davidson, Jennifer Lippincott-Schwartz, and Harald F Hess. Imaging intracellular fluorescent proteins at nanometer resolution. *Science*, 313(5793):1642–1645, 2006. URL http://science.sciencemag.org/content/313/5793/1642.

[59] Michael J. Rust, Mark Bates, and Xiaowei Zhuang. Sub-diffraction-limit imaging by stochastic optical reconstruction microscopy (STORM). *Nat. Methods*, 3(10):793–796, October 2006. ISSN 1548-7105. doi: 10.1038/nmeth929. URL https://www.nature.com/articles/nmeth929.

[60] Fabian Göttfert, Christian A Wurm, Veronika Mueller, Sebastian Berning, Volker C Cordes, Alf Honigmann, and Stefan W Hell. Coaligned dual-channel STED nanoscopy and molecular diffusion analysis at 20 nm resolution. *Biophys. J.*, 105(1):L01–L3, July 2013. ISSN 1542-0086. doi: 10.1016/j.bpj.2013.05.029. URL https://www.ncbi.nlm.nih.gov/pubmed/23823248.

[61] Janina Hanne, Henning J. Falk, Frederik Görlitz, Patrick Hoyer, Johann Engelhardt, Steffen J. Sahl, and Stefan W. Hell. STED nanoscopy with fluorescent quantum dots. *Nat. Commun.*, 6:7127, May 2015. ISSN 2041-1723. doi: 10.1038/ncomms8127. URL https://www.nature.com/articles/ncomms8127.

[62] Sina Wäldchen, Julian Lehmann, Teresa Klein, Sebastian van de Linde, and Markus Sauer. Light-induced cell damage in live-cell super-resolution microscopy. *Sci. Rep.*, 5:15348, October 2015. ISSN 2045-2322. doi: 10.1038/srep15348. URL https://www.nature.com/articles/srep15348.

[63] Fabrizio Guerrieri, Lorenzo Maccone, Franco N. C. Wong, Jeffrey H. Shapiro, Simone Tisa, and Franco Zappa. Sub-Rayleigh Imaging via N-Photon Detection. *Phys. Rev. Lett.*, 105(16):163602, October 2010. doi: 10.1103/PhysRevLett.105.163602. URL https://link.aps.org/doi/10.1103/PhysRevLett.105.163602.

[64] Joo-Eon Oh, Young-Wook Cho, Giuliano Scarcelli, and Yoon-Ho Kim. Sub-Rayleigh imaging via speckle illumination. *Opt. Lett., OL*, 38(5):682–684, March 2013. ISSN 1539-4794. doi: 10.1364/OL.38.000682. URL https://www.osapublishing.org/abstract.cfm?uri=ol-38-5-682.

[65] Yan-Hua Zhai, Xi-Hao Chen, Da Zhang, and Ling-An Wu. Two-photon interference with true thermal light. *Phys. Rev. A*, 72(4):043805, October 2005. doi: 10.1103/PhysRevA.72.043805. URL https://link.aps.org/doi/10.1103/PhysRevA.72.043805.

[66] Yanhua Zhai, Francisco E. Becerra, Jingyun Fan, and Alan Migdall. Direct measurement of sub-wavelength interference using thermal light and photon-number-resolved detection. *Appl. Phys. Lett.*, 105(10):101104, September 2014. ISSN 0003-6951. doi: 10.1063/1.4895101. URL http://aip.scitation.org/doi/10.1063/1.4895101.

[67] Vittorio Giovannetti, Seth Lloyd, Lorenzo Maccone, and Jeffrey H. Shapiro. Sub-Rayleigh-diffraction-bound quantum imaging. *Phys. Rev. A*, 79(1):013827, January 2009. doi: 10.1103/PhysRevA.79.013827. URL https://link.aps.org/doi/10.1103/PhysRevA.79.013827.

[68] Sara Mouradian, Franco N. C. Wong, and Jeffrey H. Shapiro. Achieving sub-Rayleigh resolution via thresholding. *Opt. Express, OE*, 19(6):5480–5488, March 2011. ISSN 1094-4087. doi: 10.1364/OE.19.005480. URL https://www.osapublishing.org/abstract.cfm?uri=oe-19-6-5480.

[69] Agedi N. Boto, Pieter Kok, Daniel S. Abrams, Samuel L. Braunstein, Colin P. Williams, and Jonathan P. Dowling. Quantum Interferometric Optical Lithography: Exploiting Entanglement to Beat the Diffraction Limit. *Phys. Rev. Lett.*, 85(13):2733–2736, September 2000. doi: 10.1103/PhysRevLett.85.2733. URL https://link.aps.org/doi/10.1103/PhysRevLett.85.2733.

[70] Osip Schwartz, Jonathan M Levitt, Ron Tenne, Stella Itzhakov, Zvicka Deutsch, and Dan Oron. Superresolution microscopy with quantum emitters. *Nano Lett.*, 13(12):5832–5836, 2013. URL http://dx.doi.org/10.1021/nl402552m.

[71] O. Schwartz and D. Oron. Improved resolution in fluorescence microscopy using quantum correlations. *Phys. Rev. A*, 85(3):033812, March 2012. doi: 10.1103/PhysRevA.85.033812. URL https://link.aps.org/doi/10.1103/PhysRevA.85.033812.

[72] Osip Schwartz, Jonathan M. Levitt, Ron Tenne, Stella Itzhakov, Zvicka Deutsch, and Dan Oron. Superresolution Microscopy with Quantum Emitters. *Nano Lett.*, 13(12):5832–5836, December 2013. ISSN 1530-6984. doi: 10.1021/nl402552m. URL http://dx.doi.org/10.1021/nl402552m.

[73] Yonatan Israel, Ron Tenne, Dan Oron, and Yaron Silberberg. Quantum correlation enhanced super-resolution localization microscopy enabled by a fibre bundle camera. *Nat. Commun.*, 8:14786, March 2017. ISSN 2041-1723. doi: 10.1038/ncomms14786. URL https://www.nature.com/articles/ncomms14786.

[74] Jin-Ming Cui, Fang-Wen Sun, Xiang-Dong Chen, Zhao-Jun Gong, and Guang-Can Guo. Quantum Statistical Imaging of Particles without Restriction of the Diffraction Limit. *Phys. Rev. Lett.*, 110:153901, April 2013. doi: 10.

1103/PhysRevLett.110.153901. URL https://link.aps.org/doi/10.1103/PhysRevLett.110.153901.

[75] D. Gatto Monticone, K. Katamadze, P. Traina, E. Moreva, J. Forneris, I. Ruo-Berchera, P. Olivero, I. P. Degiovanni, G. Brida, and M. Genovese. Beating the Abbe Diffraction Limit in Confocal Microscopy via Nonclassical Photon Statistics. *Phys. Rev. Lett.*, 113(14):143602, September 2014. doi: 10.1103/PhysRevLett.113.143602. URL https://link.aps.org/doi/10.1103/PhysRevLett.113.143602.

[76] Eva Rittweger, Kyu Young Han, Scott E. Irvine, Christian Eggeling, and Stefan W. Hell. STED microscopy reveals crystal colour centres with nanometric resolution. *Nat. Photonics*, 3(3):144–147, March 2009. ISSN 1749-4893. doi: 10.1038/nphoton.2009.2. URL https://www.nature.com/articles/nphoton.2009.2.

[77] Ron Tenne, Uri Rossman, Batel Rephael, Yonatan Israel, Alexander Krupinski-Ptaszek, Radek Lapkiewicz, Yaron Silberberg, and Dan Oron. Super-resolution enhancement by quantum image scanning microscopy. *Nat. Photon.*, 13(2):116, February 2019. ISSN 1749-4893. doi: 10.1038/s41566-018-0324-z. URL https://www.nature.com/articles/s41566-018-0324-z.

[78] Milena D'Angelo, Maria V. Chekhova, and Yanhua Shih. Two-Photon Diffraction and Quantum Lithography. *Phys. Rev. Lett.*, 87(1):013602, June 2001. doi: 10.1103/PhysRevLett.87.013602. URL https://link.aps.org/doi/10.1103/PhysRevLett.87.013602.

[79] Hye Jeong Chang, Heedeuk Shin, Malcolm N. O'Sullivan-Hale, and Robert W. Boyd. Implementation of sub-Rayleigh-resolution lithography using an N -photon absorber. *J. Mod. Opt.*, 53(16-17):2271–2277, November 2006. ISSN

0950-0340. doi: 10.1080/09500340600895656. URL https://doi.org/10.1080/09500340600895656.

[80] Christian Kothe, Gunnar Björk, Shuichiro Inoue, and Mohamed Bourennane. On the efficiency of quantum lithography. *New J. Phys.*, 13(4):043028, April 2011. ISSN 1367-2630. doi: 10.1088/1367-2630/13/4/043028. URL https://doi.org/10.1088%2F1367-2630%2F13%2F4%2F043028.

[81] Mankei Tsang. Quantum Imaging beyond the Diffraction Limit by Optical Centroid Measurements. *Phys. Rev. Lett.*, 102(25):253601, June 2009. doi: 10.1103/PhysRevLett.102.253601. URL http://link.aps.org/doi/10.1103/PhysRevLett.102.253601.

[82] Heedeuk Shin, Kam Wai Clifford Chan, Hye Jeong Chang, and Robert W. Boyd. Quantum Spatial Superresolution by Optical Centroid Measurements. *Phys. Rev. Lett.*, 107(8):083603, August 2011. doi: 10.1103/PhysRevLett.107.083603. URL https://link.aps.org/doi/10.1103/PhysRevLett.107.083603.

[83] G. D. Boreman. MTF MEASUREMENT METHODS. In *Modulation Transfer Function in Optical and Electro-Optical Systems*, pages 69–76. SPIE Press, Bellingham, WA, 2001. URL https://doi.org/10.1117/3.419857.

[84] The Editors of Encyclopaedia Britannica. Photon, February 2019. URL https://www.britannica.com/science/photon. (Accessed 12/03/2019).

[85] Max Planck. Ueber das Gesetz der Energieverteilung im Normalspectrum. *Ann. Phys.*, 309(3):553–563, 1901. ISSN 1521-3889. doi: 10.1002/andp.19013090310. URL https://onlinelibrary.wiley.com/doi/abs/10.1002/andp.19013090310.

[86] A. Einstein. Über einen die Erzeugung und Verwandlung des Lichtes betreffenden heuristischen Gesichtspunkt. *Ann. Phys.*, 322(6):132–148, 1905. ISSN

1521-3889. doi: 10.1002/andp.19053220607. URL https://onlinelibrary.wiley.com/doi/abs/10.1002/andp.19053220607.

[87] Maximilian Schlosshauer, Johannes Kofler, and Anton Zeilinger. A snapshot of foundational attitudes toward quantum mechanics. *Studies in History and Philosophy of Science Part B: Studies in History and Philosophy of Modern Physics*, 44(3):222–230, August 2013. ISSN 1355-2198. doi: 10.1016/j.shpsb.2013.04.004. URL http://www.sciencedirect.com/science/article/pii/S1355219813000397.

[88] Don Howard. Who Invented the "Copenhagen Interpretation"? A Study in Mythology. *Philosophy of Science*, 71(5):669–682, December 2004. ISSN 0031-8248. doi: 10.1086/425941. URL https://doi.org/10.1086/425941.

[89] Steven Weinberg. Einstein's Mistakes. *Physics Today*, 58(11):31–35, November 2005. ISSN 0031-9228. doi: 10.1063/1.2155755. URL https://physicstoday.scitation.org/doi/10.1063/1.2155755.

[90] F David Peat and John Briggs. THE COPENHAGEN INTERPRETATION. In *Einstein's Moon: Bell's Theorem and the Curious Quest for Quantum Reality*, pages 58–65. Contemporary books Chicago, 1990.

[91] Henry Pierce Stapp. The Copenhagen Interpretation. *American Journal of Physics*, 40(8):1098–1116, August 1972. ISSN 0002-9505. doi: 10.1119/1.1986768. URL https://aapt.scitation.org/doi/abs/10.1119/1.1986768.

[92] David J. Griffiths. THE STATISTICAL INTERPRETATION. In *Introduction to Quantum Mechanics*, pages 2–5. Pearson Prentice Hall, Upper Saddle River, NJ, 2nd edition edition, April 2004. ISBN 978-0-13-111892-8.

[93] E. Schrödinger. Die gegenwärtige Situation in der Quantenmechanik. *Naturwissenschaften*, 23(48):807–812, November 1935. ISSN 1432-1904. doi: 10.1007/BF01491891. URL https://doi.org/10.1007/BF01491891.

[94] Shirley Dowdy, Stanley Weardon, and Daniel Chilko. Distributions of two variables. In *Statistics for Research*, pages 218–219. Wiley-Interscience, third edition, 2004.

[95] Eleonora Alabrese, Sascha O. Becker, Thiemo Fetzer, and Dennis Novy. Who voted for Brexit? Individual and regional data combined. *European Journal of Political Economy*, 56:132–150, January 2019. ISSN 0176-2680. doi: 10.1016/j.ejpoleco.2018.08.002. URL http://www.sciencedirect.com/science/article/pii/S0176268018301320.

[96] A. Einstein, B. Podolsky, and N. Rosen. Can Quantum-Mechanical Description of Physical Reality Be Considered Complete? *Phys Rev*, 47(10):777–780, May 1935. doi: 10.1103/PhysRev.47.777. URL http://link.aps.org/doi/10.1103/PhysRev.47.777.

[97] David Bohm. *Quantum Theory*. Prentice-Hall, Englewood Cliffs, 1st edition, 1951.

[98] J. S. Bell. On the Einstein Podolsky Rosen paradox. *Phys. Phys. Fiz.*, 1 (3):195–200, November 1964. doi: 10.1103/PhysicsPhysiqueFizika.1.195. URL https://link.aps.org/doi/10.1103/PhysicsPhysiqueFizika.1.195.

[99] John F. Clauser, Michael A. Horne, Abner Shimony, and Richard A. Holt. Proposed Experiment to Test Local Hidden-Variable Theories. *Phys. Rev. Lett.*, 23(15):880–884, October 1969. doi: 10.1103/PhysRevLett.23.880. URL https://link.aps.org/doi/10.1103/PhysRevLett.23.880.

[100] Alain Aspect, Philippe Grangier, and Gérard Roger. Experimental Realization of Einstein-Podolsky-Rosen-Bohm Gedankenexperiment: A New Violation of Bell's Inequalities. *Phys. Rev. Lett.*, 49(2):91–94, July 1982. doi: 10.1103/PhysRevLett.49.91. URL https://link.aps.org/doi/10.1103/PhysRevLett.49.91.

[101] Lynden K. Shalm, Evan Meyer-Scott, Bradley G. Christensen, Peter Bierhorst, Michael A. Wayne, Martin J. Stevens, Thomas Gerrits, Scott Glancy, Deny R. Hamel, Michael S. Allman, Kevin J. Coakley, Shellee D. Dyer, Carson Hodge, Adriana E. Lita, Varun B. Verma, Camilla Lambrocco, Edward Tortorici, Alan L. Migdall, Yanbao Zhang, Daniel R. Kumor, William H. Farr, Francesco Marsili, Matthew D. Shaw, Jeffrey A. Stern, Carlos Abellán, Waldimar Amaya, Valerio Pruneri, Thomas Jennewein, Morgan W. Mitchell, Paul G. Kwiat, Joshua C. Bienfang, Richard P. Mirin, Emanuel Knill, and Sae Woo Nam. Strong Loophole-Free Test of Local Realism. *Phys. Rev. Lett.*, 115(25):250402, December 2015. doi: 10.1103/PhysRevLett.115.250402. URL https://link.aps.org/doi/10.1103/PhysRevLett.115.250402.

[102] Marissa Giustina, Marijn A. M. Versteegh, Sören Wengerowsky, Johannes Handsteiner, Armin Hochrainer, Kevin Phelan, Fabian Steinlechner, Johannes Kofler, Jan-Åke Larsson, Carlos Abellán, Waldimar Amaya, Valerio Pruneri, Morgan W. Mitchell, Jörn Beyer, Thomas Gerrits, Adriana E. Lita, Lynden K. Shalm, Sae Woo Nam, Thomas Scheidl, Rupert Ursin, Bernhard Wittmann, and Anton Zeilinger. Significant-Loophole-Free Test of Bell's Theorem with Entangled Photons. *Phys. Rev. Lett.*, 115(25):250401, December 2015. doi: 10.1103/PhysRevLett.115.250401. URL https://link.aps.org/doi/10.1103/PhysRevLett.115.250401.

[103] M. D. Reid. Demonstration of the Einstein-Podolsky-Rosen paradox using nondegenerate parametric amplification. *Phys. Rev. A*, 40(2):913–923, July 1989. doi: 10.1103/PhysRevA.40.913. URL https://link.aps.org/doi/10.1103/PhysRevA.40.913.

[104] John C. Howell, Ryan S. Bennink, Sean J. Bentley, and R. W. Boyd. Realization of the Einstein-Podolsky-Rosen Paradox Using Momentum- and Position-Entangled Photons from Spontaneous Parametric Down Conversion. *Phys.*

Rev. Lett., 92(21):210403, May 2004. doi: 10.1103/PhysRevLett.92.210403. URL https://link.aps.org/doi/10.1103/PhysRevLett.92.210403.

[105] Deutsch David and Jozsa Richard. Rapid solution of problems by quantum computation. *Proceedings of the Royal Society of London. Series A: Mathematical and Physical Sciences*, 439(1907):553–558, December 1992. doi: 10.1098/rspa.1992.0167. URL https://royalsocietypublishing.org/doi/abs/10.1098/rspa.1992.0167.

[106] A. Galindo and M. A. Martín-Delgado. Information and computation: Classical and quantum aspects. *Rev. Mod. Phys.*, 74(2):347–423, May 2002. doi: 10.1103/RevModPhys.74.347. URL https://link.aps.org/doi/10.1103/RevModPhys.74.347.

[107] Samuel L. Braunstein and Peter van Loock. Quantum information with continuous variables. *Rev. Mod. Phys.*, 77(2):513–577, June 2005. doi: 10.1103/RevModPhys.77.513. URL https://link.aps.org/doi/10.1103/RevModPhys.77.513.

[108] Sean D. Huver, Christoph F. Wildfeuer, and Jonathan P. Dowling. Entangled Fock states for robust quantum optical metrology, imaging, and sensing. *Phys. Rev. A*, 78(6):063828, December 2008. doi: 10.1103/PhysRevA.78.063828. URL https://link.aps.org/doi/10.1103/PhysRevA.78.063828.

[109] Vittorio Giovannetti, Seth Lloyd, and Lorenzo Maccone. Advances in quantum metrology. *Nat. Photonics*, 5(4):222–229, April 2011. ISSN 1749-4893. doi: 10.1038/nphoton.2011.35. URL https://www.nature.com/articles/nphoton.2011.35.

[110] Paul-Antoine Moreau, Ermes Toninelli, Thomas Gregory, and Miles J. Padgett. Ghost Imaging Using Optical Correlations. *Laser & Photonics Reviews*, 12(1),

January 2018. ISSN 1863-8899. doi: 10.1002/lpor.201700143. URL http://onlinelibrary.wiley.com/doi/10.1002/lpor.201700143/abstract.

[111] W. Heisenberg. Über den anschaulichen Inhalt der quantentheoretischen Kinematik und Mechanik. *Z. Physik*, 43(3):172–198, March 1927. ISSN 0044-3328. doi: 10.1007/BF01397280. URL https://doi.org/10.1007/BF01397280.

[112] M.H. Al-Hashimi and U.-J. Wiese. From a particle in a box to the uncertainty relation in a quantum dot and to reflecting walls for relativistic fermions. *Annals of Physics*, 327(1):1–28, January 2012. ISSN 0003-4916. doi: 10.1016/j.aop.2011.05.003. URL http://www.sciencedirect.com/science/article/pii/S0003491611000911.

[113] M. H. Al-Hashimi. Harmonic oscillator in a 1D or 2D cavity with general perfectly reflecting walls. *Mol. Phys.*, 111(2):225–241, January 2013. ISSN 0026-8976. doi: 10.1080/00268976.2012.716526. URL https://doi.org/10.1080/00268976.2012.716526.

[114] Oleg Olendski. Comparative analysis of electric field influence on the quantum wells with different boundary conditions. *Ann. Phys.*, 527(3-4):278–295, 2015. ISSN 1521-3889. doi: 10.1002/andp.201400228. URL https://onlinelibrary.wiley.com/doi/abs/10.1002/andp.201400228.

[115] P. Hariharan and P. A. Robinson. The gouy phase shift as a geometrical quantum effect. *J. Mod. Opt.*, 43(2):219–221, February 1996. ISSN 0950-0340. doi: 10.1080/09500349608232735. URL https://doi.org/10.1080/09500349608232735.

[116] Simin Feng and Herbert G. Winful. Physical origin of the Gouy phase shift. *Opt. Lett., OL*, 26(8):485–487, April 2001. ISSN 1539-4794. doi: 10.1364/OL.26.000485. URL https://www.osapublishing.org/ol/abstract.cfm?uri=ol-26-8-485.

[117] T. C. Petersen, D. M. Paganin, M. Weyland, T. P. Simula, S. A. Eastwood, and M. J. Morgan. Unifying interpretations of the Gouy phase anomaly for electron waves. *Phys. Rev. A*, 89(6):063801, June 2014. doi: 10.1103/PhysRevA.89.063801. URL https://link.aps.org/doi/10.1103/PhysRevA.89.063801.

[118] Robert J. C. Spreeuw. A Classical Analogy of Entanglement. *Foundations of Physics*, 28(3):361–374, March 1998. ISSN 1572-9516. doi: 10.1023/A:1018703709245. URL https://doi.org/10.1023/A:1018703709245.

[119] Ebrahim Karimi and Robert W. Boyd. Classical entanglement? *Science*, 350(6265):1172–1173, December 2015. ISSN 0036-8075, 1095-9203. doi: 10.1126/science.aad7174. URL http://science.sciencemag.org/content/350/6265/1172.

[120] Matias A. Goldin, Diego Francisco, and Silvia Ledesma. Simulating Bell inequality violations with classical optics encoded qubits. *J. Opt. Soc. Am. B, JOSAB*, 27(4):779–786, April 2010. ISSN 1520-8540. doi: 10.1364/JOSAB.27.000779. URL https://www.osapublishing.org/josab/abstract.cfm?uri=josab-27-4-779.

[121] Falk Töppel, Andrea Aiello, Christoph Marquardt, Elisabeth Giacobino, and Gerd Leuchs. Classical entanglement in polarization metrology. *New J. Phys.*, 16(7):073019, July 2014. ISSN 1367-2630. doi: 10.1088/1367-2630/16/7/073019. URL https://doi.org/10.1088%2F1367-2630%2F16%2F7%2F073019.

[122] Xiao-Feng Qian, Bethany Little, John C. Howell, and J. H. Eberly. Shifting the quantum-classical boundary: Theory and experiment for statistically classical optical fields. *Optica, OPTICA*, 2(7):611–615, July 2015. ISSN 2334-2536. doi: 10.1364/OPTICA.2.000611. URL https://www.osapublishing.org/optica/abstract.cfm?uri=optica-2-7-611.

[123] Xinbing Song, Yifan Sun, Pengyun Li, Hongwei Qin, and Xiangdong Zhang. Bell's measure and implementing quantum Fourier transform with orbital angular momentum of classical light. *Sci. Rep.*, 5:14113, September 2015. ISSN 2045-2322. doi: 10.1038/srep14113. URL https://www.nature.com/articles/srep14113.

[124] Ermes Toninelli, Bienvenu Ndagano, Adam Vallés, Bereneice Sephton, Isaac Nape, Antonio Ambrosio, Federico Capasso, Miles J. Padgett, and Andrew Forbes. Concepts in quantum state tomography and classical implementation with intense light: A tutorial. *Adv. Opt. Photon., AOP*, 11(1):67–134, March 2019. ISSN 1943-8206. URL https://www.osapublishing.org/aop/abstract.cfm?uri=aop-11-1-67.

[125] Michael R Peres. Advances in Photographic Technology. In *The Focal Encyclopedia of Photography*, pages 3–22. Taylor & Francis, 4th edition, 2013.

[126] Patrick Llull, Xuejun Liao, Xin Yuan, Jianbo Yang, David Kittle, Lawrence Carin, Guillermo Sapiro, and David J. Brady. Coded aperture compressive temporal imaging. *Opt. Express, OE*, 21(9):10526–10545, May 2013. ISSN 1094-4087. doi: 10.1364/OE.21.010526. URL https://www.osapublishing.org/oe/abstract.cfm?uri=oe-21-9-10526.

[127] S. P. Walborn, C. H. Monken, S. Pádua, and P. H. Souto Ribeiro. Spatial correlations in parametric down-conversion. *Phys. Rep.*, 495(4):87–139, October 2010. ISSN 0370-1573. doi: 10.1016/j.physrep.2010.06.003. URL http://www.sciencedirect.com/science/article/pii/S0370157310001602.

[128] John C. Howell, Ryan S. Bennink, Sean J. Bentley, and R. W. Boyd. Realization of the Einstein-Podolsky-Rosen Paradox Using Momentum- and Position-Entangled Photons from Spontaneous Parametric Down Conversion. *Phys.*

Rev. Lett., 92(21):210403, May 2004. doi: 10.1103/PhysRevLett.92.210403. URL https://link.aps.org/doi/10.1103/PhysRevLett.92.210403.

[129] Takafumi Ono, Ryo Okamoto, and Shigeki Takeuchi. An entanglement-enhanced microscope. *Nat. Commun.*, 4:2426, September 2013. ISSN 2041-1723. doi: 10.1038/ncomms3426. URL https://www.nature.com/articles/ncomms3426.

[130] Baris I. Erkmen and Jeffrey H. Shapiro. Ghost imaging: From quantum to classical to computational. *Adv. Opt. Photon., AOP*, 2(4):405–450, December 2010. ISSN 1943-8206. doi: 10.1364/AOP.2.000405. URL https://www.osapublishing.org/aop/abstract.cfm?uri=aop-2-4-405.

[131] Chuan Wang, Fu-Guo Deng, Yan-Song Li, Xiao-Shu Liu, and Gui Lu Long. Quantum secure direct communication with high-dimension quantum superdense coding. *Phys. Rev. A*, 71(4):044305, April 2005. doi: 10.1103/PhysRevA.71.044305. URL https://link.aps.org/doi/10.1103/PhysRevA.71.044305.

[132] Marcus Huber and Marcin Pawłowski. Weak randomness in device-independent quantum key distribution and the advantage of using high-dimensional entanglement. *Phys. Rev. A*, 88(3):032309, September 2013. doi: 10.1103/PhysRevA.88.032309. URL https://link.aps.org/doi/10.1103/PhysRevA.88.032309.

[133] Seth Lloyd. Enhanced Sensitivity of Photodetection via Quantum Illumination. *Science*, 321(5895):1463–1465, September 2008. ISSN 0036-8075, 1095-9203. doi: 10.1126/science.1160627. URL http://science.sciencemag.org/content/321/5895/1463.

[134] Mohammad Mirhosseini, Omar S. Magaña-Loaiza, Malcolm N. O'Sullivan, Brandon Rodenburg, Mehul Malik, Martin P. J. Lavery, Miles J. Padgett,

Daniel J. Gauthier, and Robert W. Boyd. High-dimensional quantum cryptography with twisted light. *New J. Phys.*, 17(3):033033, March 2015. ISSN 1367-2630. doi: 10.1088/1367-2630/17/3/033033. URL https://doi.org/10.1088%2F1367-2630%2F17%2F3%2F033033.

[135] H. Bechmann-Pasquinucci and W. Tittel. Quantum cryptography using larger alphabets. *Phys. Rev. A*, 61(6):062308, May 2000. doi: 10.1103/PhysRevA.61.062308. URL https://link.aps.org/doi/10.1103/PhysRevA.61.062308.

[136] Ryszard Horodecki, Paweł Horodecki, Michał Horodecki, and Karol Horodecki. Quantum entanglement. *Rev. Mod. Phys.*, 81(2):865–942, June 2009. doi: 10.1103/RevModPhys.81.865. URL https://link.aps.org/doi/10.1103/RevModPhys.81.865.

[137] Helle Bechmann-Pasquinucci and Asher Peres. Quantum Cryptography with 3-State Systems. *Phys. Rev. Lett.*, 85(15):3313–3316, October 2000. doi: 10.1103/PhysRevLett.85.3313. URL https://link.aps.org/doi/10.1103/PhysRevLett.85.3313.

[138] Jianming Wen, Shengwang Du, and Min Xiao. Improving spatial resolution in quantum imaging beyond the Rayleigh diffraction limit using multiphoton W entangled states. *Phys. Lett. A*, 374(38):3908–3911, August 2010. ISSN 03759601. doi: 10.1016/j.physleta.2010.07.068. URL http://linkinghub.elsevier.com/retrieve/pii/S0375960110009552.

[139] T. Gregory, P.-A. Moreau, E. Toninelli, and M. J. Padgett. Imaging through noise with quantum illumination. *Sci. Adv.*, 6(6):eaay2652, February 2020. ISSN 2375-2548. doi: 10.1126/sciadv.aay2652. URL https://advances.sciencemag.org/content/6/6/eaay2652.

[140] Milena D'Angelo, Yoon-Ho Kim, Sergei P. Kulik, and Yanhua Shih. Identifying Entanglement Using Quantum Ghost Interference and Imaging. *Phys. Rev.*

Lett., 92(23):233601, June 2004. doi: 10.1103/PhysRevLett.92.233601. URL http://link.aps.org/doi/10.1103/PhysRevLett.92.233601.

[141] C. K. Law and J. H. Eberly. Analysis and Interpretation of High Transverse Entanglement in Optical Parametric Down Conversion. *Phys. Rev. Lett.*, 92 (12):127903, March 2004. doi: 10.1103/PhysRevLett.92.127903. URL https://link.aps.org/doi/10.1103/PhysRevLett.92.127903.

[142] D. V. Strekalov, A. V. Sergienko, D. N. Klyshko, and Y. H. Shih. Observation of Two-Photon "Ghost" Interference and Diffraction. *Phys. Rev. Lett.*, 74(18): 3600–3603, May 1995. doi: 10.1103/PhysRevLett.74.3600. URL https://link.aps.org/doi/10.1103/PhysRevLett.74.3600.

[143] T. B. Pittman, Y. H. Shih, D. V. Strekalov, and A. V. Sergienko. Optical imaging by means of two-photon quantum entanglement. *Phys. Rev. A*, 52 (5):R3429–R3432, November 1995. doi: 10.1103/PhysRevA.52.R3429. URL http://link.aps.org/doi/10.1103/PhysRevA.52.R3429.

[144] C. H. Monken, P. H. Souto Ribeiro, and S. Pádua. Transfer of angular spectrum and image formation in spontaneous parametric down-conversion. *Phys. Rev. A*, 57(4):3123–3126, April 1998. doi: 10.1103/PhysRevA.57.3123. URL https://link.aps.org/doi/10.1103/PhysRevA.57.3123.

[145] A. F. Abouraddy, M. B. Nasr, B. E. A. Saleh, A. V. Sergienko, and M. C. Teich. Demonstration of the complementarity of one- and two-photon interference. *Phys. Rev. A*, 63(6):063803, May 2001. doi: 10.1103/PhysRevA.63.063803. URL https://link.aps.org/doi/10.1103/PhysRevA.63.063803.

[146] Paul-Antoine Moreau, Fabrice Devaux, and Eric Lantz. Einstein-Podolsky-Rosen Paradox in Twin Images. *Phys. Rev. Lett.*, 113(16):160401, October 2014. doi: 10.1103/PhysRevLett.113.160401. URL http://link.aps.org/doi/10.1103/PhysRevLett.113.160401.

[147] Matthew Reichert, Hugo Defienne, and Jason W. Fleischer. Massively Parallel Coincidence Counting of High-Dimensional Entangled States. *Scientific Reports*, 8(1):7925, May 2018. ISSN 2045-2322. doi: 10.1038/s41598-018-26144-7. URL https://doi.org/10.1038/s41598-018-26144-7.

[148] J. Leach, R. E. Warburton, D. G. Ireland, F. Izdebski, S. M. Barnett, A. M. Yao, G. S. Buller, and M. J. Padgett. Quantum correlations in position, momentum, and intermediate bases for a full optical field of view. *Phys. Rev. A*, 85(1): 013827, January 2012. doi: 10.1103/PhysRevA.85.013827. URL https://link.aps.org/doi/10.1103/PhysRevA.85.013827.

[149] D. S. Tasca, S. P. Walborn, P. H. Souto Ribeiro, and F. Toscano. Detection of transverse entanglement in phase space. *Phys. Rev. A*, 78(1):010304, July 2008. doi: 10.1103/PhysRevA.78.010304. URL https://link.aps.org/doi/10.1103/PhysRevA.78.010304.

[150] D. S. Tasca, S. P. Walborn, P. H. Souto Ribeiro, F. Toscano, and P. Pellat-Finet. Propagation of transverse intensity correlations of a two-photon state. *Phys. Rev. A*, 79(3):033801, March 2009. doi: 10.1103/PhysRevA.79.033801. URL https://link.aps.org/doi/10.1103/PhysRevA.79.033801.

[151] R. M. Gomes, A. Salles, F. Toscano, P. H. Souto Ribeiro, and S. P. Walborn. Quantum entanglement beyond Gaussian criteria. *PNAS*, 106(51):21517–21520, December 2009. ISSN 0027-8424, 1091-6490. doi: 10.1073/pnas.0908329106. URL https://www.pnas.org/content/106/51/21517.

[152] S. P. Walborn, A. Salles, R. M. Gomes, F. Toscano, and P. H. Souto Ribeiro. Revealing Hidden Einstein-Podolsky-Rosen Nonlocality. *Phys. Rev. Lett.*, 106 (13):130402, March 2011. doi: 10.1103/PhysRevLett.106.130402. URL https://link.aps.org/doi/10.1103/PhysRevLett.106.130402.

[153] H. Di Lorenzo Pires, C. H. Monken, and M. P. van Exter. Direct measurement of transverse-mode entanglement in two-photon states. *Phys Rev A*, 80(2): 022307, August 2009. doi: 10.1103/PhysRevA.80.022307. URL http://link.aps.org/doi/10.1103/PhysRevA.80.022307.

[154] Bradley M. Jost, Alexander V. Sergienko, Ayman F. Abouraddy, Bahaa E. A. Saleh, and Malvin C. Teich. Spatial correlations of spontaneously down-converted photon pairs detected with a single-photon-sensitive CCD camera. *Opt. Express, OE*, 3(2):81–88, July 1998. ISSN 1094-4087. doi: 10.1364/OE.3.000081. URL https://www.osapublishing.org/oe/abstract.cfm?uri=oe-3-2-81.

[155] Matthew Reichert, Xiaohang Sun, and Jason W. Fleischer. Quality of Spatial Entanglement Propagation. *Phys. Rev. A*, 95(6), June 2017. ISSN 2469-9926, 2469-9934. doi: 10.1103/PhysRevA.95.063836. URL http://arxiv.org/abs/1611.07967.

[156] Matthew Reichert, Hugo Defienne, Xiaohang Sun, and Jason W. Fleischer. Biphoton transmission through non-unitary objects. *J. Opt.*, 19(4):044004, 2017. ISSN 2040-8986. doi: 10.1088/2040-8986/aa6175. URL http://stacks.iop.org/2040-8986/19/i=4/a=044004.

[157] Paul-Antoine Moreau, Ermes Toninelli, Thomas Gregory, Reuben S. Aspden, Peter A. Morris, and Miles J. Padgett. Imaging Bell-type nonlocal behavior. *Sci. Adv.*, 5(7):eaaw2563, July 2019. ISSN 2375-2548. doi: 10.1126/sciadv.aaw2563. URL https://advances.sciencemag.org/content/5/7/eaaw2563.

[158] D. S. Tasca, R. M. Gomes, F. Toscano, P. H. Souto Ribeiro, and S. P. Walborn. Continuous-variable quantum computation with spatial degrees of freedom of photons. *Phys. Rev. A*, 83(5):052325, May 2011. doi: 10.1103/PhysRevA.83.052325. URL https://link.aps.org/doi/10.1103/PhysRevA.83.052325.

[159] Paul-Antoine Moreau, Ermes Toninelli, Thomas Gregory, and Miles J. Padgett. Imaging with quantum states of light. *Nat. Rev. Phys.*, 1(6):367–380, June 2019. ISSN 2522-5820. doi: 10.1038/s42254-019-0056-0. URL https://www.nature.com/articles/s42254-019-0056-0.

[160] Mikhail I. Kolobov. The spatial behavior of nonclassical light. *Rev. Mod. Phys.*, 71(5):1539–1589, October 1999. doi: 10.1103/RevModPhys.71.1539. URL https://link.aps.org/doi/10.1103/RevModPhys.71.1539.

[161] G. Fubini. Sugli integrali multipli. *Rom Acc Rend 5*, 16(1):608–614, 1907. ISSN 0001-4435.

[162] E. Toninelli, P.-A. Moreau, T. Gregory, and M. J. Padgett. A model for quantum imaging and sensing experiments based on the detection of correlated biphotons using a photon-counting camera. March 2019. (submitted and under consideration).

[163] Leonard Mandel and Emil Wolf. Semiclassical theory of photoelectric detection of light. In *Optical Coherence and Quantum Optics*, page 439. Cambridge university press, 1995.

[164] Rodney Loudon. Chapter 4. In *The Quantum Theory of Light*, page 106. Clarendon Oxford, 2nd edition, 1983.

[165] R. Hanbury Brown and R. Q. Twiss. Correlation between Photons in two Coherent Beams of Light. *Nature*, 177(4497):27–29, January 1956. ISSN 1476-4687. doi: 10.1038/177027a0. URL https://www.nature.com/articles/177027a0.

[166] H. J. Kimble, M. Dagenais, and L. Mandel. Photon Antibunching in Resonance Fluorescence. *Phys. Rev. Lett.*, 39(11):691–695, September 1977. doi: 10.1103/PhysRevLett.39.691. URL https://link.aps.org/doi/10.1103/PhysRevLett.39.691.

[167] J.G. Webster and H. Eren. Detector Performance Parameters. In *Measurement, Instrumentation, and Sensors Handbook, Second Edition: Spatial, Mechanical, Thermal, and Radiation Measurement*, Measurement, Instrumentation, and Sensors Handbook, page 56.1. Taylor & Francis, 2014. ISBN 978-1-4398-4888-3. URL http://books.google.co.uk/books?id=JaPAAgAAQBAJ.

[168] Constant A. J. Putman, Bart G. De Grooth, Niek F. Van Hulst, and Jan Greve. A detailed analysis of the optical beam deflection technique for use in atomic force microscopy. *Journal of Applied Physics*, 72(1):6–12, July 1992. ISSN 0021-8979. doi: 10.1063/1.352149. URL https://aip.scitation.org/doi/abs/10.1063/1.352149.

[169] Mikhail I Kolobov. Quantum imaging. In *Quantum Imaging*, pages 158–159. Springer Science & Business Media, 2007.

[170] Mikhail I. Kolobov and Claude Fabre. Quantum Limits on Optical Resolution. *Phys. Rev. Lett.*, 85(18):3789–3792, October 2000. doi: 10.1103/PhysRevLett.85.3789. URL https://link.aps.org/doi/10.1103/PhysRevLett.85.3789.

[171] Rodney Loudon. Fluctuations in laser light. In *The Quantum Theory of Light*, page 310. OUP Oxford, 2000.

[172] Leonard Mandel and Emil Wolf. Thermal light. In *Optical Coherence and Quantum Optics*. Cambridge university press, 1995.

[173] E. Jakeman and J. G. Walker. Analysis of a method for the generation of light with sub-Poissonian photon statistics. *Opt. Commun.*, 55:219–222, September 1985. doi: 10.1016/0030-4018(85)90051-3. URL http://adsabs.harvard.edu/abs/1985OptCo..55..219J.

[174] E. Jakeman and J. G. Rarity. The use of pair production processes to reduce quantum noise in transmission measurements. *Optics Communications*,

59(3):219–223, September 1986. ISSN 0030-4018. doi: 10.1016/0030-4018(86)90288-9. URL http://www.sciencedirect.com/science/article/pii/0030401886902889.

[175] Venkatarama Krishnan. Poisson distribution. In *Probability and Random Processes*, pages 48–55. John Wiley & Sons, 2015.

[176] Pieter Kok, Hwang Lee, and Jonathan P. Dowling. Creation of large-photon-number path entanglement conditioned on photodetection. *Phys. Rev. A*, 65 (5):052104, April 2002. doi: 10.1103/PhysRevA.65.052104. URL https://link.aps.org/doi/10.1103/PhysRevA.65.052104.

[177] Barry C. Sanders. Quantum dynamics of the nonlinear rotator and the effects of continual spin measurement. *Phys. Rev. A*, 40(5):2417–2427, September 1989. doi: 10.1103/PhysRevA.40.2417. URL https://link.aps.org/doi/10.1103/PhysRevA.40.2417.

[178] Itai Afek, Oron Ambar, and Yaron Silberberg. High-NOON States by Mixing Quantum and Classical Light. *Science*, 328(5980):879–881, May 2010. ISSN 0036-8075, 1095-9203. doi: 10.1126/science.1188172. URL https://science.sciencemag.org/content/328/5980/879.

[179] Y. Israel, I. Afek, S. Rosen, O. Ambar, and Y. Silberberg. Experimental tomography of NOON states with large photon numbers. *Phys. Rev. A*, 85(2):022115, February 2012. doi: 10.1103/PhysRevA.85.022115. URL https://link.aps.org/doi/10.1103/PhysRevA.85.022115.

[180] Jonathan A. Jones, Steven D. Karlen, Joseph Fitzsimons, Arzhang Ardavan, Simon C. Benjamin, G. Andrew D. Briggs, and John J. L. Morton. Magnetic Field Sensing Beyond the Standard Quantum Limit Using 10-Spin NOON States. *Science*, 324(5931):1166–1168, May 2009. ISSN 0036-8075, 1095-9203. doi:

10.1126/science.1170730. URL https://science.sciencemag.org/content/324/5931/1166.

[181] Seth T. Merkel and Frank K. Wilhelm. Generation and detection of NOON states in superconducting circuits. *New J. Phys.*, 12(9):093036, September 2010. ISSN 1367-2630. doi: 10.1088/1367-2630/12/9/093036. URL https://doi.org/10.1088%2F1367-2630%2F12%2F9%2F093036.

[182] Frederick W. Strauch, Kurt Jacobs, and Raymond W. Simmonds. Arbitrary Control of Entanglement between two Superconducting Resonators. *Phys. Rev. Lett.*, 105(5):050501, July 2010. doi: 10.1103/PhysRevLett.105.050501. URL https://link.aps.org/doi/10.1103/PhysRevLett.105.050501.

[183] DF Walls et al. Squeezed states of light. *Nature*, 306(5939):141–146, 1983. URL https://www.nature.com/articles/306141a0.

[184] R. Loudon and P. L. Knight. Squeezed Light. *J. Mod. Opt.*, 34(6-7):709–759, June 1987. ISSN 0950-0340. doi: 10.1080/09500348714550721. URL https://doi.org/10.1080/09500348714550721.

[185] M. C. Teich and B. E. A. Saleh. Squeezed state of light. *Quantum Opt.*, 1(2):153–191, December 1989. ISSN 0954-8998. doi: 10.1088/0954-8998/1/2/006. URL https://doi.org/10.1088%2F0954-8998%2F1%2F2%2F006.

[186] Malvin C. Teich and Bahaa E. A. Saleh. Squeezed and Antibunched Light. *Phys, Today*, 43(6):26, 1990. ISSN 0031-9228. doi: 10.1063/1.881246. URL https://physicstoday.scitation.org/doi/abs/10.1063/1.881246.

[187] E. Abbe. Beiträge zur Theorie des Mikroskops und der mikroskopischen Wahrnehmung. *Archiv f. mikrosk. Anatomie*, 9(1):413–418, December 1873. ISSN 0176-7364. doi: 10.1007/BF02956173. URL https://link.springer.com/article/10.1007/BF02956173.

[188] F. R. S. Lord Rayleigh. XV. On the theory of optical images, with special reference to the microscope. *Lond. Edinb. Dublin Philos. Mag. J. Sci.*, 42(255): 167–195, August 1896. ISSN 1941-5982. doi: 10.1080/14786449608620902. URL https://doi.org/10.1080/14786449608620902.

[189] George Biddell Airy. On the diffraction of an object-glass with circular aperture. In *Transactions of the Cambridge Philosophical Society*, volume 5, pages 283–291. 1835.

[190] E. Hecht. Resolution of imaging systems. In *Optics*, Pearson Education, pages 471–474. Addison-Wesley, 2002. ISBN 978-0-8053-8566-3. URL https://books.google.co.uk/books?id=7aG6QgAACAAJ.

[191] Ozgur Yilmaz and Ozgur Selimoglu. MTF measurement of a SWIR imaging telescope using star test images. *AIP Conference Proceedings*, 1476(1):131–135, September 2012. ISSN 0094-243X. doi: 10.1063/1.4751581. URL https://aip.scitation.org/doi/10.1063/1.4751581.

[192] InCheon Song, HongKi Yoo, Jaebum Choo, and Dae-Gab Gweon. Measurement of point-spread function (PSF) for confocal fluorescence microscopy. In *Advanced Characterization Techniques for Optics, Semiconductors, and Nanotechnologies II*, volume 5878, page 58781B. International Society for Optics and Photonics, August 2005. doi: 10.1117/12.616701. URL https://www.spiedigitallibrary.org/conference-proceedings-of-spie/5878/58781B/Measurement-of-point-spread-function-PSF-for-confocal-fluorescence-micros 10.1117/12.616701.short.

[193] Carroll Mason Sparrow. On spectroscopic resolving power. *Astrophys. J.*, 44:76–79, 1916. URL http://adsabs.harvard.edu/full/1916ApJ....44...76S. (Accessed 20/03/2019).

[194] Michael W. Davidson. Numerical Aperture (Accessed 04/03/2019). URL https://www.microscopyu.com/microscopy-basics/numerical-aperture.

[195] Xujie Zhang, Tamar Kashti, Dror Kella, Tal Frank, Doron Shaked, Robert Ulichney, Mani Fischer, and Jan P. Allebach. Measuring the modulation transfer function of image capture devices: What do the numbers really mean? In *Proc. SPIE 8293*, volume 8293, pages 829307–829307–11, 2012. doi: 10.1117/12.912989. URL http://dx.doi.org/10.1117/12.912989.

[196] Steven W Smith et al. Convolution. In *The Scientist and Engineer's Guide to Digital Signal Processing*, page 109. California Technical Pub. San Diego, San Diego, California, 2nd edition, 1999. ISBN ISBN 0-9660176-6-8.

[197] Peter D. Burns. Sfrmat3: SFR evaluation for digital cameras and scanners, (accessed 07/03/2019), May 2015. URL http://losburns.com/imaging/software/SFRedge/sfrmat3_post/index.html. pdburns@ieee.org.

[198] Ehsan Samei, Michael J. Flynn, and David A. Reimann. A method for measuring the presampled MTF of digital radiographic systems using an edge test device. *Med. Phys.*, 25(1):102–113, January 1998. ISSN 2473-4209. doi: 10.1118/1.598165. URL http://onlinelibrary.wiley.com/doi/10.1118/1.598165/abstract.

[199] Peter D Burns. Slanted-edge MTF for digital camera and scanner analysis. In *Is and Ts Pics Conference*, pages 135–138, 2000. URL http://www.losburns.com/imaging/pbpubs/26pics2000burns.pdf. (Accessed 20/03/2019).

[200] ISO 12233:2017 - Photography – Electronic still picture imaging – Resolution and spatial frequency responses. URL https://www.iso.org/standard/71696.html.

[201] K. Masaoka. Accuracy and Precision of Edge-Based Modulation Transfer Function Measurement for Sampled Imaging Systems. *IEEE Access*, 6:41079–41086, 2018. ISSN 2169-3536. doi: 10.1109/ACCESS.2018.2856742. URL https://ieeexplore.ieee.org/document/8412181.

[202] ISO 12233:2017. Resolution and spatial frequency responses, January 2017. URL https://www.iso.org/standard/71696.html.

[203] Norman Koren. Sharpness: What is it and how is it measured?, Accessed 17/01/2018. URL http://www.imatest.com/docs/sharpness/.

[204] G. D. Boreman. MTF and resolution. In *Modulation Transfer Function in Optical and Electro-Optical Systems*, page 17. SPIE Press, Bellingham, WA, 2001. URL https://doi.org/10.1117/3.419857.

[205] Carl A. Kocher and Eugene D. Commins. Polarization Correlation of Photons Emitted in an Atomic Cascade. *Phys. Rev. Lett.*, 18(15):575–577, April 1967. doi: 10.1103/PhysRevLett.18.575. URL https://link.aps.org/doi/10.1103/PhysRevLett.18.575.

[206] Stuart J. Freedman and John F. Clauser. Experimental Test of Local Hidden-Variable Theories. *Phys. Rev. Lett.*, 28(14):938–941, April 1972. doi: 10.1103/PhysRevLett.28.938. URL https://link.aps.org/doi/10.1103/PhysRevLett.28.938.

[207] Alain Aspect, Jean Dalibard, and Gérard Roger. Experimental Test of Bell's Inequalities Using Time-Varying Analyzers. *Phys. Rev. Lett.*, 49(25):1804–1807, December 1982. doi: 10.1103/PhysRevLett.49.1804. URL https://link.aps.org/doi/10.1103/PhysRevLett.49.1804.

[208] S. E. Harris, M. K. Oshman, and R. L. Byer. Observation of Tunable Optical Parametric Fluorescence. *Phys. Rev. Lett.*, 18(18):732–734, May 1967.

doi: 10.1103/PhysRevLett.18.732. URL https://link.aps.org/doi/10.1103/PhysRevLett.18.732.

[209] S. A. Akhmanov, V. V. Fadeev, R. V. Khokhlov, and O. N. Chunaev. Quantum Noise in Parametric Light Amplifiers. *ZhETF Pisma Redaktsiiu*, 6:575, August 1967. URL http://adsabs.harvard.edu/abs/1967ZhPmR...6..575A.

[210] David C. Burnham and Donald L. Weinberg. Observation of simultaneity in parametric production of optical photon pairs. *Phys. Rev. Lett.*, 25(2):84, 1970. URL http://journals.aps.org/prl/abstract/10.1103/PhysRevLett.25.84.

[211] Robert W. Boyd. *Nonlinear Optics, Third Edition*. Academic Press, 3 edition, 2008. ISBN 0-12-369470-1 978-0-12-369470-6.

[212] W. H. Louisell, A. Yariv, and A. E. Siegman. Quantum Fluctuations and Noise in Parametric Processes. I. *Phys. Rev.*, 124(6):1646–1654, December 1961. doi: 10.1103/PhysRev.124.1646. URL https://link.aps.org/doi/10.1103/PhysRev.124.1646.

[213] H. A. Haus and J. A. Mullen. Quantum Noise in Linear Amplifiers. *Phys. Rev.*, 128(5):2407–2413, December 1962. doi: 10.1103/PhysRev.128.2407. URL https://link.aps.org/doi/10.1103/PhysRev.128.2407.

[214] DN Klyshko. Scattering of light in a medium with nonlinear polarizability. *Sov Phys JETP*, 28:522, 1969. URL http://jetp.ac.ru/cgi-bin/dn/e_028_03_0522.pdf.

[215] D. A. Kleinman. Theory of Optical Parametric Noise. *Phys. Rev.*, 174(3):1027–1041, October 1968. doi: 10.1103/PhysRev.174.1027. URL https://link.aps.org/doi/10.1103/PhysRev.174.1027.

[216] S. P. Walborn, P. H. Souto Ribeiro, L. Davidovich, F. Mintert, and A. Buchleitner. Experimental determination of entanglement with a single measurement. *Nature*, 440(7087):1022–1024, April 2006. ISSN 0028-0836. doi: 10.1038/nature04627. URL http://dx.doi.org/10.1038/nature04627.

[217] F. Devaux and E. Lantz. Spatial and temporal properties of parametric fluorescence around degeneracy in a type I LBO crystal. *Eur. Phys. J. D*, 8(1): 117–124, January 2000. ISSN 1434-6079. doi: 10.1007/s10053-000-9073-9. URL https://doi.org/10.1007/s10053-000-9073-9.

[218] Walter Koechner. Nonlinear devices. In *Solid-State Laser*, volume 1 of *Optical Sciences*, page 612. Springer, Berlin, 6th edition, 2006. ISBN 978-3-540-65064-5.

[219] James Schneeloch and John C Howell. Introduction to the transverse spatial correlations in spontaneous parametric down-conversion through the biphoton birth zone. *J. Opt.*, 18(5):053501, 2016. URL http://stacks.iop.org/2040-8986/18/i=5/a=053501.

[220] Walter Koechner. Nonlinear devices. In *Solid-State Laser*, volume 1 of *Optical Sciences*, page 638. Springer, Berlin, 6th edition, 2006. ISBN 978-3-540-65064-5.

[221] So-Young Baek and Yoon-Ho Kim. Spectral properties of entangled photon pairs generated via frequency-degenerate type-I spontaneous parametric down-conversion. *Phys. Rev. A*, 77(4):043807, April 2008. doi: 10.1103/PhysRevA.77.043807. URL http://link.aps.org/doi/10.1103/PhysRevA.77.043807.

[222] Robert W. Boyd. Phase Matching. In *Nonlinear Optics, Third Edition*, pages 79–84. Academic Press, 3 edition, 2008. ISBN 0-12-369470-1 978-0-12-369470-6. URL http://gen.lib.rus.ec/book/index.php?md5=3CD5E7A159D163E646426DDA97A8B91B.

[223] D. Eimerl, L. Davis, S. Velsko, E. K. Graham, and A. Zalkin. Optical, mechanical, and thermal properties of barium borate. *Journal of Applied Physics*, 62 (5):1968–1983, September 1987. ISSN 0021-8979. doi: 10.1063/1.339536. URL https://aip.scitation.org/doi/10.1063/1.339536.

[224] Pablo L. Saldanha and C. H. Monken. Energy and momentum entanglement in parametric downconversion. *American Journal of Physics*, 81(1): 28–32, December 2012. ISSN 0002-9505. doi: 10.1119/1.4757623. URL http://aapt.scitation.org/doi/full/10.1119/1.4757623.

[225] K. W. Chan, J. P. Torres, and J. H. Eberly. Transverse entanglement migration in Hilbert space. *Phys. Rev. A*, 75(5):050101, May 2007. doi: 10.1103/PhysRevA.75.050101. URL https://link.aps.org/doi/10.1103/PhysRevA.75.050101.

[226] Daniel S. Tasca, Matthew P. Edgar, Frauke Izdebski, Gerald S. Buller, and Miles J. Padgett. Optimizing the use of detector arrays for measuring intensity correlations of photon pairs. *Phys. Rev. A*, 88(1), July 2013. ISSN 1050-2947, 1094-1622. doi: 10.1103/PhysRevA.88.013816. URL http://link.aps.org/doi/10.1103/PhysRevA.88.013816.

[227] Robert H. Hadfield. Single-photon detectors for optical quantum information applications. *Nat. Photonics*, 3(12):696–705, December 2009. ISSN 1749-4893. doi: 10.1038/nphoton.2009.230. URL https://www.nature.com/articles/nphoton.2009.230.

[228] Peter Seitz and Albert JP Theuwissen. Avalanche effect and excess noise factor. In *Single-Photon Imaging*, volume 160, pages 15–16. Springer Science & Business Media, 2011.

[229] Lijian Zhang, Leonardo Neves, Jeff S. Lundeen, and Ian A. Walmsley. A characterization of the single-photon sensitivity of an electron multiplying charge-coupled device. *J. Phys. B At. Mol. Opt. Phys.*, 42(11):114011, 2009. URL http://stacks.iop.org/0953-4075/42/i=11/a=114011.

[230] M.S. Robbins and B.J. Hadwen. The noise performance of electron multiplying charge-coupled devices. *IEEE T. Electron Dev.*, 50(5):1227–1232, May 2003. ISSN 0018-9383. doi: 10.1109/TED.2003.813462. URL http://ieeexplore.ieee.org/lpdocs/epic03/wrapper.htm?arnumber=1210766.

[231] AG Basden and CA Haniff. Low light level CCDs and visibility parameter estimation. *Mon R Astron Soc*, 347(4):1187–1197, 2004. URL https://doi.org/10.1111/j.1365-2966.2004.07283.x.

[232] Peter W. Sullivan, Bryce Croll, and Robert A. Simcoe. Precision of a Low-Cost InGaAs Detector for Near Infrared Photometry. *PASP*, 125(931):1021–1030, September 2013. ISSN 1538-3873. doi: 10.1086/672573. URL https://doi.org/10.1086%2F672573.

[233] Martin A. Green and Mark J. Keevers. Optical properties of intrinsic silicon at 300 K. *Prog. Photovolt. Res. Appl.*, 3(3):189–192, 1995. ISSN 1099-159X. doi: 10.1002/pip.4670030303. URL https://onlinelibrary.wiley.com/doi/abs/10.1002/pip.4670030303.

[234] Andor. Low Dark Current Deep-Depletion (LDC-DD) Technology - Andor Learning Centre, . URL https://andor.oxinst.com/learning/view/article/low-dark-current-deep-depletion-(ldc-dd)-technology. (accessed 15/03/2019).

[235] Andor. Deep Vacuum TE Cooling and EMCCDs - Andor Learning Centre, . URL https://andor.oxinst.com/learning/view/article/deep-vacuum-te-cooling-and-emccds. (Accessed 15/03/2019).

[236] Andor. Count Convert - Andor Learning Centre, . URL https://andor.oxinst.com/learning/view/article/count-convert. (Accessed 15/03/2019).

[237] ANDOR. iXon Ultra The World's Highest Performance Back-illuminated EMCCDs. URL http://www.andor.com/pdfs/specifications/Andor_iXon_ULTRA_EMCCD_Specifications.pdf. (Accessed 10/05/2018).

[238] Andor. Cropped Sensor Mode - Andor Learning Centre. URL https://andor.oxinst.com/learning/view/article/what-is-cropped-sensor-mode. (Accessed 15/03/2019).

[239] Eric Lantz, Jean-Luc Blanchet, Luca Furfaro, and Fabrice Devaux. Multi-imaging and Bayesian estimation for photon counting with EMCCDs. *Mon. Not. R. Astron. Soc.*, 386(4):2262–2270, June 2008. doi: 10.1111/j.1365-2966.2008.13200.x. URL http://mnras.oxfordjournals.org/content/386/4/2262.abstract.

[240] A. Avella, I. Ruo-Berchera, I. P. Degiovanni, G. Brida, and M. Genovese. Absolute calibration of an EMCCD camera by quantum correlation, linking photon counting to the analog regime. *Opt. Lett., OL*, 41(8):1841–1844, April 2016. ISSN 1539-4794. doi: 10.1364/OL.41.001841. URL http://www.osapublishing.org/abstract.cfm?uri=ol-41-8-1841.

[241] Eric Lantz, Séverine Denis, Paul-Antoine Moreau, and Fabrice Devaux. Einstein-Podolsky-Rosen paradox in single pairs of images. *Opt. Express, OE*, 23(20):26472–26478, 2015. URL https://doi.org/10.1364/OE.23.026472.

[242] Peter Seitz and Albert JP Theuwissen. Single-photon imaging. In *Single-Photon Imaging*, volume 160, pages 9–12. Springer Science & Business Media, 2011.

[243] Morton H. Rubin, David N. Klyshko, Y. H. Shih, and A. V. Sergienko. Theory of two-photon entanglement in type-II optical parametric down-conversion.

Phys. Rev. A, 50(6):5122–5133, December 1994. doi: 10.1103/PhysRevA.50.5122. URL https://link.aps.org/doi/10.1103/PhysRevA.50.5122.

[244] Morton H. Rubin. Transverse correlation in optical spontaneous parametric down-conversion. *Phys. Rev. A*, 54(6):5349–5360, December 1996. doi: 10.1103/PhysRevA.54.5349. URL https://link.aps.org/doi/10.1103/PhysRevA.54.5349.

[245] Mattias Jönsson and Gunnar Björk. Evaluating Performance of Photon-Number-Resolving Detectors. *ArXiv Prepr. ArXiv181205422*, 2018. URL https://arxiv.org/abs/1812.05422.

[246] A. G. Basden, C. A. Haniff, and C. D. Mackay. Photon counting strategies with low-light-level CCDs. *Mon. Not. R. Astron. Soc.*, 345(3):985, 2003. doi: 10.1046/j.1365-8711.2003.07020.x. URL http://dx.doi.org/10.1046/j.1365-8711.2003.07020.x.

[247] Michael Vasilyev, Sang-Kyung Choi, Prem Kumar, and G. Mauro D'Ariano. Tomographic Measurement of Joint Photon Statistics of the Twin-Beam Quantum State. *Phys. Rev. Lett.*, 84(11):2354–2357, March 2000. doi: 10.1103/PhysRevLett.84.2354. URL https://link.aps.org/doi/10.1103/PhysRevLett.84.2354.

[248] E. Brambilla, A. Gatti, M. Bache, and L. A. Lugiato. Simultaneous near-field and far-field spatial quantum correlations in the high-gain regime of parametric down-conversion. *Phys. Rev. A*, 69(2):023802, February 2004. doi: 10.1103/PhysRevA.69.023802. URL https://link.aps.org/doi/10.1103/PhysRevA.69.023802.

[249] Eric Lantz, Paul-Antoine Moreau, and Fabrice Devaux. Optimizing the signal-to-noise ratio in the measurement of photon pairs with detector arrays.

Phys. Rev. A, 90(6):063811, 2014. URL https://journals.aps.org/pra/abstract/10.1103/PhysRevA.90.063811.

[250] Mankei Tsang, Ranjith Nair, and Xiao-Ming Lu. Quantum Theory of Superresolution for Two Incoherent Optical Point Sources. *Phys. Rev. X*, 6 (3):031033, August 2016. doi: 10.1103/PhysRevX.6.031033. URL https://link.aps.org/doi/10.1103/PhysRevX.6.031033.

[251] Ayman F. Abouraddy, Bahaa E. A. Saleh, Alexander V. Sergienko, and Malvin C. Teich. Entangled-photon Fourier optics. *J. Opt. Soc. Am. B, JOSAB*, 19(5):1174–1184, May 2002. ISSN 1520-8540. doi: 10.1364/JOSAB.19.001174. URL https://www.osapublishing.org/abstract.cfm?uri=josab-19-5-1174.

[252] Bahaa E. A. Saleh, Malvin C. Teich, and Alexander V. Sergienko. Wolf Equations for Two-Photon Light. *Phys. Rev. Lett.*, 94(22):223601, June 2005. doi: 10.1103/PhysRevLett.94.223601. URL https://link.aps.org/doi/10.1103/PhysRevLett.94.223601.

[253] Frauke Izdebski et al. *Quantum Correlations Measured with Multi-Pixel Detectors*. PhD thesis, Heriot-Watt University, 2013. URL http://hdl.handle.net/10399/2705.

[254] G. D. Boreman. Effect of defocus on MTF. In *Modulation Transfer Function in Optical and Electro-Optical Systems*, pages 27–29. SPIE Press, Bellingham, WA, 2001. URL https://doi.org/10.1117/3.419857.

[255] G. D. Boreman. Other MTF contributions. In *Modulation Transfer Function in Optical and Electro-Optical Systems*, pages 59–67. SPIE Press, Bellingham, WA, 2001. URL https://doi.org/10.1117/3.419857.

[256] I. Gyongy, N. Calder, A. Davies, N. A. W. Dutton, R. R. Duncan, C. Rickman, P. Dalgarno, and R. K. Henderson. A 256x256, 100-kfps, 61% Fill-Factor SPAD

Image Sensor for Time-Resolved Microscopy Applications. *IEEE Trans. Electron Devices*, 65(2):547–554, February 2018. ISSN 0018-9383. doi: 10.1109/TED.2017.2779790. URL https://doi.org/10.1109/TED.2017.2779790.

[257] Arin Can Ulku, Claudio Bruschini, Ivan Michel Antolović, Yung Kuo, Rinat Ankri, Shimon Weiss, Xavier Michalet, and Edoardo Charbon. A 512 × 512 SPAD Image Sensor With Integrated Gating for Widefield FLIM. *IEEE J. Sel. Top. Quantum Electron.*, 25(1):1–12, January 2019. ISSN 1558-4542. doi: 10.1109/JSTQE.2018.2867439. URL https://doi.org/10.1109/JSTQE.2018.2867439.

[258] A. Meda, E. Losero, N. Samantaray, F. Scafirimuto, S. Pradyumna, A. Avella, I. Ruo-Berchera, and M. Genovese. Photon-number correlation for quantum enhanced imaging and sensing. *J. Opt.*, 19(9):094002, August 2017. ISSN 2040-8986. doi: 10.1088/2040-8986/aa7b27. URL https://doi.org/10.1088%2F2040-8986%2Faa7b27.

[259] Eliot Bolduc, Daniele Faccio, and Jonathan Leach. Acquisition of multiple photon pairs with an EMCCD camera. *J. Opt.*, 19(5):054006, April 2017. ISSN 2040-8986. doi: 10.1088/2040-8986/aa52d8. URL https://doi.org/10.1088%2F2040-8986%2Faa52d8.

[260] Lothar Schermelleh, Rainer Heintzmann, and Heinrich Leonhardt. A guide to super-resolution fluorescence microscopy. *J. Cell Biol.*, 190(2):165–175, 2010. URL http://jcb.rupress.org/content/190/2/165.

[261] Bo Huang, Hazen Babcock, and Xiaowei Zhuang. Breaking the diffraction barrier: Super-resolution imaging of cells. *Cell*, 143(7):1047–1058, 2010. URL https://doi.org/10.1016/j.cell.2010.12.002.

[262] Manuel Unternährer, Bänz Bessire, Leonardo Gasparini, Matteo Perenzoni, and André Stefanov. Super-resolution quantum imaging at the Heisenberg

limit. *Optica*, 5(9):1150–1154, September 2018. ISSN 2334-2536. doi: 10.1364/OPTICA.5.001150. URL https://www.osapublishing.org/optica/abstract.cfm?uri=optica-5-9-1150.

[263] C. K. Hong and L. Mandel. Theory of parametric frequency down conversion of light. *Phys. Rev. A*, 31(4):2409–2418, April 1985. doi: 10.1103/PhysRevA.31.2409. URL https://link.aps.org/doi/10.1103/PhysRevA.31.2409.

[264] Luo Qi, Felix Just, Gerd Leuchs, and Maria V. Chekhova. Autonomous absolute calibration of an ICCD camera in single-photon detection regime. *Opt. Express, OE*, 24(23):26444–26453, November 2016. ISSN 1094-4087. doi: 10.1364/OE.24.026444. URL https://www.osapublishing.org/oe/abstract.cfm?uri=oe-24-23-26444.

[265] S. Friberg, C. K. Hong, and L. Mandel. Measurement of Time Delays in the Parametric Production of Photon Pairs. *Phys. Rev. Lett.*, 54(18):2011–2013, May 1985. doi: 10.1103/PhysRevLett.54.2011. URL https://link.aps.org/doi/10.1103/PhysRevLett.54.2011.

[266] DN Klyshko. A simple method of preparing pure states of the optical-field, a realization of the Einstein, Podolsky, Rosen experiment and a demonstration of the complementarity principle. *Uspekhi Fiz. Nauk*, 154(1):133–152, 1988. URL https://www.researchgate.net/publication/231027093_A_simple_method_of_preparing_pure_states_of_an_optical_field_of_implementing_the_Einstein-Podolsky-Rosen_experiment_and_of_demonstrating_the_complementarity_principle. (Accessed 20/03/2019).

[267] Bo Huang, Hazen Babcock, and Xiaowei Zhuang. Breaking the Diffraction Barrier: Super-Resolution Imaging of Cells. *Cell*, 143(7):1047–1058, December 2010. ISSN 0092-8674. doi: 10.1016/j.cell.2010.12.002. URL http://www.sciencedirect.com/science/article/pii/S0092867410014200.